

Automated deep phenotyping of the cardiovascular system
using magnetic resonance imaging

Dr Anish Naresh Bhuva
MRCP (UK) MSc MA (Cantab.) MBBS
Institute of Cardiovascular Science
University College London
2019

A thesis submitted in partial fulfilment of the requirements for the degree of Doctor of
Philosophy

Supervisors

Dr Charlotte H Manisty

Professor Alun D Hughes

Declaration of originality

I, Anish Bhuvu, confirm that the work presented in this thesis is my own. Where information has been derived from other sources, I confirm that this has been indicated in the thesis.

Signature:

Copyright declaration

The copyright of this thesis rests with the author and is made available under a Creative Commons Attribution Non-Commercial No Derivatives licence (CC BY NC ND).

Researchers are free to copy, distribute or transmit the thesis on the condition that they attribute it, that they do not use it for commercial purposes and that they do not alter, transform or build upon it. For any reuse or redistribution, researchers must make clear to others the licence terms of this work.

Abstract

Across a lifetime, the cardiovascular system must adapt to a great range of demands from the body. The individual changes in the cardiovascular system that occur in response to loading conditions are influenced by genetic susceptibility, and the pattern and extent of these changes have prognostic value. Brachial blood pressure (BP) and left ventricular ejection fraction (LVEF) are important biomarkers that capture this response, and their measurements are made at high resolution. Relatively, clinical analysis is crude, and may result in lost information and the introduction of noise. Digital information storage enables efficient extraction of information from a dataset, and this strategy may provide more precise and deeper measures to breakdown current phenotypes into their component parts.

The aim of this thesis was to develop automated analysis of cardiovascular magnetic resonance (CMR) imaging for more detailed phenotyping, and apply these techniques for new biological insights into the cardiovascular response to different loading conditions. I therefore tested the feasibility and clinical utility of computational approaches for image and waveform analysis, recruiting and acquiring additional patient cohorts where necessary, and then applied these approaches prospectively to participants before and after six-months of exercise training for a first-time marathon. First, a multi-centre, multi-vendor, multi-field strength, multi-disease CMR resource of 110 patients undergoing repeat imaging in a short time-frame was assembled. The resource was used to assess whether automated analysis of LV structure and function is feasible on real-world data, and if it can improve upon human precision. This showed that clinicians can be confident in detecting a 9% change in EF or a 20g change in LV mass. This will be difficult to improve by clinicians because the greatest source of

human error was attributable to the observer rather than modifiable factors. Having understood these errors, a convolutional neural network was trained on separate multi-centre data for automated analysis and was successfully generalizable to the real-world CMR data. Precision was similar to human analysis, and performance was 186 times faster. This real-world benchmarking resource has been made freely available (thevolumesresource.com).

Precise automated segmentations were then used as a platform to delve further into the LV phenotype. Global LVEFs measured from CMR imaging in 116 patients with severe aortic stenosis were broken down into ~10 million regional measurements of structure and function, represented by computational three-dimensional LV models for each individual. A cardiac atlas approach was used to compile, label, segment and represent these data. Models were compared with healthy matched controls, and co-registered with follow-up one year after aortic valve replacement (AVR). This showed that there is a tendency to asymmetric septal hypertrophy in all patients with severe aortic stenosis (AS), rather than a characteristic specific to predisposed patients. This response to AS was more unfavourable in males than females (associated with higher NT-proBNP, and lower blood pressure), but was more modifiable with AVR. This was not detected using conventional analysis.

Because cardiac function is coupled with the vasculature, a novel integrated assessment of the cardiovascular system was developed. Wave intensity theory was used to combine central blood pressure and CMR aortic blood flow-velocity waveforms to represent the interaction of the heart with the vessels in terms of traveling energy waves. This was performed and then validated in 206 individuals (the largest cohort to date), demonstrating inefficient ventriculo-arterial coupling in female sex and healthy ageing.

CMR imaging was performed in 236 individuals before training for a first-time marathon and 138 individuals were followed-up after marathon completion. After training, systolic/diastolic blood pressure reduced by 4/3mmHg, descending aortic stiffness decreased by 16%, and ventriculo-arterial coupling improved by 14%. LV mass increased slightly, with a tendency to more symmetrical hypertrophy. The reduction in aortic stiffness was equivalent to a 4-year reduction in estimated biological aortic age, and the benefit was greater in older, male, and slower individuals. In conclusion, this thesis demonstrates that automating analysis of clinical cardiovascular phenotypes is precise with significant time-saving. Complex data that is usually discarded can be used efficiently to identify new biology. Deeper phenotypes developed in this work inform risk reduction behaviour in healthy individuals, and demonstrably deliver a more sensitive marker of LV remodelling, potentially enhancing risk prediction in severe aortic stenosis.

Acknowledgments

I have benefited from and enjoyed the discussions, teaching and collaborations with a number of people from a variety of disciplines to inform this research.

Primarily, I have been supervised by three individuals who have challenged my skills in intellectual curiosity, clinical research and penmanship. I am thankful to Professor James Moon for building an exciting research environment, driven by his energy and inquiry. Professor Alun Hughes has often understood what I was trying to accomplish before I did, and has used his understanding of many disciplines to guide me. The work of this thesis (and more) has diverged from the initial discussions in the basement of the Heart Hospital. Since that early stage, I have been grateful to the constant confidence and guidance from Dr Charlotte Manisty, particularly for supporting me when I chose and pursued often variable and unpredictable directions.

I have learnt about topics that I previously knew little about from many people - at an early stage this was from Drs Thomas Treibel, Heeraj Bulluck, and Antonio de Marvao. Several colleagues have also provided teamwork, assistance and company, despite stretches of apparent absence whilst working across multiple sites- the team (more aptly, family) at the old Heart Hospital; the cardiac imaging group at Barts Heart Centre, the staff at the Institute of Cardiovascular Sciences (University College London), the students and post-doctoral staff at the Robert Steiner MRI Unit and Department of Computer Sciences (both Imperial College London), and the whole Marathon study team. A particular thanks to Professor Kellman for the opportunity to apply his work, and his consideration of my ideas.

Thanks also to the many patients and volunteers, friends and family who were scanned as part of this research, and the funders who made it possible.

I am most grateful to my family. To my mother, father and sister, what I have done, hope to do and can do, is thanks to your influence. To Shantilal Hergovindas Bhuvra, Lilaben Mehta, and Manilal Mehta, for valuing wisdom. The most important and greatest accomplishment of this period has, however, been with my wife. To Giulia, this doctoral work was carried out in parallel to starting our life together, and the latter was without doubt more than I could have hoped to achieve. I am excited that the completion of this thesis marks the start from where the rest of our life will lead.

Impact statement

People in modern society are living longer because of medical advances and public health initiatives. For the healthcare service to meet the needs of an ageing society it must provide care more efficiently. This can be through a preventative approach, by ensuring the lifestyle choices we make enable healthier living. Once disease is established, better sub-stratification and refined risk prediction can improve outcomes and reduce treatment costs by targeting therapies to those with the greatest potential for benefit. More precise, detailed (personalized) biomarkers can achieve this, and there is an increasing reliance on medical imaging. Automated analysis of large structured imaging datasets, as presented in this thesis, can help to derive the necessary phenotypes. This approach can improve decision-making by cardiologists through increased precision and speed. Doctors can then allocate time to more patient-centred activities, and cascade actionable measurements through the system to maximise efficiency of resource allocation. Put simply, the workforce and the healthcare system can become more effective. The potential impact is recognized by HM Government and the NHS.^{1,2}

Cardiovascular magnetic resonance (CMR) imaging is probably the best test to visualize the structure of the beating heart. Current analysis requires human contouring of heart muscle boundaries to quantify structure and function. These provide important markers of risk and are used daily in clinical decision-making, but sources of error are imperfectly known. These data show that currently, clinicians are able to detect only a rather large change of 9% in ejection fraction with confidence, because of human error. This means that disease diagnosis and progression are not detected until late. Sample sizes are also calculated to plan future clinical trials. Automated techniques using machine learning may provide an approach to improve confidence in absolute values,

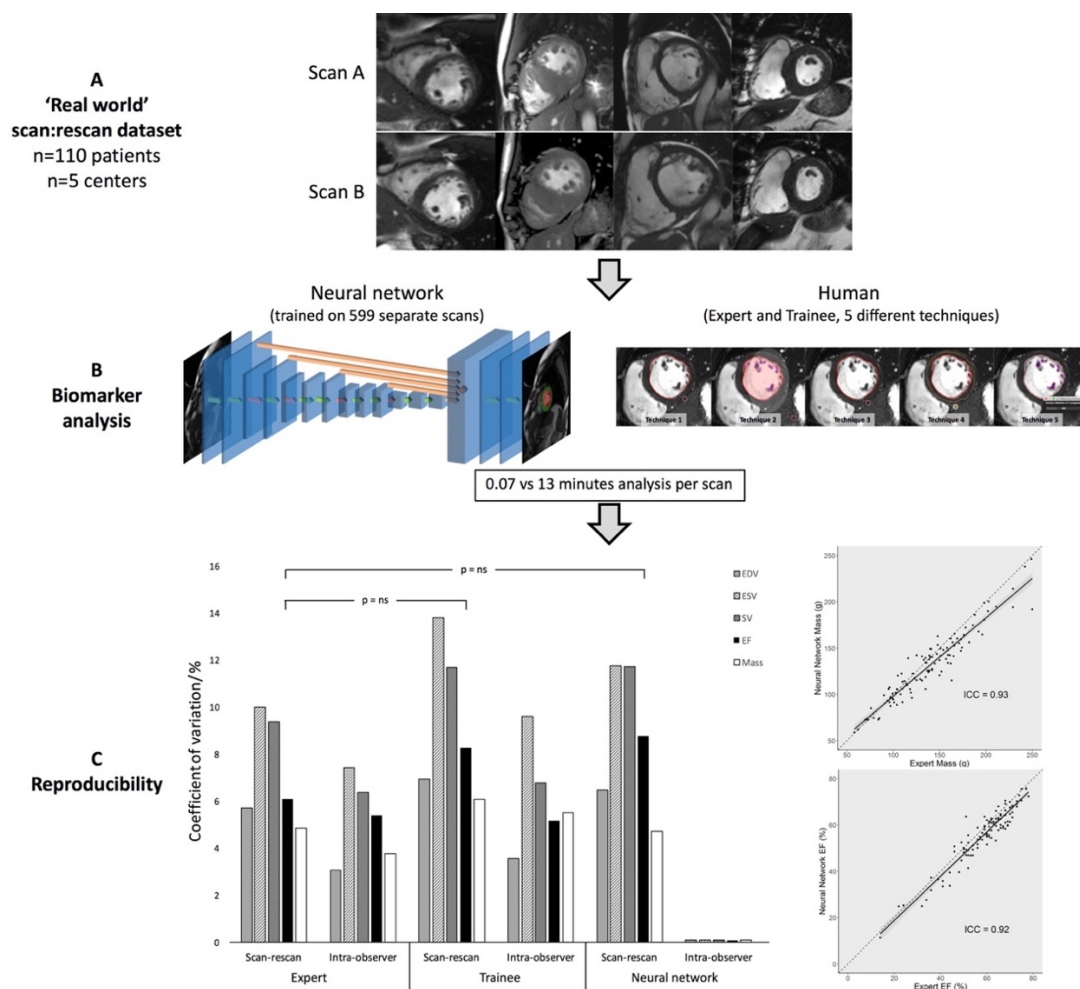
but should be reliable, valid and generalizable before widespread adoption. This was examined in this thesis using real-world CMR data, and automated performance was shown to be 186 times faster than using conventional techniques with no reduction in accuracy or precision. This supports the global adoption of automated CMR analysis to gain from time-saving and standardization benefits. The real-world benchmarking resource has also been made available to the research community at thevolumesresource.com, and includes a built-in web application to perform precision benchmarking against experts. It has already been used in two further studies validating new measures of remodelling, and a deep learning analysis technique.

Accurate automated segmentation is a bridge to develop more personalized cardiovascular phenotypes. Techniques to extract more information from clinical CMR datasets were used to understand the 3-dimensional structure of the left ventricle (LV), and its complex interaction with the circulation. This thesis describes feasible approaches, that are possible at scale in health and disease. Because more personalized LV phenotyping showed greater sensitivity than conventional phenotypes in patients with severe AS, it potentially provides a framework to enhance risk stratification.

Ventriculo-arterial coupling was measured simply and non-invasively, and so the technique is now being used to understand changes in hypertensive patients, Anderson-Fabry disease, obesity and Conn's syndrome. In the future, this may help to understand what contributes to adverse cardiac remodelling, particularly in patients with heart failure and preserved ejection fraction.

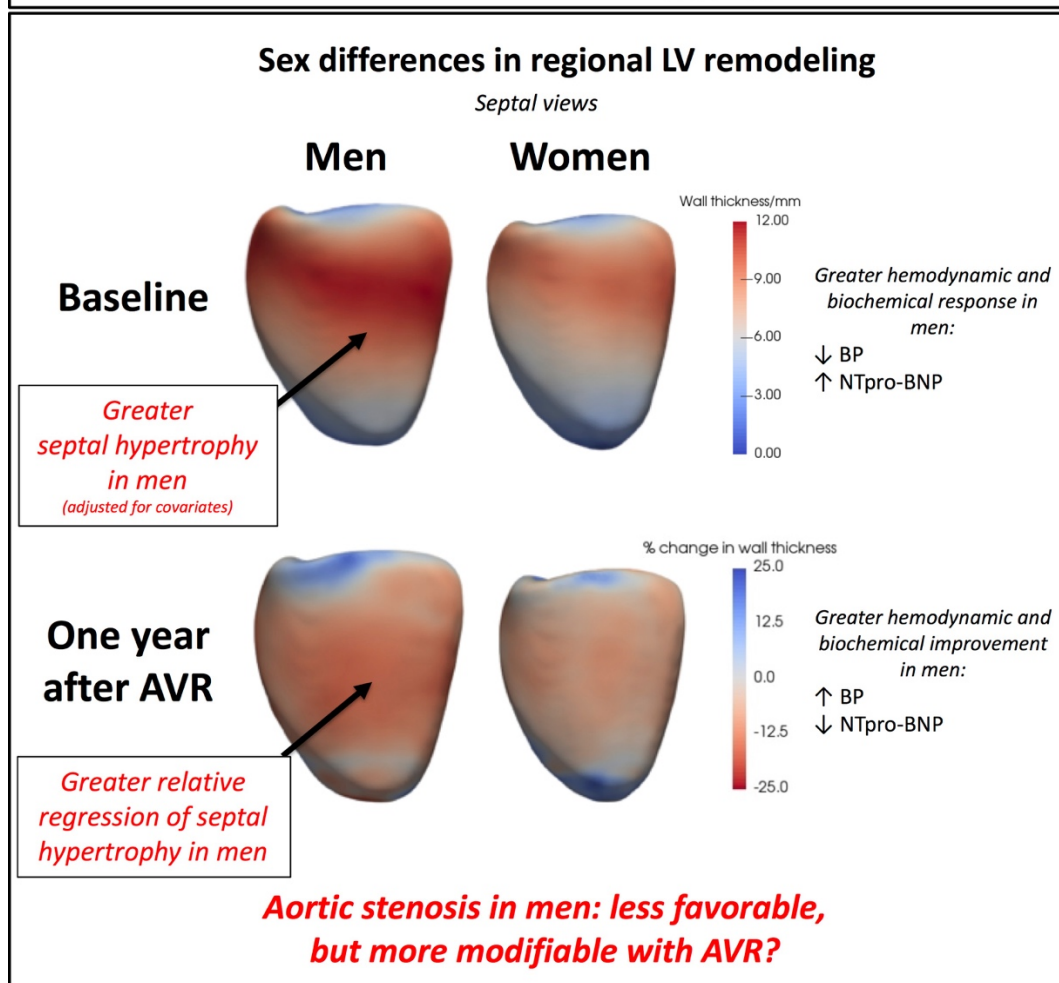
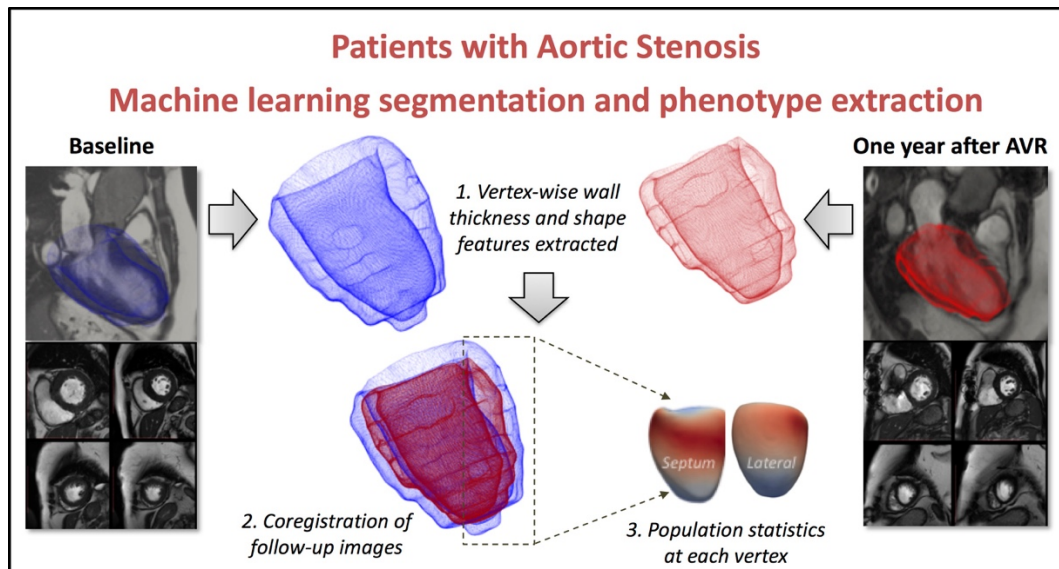
Prospectively, detailed descriptions of cardiovascular function were studied in individuals undertaking exercise training for a first-time marathon. Whilst the benefits of supervised or lifelong exercise are well studied, it is not known if benefits are generalisable to recreational exercise, and what exercise dose is needed. The

Visual abstracts of Results



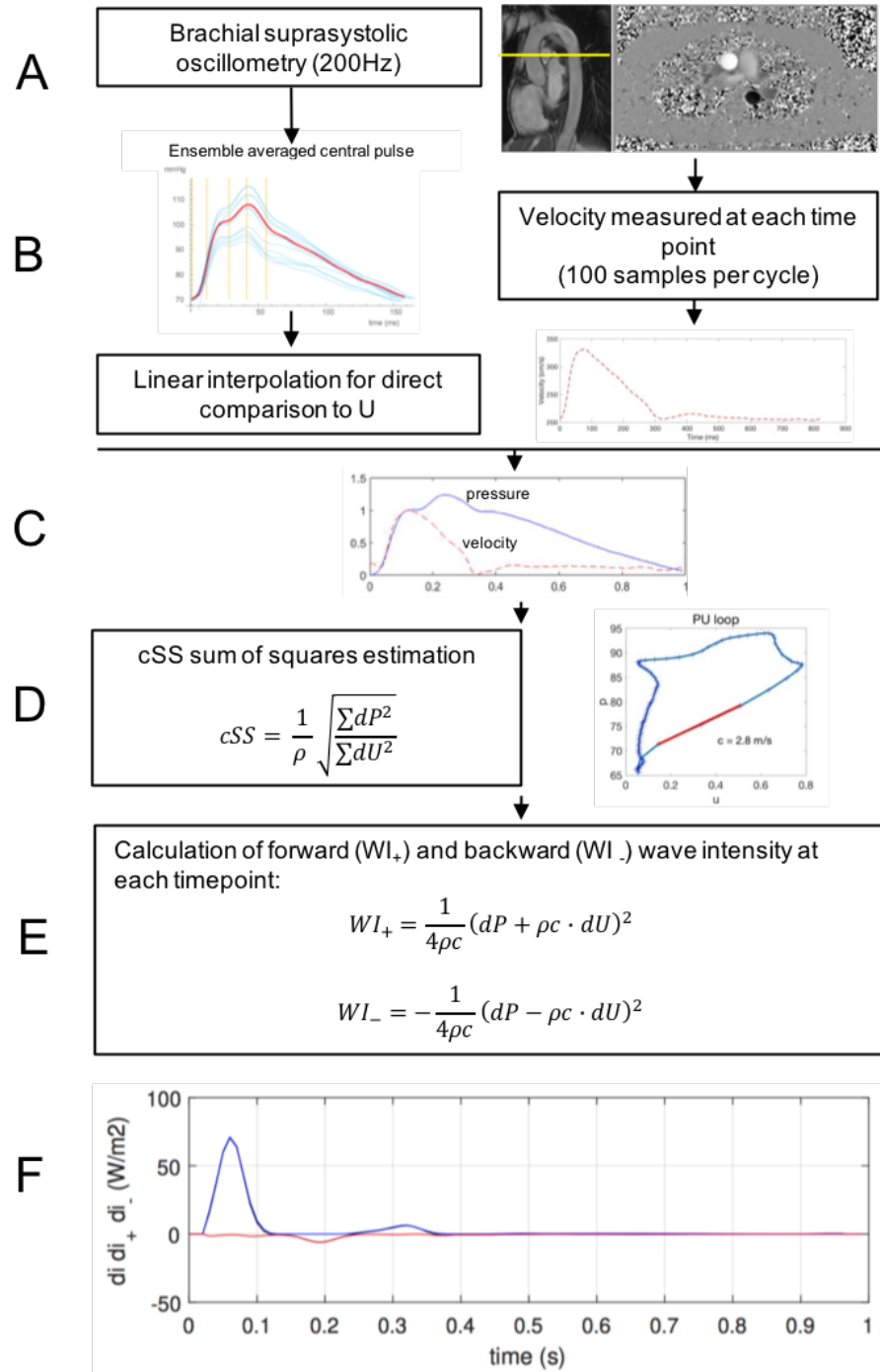
Visual Abstract 1 (Chapter 4): Head-to-head performance of image biomarker analysis using human and machine learning approaches.

(A) Real world imaging biomarker analysis using 110 patients undergoing multi-centre, multi-disease, multi-vendor, multi-field strength cardiovascular magnetic resonance imaging on two consecutive occasions in a short time frame. **(B)** Machine learning using a convolutional neural network approach, and human analysis with five different approaches are used to extract left ventricular ejection fraction (LVEF), mass, end-diastolic volume (EDV), end-systolic volume (ESV) and stroke volume (SV). **(C)** There is equivalent precision for all LV metrics (scan-rescan coefficient of variation, CV) between an expert and neural network approach, in addition to good inter-observer accuracy. A significant source of human error is attributable to intra-observer error (CV). *Abbreviations: ICC= Lin's intra-class coefficient; ns= non-significant.*



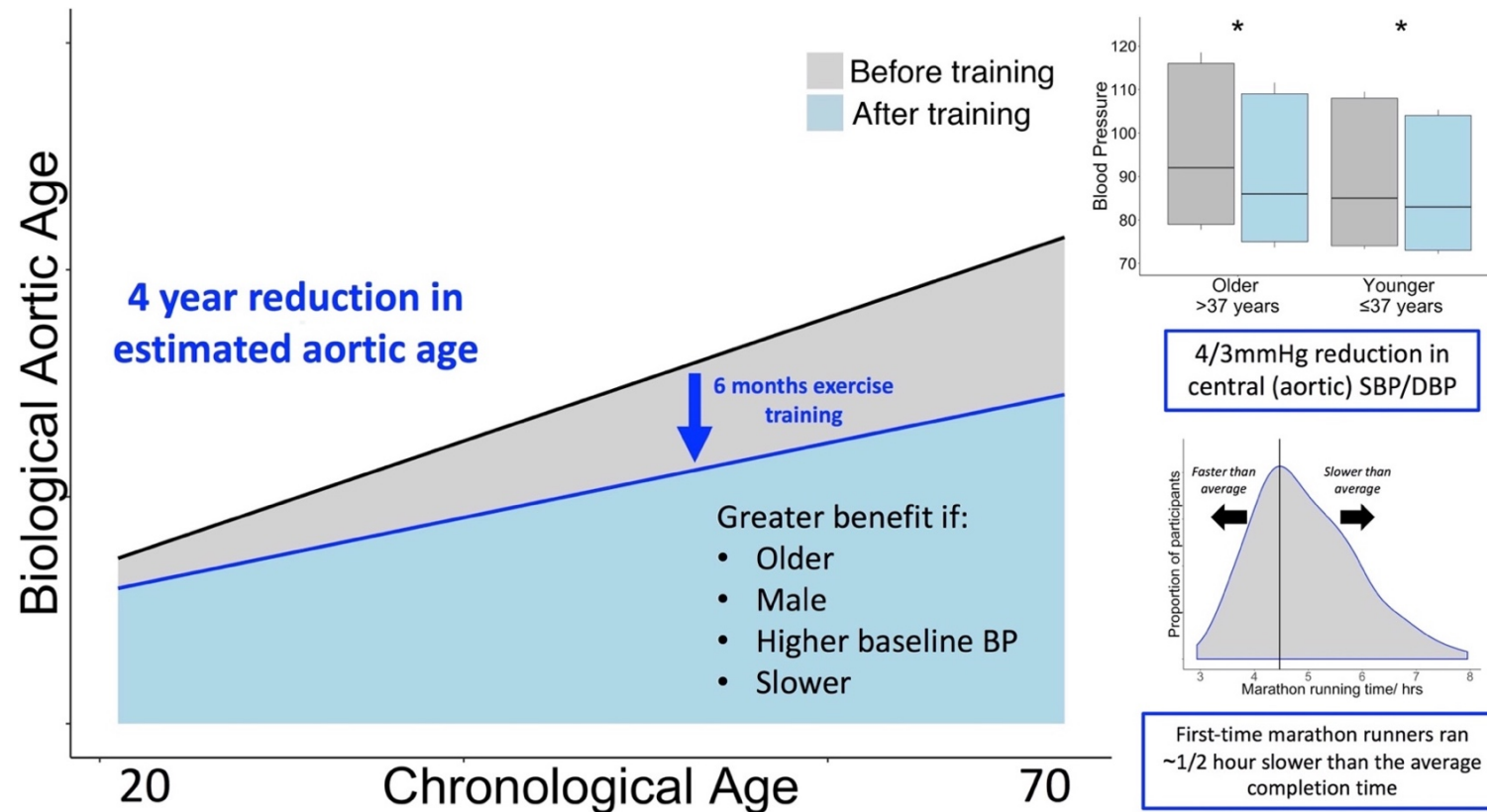
Visual Abstract 2 (Chapter 5): 3D phenotype assessment to identify sex differences in regional LV remodelling in aortic stenosis.

Top: Imaging data is used to construct 3D ventricular models which are co-registered with follow-up studies. This approach permits regional analysis of shape and wall thickness. **Bottom:** Male patients have a greater hemodynamic, biochemical and remodelling response to aortic stenosis which is more modifiable with valve replacement. *Abbreviations: AVR = aortic valve replacement; BP= blood pressure; NTpro-BNP: N-terminal pro brain natriuretic peptide.*



Visual Abstract 3 (Chapter 6): Construction of aortic wave intensity analysis using blood pressure and CMR-derived velocity data

(A) After a period of rest the patient underwent oscillometric brachial blood pressure on two occasions immediately prior to MRI. A Pulsecor BP+ device acquired 10s of brachial waveforms at 200Hz. After, phase-contrast MRI was acquired at the level of the pulmonary artery using a free-breathing ECG gated sequence, acquired at c.100Hz at 60bpm. **(B)** A single ensemble averaged central pressure (P) was estimated and velocity (U) measured at each time point. **(C)** Data was aligned by waveform foot to foot. **(D)** wave speed measured in early systole using the pressure-velocity loop and sum of squares method after the application of a Savitsky-Golay filter. **(E)** Wave intensity calculated using the derivatives of pressure and velocity. ρ : density of blood (1050kg/m³), c : P-U derived wave speed; cSS: sum of squares estimated c . **(F)** Wave intensity analysis example showing initial forward compression, backward compression and protodiastolic decompression waves.



Visual Abstract 4 (Chapter 7): Training and completion of a first-time marathon reverses age-related aortic stiffening and reduces central (aortic) blood pressure.

Aortic age was calculated from the baseline age-stiffness relationship at assessment six months before and two weeks after a first marathon. The reduction in aortic stiffness was equivalent to a four-year reduction in estimated aortic age. These benefits were greater in older, male, slower runners with higher baseline blood pressure (BP), in adjusted models. In the main graph, data are the linear age-stiffness relationship before and after exercise training. *Abbreviations: **= $p<0.05$.

Table of Contents

<i>Declaration of originality</i>	<i>i</i>
<i>Copyright declaration</i>	<i>i</i>
<i>Acknowledgments</i>	<i>v</i>
<i>Impact statement</i>	<i>vii</i>
<i>Visual abstracts of Results</i>	<i>x</i>
<i>Table of Contents</i>	<i>15</i>
<i>List of Figures</i>	<i>17</i>
<i>List of Tables</i>	<i>19</i>
<i>List of equations</i>	<i>20</i>
<i>Abbreviations</i>	<i>21</i>
1. Introduction	23
1.1. Scope of thesis	23
1.2. Cardiac remodelling	26
1.3. Cardiovascular assessment using MRI	41
1.4. A deep phenotyping approach	58
1.5. Arterial function	76
1.6. Remodelling in aortic stenosis	91
1.7. Remodelling and exercise training	94
2. Research aims and objectives	100
2.1. Hypothesis	100
2.2. Aims	101
3. Methods	102
3.1. Outline and personal contribution	102
3.2. Scan-rescan precision cohort	105
3.3. Patients with severe aortic stenosis	107
3.4. Novice marathon runners	110
3.5. CMR protocols used across all studies	115
3.6. Haemodynamic measurements	119
3.7. CMR analysis	120
3.8. 3D ventricular phenotyping using a cardiac atlas approach	122
3.9. Aortic stiffness analysis	138
4. Generalizability and precision of automated LV structure and function	141
4.1. Introduction	142
4.2. Methods	144
4.3. Results	153
4.4. Discussion	165
4.5. Conclusion	171
5. Utility of 3D LV modelling in patients with aortic stenosis	172
5.1. Introduction	173
5.2. Methods	175
5.3. Results	182
5.4. Discussion	197
5.5. Conclusion	203

6.	<i>Feasibility and validation of aortic wave intensity analysis</i>	204
6.1.	Introduction	205
6.2.	Methods	207
6.3.	Results	219
6.4.	Discussion	224
6.5.	Conclusion	227
7.	<i>Application of automated analysis techniques to assess cardiovascular remodelling in novice marathon runners</i>	228
7.1.	Introduction	229
7.2.	Methods	231
7.3.	Results	238
7.4.	Discussion	249
7.5.	Conclusion	255
8.	<i>Discussion</i>	257
8.1.	Summary of key contributions	257
8.2.	Future directions	262
8.3.	Limitations	266
8.4.	Conclusions	267
9.	<i>Academic Outputs</i>	268
9.1.	Awards during this studentship	268
9.2.	Publications during this studentship	269
9.3.	Presentations	275
9.4.	Invited presentations during this studentship	277
9.5.	Co-authored presentations and abstracts	278
9.6.	Collaborations	281
9.7.	Teaching	282
9.8.	Funding enabling this work	283
10.	<i>References</i>	284

List of Figures

Figure 1-1 Cardiac remodelling in the Burmese python	30
Figure 1-2 Different patterns of hypertrophy	32
Figure 1-3 Non-invasive assessment of LVH over the last sixty years	35
Figure 1-4 Accuracy and precision	36
Figure 1-5 Impact of precision on clinical decision-making (simulated data)	38
Figure 1-6 T1 and T2 relaxation curves	44
Figure 1-7 Signal encoding and decoding in MRI	45
Figure 1-8 Fourier transformation of periodic sine waves	46
Figure 1-9 Spoiled gradient echo pulse sequence	51
Figure 1-10 Steady-state free precession pulse sequence	53
Figure 1-11 3D-cine imaging	55
Figure 1-12 Quantification of eye colour	58
Figure 1-13 Increasing publication rate of articles related to “Phenomixs”	60
Figure 1-14 Pixel classification method using Gaussian Mixture Models	63
Figure 1-15 Good experimental performance is not good clinical performance	66
Figure 1-16 Principal Component Analysis	71
Figure 1-17 Central aortic pressure waveform	82
Figure 1-18 Westerhof's experiments on wave shape and timing	83
Figure 1-19 Non-invasive pressure waveforms	85
Figure 1-20 Aortic wave intensity analysis	89
Figure 3-1 Imaging data collaborations proposal	106
Figure 3-2 RELIEF-AS study flow chart	108
Figure 3-3 Marathon Study flow chart	111
Figure 3-4 “Beginner's Training Programme” for first time marathon runners	112
Figure 3-5 Manual labelling of a cardiac atlas	123
Figure 3-6 Location of six landmarks to initialize a segmentation	124
Figure 3-7 Example of a good target segmentation	125
Figure 3-8 Example of an unacceptable segmentation with slice-misregistration	126
Figure 3-9 3D wall thickness for one patient with aortic stenosis	128
Figure 3-10 3D surface displacement relative to an average template shape	129
Figure 3-11 Mean wall stress in patients with aortic stenosis	131
Figure 3-12 2D vs 3D cine imaging	132
Figure 3-13 Segmentations from 2D and 3D cine imaging	132
Figure 3-14 Inaccurate atlas-based segmentations 3D-cine imaging	133
Figure 3-15 Failed segmentations examples	134
Figure 3-16 Smoothing of left ventricular curvature models	135
Figure 3-17 Application of a Savistky-Golay smoothing filter	136
Figure 3-18 Smoothed target segmentation overlaid onto original dicom data	137
Figure 3-19 Successfully smoothed ventricular geometry and wall thickness	137
Figure 3-20 Phase contrast CMR analysis	138
Figure 4-1 VOLUMES study flow chart	145
Figure 4-2 Manual and semi-automated endocardial segmentation techniques	146
Figure 4-3 Request for analysis technique collaborations	148
Figure 4-4 Segmentations after training on ~300 annotated datasets	150

List of Figures

Figure 4-5 Segmentations after training on all annotated datasets	150
Figure 4-6 Correlation plots and Bland-Altman plots for ejection fraction	157
Figure 4-7 Correlation plots and Bland-Altman plots for mass	157
Figure 4-8 Scan-rescan coefficient of variation	160
Figure 4-9 Examples of different observer contours	162
Figure 4-10 Contributions of intra-, inter-observer and scan-rescan error	163
Figure 5-1 Co-registration of 3D LV models from a CMR scan and rescan	179
Figure 5-2 Number of pairs needed to detect a 1mm change in wall thickness	183
Figure 5-3 Correlations and Bland-Altman plots for atlas and human analysis.	184
Figure 5-4 LV shape and wall thickness in patients with aortic stenosis	187
Figure 5-5 Sex difference in regional wall thickness	190
Figure 5-6 Changes in remodelling categories at one year after AVR	191
Figure 5-7 Percentage change in wall thickness at one year after AVR	191
Figure 5-8 Patients with AS and normal baseline geometry	195
Figure 6-1 Original ensemble-averaged and interpolated waveforms	209
Figure 6-2 Waveform alignment	210
Figure 6-3 Measurement of ρc with good and poor waveform alignment	212
Figure 6-4 Aortic wave intensity analysis	213
Figure 6-5 Quantification of wave area	214
Figure 6-6 Quantification of an asymmetric peak	215
Figure 6-7 Correlation and Bland-Altman plots for wave speed and PWV	220
Figure 6-8 Influence of age on wave speed and wave intensity indices	221
Figure 7-1 Baseline associations of age and aortic stiffness measures	234
Figure 7-2 3D LV models for marathon trainees at baseline and follow-up	235
Figure 7-3 London Marathon running times for study participants	238
Figure 7-4 Changes in vascular measures with exercise training	241
Figure 7-5 Aortic blood pressure, aortic stiffness and estimated aortic age	242
Figure 7-6 Increase in 3D LV wall thickness with exercise training	248
Figure 7-7 Non-septal redistribution of LV mass with exercise training	248
Figure 7-8 Mechanisms of aortic stiffness reduction	251

List of Tables

Table 1-1 Classification of left ventricular hypertrophy	29
Table 1-2 Cellular, tissue and macroscopic LV remodelling	31
Table 1-3 International vocabulary of Metrology	36
Table 1-4 Contrast weighting for MR sequences	44
Table 1-5 Types of MR signals	48
Table 1-6 Sequence parameters to adjust contrast weighting	49
Table 1-7 “Grand Challenges” contestants in CMR imaging analysis	75
Table 1-8 Clinical conditions associated with increased aortic stiffness	88
Table 1-9 Physiologic versus pathologic hypertrophy	94
Table 3-1 Cohorts and CMR sequences used in this thesis	102
Table 3-2 CMR protocols for the Marathon and RELIEF-AS studies	115
Table 3-3 Cine sequence parameters for the RELIEF-AS and Marathon studies	117
Table 3-4 Cine sequence parameters for the VOLUMES study	117
Table 3-5 CMR Phase- contrast sequence parameters in the Marathon Study	118
Table 4-1 Study participant characteristics	153
Table 4-2 Inter-observer improvement in agreement after training	154
Table 4-3 Manual and semi-automated technique precision	155
Table 4-4 Observer bias	156
Table 4-5 Observer precision	158
Table 4-6 Scan-rescan and intra-observer reproducibility	159
Table 4-7 Sample size estimates stratified by observer and pathology	164
Table 5-1 Characteristics of matched controls	176
Table 5-2 Accuracy of atlas-based global LV metrics	182
Table 5-3 Baseline clinical characteristics of patients with AS	186
Table 5-4 Association of gender with LV mass and age	189
Table 5-5 Global LV metrics at baseline	189
Table 5-6 Global LV metrics one year after AVR	192
Table 5-7 Clinical characteristics one year after AFR	194
Table 5-8 Baseline characteristics split by LV remodelling category	196
Table 6-1 Study participant characteristics stratified by sex and age decile	218
Table 6-2 Wave intensity analysis stratified by sex and age decile	222
Table 6-3 Associations of wave intensity peaks with age	223
Table 7-1 Baseline follow-up characteristics after exercise training	239
Table 7-2 Baseline and follow-up vascular measures after exercise training	243
Table 7-3 Associations between change in aortic stiffness and training	246

List of equations

Equation 1-1 The Boltzmann distribution	42
Equation 1-2 The Larmor equation	42
Equation 3-1 Wall stress estimation	130
Equation 3-2 Pulse wave velocity	138
Equation 3-3 Aortic distensibility	139
Equation 6-1 Water-hammer equation	211
Equation 6-2 Wave speed using the pressure velocity loop	211
Equation 6-3 Wave speed estimated from the sum of squared differences	212
Equation 6-4 Net wave intensity	213
Equation 6-5 Forward and backward wave intensities	213
Equation 6-6 Integration of a gaussian peak area	215
Equation 7-1 Beta-stiffness	232

Abbreviations

2D	Two-dimensional
3D	Three-dimensional
β -stiffness	Beta-stiffness (pressure-independent stiffness)
BSA	Body-surface area
AHA	American Heart Association
AS	Aortic stenosis
AVR	Aortic valve replacement
BCW	Backward compression wave
BP	Blood pressure
BSA	Body-surface area
bSSFP	balanced steady-state free precession
c	Local wave speed estimated from the pressure-velocity loop
CMR	Cardiovascular magnetic resonance imaging
CNN	Convolutional neural network
CPET	Cardio-Pulmonary Exercise Test
c SS	Local wave speed estimated from sum of squares method
CV	Coefficient of variation
DBP	Diastolic Blood Pressure
EDV	End diastolic volume
ECG	Electrocardiography
ESV	End systolic volume
FCW	Forward compression wave
FDW	Forward (holodiastolic) decompression wave
GRE	Gradient echo
LoA	Limits of agreement
LV	Left ventricular
LVEF	Ejection fraction
LVM	Left ventricular mass
LVH	Left ventricular hypertrophy
LVMi	Left ventricular mass indexed to body surface area
MVR	Mass to end-diastolic volume ratio
NT-proBNP	N-terminal pro-brain natriuretic peptide
Peak VO_2	Maximal oxygen consumption
PP	Pulse Pressure
FDW	Forward (protodiastolic) decompression wave
HR	Heart rate
MAP	Mean arterial pressure
MDC	Minimal detectable change
MR	Magnetic resonance
P	Pressure
PWV _(tt)	Pulse wave velocity (calculated using transit time)

Abbreviations

RELIEF	REgression in Left ventricular Interstitial Expansion and myocardial Fibrosis after aortic valve replacement
RI	Reflection index
RM	Reflection magnitude
RWT	Relative wall thickness
SBP	Systolic Blood Pressure
T	Tesla
T1	Longitudinal relaxation
T2	Transverse relaxation
TE	Echo time
TR	Repetition time
U	Velocity
VOLUMES	Validation Of Left ventricular and Myocardial and Endocardial Segmentation
WIA	Wave intensity analysis

1. Introduction

1.1. Scope of thesis

In this Chapter, I will discuss how across a lifetime, the cardiovascular system must adapt to a great range of demands from the body. Part of this adaptation involves structural remodelling of the cardiovascular system. I will describe how remodelling is characterized by changes in both left ventricular (LV) structure to maintain stroke volume ejection, and the aorta to buffer pulsatile stroke volume and translate it into more steady peripheral flow. I will explain how cardiovascular assessment can be made using cardiovascular magnetic resonance (CMR) imaging for both the LV and the aorta. Whilst this is performed at high spatial resolution, clinical analysis is remarkably crude. I will therefore explain measurement metrology standards, and how digital information storage enables efficient extraction of information from a dataset, and why this strategy may provide more precise and deeper measures to breakdown current phenotypes into their component parts. Because the individual response to similar loading conditions shows great variation, I will describe remodelling patterns in volume (exercise training) and pressure (aortic stenosis) overload, in which deeper phenotypes are later studied. In Chapter 2, I will state the aims of this thesis. Broadly, this work aims to determine the feasibility and additional benefit of more detailed cardiovascular phenotypes derived from automated CMR analysis, and their application to understanding cardiovascular remodelling under different loading conditions.

In Chapter 3, I will outline study recruitment, my contributions, and the use of previously published analysis methodologies.

Results in Chapters 4 to 6 describe the feasibility and incremental utility of extracting different cardiovascular biomarkers from CMR imaging. In Chapter 7, these techniques

are applied prospectively to participants before and after six-months of exercise training for a first-time marathon.

In Chapter 4, I will describe the assembly and use of a multi-centre, multi-vendor, multi-field strength, multi-disease CMR resource to assess whether automated LV analysis is feasible on real-world data, and if it can improve upon human precision.

After understanding human errors in precision, a convolutional neural network is then trained, successfully generalized to the real-world CMR data, and compared to the most precise human technique. This real-world data is compiled into a benchmarking resource and is made freely available (thevolumesresource.com).

In Chapter 5, precise automated segmentations will be used as a platform to delve further into the LV phenotype. CMR derived global LVEFs in 116 patients with severe aortic stenosis are broken down into ~10 million regional samples of structure and function, represented by computational three-dimensional LV models for each individual. A cardiac atlas approach is used to compile, label, segment and represent these data. Models are compared with healthy matched controls, and co-registered with follow-up one year after aortic valve replacement (AVR). This approach is used to detect a more unfavourable remodelling response in males than females with AS, and is shown to be more sensitive than conventional assessment.

In Chapter 6, because cardiac function is coupled to the vasculature, an integrated assessment of the cardiovascular system based on CMR is developed. Wave intensity analysis was used to analyse central blood pressure and CMR aortic blood flow-velocity waveforms to characterise the interaction of the heart with the vessels in terms of traveling energy waves. This is performed and then validated in 206 individuals (the largest cohort of aortic wave intensity to date), providing insights into sex differences and healthy ageing.

Introduction

In Chapter 7, these techniques are applied prospectively to understand the cardiovascular effects of aerobic exercise training. I performed CMR imaging in 236 individuals training for a first-time marathon. 138 individuals are followed-up after six-months of training and completion of a marathon. The change in phenotypes relating to blood pressure, aortic stiffness, ventriculo-arterial coupling and left ventricular remodelling are described.

In Chapter 8, I provide a summary of findings, future work and limitations.

In Chapter 9, I state the academic outputs from this work.

1.2. Cardiac remodelling

Across our lifetime, the heart is capable of adapting to the great range of demands which the environment makes on the body. Short-term adaptations are largely mediated by neuro-endocrine or “myogenic” responses but in the longer term, adaptation frequently involves growth and structural remodelling of the heart and arteries.

Exercise, pregnancy and development from embryo to adulthood are strong drivers to physiological myocardial growth, but similar magnitudes of morphological changes are also observed in pathological loading conditions where this is associated with increased cardiovascular mortality, most notably because of heart failure. Whilst rates of most cardiovascular diseases are declining in the UK, the burden of heart failure is increasing, costing 2% of total NHS resources.^{3,4}

Changes take place anatomically and at a cellular level before the onset of heart failure; these can be considered components of “cardiac remodelling”. William Osler noted this in 1892 where he describes in *Affections of the Myocardium* that this was a key stage in developing heart failure with aortic stenosis, as hypertrophy is followed by a “period of broken compensation... that commonly takes place slowly and results from degeneration and weakening of the heart muscle”.⁵ These observations heralded the transition in late nineteenth century Cardiology from post-mortem anatomy to an infant medical specialty where the heart was assigned adaptive living properties that could be measured by new technology, including the polygraph (electrocardiography, ECG), chest roentgenograph (radiograph) and sphygmomanometer.⁶ Osler appreciated that hypertrophy varied - “the limits to which hypertrophy may progress are small, though very marked hypertrophy is sometimes seen in the aged”.⁷ Only seven years later, similar remodelling changes were described in cross-country skiers by percussion of the chest wall and that contrastingly these changes were normal and favourable.⁸ In practice today, the distinction between adaptive

and maladaptive remodelling is still blurred, and the continuing endeavour to understand mechanisms that underpin this dichotomy can allow us to identify modifiable risk factors⁹ and target therapies.¹⁰

1.2.1. The relationship between left ventricular structure and function

William Harvey proposed that the heart functioned like “water bellows... constricting to eject and dilating to fill”.¹¹ Since 1628, there has been an increase in our understanding of how cardiac structure can perform this function, and it is unsurprising that the literature describes this primarily in the left ventricle (LV), the chamber that performs the chief component of cardiac work.⁷ LV structure and function are complex; Harvey described the left ventricle as consisting of a “massive circular expelling coat set between an outer and inner spiral coat”, contracting on a fixed axis from the aorta to apex.¹² The complex link between ventricular structure and function was further appreciated in the 17th century when Lower and Borelli both attributed the spiral fibre structure to ventricular torsion.¹¹ Debate exists whether helical and circumferential muscle fibres constitute separate bundle tracts, or one unified ventricular band that when twisted produces different fibre orientations.¹¹ Nevertheless, bioengineering models of fibre orientation and ventricular geometry show that such structural adaptations are useful to provide a mechanical advantage for ejection performance.¹³ The LV is designed to compress, dilate, shorten, lengthen, twist and untwist, in order to work efficiently to eject blood against the resistance of aortic blood pressure. Whilst the LV pumps ~7200L of blood each day against a mean arterial pressure of ~100mmHg, it still needs to adapt to increase cardiac output by up to 50% observed in pregnancy¹⁴ or simply to maintain cardiac output against a sustained increase in afterload, as with aortic stenosis or hypertension.

In the face of a haemodynamic burden, the LV is able to compensate by four approaches:¹⁵

1. Stretch-dependent increase in force generation through the Frank-Starling relationship;¹⁶
2. Heart rate increase which increases peak isometric force in cardiac muscle through a force-frequency relationship (the Treppe effect);¹⁷
3. Neuro-hormonal modulation, including the autonomic nervous (sympathetic and parasympathetic), and renin-angiotensin-aldosterone systems;
and
4. Normalisation of wall stress by changes in LV cavity size and wall thickness.

The Frank – Starling mechanism and force-frequency effect are attenuated in the failing human myocardium;^{15,17} and long-term neuro-hormonal activation is detrimental in heart failure. Thus, geometric remodelling, and in particular LV hypertrophy (LVH) may be a key adaptation.

1.2.2. Left ventricular remodelling

Remodelling in the cardiovascular system can occur with or without hypertrophy (i.e. increase in tissue mass). Left ventricular hypertrophy has been characterized using different approaches, and these labelling systems highlight that such simplicity, whilst appealing, fails to recognize the complexity in the process, Table 1-1.

Categorization paradigm	Explanation
Concentric versus eccentric	<i>Chamber morphology</i>
Physiological versus pathological	<i>Nature of the loading condition</i>
Compensated versus decompensated	<i>Presence of heart failure</i>
Adaptive versus maladaptive	<i>Outcome</i>

Table 1-1 Different classification approaches to left ventricular hypertrophy.

The underlying goal is to identify hypertrophy that contributes (or does not contribute) to morbidity and mortality. However, there are few circumstances where remodelling can be so easily defined. The Burmese python, when faced with a massive meal (~25% of body weight) can increase ventricular mass by 40% in 48 hours which regresses over weeks, Figure 1-1.¹⁸ In humans, purely physiological myocardial changes in LV mass are not as profound, but do exist. In pregnancy, LV mass increases 16% and regresses over a period of months.^{19,20} Zebra fish are able to remodel their heart in more extreme ways as they are able to differentiate new cardiac myocytes after 20% of myocardium has been surgically removed, representing a form of cardiac plasticity that is not available to humans.²¹

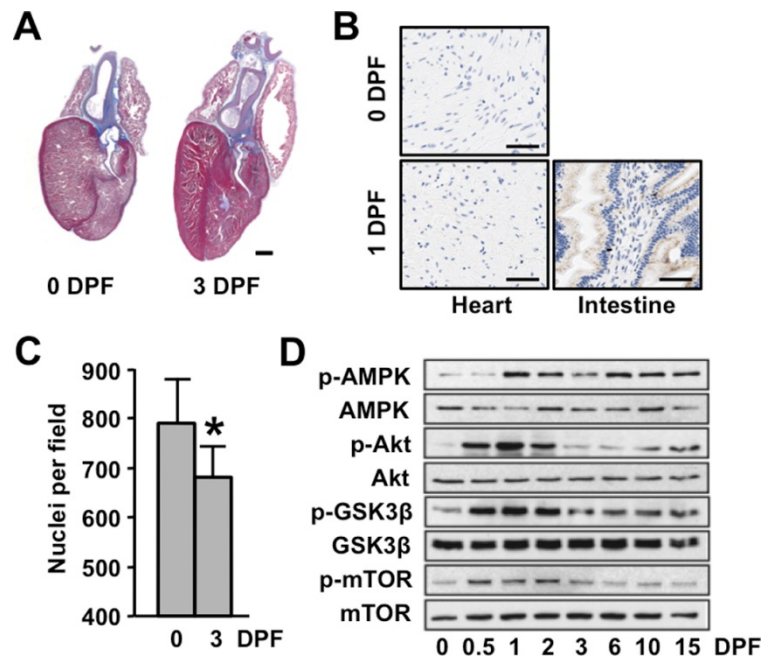


Figure 1-1 Cardiac remodelling by changes in morphology and protein synthesis in the Burmese python, from *Riquelme et al.*²².

There is pronounced post prandial cardiac hypertrophy (A), no cellular proliferation (B), but cellular hyperplasia (C). Immunoblot analysis (D) reveals increased phosphorylation of proteins in the postprandial python heart activated in protein synthesis pathways. An increase in myocyte fatty acid transport and oxidation was also noted. *DPF*= day post feed. Reproduced with permission from *The American Association for the Advancement of Science*.

Defining such examples allows us to understand the genomic, metabolic, cellular and interstitial pathways that are represented at a structural level, Table 1-2.²³ In humans however, cardiac remodelling is a spectrum which often simultaneously represent physiological and pathological adaptation.^{24,25}

In early experimental models of aortic constriction by Meerson,²⁶ hypertrophy was described as a continuum initially to normalise the workload to mass ratio resulting in “compensatory hyperfunction”. Over time in aortic constriction models, heart failure developed with gross left ventricular systolic impairment and dilatation, and fibrosis at a cellular level. Grossman explained this process as an adaptive mechanism to normalise wall stress as a result of increased LV pressure.²⁷ This concept relied on an extension of

the Laplace law to the heart, as this was initially applied to thin walled curved membranes.²⁸

Alterations in myocyte processes
Excitation-contraction coupling
Myosin heavy chain (fetal) gene expression
Beta-adrenergic desensitization
Myocyte hypertrophy
Myocytolysis
Cytoskeletal proteins
Myocardial changes
Myocyte loss via necrosis, apoptosis or autophagy
Alterations in extra cellular matrix via matrix degradation or fibrosis
Alterations in left ventricular structure
Cavity size
Sphericity
Wall thickness

Table 1-2 Left ventricular remodelling at the cellular, tissue and organ level.

Adapted from Braunwald's Heart disease, 9th Edition, Elsevier.

In this example, pressure overload results in concentric hypertrophy with a greater wall thickness than radius as a response to increased peak systolic stress. Volume overload conversely results in equivalent increases in both wall thickness and volume as a response to increased end diastolic stress.²⁷ The transduction of changes in wall stress into myocardial adaptation is poorly understood.²⁹ Cavity dilatation has been linearly associated with the degree of volume overload, but the relationship between wall thickness with pressure overload is less consistent.^{30,31} Morphological changes are also paralleled in the myocyte - pressure overload is associated with wider myocytes due to parallel addition of myofibrils, and volume overload is associated with both wider and longer myocytes due to sarcomere elongation, Figure 1-2.³²

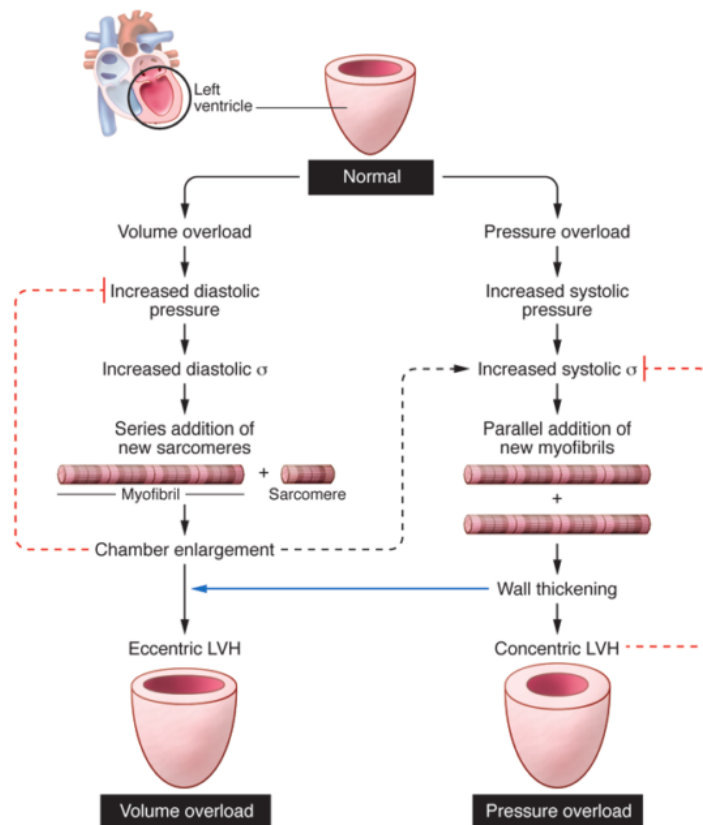


Figure 1-2 Development of different patterns of hypertrophy in response to pressure and volume overload.

From Grossman and Paulus, 2013³³. Reproduced with permission from the American Society for Clinical investigation.

The view that hypertrophy is always beneficial however is not clear for two reasons. Firstly, LV hypertrophy is a marker for increased cardiovascular risk. Left ventricular hypertrophy itself may subsequently lead to increased oxygen demand resulting in myocardial tissue fibrosis and apoptosis,^{23,34–36} an increase in LV end diastolic pressure, and finally a reduction in LV contractility, dilatation and decline in ejection fraction.^{23,35} It predicts adverse outcomes including coronary artery disease,^{37–39} arrhythmia,⁴⁰ stroke,⁴¹ heart failure,³⁸ sudden death,^{37,42} and all-cause mortality.^{42–45} This is not simply a reflection of disease severity.^{31,46,47} Secondly, animal studies suggest that normalisation of wall stress is not necessary to maintain compensation despite

increasing afterload. In fact, there can be an increased contractile state even in the absence of hypertrophy against increased afterload.⁴⁸ Esposito et al. described improved cardiac function despite the inability to normalize wall stress after partial aortic constriction in transgenic mice where angiotensin II and endothelin pathways were blocked.⁴⁹

Because the wall stress calculations relied on measurement of left ventricular cavity and wall thickness, the observed improvement in function may be explained by changes in fibre orientation, which are not captured by classical measures.⁵⁰ Becker et al. and Greenbaum et al. both noted that gross dissection could distinguish a pattern in cardiac fibre orientation from endo to epicardium, but without distinct layering.^{51,52} Trabecular fibres were longitudinal, mid-myocardial fibres were circumferential, sub-endocardial and sub-epicardial fibres were oblique. Greenbaum and colleagues noted that this pattern was regional, and particularly, fibre orientation was more circumferential within the septum. Becker et al. extended this by describing that these septal fibres were located in a more mid-myocardial layer. This pattern was almost absent at the apex, whilst oblique fibres were more pronounced in an endocardial and epicardial location. The inner fibres, described by Becker as longitudinal-oblique, appear to contribute greatest to wall thickening across different loading conditions.⁵³

In addition to simple measures of mass and volume, the change in wall thickness relative to cavity dimension is effective at distinguishing clinical and haemodynamic characteristics between subgroups.⁴⁷ A change in the ratio of wall thickness to chamber dimension can occur without a net increase in wall mass (effectively the same wall mass is arranged around a smaller chamber dimension – this results in a thicker wall simply as a consequence of the altered geometry). In the arterial circulation this has been termed “eutrophic remodelling” to emphasize the lack of hypertrophy.⁵⁴ In the heart,

this phenomenon was first described using two- dimensional (2D) echocardiography, by subdividing hypertensive patients based on the presence of increased mass and the ratio of LV wall thickness to chamber (“relative wall thickness”, RWT). If RWT was low with increased mass (“eccentric hypertrophy”), patients had more severe systolic dysfunction or increased N- terminal pro-brain natriuretic peptide (NT-proBNP), albeit representing a small proportion of hypertensive cohorts.^{47,55} If RWT was high with normal mass (“concentric remodelling”), overall ejection fraction was normal but subtle measures of systolic dysfunction have been observed.^{46,56} This classification has extended to valvular disease,⁵⁷ renal failure,⁵⁸ storage disease,⁵⁹ endocrine disease^{60,61} and obesity⁶² although capturing the integrated stressor over time is often a limitation of such studies.

It is controversial whether knowledge of geometric remodelling offers additional prognostic value beyond LV mass.^{46,63–67} Although 2D echocardiography is the most common method used clinically to assess LV structure and function,⁶⁸ it is reliant on geometric assumptions and is therefore unable to assess regional variations in LV geometry systematically. Cardiovascular magnetic resonance (CMR) imaging overcomes this limitation by using standardised cross-sectional imaging. 3D echocardiography is more comparable to CMR,⁶⁹ but 2D CMR remains the clinical gold standard for quantifying structure and function because of high blood-myocardial contrast. Measuring a *relative* wall thickness is also limited because it does not isolate independent changes in mass and volume. LVH classification has therefore moved towards identifying concentricity and cavity dilatation separately and there has been a growing appreciation of regional architecture, particularly in patients with hypertension and aortic stenosis, Figure 1-3.^{31,70–74}

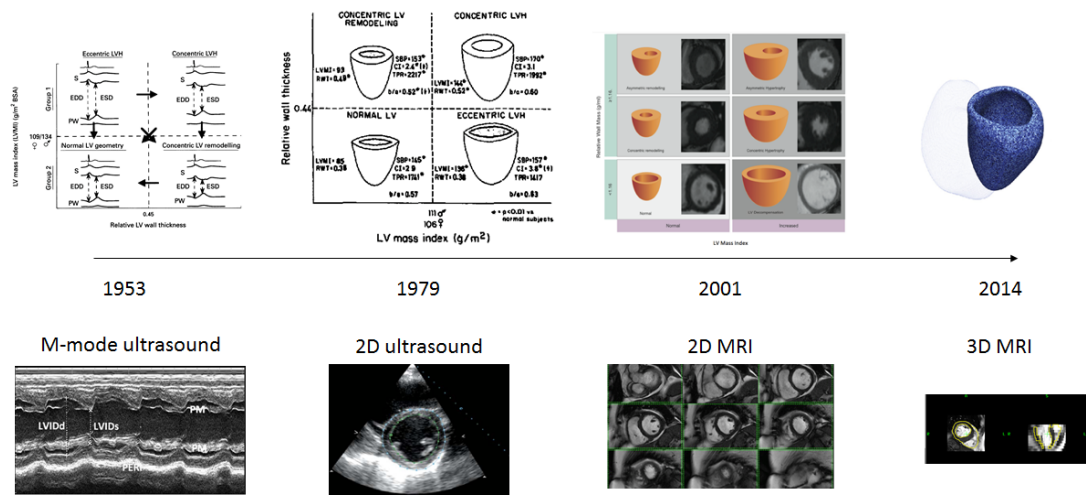


Figure 1-3 Non-invasive assessment of left ventricular hypertrophy over the last sixty years.

Left to right: M Mode echocardiography describing remodelling using the ellipsoid formula⁷⁵; 2D echocardiography describing relative wall thickness⁴⁷; 2D CMR describing the mass to volume ratio and asymmetry;³¹ 3D CMR representing wall thickness across each point of the heart.⁷⁶ Dates represent the advent of each technique. Top left, centre-left, and centre-right tiles are reproduced with permissions from Elsevier, BMJ Publishing Group, and Springer Nature.

The remodelled ventricle can also be viewed as a shape transformation. A more spherical ventricle has been a consistent observation in adverse cardiac remodelling for over sixty years. It is considered adverse because it results in greater LV meridional wall stress.^{77–79} This has implications for mechanical efficiency and myocardial perfusion, and may contribute to a self-perpetuating decline. After myocardial infarction, the heart becomes less elliptical and more spherical and is associated with increased 10-year mortality and functional mitral regurgitation – such shape-related features cannot be understood using global metrics.^{80–82} Capturing shape differences is recommended by European guidelines but is either difficult or performed crudely using conventional analyses.^{68,83}

1.2.3. Variability in measurements

Remodelling parameters can be considered as imaging biomarkers which guide clinical decisions including pharmacotherapy, device therapy and surgical intervention.^{84–86}

These can provide individualized assessments but are prone to errors that may arise from many sources.

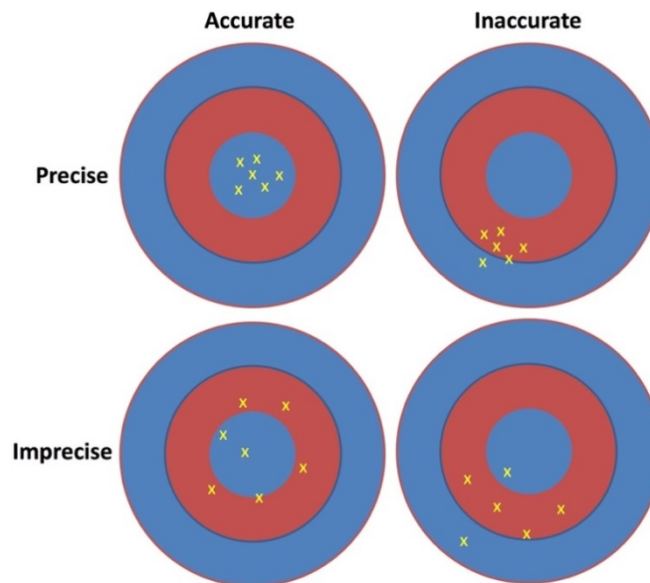


Figure 1-4 Accuracy and precision. Adapted from Kellman et al.⁸⁷

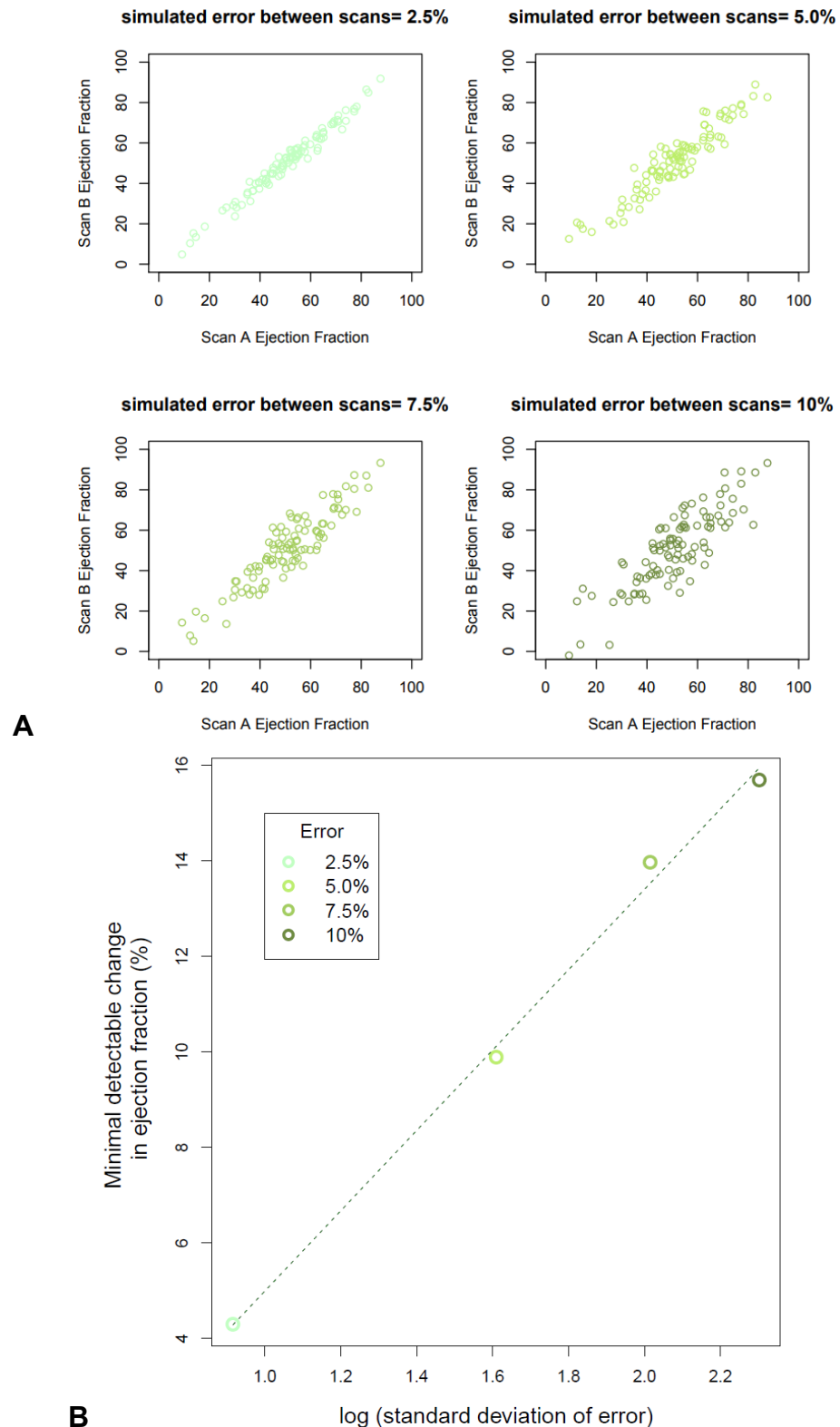
Metrology term	Definition
Precision	Closeness of agreement between indications or measured quantity values obtained by replicate measurements on the same or similar objects under specified conditions
Accuracy	Closeness of agreement between a measured quantity value and a true quantity value of a measurand
Repeatability	Measurement precision under the same measurement conditions over a short period of time.
Reproducibility	Measurement precision under a set of reproducibility conditions (e.g. different operators, locations or systems).

Table 1-3 International vocabulary of Metrology.

Metrology is the science of measuring uncertainty. For repeatability, the set of conditions are the operator, measurement system, operating conditions, locations, and the timeframe must be short. For reproducibility, conditions are intentionally varied such as different locations, operators, and measuring systems – but measurements are on the same subject.⁸⁸

Errors may be viewed in terms of imprecision (e.g. random measurement error) or inaccuracy (one observer may use different criteria to detect an edge with another, leading to systematic bias - see Figure 1-4).^{89,90} Table 1-3 outlines accepted definitions of terms relating to errors. Errors in accuracy may result in numerical values exceeding absolute cut-offs used in decision-making inappropriately. Errors in precision (e.g. data dispersion due to intra-observer error), may result in decreased confidence in absolute values either for follow-up or at initial assessments. Increased dispersion around the true value means clinical decisions are less effective (e.g. confidence in defining a patient with a measured LVEF of 54% as normal or abnormal).⁸⁸ In combination, less effective decision-making may result in under-treatment (e.g. withholding chemotherapy due to suspected cardiotoxicity), or over-treatment (e.g. implantation of a cardioverter-defibrillator even if LV function is relatively preserved).

Importantly, an increase in the magnitude of the error has a clinical impact an order of magnitude greater- a doubling in error is squared in sample size calculations. There are different ways to apply knowledge of this error in healthcare. For trial purposes, this may involve calculating sample sizes. For patient-level decisions, the minimal detectable change (MDC) is a more appropriate measure. The MDC is a property of the measurement. It describes the change in a measurement which a clinician can consider truly different (is a reduction in EF from 55 to 50% real?). Its relationship to the minimal clinically important difference is key for decision-making.⁹¹ The importance of minimising error is illustrated using a simulated dataset to estimate the minimal detectable change (MDC) as a measure of imprecision, Figure 1-5.⁹² The simulated data shows that as average error between two measurements increases linearly, the minimal detectable difference increases exponentially- minimising sources of error is therefore highly relevant to any clinical practice.



A Simulated observer error **B** Impact on minimal detectable change in ejection fraction by an observer. As error doubles, the minimal detectable changes by a square or natural logarithmic relationship – a non-linear relationship. The relationship is better fitted by a logarithmic fit, so as error increases linearly, the minimal detectable difference increases exponentially. Data are simulated and so do not fall exactly on the line of best fit.

For CMR analysis, contouring is performed by clinicians. International guidelines describe standards for quantitative analysis, although despite these, there is high variability and little consensus.^{93–95} Training programs and semi-automated contouring speed segmentation and improve inter-observer agreement but techniques still vary considerably.^{96–98} Basal slice variability can contribute up to 15% of error and can influence both accuracy and precision.⁹⁹ Robust valve-plan tracking methods or careful piloting of the short-axis cine stack may reduce this.⁹⁹ Inclusion of trabeculae, rounded or detailed contouring, and end-systolic definitions also contribute to accuracy and precision.^{96,100} The relative contribution of different factors is unknown.

Accuracy of a metric is usually measured against a reference standard that is accepted to be valid (reflect true biology), and show high precision. A reference standard does not exist for cardiac chamber measurements. The use of scan-rescan reproducibility permits assessment of measurement precision itself, but places greater demands on patients, clinicians and scanners. Precision additionally captures normal physiological variability, and so offers greater clinical and research (sample size) relevance. Single centre scan-rescan studies have shown precise CMR measurements.⁸⁹ Over one year, the MDC for LVEF is 6%.⁹⁴ In heart failure patients, Bellenger et al. observed greater intra-observer EF error than inter-study; but for LV mass, greater inter-observer than inter-scan differences.⁸⁹ However, no multi-centre data studies exist, which would be important for designing multi-centre trials and for clinical generalizability. Using real-world data is important, because clinicians in clinical practice are prone to bias and imprecision than in a more standardized setting.⁹⁰ Semi-automated and fully automated analysis are a natural step to reduce human error.¹⁰¹ Fully automated methods applied to CMR now achieve similar inter-observer agreement to two experts.^{102,103} Using scan-rescan precision methodology, it may be possible to provide a head-to-head comparison of

Introduction

volumetric analysis techniques, and to determine the relative contribution of error sources.

1.3. Cardiovascular assessment using MRI

1.3.1. The nature of MR signal

Clinical MRI is built on the observation that it is possible to flip the magnetic moment of a nucleus by an oscillatory magnetic field. In 1938, Isaac Rabi used an experimental set-up employing a vacuum chamber to pass a beam of Lithium Chloride molecules through two magnetic fields - a static magnetic field of 6000 gauss (approximately 0.2 Tesla, T), and a perpendicular, oscillatory, radiofrequency (RF) magnetic field of 3.5MHz. He noted that when the smaller RF field was applied perpendicular to the much larger constant field, there was a re-orientation of the nuclear spin and magnetic moment when the frequency of the oscillating field was close to the Larmor frequency of the precession of the particular angular momentum vector in question.¹⁰⁴ This field can then induce a current in a nearby metallic coil by rotation of the magnetization vector, as described ten years later.¹⁰⁵

For clinical MRI, this experimental set-up is usually adapted for hydrogen, because it is contained throughout the body as free water and lipid. It can also be adapted for other nuclei that have unpaired particles (and so possess spin), such as ^{13}Na , ^{13}C and ^{13}P . It is clear that the signal from an individual nucleus would be too tiny to detect by a receiver coil, and so the signal is aggregated through alignment within the static magnetic field as described by Rabi. In clinical MR, this is known as the B_0 field. The size of the MR signal is proportional to the number of excess spins that align in the magnetic field and therefore contribute to the net magnetization. Stronger magnets are used for modern MR than were accessible to Rabi, and are typically between 1.5 and 3T. At a magnet of 1.5T strength, the net signal is equivalent to 4 protons in net alignment per million. The

strength of this signal (M_0) is described by the Boltzmann distribution. Signal strength is proportional to the static magnetic field, and the temperature:

$$M_0 = \frac{\gamma^2 \cdot h^2 \cdot N_s \cdot B_0}{4kT}$$

Equation 1-1 The Boltzmann distribution.

M_0 is the net magnetization vector. B_0 is the main magnetic field. γ is the gyromagnetic ratio for the nucleus, k is the Boltzmann constant, T is the temperature, and h is Planck's constant – which describes the energy carried by a photon over a given time.

The frequency of the perpendicular oscillatory magnetic pulse, the B_1 field, must also be defined to successfully induce a re-orientation of nuclear spin. For hydrogen at 1.5T, this is 63.9MHz. This frequency (f_0) is proportional to the strength of the magnetic field applied (B_0), and the charge/mass ratio of the particle (the gyromagnetic ratio, γ):

$$f_0 = \gamma \cdot B_0$$

Equation 1-2 The Larmor equation.

The gyromagnetic ratio of hydrogen is 42.58 MHz/Tesla.

Whilst the net longitudinal magnetisation in the B_0 field is small, there is no magnetization in the perpendicular plane, known as M_{xy} . The perpendicular B_1 RF pulse of the appropriate Larmor frequency is able to tip a portion of the magnetisation into this transverse direction. This generates a measurable signal known as free induction decay, which can be detected by an adjacent coil. Once the RF pulse ceases, the components of the nuclear spin magnetization vector parallel to the external magnetic field, B_0 decay. This return to alignment with B_0 is known as longitudinal relaxation and is characterised in terms of the longitudinal (or spin lattice) relaxation time constant (T_1). The gradual disappearance of magnetisation (“dephasing”) in the transverse plane (i.e. components of the magnetisation vector perpendicular to B_0) is known as T_2

relaxation. The rate of T2 decay is also related to non-uniformities in the B0 field, which can accelerate T2 dephasing. This actual rate of dephasing (T2 + effect of inhomogeneity) is known as T2-star relaxation.

The MR signal characteristics described by relaxometry, vary by tissue composition. Measuring these parameters therefore provide a key utility of MRI compared to other imaging modalities– interrogation of tissue character. This was first used by Damadian in 1971 who was able to demonstrate that T1 and T2 relaxation times of solid tumour tissue were distinctly outside the range of normal tissue.¹⁰⁶ This is because different tissues components have varying T1 and T2 values. For three common tissue components, T1 for fat, soft tissue and water/CSF are 250, 1000 and 4000ms respectively. Corresponding T2 values are 70, 90 and 2000ms. For human tissue, T1 relaxation is longer than T2, which is longer than T2-star relaxation. Pure liquids have very long T1 and T2 values, whilst solids have short T2 values. There are many mechanisms that govern the relaxometry of complex biological molecules. The most important mechanism is dipole-dipole interaction, but other mechanisms include chemical shift anisotropy, and chemical exchange.

These parameters can be modelled by a set of equations proposed by Bloch in 1946, modelling the magnetization decay in x-, y- and z-planes. These equations assume that decay follows first-order kinetics. Because longitudinal magnetization is at a maximum at long T1 time-constants, water appears dark on T1 weighted images as it has a long T1. Conversely, T2 magnetization is a maximum at short T2 time-constants, and so water appears bright because it has a long T2, whilst fat appears darker. This is illustrated in Figure 1-6.

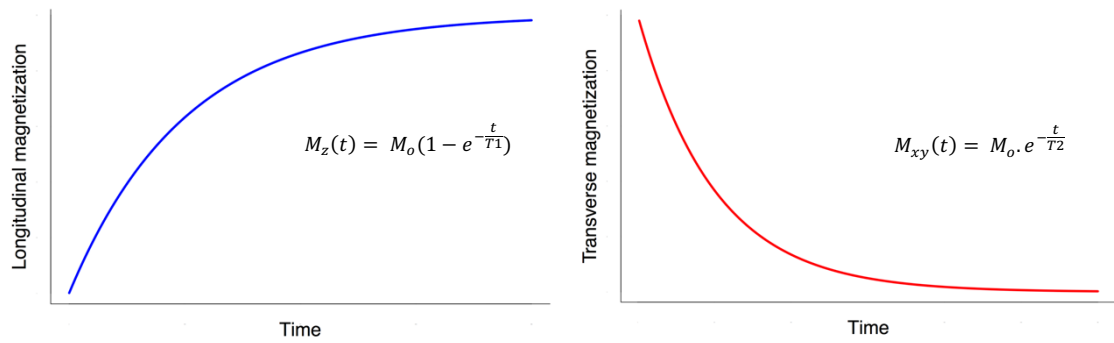


Figure 1-6 T1 and T2 relaxation curves.

These data are modelled by Bloch equations. It is also assumed that, around a B0 field, longitudinal magnetization (T1) returns to maximal signal in the direction of B0, and transverse magnetization (T2) decays to zero. The time constants for these processes are a ~63% ($1 - \frac{1}{e}$) and 37% ($\frac{1}{e}$) of maximal T1 and T2 values respectively. As an example, water which has a longer T1 constant than other tissues, results in a curve shift to the right, meaning that it appears darker than other tissues as it will have recovered less longitudinal magnetization signal at the timepoint of curve sampling. *Abbreviations: t = time point of decay after nuclear induction; M_z = Net longitudinal magnetization; M_{xy} = Net transverse magnetization. M is a magnetization vector which represents all sampled nuclei.*

These properties can be manipulated by basic parameters to achieve different image contrast weighting. Repetition time (TR) is the time allowed for recovery between radiofrequency pulses. The echo time (TE) is the time after a pulse before data acquisition. Manipulation of these parameters to weight image contrast are detailed in Table 1-4.

		Repetition time	
		Short	Long
Echo time	Short	T1	Proton -density
	Long		T2

Table 1-4 Contrast weighting for MR sequences.

A longer repetition time (TR) permits greater longitudinal recovery (T1) in signal. Therefore a shorter TR enhances tissue differences in T1 recovery. A longer echo time emphasizes differences in tissues due to transverse (T2 or T2-star) recovery. By controlling the combination of these two signals, it is possible to weight signal according to T1 and T2 of tissues. Proton-density imaging maximizes both T1 and T2 which can be useful for structural imaging without tissue characterization.

1.3.2. Signal encoding and decoding

Signal encoding is the process of converting information into a specified format for transmission. Decoding is the reverse process to represent the information intuitively,

Figure 1-7.

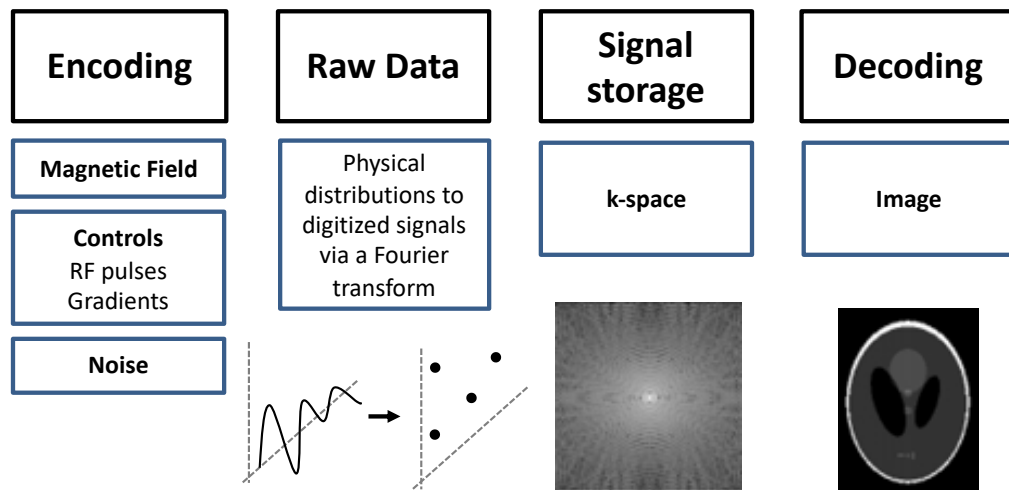


Figure 1-7 Signal encoding and decoding in MRI. The manipulation of the magnetic field serves as a control to generate the original signal. This is encoded using Fourier transformation digitally. These signals are then stored in *k*-space, from where they are decoded into an image representation of the original data.

For MR, the signal consists of a number of decaying spectra, and this requires coding for transmission to an interface that can reconstruct the final image. The signals themselves (the spectra) simply represents the magnetic properties of the tissue. As described, varying pulse sequences can be used additionally to weight the signals towards specific magnetic relaxation properties. Spatial information is also necessary to guide the final image reconstruction. To achieve an efficient, sustainable, process for the purposes of clinical MR, refinements were necessary at each step - signal encoding, storage and reconstruction. This process was achieved by using the property of MR signal that it can be described in waves, consisting of peaks, and varying cycle length (frequency), Figure 1-8.

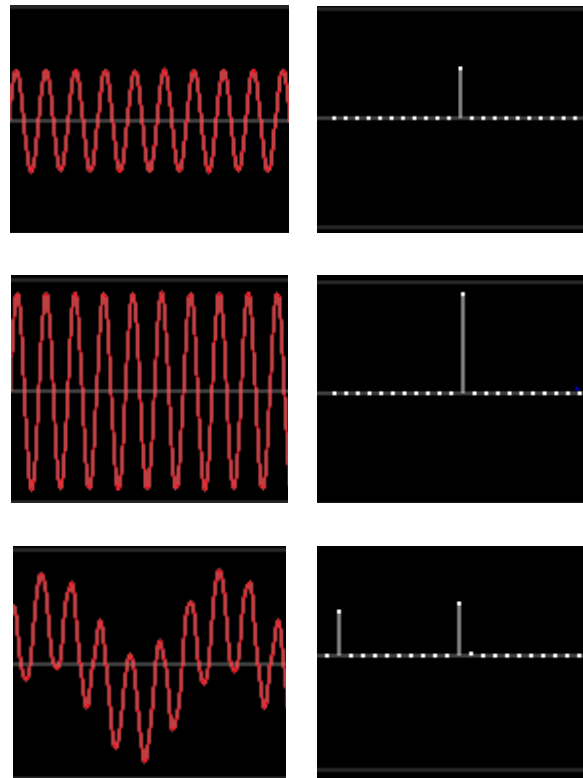


Figure 1-8 Fourier transformation of periodic sine waves.

Original waves are shown on the left, and their expression as a frequency and amplitude. **Top:** A sine wave of 890Hz of amplitude $0.5 \cdot \sin(x)$. **Middle:** amplitude increase to $1 \cdot \sin(x)$. **Bottom:** an overlay of an additional, higher frequency sine wave.

In 1973, Lauterbur developed a technique to encode spatial information into the MR signal. Spatial information was encoded by applying multiple linear field gradients at different angles.¹⁰⁷ This can be repeated for 360 degrees and reconstructed into a complete 3D visualisation. This is therefore dependent on the width of the frequency pulse and degree of rotation, and is a slow process.

More advanced Fourier methods offered an improvement in sampling the spectra, but in order to achieve that, it required pulse sequences to encode data spatially. A number of different Fourier sampling methods exist, including spin-warp, reconstruction from projection, echo-planar and the original Lauterbur method.¹⁰⁸ The method commonly used now was initially applied to nuclear MR data in 1975 by Richard Ernst. This

unlocked the potential of rapid information processing required for clinical MR imaging, and was achievable (even at that time) on a small on-line computer.¹⁰⁹ Ernst et al. modified the approach of using individual radiofrequency pulses, to using sequences of pulsed gradients. Time-varying magnetic gradients encode additional information directly into the spectra. In this case, Ernst encoded spatial information into the temporal decay of the signal. This forms the anatomy of modern pulse sequences. These are composed of an initial radiofrequency pulse, and gradients for slice selection, phase-encoding and frequency encoding, before a final echo is read-out.

A Fourier transformation can then transform these time-domain data, so wave amplitude is represented by a peak, and cycle length by location of frequency, Figure 1-8.¹⁰⁸

Twieg noted that the Fourier pulse sequencing and signal coding was necessary because the signal-to-noise from MR is inherently low.¹⁰⁸ Sampling the entire imaging region simultaneously is therefore necessary to achieve maximal signal, with built-in spatial encoding.

Fourier analysis can therefore sample points over time in a given spatial domain (frequency and phase). The detailed time dependence of the trajectory of the sample points is known as the k trajectory.¹¹⁰ k is a vector at a spatial domain, and is stored in k -space arrays that cover all spatial domains.¹¹¹ The spatial frequency at each coordinate represents that frequency's contribution to the whole image, and the location describes the rate at which image features change.¹¹² For example, low spatial frequencies, encoding images that are visually homogenous, are situated in central k -space; and high spatial frequencies reflecting rapid changes in signal (e.g. edges), are encoded more peripherally. The dimensions of k -space are the number of phase encoding steps in the phase encoding direction, and the number of samples that each signal is digitized into in the frequency encoding direction (a more rapid process). The acquisition time is

therefore related to the number of phase encoding steps and the time interval between each step (the repetition time, TR). Because the distribution of k-space is intimately linked to characteristics of the magnetic field, it provides the flexibility within MR imaging of modifying resolution, contrast, field of view and artefact that is specific to MR compared to other imaging modalities.¹¹¹

1.3.3. Pulse sequence anatomy

Whilst signal can be measured as a free induction decay, the signal can also be measured by other methods, commonly known as echoes. This allows for the more complex signal encoding described above, which would disrupt a simple free induction decay curve. The main families of MR signals are listed in Table 1-5. The two main groups used for cardiac imaging include gradient and spin echoes.

Type of MR signal	Method of formation
Free induction decay	1 RF pulse
Gradient echo	1 RF pulse + gradient reversal
Spin echo	2 RF pulses
Stimulated echo	>3 RF pulses

Table 1-5 Types of MR signals. *Abbreviations: RF = radiofrequency.* Adapted from mriquestions.com.

Spin echo sequences are those that use an initial RF pulse followed by a second 180° pulse. The initial pulse flips magnetisation in the transverse plane. Because inhomogeneities exist, these spins precess at slightly different frequencies. The second inversion pulse serves as a refocusing pulse. This means the spins with greater magnetization precess faster after a flip, and so can converge onto the slower precessing spins. This convergence occurs at twice the pulse interval, resulting in a maximal signal for read-out at that time. The benefits of using a spin echo strategy therefore include robustness to field inhomogeneity (e.g. susceptibility due to metallic artefact), and less

chemical shift artefact. However, because a refocusing pulse is used, transverse magnetization needs to recover sufficiently prior to the next pulse, resulting in a longer acquisition. Examples of spin echo sequences in CMR include late gadolinium enhancement, spectral inversion recovery (SPIR), short T1 readout (STIR) or double-inversion recover black blood (HASTE) sequences.

Gradient echo sequences are designed differently. They use a bipolar gradient magnetic field to manipulate the free induction decay. This alters the Larmor frequency across the tissue, so that some of the sample has accelerated dephasing, resulting in an overall shorter signal. A gradient echo pulse also has a second lobe, Figure 1-9. This is a gradient of opposite polarity that refocuses the spins and allows the original free induction decay signal to reappear. In the frequency encoding step, this second lobe gradient is twice the duration of the first, producing a symmetrical signal known as the gradient echo, Figure 1-9. The initial excitation RF pulses require a smaller flip angle, less than 90°. This makes the sequence much faster, and results in a lower specific absorption rate (SAR); however, the sequence is prone to intravoxel signal loss from susceptibility artefact.

	Spin echo		Gradient echo	
	Short	Long	Short	Long
TE (ms)	6-25	>60	15	>30
TR (ms)	400-800	>1500	3-400	>400

Table 1-6 Sequence parameters to adjust contrast weighting.

For the two main families of MR sequences, both the echo time (TE), and repetition time (TR) can be modified to change contrast weight to either T1 or T2. The time for an individual sequence will be dependent on the flip angle used. Note that all times for spin echo are longer than for gradient echo. Examples collated from *Cardiovascular MR manual*, Plein et al. (Springer); *CMR Physics Handbook*, Plein et al. (EACVI); and *Clinical Cardiac MRI*, Bogaert et al. (Springer). For cine imaging, the TR should typically be 30-40ms- sufficient for sampling end-systole.

1.3.4. Cine cardiac MR imaging

Cine imaging is used to provide accurate assessment of both cardiac structure and function. This requires high blood to myocardial tissue contrast. An ideal pulse sequence therefore must provide adequate signal weighting, and be fast enough for high temporal resolution within a breath-hold (so the heart undergoes minimal motion associated with respiration). Gradient echo sequences use excitation pulses with a flip angle less than 90° . Whilst this generates less signal in the longitudinal direction, there is still significant signal in the transverse direction which can generate the final echo. Because longitudinal recovery is much faster with a lower flip angle, the repetition time between pulses is shorter, and the image can be acquired quicker – approximately four times faster than a spin echo sequence, Table 1-6. The final gradient applied is the frequency encoding direction (G_{FE}). This, in practice, is two gradients. The first gradient is applied in the frequency encoding direction to cause dephasing. This is then followed by a gradient in the opposite direction of the same amplitude. This is applied for twice as long, so the spins dephase equally in the opposite direction, and then rephase. This means it forms a symmetrical signal. Repetitive excitations are applied to image every phase of the cardiac cycle in one acquisition. Because the TR is short, the transverse magnetization is not fully rephased by the time of the next RF pulse. This can be overcome by the use of a spoiler gradient that destroys the remaining transverse magnetization before the next RF pulse. Therefore gradient echo sequences are mostly T1-weighted.

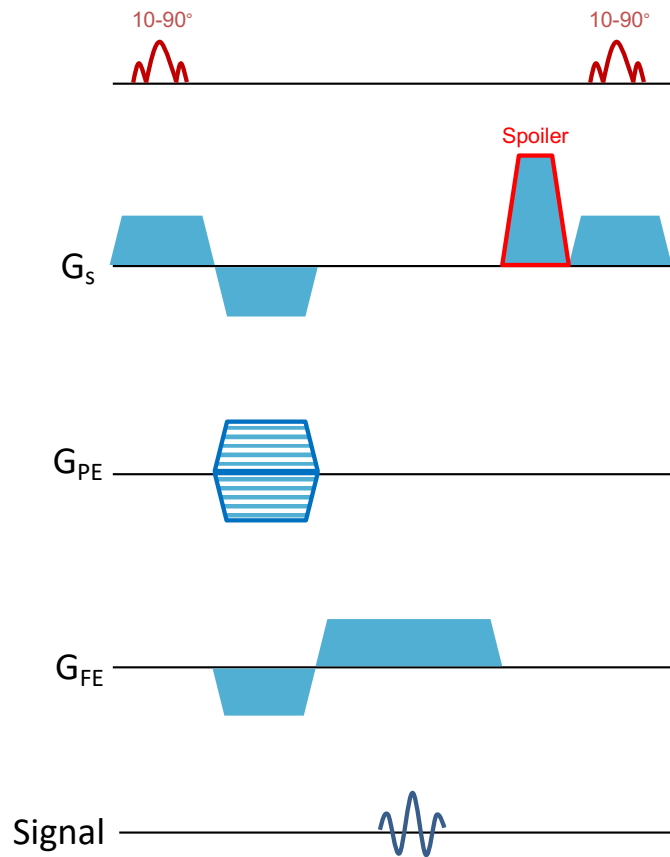


Figure 1-9 Spoiled gradient echo pulse sequence.

From top to bottom, the lines represent the initial radiofrequency magnetic pulse, slice-encoding gradient (G_s), phase-encoding gradient (G_{PE}), and the frequency-encoding gradient (G_{FE}). The spoiler gradient required to remove residual transverse magnetization is highlighted in red. In this diagram, the height of a polygon is proportional to the strength of the gradient, and the length proportional to duration. Polygons in opposite directions show gradients of opposite polarity.

The blood-myocardial signal differentiation is the major limitation of gradient echo sequences. Repetitive excitations result in complete suppression of signal in stationary tissue. Because blood continuously flows through, it appears brighter (T_1 remains long) than surrounding, suppressed myocardium. This however is dependent on a sufficient volume of flowing blood, meaning the blood-myocardial contrast can be limited. This is particularly pronounced in long-axis imaging, where through-plane flow is limited.

A significant advance arose from the development of balanced steady-state free precession (bSSFP) imaging. This is designed so that the residual transverse

magnetization is used, rather than spoilt. Extra gradients are applied that rephase the residual signal, and these are superimposed onto the transverse magnetization after the RF pulse. These gradients are known as “rewinder” and “dephasing” gradients, Figure 1-10. This generates progressively more signal than gradient echo because it is reliant on multiple signals compounding, reaching a maximal steady state after multiple RF pulses. The signal is acquired at the midpoint of the sequence, so that the TE is half of the TR. This means the image contrast is related to the T2/T1 ratio. bSSFP cine imaging requires multiple rephasing, any so inhomogeneity becomes more pronounced. This can result in significant artefact banding. The spatial frequency of these bands is proportional to $1/TR$. Careful shimming of the B0 field can help to avoid these. These sequences are also less flow sensitive because they do not rely on dephasing due to flow.

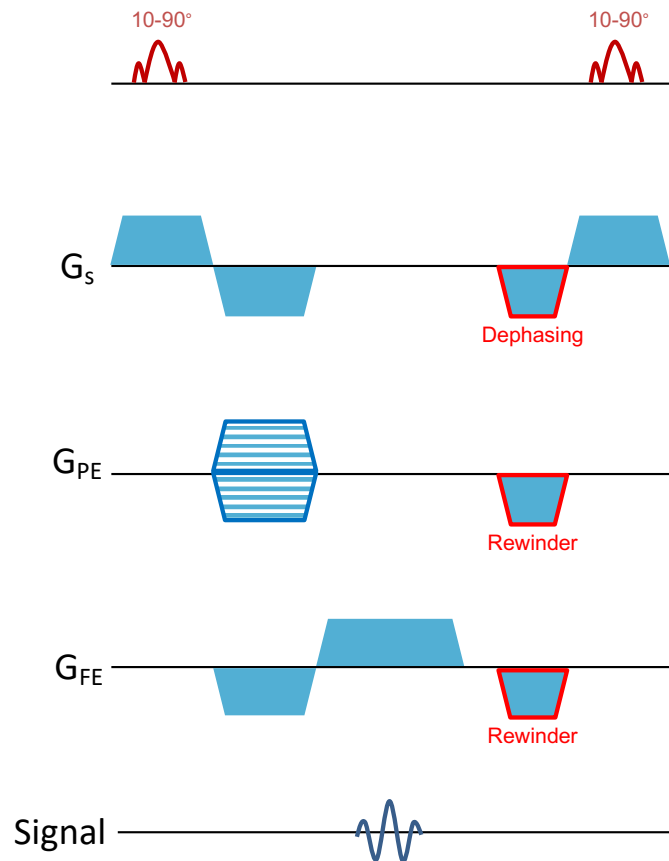


Figure 1-10 Steady-state free precession pulse sequence.

From top to bottom, the lines represent the initial radiofrequency pulse, slice-encoding gradient (G_s), phase-encoding gradient (G_{PE}), and the frequency-encoding gradient (G_{FE}). The dephasing andrewinder pulses used to dephase residual transverse magnetization are highlighted in red. These increase signal-to-noise by compounding signal over multiple RF pulses. The echo time is half of the TR, as shown by the signal read-out occurring half-way between the two RF pulses.

Thick 2D slices are acquired in standardized imaging planes to build a cross-sectional stack through the heart. This typically requires 8-12 slices to cover the entire ventricular volume in a short-axis view. Protocols vary between institutions, requiring pre-determined slice thickness and gaps between slices. Thinner slices increase the through-plane resolution, but mean a loss of signal-to-noise and increased acquisition time. The use of gaps between slices permits faster stack acquisition, with loss of fully sampled long-axis geometry.

The properties of the heart are important in each orthogonal vector. Isotropic 3D cine-imaging can capture this, but is challenging due to long acquisition times for acceptable spatial resolution.^{113,114} Techniques to reduce scan time are necessary to ensure clinically acceptable acquisition protocols. These include: compressed sensing, partial Fourier, parallel imaging, and navigators. Because acquisition time is proportional to the number of k-space lines acquired and the repetition time, reduction of the acquisition matrix or a rectangular field of view (FoV) will also shorten the acquisition. Compressed sensing allows sparse sampling of k-space with iterative reconstruction.¹¹⁵ Partial Fourier imaging techniques also undersample k-space, but use the conjugate symmetry of k-space to reconstruct the image (i.e. rotate the data into a different axis). Both techniques have also been combined, to speed acquisition.¹¹⁶

Parallel imaging uses the fact that multiple receiver coils, or coil elements, acquire the MR signal at different sensitivities. Multiple receiver coils are also used in normal MR imaging when the data from each coil is combined across the whole field of view, improving signal to noise and resolution. In parallel imaging, the different images acquired from each coil are used instead to gain speed. First, fewer lines of k-space are acquired to save time. The number of lines acquired determines the acceleration factor. Because fewer lines of k-space are acquired, images are prone to aliasing, seen as wrap-around artefact. It is possible to reconstruct the image to avoid this artefact because each separate image varies according to coil sensitivity can be compared to a reference image. This can be related to true voxel intensity by known mathematical relationships.¹¹⁷ The coil sensitivity, combined with the aliased image, can therefore be used to generate a final “un-aliased” image. The reconstruction techniques can be either based on the image, or k-space. Image domain techniques vary by manufacturer, e.g.

Siemens (mSENSE), GE (ASSET), Philips (SENSE). k-space techniques (Siemens-GRAPPA; Philips-ARC) can also be vendor specific.

Free-breathing techniques using a navigator beam can permit 3D-whole heart acquisitions at a single cardiac phase, but cannot be used in cine imaging because they require a pause in acquisition to allow a navigator beam to track motion of organs or structures. Self-navigated sequences adjust the acquisition sequence in real-time based on the trajectory of central k-space over time. To acquire this trajectory, it is necessary to perform a scout acquisition of approximately 16 seconds beforehand.¹¹³

3D cine imaging may permit acquisition at multiple cardiac phases within a single breath-hold. This has the potential benefit of high spatial resolution imaging, avoidance of slice misalignment, and a reduction in total acquisition time. The use of simultaneous parallel imaging (SENSE) in two encoding directions has been reported as one strategy to achieve this within a feasible breath-hold duration, using a Philips 1.5T MRI system with a 32 element phased-array coil.⁷⁶ The parallel imaging strategy was reported to reduce geometry-related noise enhancement with an acceptable reduction in contrast and image quality. Lower temporal resolution (20 cardiac phases) was acquired compared to conventional 2D cine imaging (30 cardiac phases), Figure 1-11.

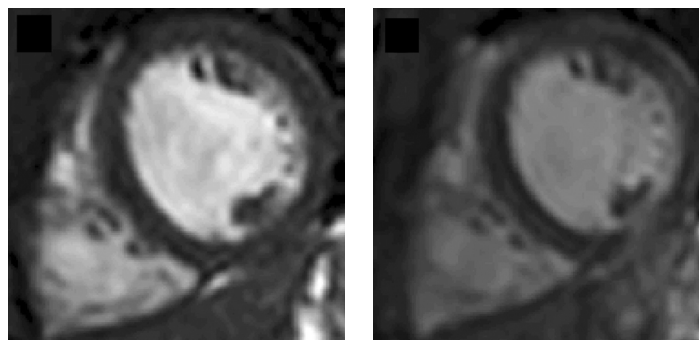


Figure 1-11 3D-cine imaging.

Left: conventional 2D-cine **Right:** 3D-cine imaging showing reduced blood-myocardial contrast but acceptable image quality, achievable through parallel imaging (SENSE) in two spatial directions.

1.3.5. Phase-contrast imaging

A key utility of CMR is the ability to interrogate volumes of interest for velocity information. Flow can be measured by different methods: “time-of-flight”, contrast-enhanced MR angiography or phase-contrast imaging. Phase-contrast imaging permits quantification and so will be discussed here. One advantage of phase contrast MR for flow measurement is the ability to interrogate central vessels (aorta, pulmonary artery etc), which can be difficult to access using ultrasound Doppler techniques. Clinically it is used for assessment of functional valvular abnormalities and for estimation of intra-cardiac shunt severity by calculating aortic and pulmonary flows – particularly in patients with congenital heart disease.

When a gradient is applied, stationary tissue acquires a difference in rotary phase according to the position on the gradient.¹¹⁸ When the gradient is switched off, affected spins continue out of phase. If a gradient in the opposite direction is applied, stationary spins return to normal. Moving tissue such as blood, however, remains out of phase.

Velocity of moving tissue can be quantified because the shift in phase is proportional to the velocity of the spins. The strength of the signal is proportional to the strength and duration of the magnetic field gradient.

Quantitative velocity mapping is performed using fast gradient echo cine imaging sequences. The first image obtained (the magnitude image or modulus) is similar to a normal cine. After applying a bipolar gradient, a phase image is generated which is subtracted to visualise only the moving spins. Velocity is encoded into each voxel in a separate velocity image. Images are typically acquired as a cine image over multiple cardiac cycles to obtain interpolated data of adequate temporal resolution and data are retrospectively gated to ECG signal to provide information about cycle timing. The use of multiple cardiac cycles and interpolation means there are small inaccuracies due to

beat-to-beat flow variation. Free-breathing sequences can permit greater signal averaging, but are prone to in plane motion.

Velocity encoding is predetermined for the sequence, to control the maximum and minimum measurable flow. If this is set too low, image aliasing occurs (positive velocities look negative). If it is set too high, signal-to-noise decreases due to greater noise.¹¹⁸ Velocity information can also be encoded in-plane or through-plane, depending on the information required. The temporal resolution is determined by the number of lines of k-space acquired for each phase per cardiac cycle multiplied by the repetition time. This is multiplied by 2 because both a magnitude and velocity image are acquired. It is possible to improve apparent resolution by linear interpolation between frames and most sequences reconstruct data to a pre-determined number of frames per cardiac cycle. Phase-contrast imaging has been validated against Doppler, phantom and invasive measurements.^{119,120}

1.4. A deep phenotyping approach

1.4.1. Developing deeper phenotypes

Automated analysis provides the capacity to use all the information within a dataset with an acceptable workload burden. This is necessary to understand the complex web of cardiac remodelling.¹²¹ Our limited ability to make associations may be because we are missing important variables or interactions between variables, Figure 1-12. Research currently works by deciding *a priori* what the important variables are to study and these are inevitably limited by workflow capacity. Phenomics however refers to the layered representations of a phenotype in their entirety. It is based on the assumption that it may be more fruitful to accept that what we know, is overshadowed by what do not know, and therefore we should measure “everything” in an unbiased approach. This has its own data analytical challenges, but one study of the human genome suggests that measurement of the 95% of DNA in-between protein-coding genes is worthwhile.¹²²

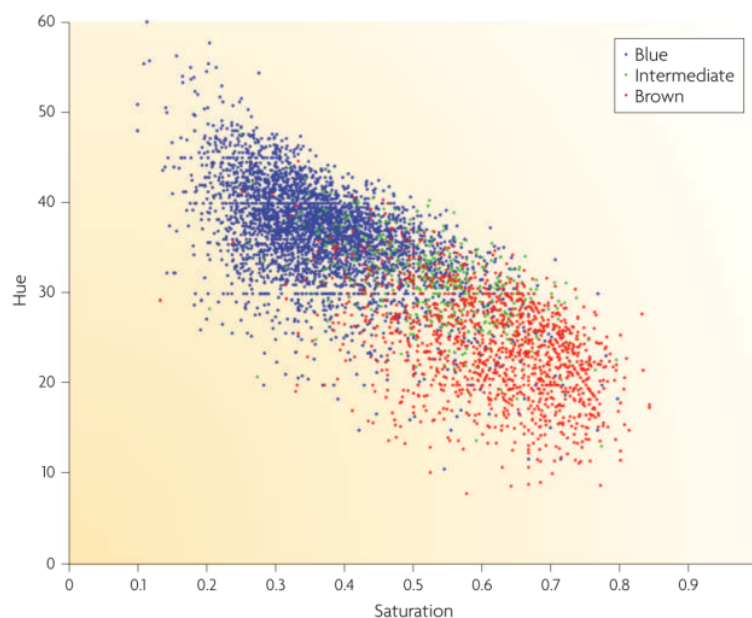


Figure 1-12 Quantification of eye colour.

Eye colour can be categorised into blue, brown or intermediate, but when qualitative hue is represented in hue saturation space, there is clear overlap. A completely phenomic approach to eye colour would also capture the spatial pattern of eye colour, resulting in a potentially much higher dimensional phenotype space. From Houle *et al.*¹²¹ Reproduced with permission from Springer Nature.

The approach can be difficult. There has been increasing recognition that such data processing requires collaborative efforts which are now possible for the following reasons:

1. Infrastructure development.

Rapid development of generalizable approaches to data analysis are becoming available. This was recognised by the Human Genome Project when faced with the high cost of sequencing genomes.¹²² The project therefore modified its objectives to improve sequencing technology prior to understanding the genome itself. The European Union has also recognized that a collaborative effort is necessary to understand the complexity of the human brain by committing €643 million to computing-based brain research.¹²³ In Cardiology, a few projects, such as the Cardiac Atlas Project, allow open sharing of data to train or test new image processing techniques.⁹³

2. Increased processing power.

These efforts require adequate processing power, in the form of computers. In an era where information transistor processing capacity is still doubling every two years (“Moore’s Law”), this is becoming increasingly possible. The UK government has recognised this at a high level and has put forward four grand challenges, including the use of machine learning and healthcare needs in an ageing society. Combining both sectors is viewed as having the potential to boost productivity with the ultimate aim of transforming society.²

3. Digitalised medical data.

The volume of data we can now capture is massive at increasingly affordable cost, Figure 1-13. This is occurring at different levels that contribute to an individual human phenome. Gene and mRNA profiling is rapidly decreasing in cost.¹²⁴ More recently, nuclear magnetic resonance (NMR) and mass spectroscopy have enabled automated

robust high throughput profiling of tissue.¹²⁵ This can be applied to proteins or smaller molecules, and are known as “proteomics” and “metabolomics” respectively. The human proteome consists of a known ten thousand proteins in humans, and reflects post translational gene expression.¹²⁶ Metabolomics capture biochemical intermediates and small molecules less than 1200 Dalton. These are part of a more downstream process that reflects genetic, epigenetic and environmental influences.¹²⁴ These are being mapped on The Human Metabolome Database (www.hmdb.ca). Whilst metabolites number greater than 40,000,¹²⁷ current NMR spectroscopy platforms capture up to a few hundred.¹²⁸ This technique detects the hydrogen atoms within a molecule. Because the area of a peak is proportional to the concentration of a molecule measured, this provides a quantitative interrogation of multiple pathways in a relatively unbiased manner.¹²⁹

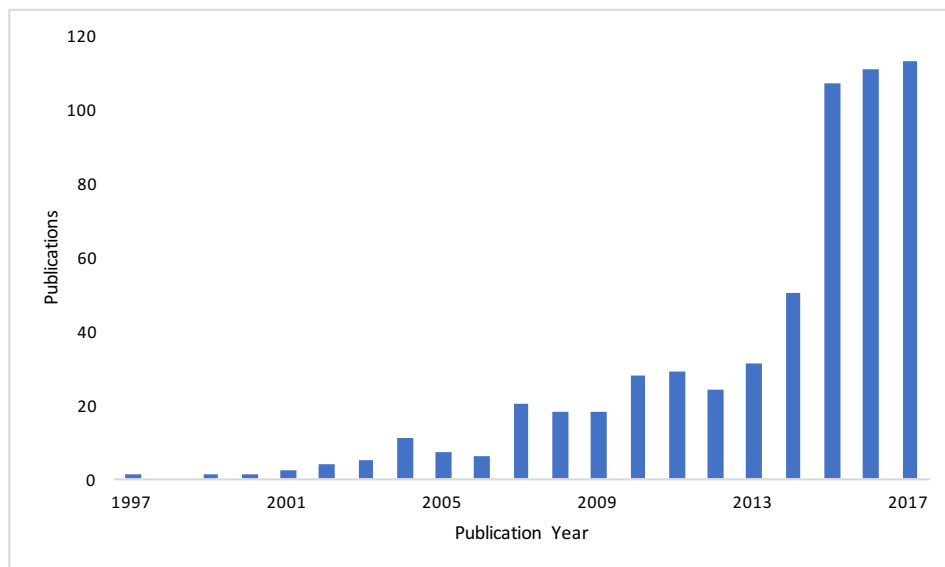


Figure 1-13 Increasing publication rate of articles related to “Phenomics”.

Literature search conducted on PubMed.

Phenomics is increasingly applied to imaging and behavioural data, Figure 1-13.

Projects such as the UK BioBank aim to capture a highly detailed cardiac phenotype using CMR, and link it to outcome data.¹³⁰ Whilst CMR is regarded as the gold standard

for LV assessment, the high spatial resolution and cross-sectional geometry is not capitalized upon by standard global LV volumetric analysis: by categorising data, we are failing to capture the variance that exists between arbitrary cut-offs. Parallel processing, field strength and receiver coil technology on modern scanners now permits unparalleled non-invasive observation of structure and function, providing us with an opportunity to exploit an in-vivo cardiac phenotype in a way that combines the work of anatomists and physiologists.

1.4.2. Progression in cardiac phenotyping

Automated image segmentation can help to analyse structure and function. The basic goal is to predict endocardial and epicardial borders to derive volumetric parameters, but because of their computational representation, these segmentations can be used to develop more detailed, quantitative, and precise (reproducible) representations. Even though cine-SSFP imaging has high blood-myocardial boundary contrast, the difficulties behind automated analysis are well-recognized because of motion, mis-gating, off-resonance or flow artefacts. In 2011, Petitjean et al. provided a comprehensive review of 70 peer-reviewed publications related to automated and semi-automated short-axis CMR cardiac segmentation approaches.⁹⁸ Peng et al. extended this classification in 2016 to reflect the growing use of neural network techniques, and to include other cardiac chambers.¹³¹ Techniques are growing rapidly, which has prompted the availability of interactive bibliographic databases to keep up-to-date with the literature.¹³² Approaches can broadly be split into those with no prior, a weak prior, or a strong prior.

Those with no prior, or a weak prior (e.g. identifying the centre of the LV blood pool) rely on image-based or pixel-classification based methods. Simpler image-based

methods use thresholding or region-growing. Because of differences in grayscale characteristics, they typically identify the endocardium and epicardium separately. These methods can result in inappropriate segmentation or boundary leakage.¹³¹ To improve segmentation accuracy, more complex image-based classification methods have been developed. Active contouring approaches, including snakes or level-set algorithms, search for a border, rather than classifying pixels directly.¹³³ The boundary curve is fitted to a change in image intensity usually by minimizing an energy function. This energy function fits image characteristics, but also includes “elastic” forces to favour retention of a certain shape, or other constraints. As such, they are regarded as deformable models that can incorporate a prior - specifically, a prior of anatomical knowledge for an expected contour pattern.

Pixel-based classifications group pixels according to the histogram patterns for specific tissue labels.¹³¹ Each group of pixels can be described by several different features that need to be learnt for classification to take place. There are different techniques to perform the learning process, broadly classed into supervised and unsupervised training strategies. Unsupervised strategies include *k*-means clustering, or expectation maximisation (EM).¹³¹ EM methods are common in cardiac imaging, and work on the principle that each pixel is classified based on its probability of being a particular label.¹³⁴ Gaussian mixture modelling is one form of EM that fits probability distributions to pixel features - most simply pixel intensity, as shown in Figure 1-14. These approaches are used in clinical tools, such as the cardiac analysis platform available from Siemens known as Argus.¹³⁴ One limitation of these approaches is that they are not contextual - they do not relate pixels to each other, or relate them to the overall image. An example is the inappropriate (but accurate) segmentation of the stomach rather than myocardium when using Argus.

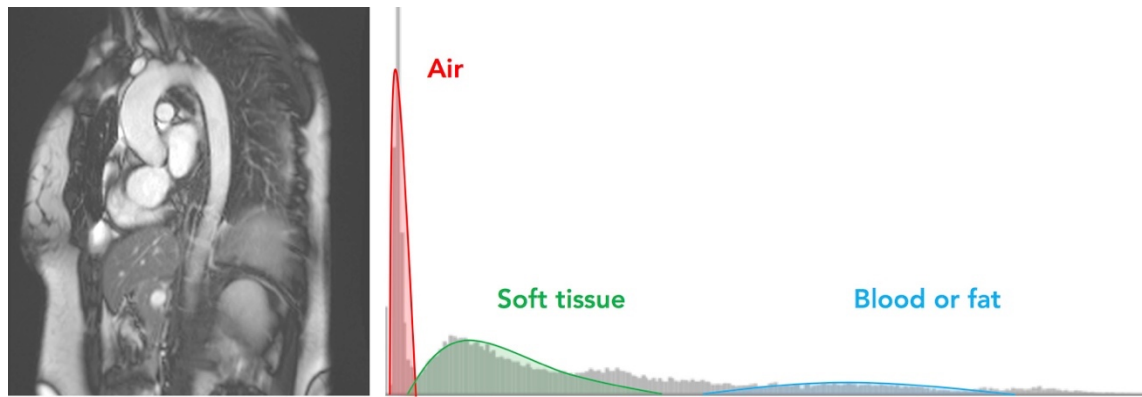


Figure 1-14 Pixel classification method using gaussian distributions to separate image features.

Left: original aortic arch dicom image. **Right:** Histogram of the number of pixels, split by image intensity. In Gaussian Mixture Models, these distributions (likelihood functions) are then fitted to a weighted normal distribution from which pixels can be classified.¹³¹ This model is a form of unsupervised learning using expectation maximization. More advanced models can use more detailed gaussian pixel distributions or in combination with other methods.¹³⁵

1.4.3. Supervised pixel-based image analysis

Unlike unsupervised strategies, supervised strategies require the use of labelled training data. Supervised approaches may perform better, but are dependent on the quality and availability of the training data used. Training datasets are typically labelled manually, which can be a time-consuming process. Training then takes place using these example data to weight a function that minimizes the risk of mis-classification. Supervised learning methods to weight this function include random decision forests or neural networks. Random decision forests use a popular method of classification, decision trees. These can function in parallel, and amalgamate to form a decision forest. Each tree within a forest uses layers of pre-defined simple decision rules to reach a classification, and training data is used to decide upon the progression through different decisions within each tree. The complexity of these layers can vary, but as with all modelling, there is a risk of over-fitting – i.e. new data is classified with low bias, but high variance and poor prediction.¹³⁶ Trees can be pruned of decisions to minimize this,

or random decision forests that randomly select training data, or features for different trees, can help to minimize over-fitting. Because of the random nature of the forests, models can be hard to reproduce.

Neural networks are an imitation of visual pattern recognition, designed to work like the neocortex when it interprets geometric similarities and overall “gestalt”. One of the earliest neural networks was designed by Fukushima et al. to model the human neuronal connections, and as such, has different layers of artificial neurons with different functions.^{137,138} The network consists of an input layer (comparable to a photoreceptor neuronal layer) followed by a cascade of a number of modular structures composed of simple cells (with afferent synapses) and complex cells (to perform processing). A specific stimulus pattern is input through the network to elicit a response in one cell in the output layer. The inputs of each simple cell are modifiable, based on training organized by the network itself, and allow for non-linear associations. The aim of the work by Fukushima et al. was primarily to model the human brain, but focus has since shifted to broader practical uses.¹³⁷ Since his work, the depth of layers in a neural network has increased, leading to the term “deep” neural networks.¹³⁹ The principle however remains that the network aims to minimise the error between the output of a network and the training data using a loss function. As a network learns, the weights for each layer are adjusted to minimize this error, and can often extend into many million adjustable parameters.

The most successful type of neural network for medical image analysis, or other computer vision tasks, is known as a convolutional neural network (CNN).^{140,141} Unlike other forms of networks where the output of each layer inputs into every neuron in the next layer (a feedforward network), CNNs maintain fewer connections. This maintains spatial information because each subsequent layer only looks at a narrow receptive

field- a smaller area of the previous layer. Like the work of Fukushima et al., each convolution in a CNN permits feature recognition across the whole image, meaning that patterns are not dependent on position. Complexity is also reduced, because features are condensed into a single weight for the whole image, rather than individual parts.^{140,142}

Pooling layers are also added that collate values from larger image regions to induce translational invariance. Other features include batch normalization (scaling and describing data as deviation from the mean) to make CNNs less dependent on the initial input. Dropout regularization has significantly boosted the performance of CNNs by averaging the performance of different models. Back propagation algorithms, introduced in the 1970s, are now integral to CNNs. These work by repeatedly adjusting the weights of connections within the network by measuring the difference between the actual output and the desired output. These can be considered as hidden units which do not directly form part of the chain from input to output.¹⁴³

CNNs have outperformed other forms of networks on medical imaging since the 1990s.

In seminal work at that time, a CNN outperformed other networks for lung nodule detection with an AUC 0.83 vs 0.65, and a rapid processing time of 15 seconds.¹⁴⁴

Convolutional neural networks have now become the standard platform for computer vision problems. Because CNNs themselves require very little engineering by hand, they are able to take advantage of high volume training datasets. Selection of training data is therefore integral to the performance of a CNN.¹⁴⁵ Whilst data is increasingly available it is logistically difficult to prepare. Imaging data needs to be standardized, and labelled, and typically requires a large volume. Depending on the population sampled by the training data, classification may be prone to bias, or fail when tested on unseen data.^{146,147} It is also important to test CNNs on balanced data that represents the real-world distribution of covariates, with realistic pre-test probabilities and imaging

characteristics. It is increasingly appreciated that receiver operator curves can be misleading on test datasets where true positives are rare (a common scenario in clinical practice), and that selection of diseased individuals may introduce biases related to selection, Figure 1-15.^{148–150}

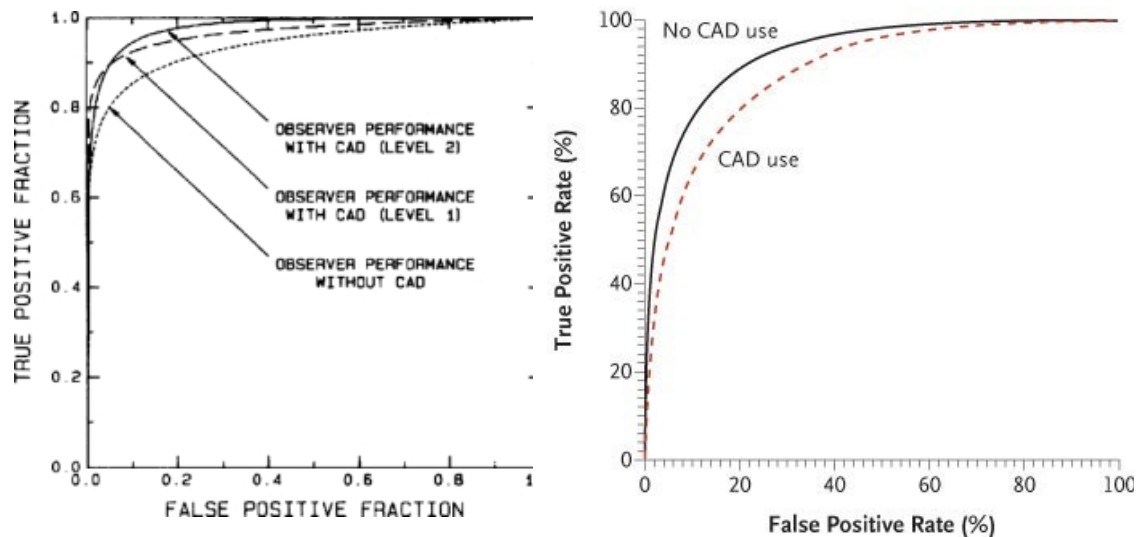


Figure 1-15 Good experimental performance (left) does not equal good clinical performance (right).

These receiver operator curves are taken from the early 1990s when computer aided diagnosis (CAD) was being developed for breast nodule detection for mammography. Early experiments using retrospective unbalanced datasets showed that radiologist performance at detecting nodules improved with CAD.¹⁵¹ Subsequent FDA approval of CAD software then became incorporated into standard radiology practice, but the impact was unclear. Real-world analyses showed that CAD use resulted in more inaccurate nodule detections, with the added time-cost of using the interface.¹⁵² Thanks to Dr Luke Oakden-Rayner with permission from *Wolters Kulwer Health Inc.*, and copyright *Massachusetts Medical Society*.

Definite real-world evidence of the benefits of AI should involve a prospective randomized clinical trial in a clinical setting measuring clinical outcomes,¹⁵³ societal and economic evaluations.¹⁵⁴ Recent multidisciplinary guidelines have acknowledged the difficulty in separating data into adequate training and separate validation cohorts.¹⁵⁵ It is important to report whether results are biased, generalizable, if there is data leakage (unauthorized transmission of data from within an organization to an external destination or recipient), or how many eligible datasets were used (particularly important with big datasets). Training data may be poorly labelled or be contaminated

by substantial intra- or inter-observer error, resulting in sub-optimal performance.

Currently no methods to detect or minimize these problems have been developed.

Newer strategies to assist the training process include adversarial learning, use of priors or circumventing data labelling altogether.^{156,157}

1.4.4. Atlas-based image analysis

A method which is more reliant on anatomical priors is the use of atlases for image segmentation. Atlases can also provide a useful framework for understanding different domains of a phenotype or population, which also merits discussion because of its relevance to this thesis. An atlas is an alignment of different layers of data to enable comparisons between them. This can be similar data from different patients, or different data from the same individual. Neurology leads this field, and atlases have been developed that incorporate anatomical, genetic and functional imaging. These can be used as open-source tools for research into a variety of fields including neuroscience, neuropharmacology, genetics and clinical neurology.¹⁵⁸

Cardiology lags behind with this, but the technology is available, and cardiac atlases of the heart have been developed encoding different information.^{159–162} The information encoded can be variable, depending on the requirement for the atlas. Typically this is structural or motion information, but this information can also be combined with other information such as electrical conduction to provide individual patient modeling.^{163–165} In cardiac imaging, atlases have been used to encode imaging data from CMR, computed topography, ultrasound, or multi-modalities.^{163,166–168} Clinically, atlases have the potential to provide imaging “reference-ranges” for voxel-wise analysis, potentially transforming clinical MRI by providing quantitative metrics to support the qualitative reading of a study by an expert.¹⁶⁹

In general, steps to consider when building an atlas are: (1) data provenance, (2) data labelling, (3) data transformation and normalisation, and (4) representation of results. Considerations for step (1) are similar to making decisions on a training dataset for a supervised image segmentation approach, as detailed above. Traditionally, atlas populations have been small in number due to the difficulty in labeling datasets. There has been a concerted effort to make this pipeline scalable both by clinicians, researchers, and industry in order to improve image analysis, driven in part by the parallel advent of promising neural network-based techniques.¹⁰³ Researchers have now contributed large datasets, including CMR imaging from the Multi-Ethnic Study of Atherosclerosis (MESA) study, consisting of 2864 asymptomatic individuals. The Digital Heart Project has also compiled a dataset of over 1000 healthy individuals.^{160,170} Image labeling for these studies, however, was manual and time-consuming. Researchers have now developed methods to automate steps to initialize segmentations, such as landmark selection.¹⁷¹ These atlases have been used to understand determinants of cardiac structure in health or sub-clinical disease.^{160,172} Additionally, these atlases have been used to guide prospective, new, image segmentations, but it is not known whether these healthy atlases can be applied to disease.^{76,170} Prior to either image segmentation or population comparisons, it is necessary to perform co-registration to find corresponding anatomical or functional regions in two images.¹⁷³ This allows comparisons to be made in a standardized way across different individuals. Transformations can include global transformations to address issues around different size, orientation and translation. These transformations are known as affine transformations and are useful to preserve the overall shape. Local transformations on the other hand, help to address issues around differences in regional shape. Local deformations can be quite variable in biology, and therefore models need to capture

variability adequately whilst providing some structure in the irregularities. Cubic b-splines (basis-splines) provide a balance between limiting the number of degrees of freedom and adequate contour motion. Cubic b-splines have been used for effective registration tools in breast and cardiac imaging.¹⁷³ The use of non-rigid registrations in addition to rigid and affine transformations significantly improves co-registration accuracy.¹⁷³

Atlases can be used for the task of image segmentation. This initially requires co-registration of an image with a reference library of images and their attached labels, as described. Once images are co-registered, the target image requiring segmentation can be labelled according to similarities with the labelled atlas image.¹⁷⁴ Selecting the most appropriate corresponding atlas is therefore important in order to achieve high labelling accuracy. There are different approaches for atlas image selection. The target image can be registered to an individual atlas image, to a population average of multiple images in the atlas, or to every image within the atlas.¹⁷⁵ Using the latter approach, there would be multiple labels per target image. Because these images are within the same coordinate space, the labels selected by each atlas image for the target image coordinate can be counted and the highest voting label is typically assigned.^{175,176} Methods that collate data from multiple labels have shown greater accuracy in human brain imaging, and have been applied to cardiac data.^{176–178} If using large atlases, a custom query based on demographics can also improve brain segmentation accuracy.¹⁷⁹ It is unlikely that image co-registration can occur exactly between images - indeed, there is no method to define the exact same point in two different hearts (except, perhaps, the apex). Later algorithms have acknowledged this difficulty, and have included the option of expanding the label search to adjacent groups of voxels, or even to similar voxel patterns from across the whole image.^{180,181} This adds robustness to poor image co-

registration or labelling errors, and new search and parallelization strategies have sped up the search process for computer vision applications.^{181,182} Atlas-based segmentations still can be computationally expensive compared to pixel-based techniques such as neural networks, and local data suggests neural networks have greater Dice coefficients (a measure of overlap between two datasets).¹⁸³

Once segmentations have been made, it is then necessary to represent these in the same template space, so comparisons can be made across similar regions within a population.

As images need to undergo transformations prior to comparison with an atlas, the segmentations must also be co-registered for standardized comparisons. In order to preserve shape, affine transformations are used for this process. Typically the co-registration is to a reference template. This may be an average template shape of a population or a specific individual. The template itself is arbitrary, as long as it is standardized for all co-registrations. Shape representations using this method show good agreement with 3D shapes derived directly from slice-based manual contours.¹⁶¹

Once segmentations are derived and co-registered, the next step is to present very complex data intuitively both qualitatively (visually) and quantitatively (for statistical comparisons). Statistical shape models can provide descriptions of morpho-functional parameters, and their variance across a population. Models have been used to characterize 3D descriptions of shape and deformation.^{184,185} Every individual mesh can be represented as a point cloud, known as a point distribution model. Principal component analysis can be applied to these statistical models to represent the variation in shape through its principal components (a data dimensionality reduction technique). Each principal component represents a mode of shape variance, and each component is by definition orthogonal to the others, Figure 1-16. Typically the first few modes represent the majority of data in a population, but modes can be difficult to

interpret.^{186,187} It is also possible to pre-specify independent components that are more clinically intuitive, using independent component analysis.¹⁶⁰

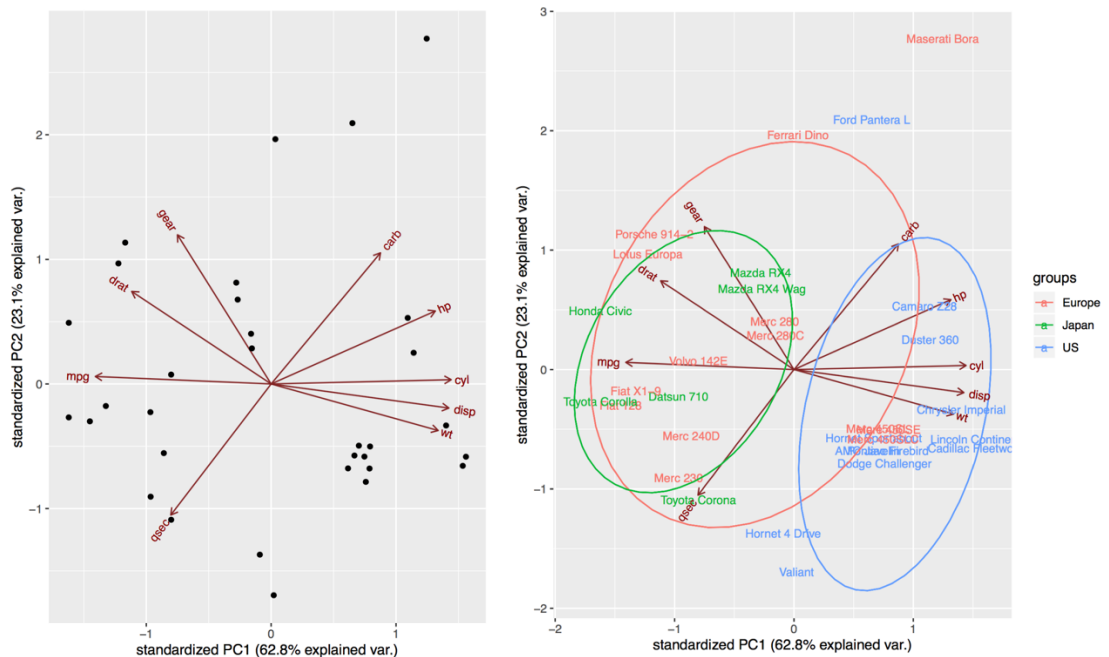


Figure 1-16 Principal Component Analysis.

This analysis uses a freely available dataset describing the features of thirty two different cars, such as engine cylinders, fuel efficiency, manufacturer, country. On the left, the first two principle components (PC1 and PC2) are presented, which explain 85.9% of total variance. PC1 is explained by horse power, cylinders, and weight. PC2 by the number of gears and carburetors. On the right, when country of manufacturer is superimposed, clusters of variance in PC1 become clearer.

Other approaches have tried to describe data in a more clinically intuitive manner, using an American Heart Association (AHA) classification model.^{188,189} Such clinical measures unfortunately require losing granularity, which may be important given that pathology is not confined to segmental boundaries. This has motivated the development of other approaches that divide the imaging dataset into homogenous parcels of information of high spatial resolution (“parcellation”).¹⁹⁰ Each parcel can contain a structural or functional measure at a small, defined anatomical region, which may be easier to interpret clinically.

One application of this technique using CMR datasets was for classification of patients with previous myocardial infarctions. Shape features were able to outperform conventional global LVM or LVEF, and incremental value was gained by using motion.¹⁹¹ Quantitative regional measures such as myocardial wall thickness, shape, wall stress and strain may also be useful but were untested. It is unclear whether dimensionality reduction techniques, or point estimates of a particular parameter (e.g. wall thickness) better characterize local or regional abnormalities. The precision of 3D co-registrations has also only had limited investigation,^{76,192} but the approach has already been used to detect regional changes from co-registered CMR LV models in obesity, pre-hypertension, pulmonary hypertension, congenital heart disease and aortic coarctation.^{161,187,193–197}

1.4.5. Presenting results of automated segmentations

A number of medical imaging “grand challenges” have attempted to accelerate the success of automated analysis. Early challenges (MICCAI 2009 and STACOM 2011) provided 45 and 195 cine-SSFP CMR datasets respectively, split between testing and validation.^{93,198} Evaluation of new automated segmentation techniques was performed against expert ground truths, and presented as contour comparisons (such as mean error or Dice index). Dice indexes or Hausdorff distances are however not intuitive for clinicians, making it difficult to identify which tools are clinically useful, or add utility.^{90,93,198} Expert segmentation for the “ground truth” comparisons used in these challenges is also time-consuming, meaning cases numbers are necessarily small, and limited to a few centres and pathologies. The limitations of small training and validation samples in early challenges has potentially been addressed by the UK BioBank data, if these data are made available. However, these data are from a single study using a

single MRI scanner type with standardized sequences, meaning that the resource may lack generalisability. The MICCAI ACDC 2017 challenge has provided scans and ground truths from different centres (n=150).

Early segmentation approaches showed reasonable success, but the more recent Kaggle Data Bowl in 2015 raised the possibility that automated CMR segmentation was a solvable problem, with the first application of deep learning approaches using convolutional neural networks, Table 1-7.¹⁹⁹ Because of the reliance on expert contours, however, it was not possible to identify a technique superior to human analysis, despite a growing appreciation of the high intra- and inter-observer variability that exists in human measurements.^{90,103,147} Competitors also noted that ground truths by an expert, seemed to be erroneous, resulting in large outlier effects.²⁰⁰ Whilst the competition used 700 datasets from one centre (70% for training), it is unclear whether the successful algorithms are generalisable to real-world CMR data.

Lead Author	Challenge	Automated	Initialisation	Papillary muscle inclusion	MV tracking	Segmentation description
Huang S	MICCAI 2009	Fully		Yes	unknown	Otsu, radial region growing blood pool. Epicardial canny edge detection.
Lu Y	MICCAI 2009	Semi	Centre of blood pool	Yes	no	Otsu, disk shaped structuring element for blood pool. Expansion from endocardium then region growing for epicardium.
Marak L	MICCAI 2009	Semi	Image contrast and centre of blood pool	no	no	Morphologic region growing.
O'Brien S	MICCAI 2009	Semi	Base and apex selection		no	Automatic shape model using 30 manually labelled models
Jolly M	MICCAI 2009	Fully		no	unknown	Otsu for blood pool. Myocardial gray scale analysis based on blood pool with multi-seeded fuzzy connectedness approach to group homogenous regions for labelling
Constantini-des C	MICCAI 2009	Semi	Centre of blood pool and sup RV insertion	yes	unknown	Image filtered to prior to a "GVF-Snake" blood pool edge detection. GVF-Snake evolution constrained using expected thickness of the myocardium.
Casta C	MICCAI 2009	Semi	Centre of blood pool, radius and wall thickness	no	unknown	Based on inputs, a single frame (static) volumetric model is built by minimising a global energy function (elastic deformable + imaging data energies). Extended to all phases based on the equation of dynamics and including temporal smoothness constraints.
Wijnhout J	MICCAI 2009	Semi	Centre of blood pool	no	unknown	Active appearance model for initial contours then optimised using image gradients at blood pool border. Epicardial 3D active shape model fit on features labelled by a fuzzy inference method.
Jolly M	STACOM 2011	Fully		yes	yes	Time based Fourier analysis plus propagation to all other frames and repeated.

Table 1-7 continued on the next page.

Lead Author	Challenge	Automated	Initialisation	Papillary muscle inclusion	MV tracking	Segmentation approach
Margeta J	STACOM 2011	Fully		no	unknown	Normalisation and layered spatio-temporal forest decision-trees.
Ahmed S	STACOM 2011	Fully		no	no	Optical flow (a computer vision technique) and refinement using an active contour model.
Ulen J	STACOM 2011	Semi	Slices and centre of blood pool	yes	no	Each voxel assigned probability of representing the LV or RV blood pools, myocardium or background based on location and image intensity. Geometric constraints applied for simultaneous LV, RV and myocardial segmentation (better than analysing each chamber separately).
Bai W	MICCA 2012	Semi	5 landmarks	no	no	3D multi-atlas based segmentation method labelling structures by ensembling opinions from multiple atlases.
Liu A, Tencia	KAGGLE 2016	Fully		NA	No	Trained on Sunnybrook data (45 cines) and 130 hand-labelled SAX images. Hand-segmented 4Ch views for LAX model for failed cases. Preprocessed data. Different CNNs trained with different parameters. CNNs trained to minimise a modified version of the sorensen-dice index. Meta-data used to detect and fix bad data. Theano tensor, Python 2.7.6.
De Grave J	KAGGLE 2016	Fully		NA	No	400 patient training data. No handlabelling. Pre processing (zoom, contrast normalisation), data augmentation. Identifying a ROI (fourier based image and Hough circles). Outliers dealt with by combining LAX and SAX models. VGG-16 architecture.
De Wit J	KAGGLE 2016	Fully		NA	No	2000 training slices hand-labelled. Batch normalisation. Elastic deformations for augmentation. Logistic regression better than RMSE. Adding more layers quickly led to diminishing returns. U-net architecture-allowed for more detail in the segmentation by using shortcut connections from the i'th layer to the n-i'th layer. Outlier patients hardest to segment.

Table 1-7 “Grand Challenges” contestants in cardiovascular magnetic resonance imaging analysis contacted for collaboration in this thesis (Chapter 4). Researchers were contacted as previous successful entrants in segmentation challenges. The aim of collaboration was to use a large dataset comprising scan-rescan data across health and disease in order to define the most precise and reproducible method for left ventricular analysis. *Abbreviations: MV= mitral valve.*

1.5. Arterial function

1.5.1. Function of the aorta

Conduit function

The main function of the aorta is to distribute blood to the body. It acts as a conduit which histologically consists of three layers delineated by the internal and external elastic laminae. The innermost layer, the *tunica intima* is composed mainly of endothelial cells (there are also myofibroblast-like cells in large animals); the *tunica media* is the thickest layer, composed of smooth muscle, elastin and collagen; and the *tunica adventitia*, composed of collagen, vasa vasora, myofibroblast-like cells, adipocytes and lymphatics.^{201,202} Blood flows peripherally down the mean pressure gradient of 2-4 mmHg from proximal to distal aorta.²⁰³

Windkessel function

Additionally, the aorta serves to dampen the oscillations in blood pressure that result from intermittent ventricular systole. This is known as the *Windkessel* function, and serves to maintain constant tissue perfusion. The haemodynamics have been modelled by a number of approaches. The original is known as the two-element Windkessel model. It recognises that there is a decay of diastolic pressure when flow is zero, and that this is related to peripheral resistance and total arterial compliance.²⁰⁴ Because of resistance, only approximately half of the stroke volume is transmitted directly to the tissues during systole. The other half is temporarily stored through the distension of the wall of the aorta as it is stretched by the pulse pressure (PP). Potential energy is therefore stored within the vessel wall in systole and provides the work required to drive blood flow through the tissues during diastole. The relationship between distension pressure and the extent of distension is governed by the compliance of the artery (aorta);

thus, when the aortic wall is more compliant (i.e. less stiff), for a given stroke volume, the PP is lower. While the 2-element Windkessel model is a comprehensible and useful model of aortic haemodynamics it is highly simplified and the agreement between predictions of flow and pressure in systole is poor.²⁰⁵ There are two major reasons for this; firstly the Windkessel is a lumped model and ignores wave transmission in the circulation; secondly the Windkessel assumed that arteries are linearly elastic (i.e. compliance is independent of pressure which is not the case. At low pressure, the tension in the aorta is largely borne by elastin fibres whilst at high pressure, the stiffer collagen fibres bear more load.²⁰⁶ Better fits to measured pressure and flow have been achieved using a modified three-element Windkessel model which includes as an additional component – aortic characteristic impedance;²⁰⁷ and even better with a four-element model that takes into account “total arterial inertance”;²⁰⁵ but all these zero-dimensional lumped models effectively ignore the contribution of waves in the circulation.

Blood pressure regulation

The mean arterial pressure required for homeostatic tissue perfusion is controlled by changing systemic vascular resistance and cardiac output (largely via heart rate). On a beat-to-beat basis this is regulated predominantly by feedback from mechanoreceptors that sense pressure in the aorta and some large elastic arteries, namely baroreceptors in the ascending aorta, aortic arch and carotid artery. An increase in blood pressure activates these mechanoreceptors that cause a decrease in both heart rate and systemic vascular resistance via a central neural feedback circuit involving the autonomic nervous system as its efferent component.

1.5.2. The blood pressure waveform

Blood pressure is a powerful predictor of cardiovascular risk.²⁰⁸ It is traditionally measured in the brachial artery at its maximum and minimum oscillations as systolic blood pressure (SBP) and diastolic blood pressure (DBP) respectively. Understanding the entirety of the waveform however not only provides more detail, it offers insight into the mechanisms that drive this risk. In terms haemodynamics, these can only be understood by considering the various factors that promote and oppose ventricular ejection over its time course.²⁰⁶

LV ejection causes a rise in pressure in the aorta resulting in flow of blood. The stroke volume and the compliance of the major elastic arteries including the aorta are the major determinants of pulse pressure.^{204,209} LV ejection is an oscillatory input, and is opposed by impedance of the arterial circulation. The impedance of the arterial circulation in turn depends on the compliance, inertance and resistance of the downstream network. These properties of the network explain the cushioning capacity of the arteries and the intensity and timing of wave reflections.²¹⁰ Arterial compliance and wave reflection have been identified as the most important determinants of isolated systolic hypertension with age and are recognised in ESC guidelines.²¹¹ They are often measured as aortic pulse wave velocity and augmentation index respectively although neither of these measures is more than an approximation of what are spatially heterogeneous, complex aspects of arterial function.^{212,213} Nevertheless both parameters independently predict survival in the general population, patients with renal failure and hypertension.^{214–217}

Safar et al. provide a haemodynamic explanation for this. With increasing age, the main drivers of higher PP are increased wave reflections and particularly higher arterial stiffness (if anything stroke volume decreases). Safar notes that SBP and PP (and by

inference its closer haemodynamic relationship with wave reflection) are more informative cardiovascular risk factors than diastolic blood pressure.²¹⁰ Specifically, after myocardial infarction and in heart failure, PP is an independent marker of cardiovascular risk whilst SBP and DBP are not.^{218,219} Understanding the properties of wave reflection and aortic stiffness may also explain why medications are more effective in reducing DBP than SBP in older patients with hypertension.²²⁰

Waves and wave reflection in the circulation

Waves transfer energy without necessarily transferring mass. Once the aortic valve is open LV contraction causes a forward travelling wave that accompanies ejection. This energy wave travels along the arterial tree; the speed of this transit is determined by the bulk compressibility of the arteries which is almost exclusively due to the compressibility (i.e. elasticity) of the arterial wall (the blood being comparatively incompressible). The propagation speed of the wave (pulse wave velocity) is considerably faster than the fluid flow velocity (5-10m/s compared with ~1m/s).

Transmission of energy from one arterial segment to another depends on the admittance (inverse of impedance) of each segment (at bifurcations the composite admittance of the two daughter branches can be regarded as the downstream segment). In healthy individuals, there is little or no difference in admittance in the segments of the large elastic arteries (i.e. no change in energy transmission properties from segment to segment - termed admittance (or impedance) matching) in the forward direction and reflections are generally small or absent. In contrast, the small muscular arteries and arteriolar tree, the principal sites of resistance, represent a large reduction in admittance which results in retrograde transmission (i.e. reflection) of energy. As there is a high degree of branching at the small artery/arteriolar level, there are a number of diffuse reflection sites at varying distances from the LV. Backward travelling reflected waves

then return towards the heart but undergo re-reflection at bifurcations (bifurcations which are matched in the forward direction are ill-matched in the backward direction) and then undergo further (re...)-re-reflection.²²¹ This means that while reflected waves return to the aorta and add to the forward wave, resulting in an increase in systolic pressure and a reduction in forward flow, they do so in a diffuse manner and the distance of reflection cannot be inferred from the arrival time of the reflection wave.^{222–}
²²⁴ Diastolic blood pressure, is likely explained by the multitude of low intensity reflected waves that persist from end-systole to end-diastole because no energy is input from the LV after closure of the aortic valve. Diastolic pressure decay occurs because wave energy slowly passes out of large arteries into the peripheral circulation. It has been suggested that fewer branches, vasoconstriction and arteriolar remodelling/hypertrophy should result in earlier reflection and increased PP, but this remains to be demonstrated, and since there is evidence that the magnitude of reflection decreases with age this idea may be questionable.²²⁵ Similarly as arteries stiffen (e.g. with age) wave speed will increase and it has been proposed that wave reflections will return earlier; however due to the complexity of retrograde wave transmission the magnitude of this effect appears to be small.²²⁶ Still, it is fair to conclude that both small and large arteries contribute to wave reflection and in turn to blood pressure.^{206,210,227}

Augmentation index

The phenomenon of reflection is probably best quantified by the reflection coefficient, which is defined as the ratio of backward and forward waves described by their magnitude and phase angle,²⁰⁴ or by the ratio of backward and forward wave intensities (or energies).²¹³ The augmentation index (AIx) can be derived noninvasively through applanation tonometry or suprasystolic oscillometry and has the benefit of only

requiring pressure measurement. It is measured as the ratio of the secondary rise in pressure and total pulse pressure.^{211,228,229}

Because reflected waves can be described in the magnitude and timing of their return, they affect the shape and amplitude of a pressure waveform. With a late backward wave for example, the augmentation index may be negative even though reflections may be significant. Such a waveform is described as a type C waveform. Conversely early and large backward waves result in a positive augmentation index, a type A waveform. Type B waveforms are those where the systolic waveform and inflection point are at similar time points. Type D are those where an inflection point is not evident, and are reported in younger individuals.²³⁰

There are a number of influences on AIx besides vessel stiffness. Height is proportional to the distance to reflected site and higher heart rate means a shorter ejection time and relatively later arrival of the reflected wave in the cardiac cycle. Thus greater height and faster heart rates are associated with lower AIx.^{231,232} Age results in arterial stiffening and it is well established that AIx increases with age.²²⁹ There is growing evidence however that this relationship is not linear, and plateaus in the elderly.²³³ Female sex also results in increased AIx, even when accounting for height differences.²³⁴

Higher AIx is also correlated with left ventricular hypertrophy and essential hypertension. There are few studies looking at outcomes and these are confined to specific groups including end stage renal failure, and patients with coronary artery disease. Studies in broader populations such as elderly hypertensive women have not found a correlation between AIx and outcome.^{233,235,236}

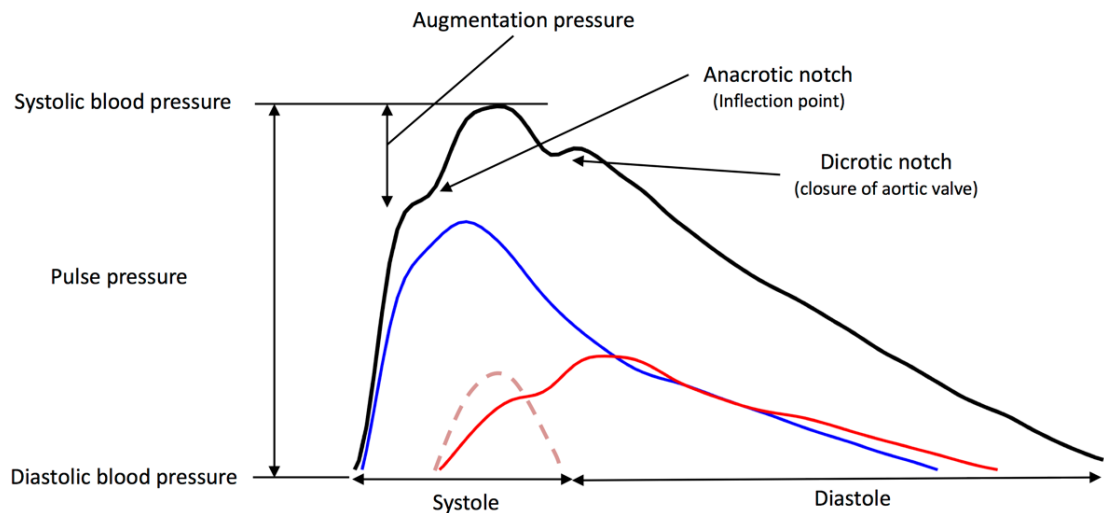


Figure 1-17 Central aortic pressure waveform.

Blue= forward wave; red= backward wave. The pink dashed line shows the inaccurate assumption behind the interpretation of the augmentation index that wave reflection is confined to systole. The first inflection point represents the arrival of reflected waves at the aortic root. The dicrotic notch is associated with closure of the aortic valve its shape probably being influenced by forward and backward waves.²³⁷ This representation does not account for the reservoir pressure, which suggests that the contribution of reflected waves to pressure may be lower than represented here, because it does not account for changes in filling and emptying of the aortic vessel wall (the "reservoir").^{238,239} Data acquired from one healthy individual prior to exercise training or a first-time marathon.

Whilst AIx is taken as a measure of wave reflection, it is a dimensionless index that partly captures the cumulative impact of reflected waves, Figure 1-17. Westerhof originally demonstrated this by showing that the timing of the backward wave influenced the AIx at similar overall reflection magnitudes, Figure 1-18.²²⁸ When type C waveforms are discarded, AIx does not correlate with age. Indeed, AIx does not correlate with gold standard measures of forward and backward wave ratios measured by carotid tonometry, even when type C waveforms are discarded.²¹³ AIx therefore provides a qualitative assessment of the reflected wave but does not provide a quantitative assessment of wavefront energetics. Waveform analysis and calculation of forward and backward waves allow for a better understanding by quantifying wave timing, intensity and proportions.^{204,227} AI shows only modest correlation with

the magnitude of reflection using reference measures combining pressure and flow.^{228,240,241}

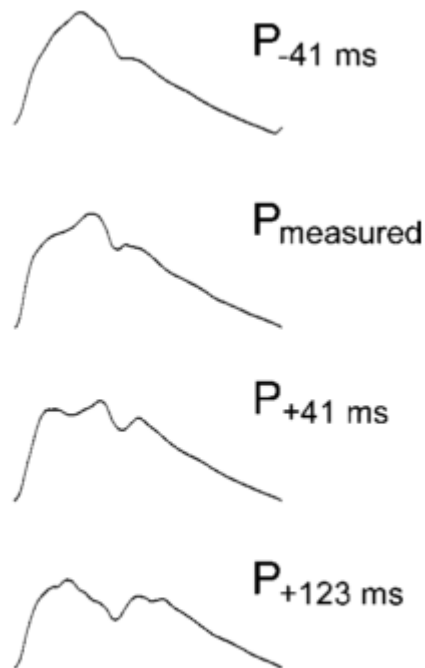


Figure 1-18 Westerhof's experiments to highlight the importance of wave shape and timing.²²⁸

The augmentation index depends not only on the magnitude but also on the time of return of the reflected wave. Pressure is represented on the y axis, and time on the x axis in these graphs. Each waveform represents the pressure waves by summation of forward and backward waves when the backward wave is shifted from a time point, P. Reproduced with permission from *Wolters Kluwer Health Ltd.*

1.5.3. Non-invasive estimation of central blood pressure

When measuring AIX, central pressure waveforms should ideally be analysed, because central (rather than peripheral) blood pressure represents the true load on the left ventricle and central arteries.²²⁷ It is not possible to measure directly central pressure using non-invasive methods, and so models have been developed to derive the central waveform from a peripheral measurement. Many studies have measured the peripheral and central waveforms simultaneously. The mathematical function that relates the two waveforms is known as a “generalised transfer function”, and has been traditionally

used to estimate aortic pressure waveforms non-invasively from a peripheral pressure waveform (typically from radial tonometry).^{242–245} This estimate correlates with invasive measures of central BP.^{246,247} This method however may lack accuracy for individual patients.²⁴⁸ More individualized methods use forward and backward waves to relate aortic with peripheral pressure, but require knowledge of peripheral velocity, and therefore two simultaneous measurements.²⁴⁹

It is also possible to model central pressure without peripheral velocity by applying a model of an elastic, thin-walled arterial tree to a supra-systolic brachial artery pressure waveform.²⁵⁰ This waveform can be obtained from an oscillometric pressure cuff. One example of this is the CardioScope BP+ device (Uscom Ltd, Sydney, Australia) used in this work, which was previously known as the Pulsecor device. The model used by this device assumes the wave travels along the artery unaffected in shape, only delayed, as per Stergiopoulos et al.²⁴⁹ The artery is also assumed to have parallel sides, and that the end-occlusion of the artery by the pressure cuff results in nearly complete reflection, and at a fixed point (rather than millimetres).²⁵⁰ By imposing an occlusion, this methodology avoids the assumption of constant reflection at the hand made by radial tonometry. Possible admittance mismatching at bifurcations is not accounted for, and this may affect measurements from the right subclavian more than the left. An estimate of both the reflection coefficient for a pressure wave, and the time taken for a pressure wave to travel from the subclavian root to site of cuff occlusion are required to derive aortic pressure from pressure under the cuff using the tube law. The reflection coefficient has been chosen based on the average diameter and wall thickness near the middle of the brachial artery entered into a finite element model of arterial occlusion.²⁵⁰ The time-delay chosen assumes a path length of 0.18m from subclavian to the cuff.²⁴⁹

Overall, the model used has been shown to yield estimates that are highly correlated with central systolic BPs and pressure waveforms measured with invasive catheter assessments. These studies demonstrated minimal bias, and good intra-and re-test reliability.^{251,252} Lin et al. measured invasive central aortic pressures in 37 individuals and compared these to the Pulsecor device measurements.²⁵¹ These assessments were however not quantitative. They report that “synthesized pressure waveforms display good concordance with directly recorded waveforms by invasive catheter method in both pulse amplitude and contour”, Figure 1-19. Lowe et al. studied 22 patients comparing quantitatively invasive aortic catheterization with simultaneous recordings using the Pulsecor device.²⁵⁰ Correlation between the estimated non-invasive and actual invasive waveforms averaged above 0.9. Other studies have also reported acceptable correlations between cuff-based and invasive pressure profiles.²⁵³

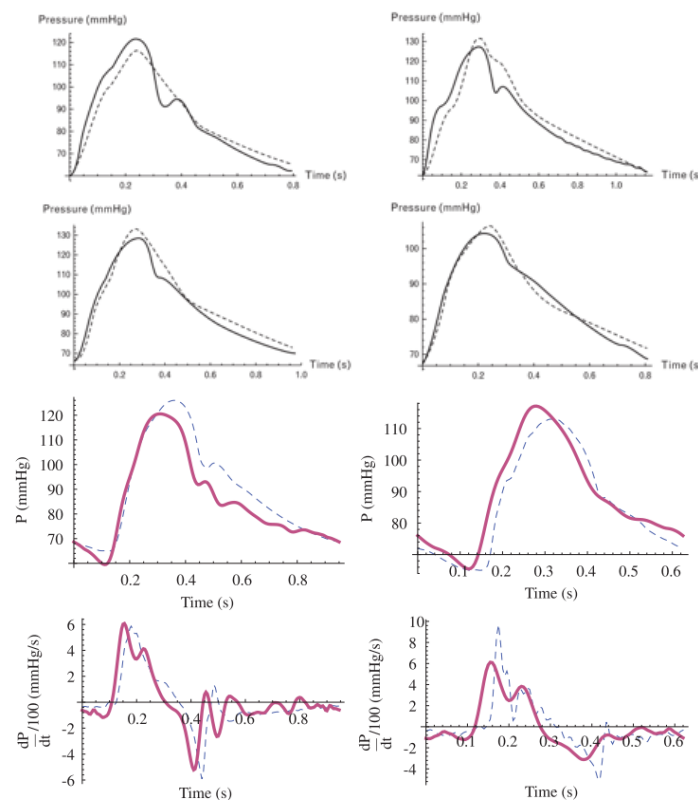


Figure 1-19 Non-invasive pressure waveforms. From Lin et al.²⁵⁰ and Lowe et al.²⁵¹ Permission from Elsevier and Wolters Kluwer Health.

1.5.4. Arterial stiffness

Local arterial stiffness

In healthy individuals distal arteries are stiffer (i.e. higher wave speed) than more central arteries, and reflection sites are closer.²²⁷ This progressive increase in stiffness along the length of the arterial tree is consistent with histological findings (elastin/collagen content) and morphology (increased wall to lumen ratio).^{210,254} The pulse pressure is higher in peripheral than central arteries, and this is known as the “amplification phenomenon”. In younger patients, amplification is more pronounced.²²⁷ Measurements of local arterial stiffness can be performed using local PP measurements coupled with local area changes, local diameter changes, or velocity profiles.^{206,255,256} None of these methods provide exact estimates of wave speed compared to theoretical model parameters.²⁵⁷

Pulse wave velocity measurement

The aorta is a major vessel of interest because it contributes the most to the Windkessel function.²⁵⁸ Aortic stiffness is an independent predictor of mortality and stroke in patients with renal failure,²⁵⁹ diabetes,²⁶⁰ hypertensives²⁶¹ and the elderly.^{262,263} It is an incremental predictor than conventional cardiovascular risks in widely used scoring systems.²²⁷ Pulse wave velocity (PWV) is a simple, accurate and non-invasive method to assess aortic stiffness. The current gold standard measurement is by calculating carotid-femoral PWV from the time difference between the “foot” of two waveforms (pressure, flow) measured in the carotid and femoral arteries and dividing the distance between the measurement sites by the transit time.²²⁷ Measurements can be made simultaneously but often measurements are performed sequentially and the foot to foot time is estimated with reference to the R wave on ECG. Other fiducial points on the

waveform have been used and it has been argued that peak or maximal upstroke may correlate better with ageing or distensibility; however these points may be differentially affected by wave reflections at different locations, potentially introducing bias into PWV estimates.²⁶⁴ Another potential source of error arises from the estimate of transit distance. Aortic length or carotid to femoral distance is usually measured across the body surface and small inaccuracies can lead to significant changes in PWV. The surface straight-line distance between measurement sites may not represent the true course of the aorta and branches which can be particularly tortuous in hypertension or elderly patients. Many of these limitations can be overcome using CMR. Because it is not limited by tissue depth, it permits direct measurement of velocity, flow and distensibility at the aorta, as well as true 3D aortic length.²⁶⁵ Measurements with CMR show good intra-, and inter-observer reproducibility, and good inter-study reproducibility.²⁶⁶

Interpretation of pulse wave velocity

The apparent stiffness of the aorta varies with pressure: as blood pressure increases, so does aortic stiffness. Therefore a change in aortic stiffness may represent changes in the aortic wall itself or changes in dynamic elasticity based on the non-linear pressure-volume relationship. Ageing results in a number of changes: elastin breakdown; collagen deposition; atherosclerotic plaque deposition and calcification.²²⁷ Ageing has a prominent effect on aortic stiffness, which has been associated with an increase in SBP and PP.²²⁵

Impact of increased arterial stiffness on cardiovascular disease

Increased arterial stiffness results in an earlier return of reflected waves, an increase in SBP and PP. These in turn increase LV afterload and result in LVH, increased

myocardial oxygen demand and subendocardial ischaemia.^{227,267} The histological changes that occur with arterial stiffening also occur in the coronary circulation and additionally contribute to CV mortality.

A number of pathophysiological conditions implicated in CV disease have independent associations with aortic stiffness and are summarised in Table 1-8. This is consistent with the known effects of blood pressure, glycaemia and lipids on the arterial wall; whether modification of these risk factors can reverse effects on arterial stiffness is uncertain.^{214,227} There is little evidence exploring whether a reduction in arterial stiffness independent of a reduction in blood pressure is associated with a reduction in cardiovascular events.

CV Risk	Genetic	Non-CV diseases
Obesity	Family history of hypertension	Renal failure
Smoking	Family history of diabetes	Rheumatoid arthritis
Hypertension	Family history of infarction	Systemic vasculitis
Hypercholesterolaemia	Genetic polymorphisms	Systemic lupus erythematosus
Diabetes	Other physiological states	Ageing
Elevated C-reactive protein	Low birth weight	
Congestive heart failure	Menopausal states	
Coronary heart disease	Lack of physical activity	

Table 1-8 Clinical conditions associated with increased aortic stiffness. Adapted from Laurent et al.²²⁷

1.5.5. Clinical application of aortic wave intensity analysis

Analysis of waves in the circulation can describe the efficiency of energy generation and transfer in the cardiovascular system. Using wave intensity analysis (WIA), the magnitude of the rate of energy transferred by a wave per unit cross-sectional area (i.e. intensity) is quantified as the product of the rate of change of pressure and flow-velocity at the same location.²⁶⁸ Waves are further characterized by their direction of travel (forwards or backwards), and the pressure gradient across them (compression or decompression waves). Both these characteristics determine their impact on pressure and flow (e.g. a forward compression wave increases pressure and accelerates flow

whereas a forward decompression decreases pressure and decelerates flow). In addition to measuring the timing and intensity of waves, WIA can quantify local wave speed, a measure of local arterial stiffness.^{268–271}

WIA can be applied to improve our understanding of pulsatile cardiovascular haemodynamics in the aorta. Three principal aortic waves have been observed, Figure 1-20. A dominant forward compression wave (FCW) in the early phase of LV ejection has been associated with myocardial contractility. A smaller forward decompression wave (FDW) has been associated with the time constant of LV relaxation.²⁷² A backward compression wave (BCW) is attributed to wave reflection originating from distal sites of impedance mismatch.²⁷³ Patterns and wave timings are similar across invasive and non-invasive studies, but slight differences in timings and intensities may reflect population characteristics or quantification differences (wave foot versus peak).^{224,274,275}

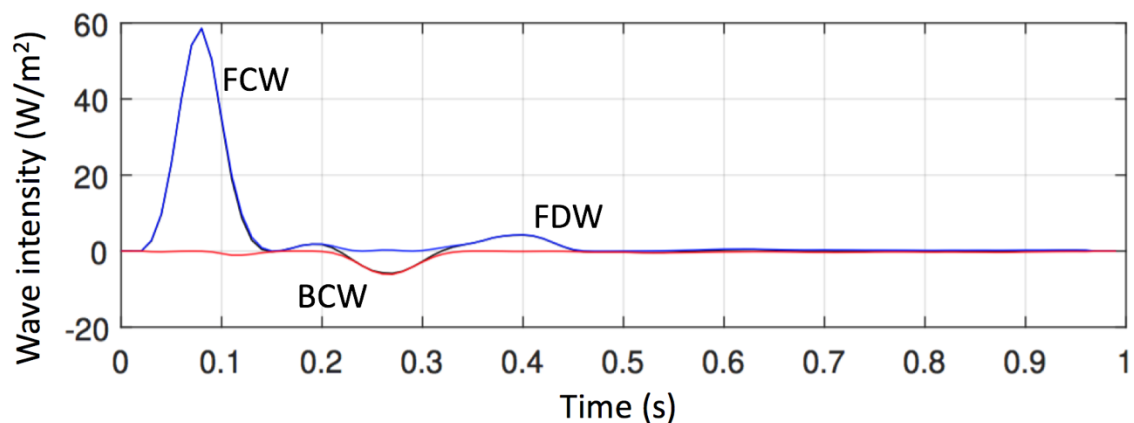


Figure 1-20 An example of aortic wave intensity analysis.

This is an example obtained from the non-invasive technique described in Chapter 6, combining CMR aortic velocity and central pressure waveforms. *Abbreviations: FCW = forward compression wave; FDW = forward decompression wave; BCW = backward compression wave.*

WIA has advanced understanding of ventricular function and arterial coupling in different pathologies. Patients with chronic heart failure have an impaired ability to

generate a systolic FCW, but wave reflection is increased, increasing afterload.²⁷⁶ Wave intensity can predict left ventricular ejection fraction recovery or quality of life improvement in patients undergoing valvular surgery, and help to identify sub-clinical systolic and diastolic dysfunction in children with heart failure and preserved ejection fraction.^{277–279} Increased wave reflection is associated with poorer outcomes in systemic hypertension independent of blood pressure.²⁸⁰ In the pulmonary circulation, an early BCW was specifically associated with pulmonary hypertension due to chronic thromboembolic disease compared to controls.²⁸¹ Whilst wave speed has been correlated with disease severity, wave reflection is unrelated, suggesting it may be an early pathological marker in the development of pulmonary hypertension.²⁸² Due to reliance on invasive measures, most of these previous insights have been derived from studies of small patient cohorts. Invasive measures are also difficult to acquire because they require multiple fluid-filled catheters, stable position to obtain steady traces, and careful calibration.²⁷⁰ Non-invasive approaches have the potential to improve our understanding of cardiovascular haemodynamics in health and disease, and can be applied to longitudinal studies. Non-invasive techniques are largely reliant on tonometry to measure pressure waveforms which can only be performed in superficial vessels.^{256,283} Because changes in the aorta are more relevant to cardiac load and neurological outcomes, CMR may be useful.^{275,284} Distensibility (area or diameter change) has been used as a surrogate for pressure, but this can be limited by the sequence (in-plane motion or low spatial resolution) and unless diameter is calibrated to pressure (as has been done in the carotid artery)²⁸⁵ the estimates of wave intensity are indirect and influenced by aortic stiffness.^{275,284} A more direct measure of central aortic pressure in combination with CMR velocity measurements may provide an alternative approach.

1.6. Remodelling in aortic stenosis

“So admirable is the adjusting power of the heart that, for example, an advancing stenosis of aortic or mitral orifice may for years be perfectly equalized by a progressive hypertrophy.” – Osler, *The principles and practice of medicine*, 1892, pp 630⁷

Aortic stenosis (AS) is a narrowing of the aortic valve. The commonest causes are degenerative calcification or a congenital bicuspid valve. Severe aortic stenosis is defined by echocardiographic features that measure valvular haemodynamics, and clinical criteria based on the presence of symptoms. Valvular replacement is indicated once symptoms develop or left ventricular function deteriorates. This can be through a surgical or transcatheter aortic valve replacement (AVR). Intervention improves survival, but risk stratification and timing is difficult because symptoms are subjective, and current grading criteria can be discordant.²⁸⁶

The LV remodelling seen with severe aortic stenosis is profound,^{287,288} with variable but significant regression post-AVR. Although LV remodelling in the early stages is thought to be an adaptive response to pressure overload, significant hypertrophy eventually can lead to adverse consequences with diastolic dysfunction, ischaemia and eventual heart failure²⁸⁹ and death.^{290,291} Left ventricular (LV) remodelling in response to AS is considered a determinant of outcome.^{287,288} It is however unclear whether asymptomatic patients with excessive LV hypertrophy should undergo AVR, or managed with active follow up.^{292,293}

1.6.1. Factors influencing left ventricular remodelling in patients with aortic stenosis

The remodelling response to aortic stenosis is variable: one large study showed that 10% of patients with severe aortic stenosis had no hypertrophy and 4% had no

detectable change in cavity size or myocardial mass whatsoever.⁷⁵ Despite this, these patients remained compensated and had better surgical outcomes, a result corroborated by animal work.^{48,49} Asymmetric septal hypertrophy is a common structural variant in 22-27% of patients with aortic stenosis, particularly in older and hypertensive patients.^{31,294} Asymmetry has been noted to be present in patients with co-existent hypertension, most commonly in the basal septum. It has been considered as a finding that is present in some patients, but not others.³¹ Plausibly, this may be attributed to genetic predisposition, such as ACE I/D polymorphism.²⁹⁵ It may also be present in patients with a more common family history of hypertrophic cardiomyopathy.²⁹⁶ Patients with “normal” mass and geometry are much more likely to be female, less hypertensive and have less coronary artery disease. The proportion of patients with “normal” LV structure and function is between 4% and 12-13% of patients using echocardiography and CMR respectively.^{31,75,297}

The myocardial response to aortic stenosis appears to be influenced by a number of factors beyond contemporary haemodynamic load.^{298–300} These include age, sex,^{301,302} obesity, diabetes,³⁰³ hypertension,³⁰⁴ and genetic background.^{305,306} Sex appears to result in significant differences in remodelling in response to aortic stenosis pre-operatively,²⁹⁷ and the extent of reverse remodelling after AVR is associated with a worse prognosis in women.³⁰⁷ Dweck et al. reported the mean difference in global LV mass between men and women 14g/m² in a cohort including moderate AS.³¹ This however did not adjust for hypertension. Treibel et al. previously showed that remodelling using CMR detects more concentric remodelling in women compared to echocardiography.²⁹⁷ Following AVR, regression of hypertrophy is prolonged and variable.^{308,309} The variability in LV mass regression due to male sex in echocardiographic studies has been variable, both positive and negatively associated with LV mass regression,^{310–312} or exerting no

influence.³¹³ One CMR study by Dobson et al³¹⁴ observed that men had greater absolute LV mass regression than women, but this was similar when expressed as a percentage of baseline. Treibel et al. have shown that fibrosis is at least partially plastic, and a comparison of fibrosis regression between sexes may also contribute to our understanding of remodelling after AVR.³¹⁵

1.7. Remodelling and exercise training

Participation in sustained exercise training is increasing partly due to the recognised positive impact on cardiovascular risk, at least partly mediated by beneficial LV remodelling, Table 1-9.

	Physiological	Pathologic
Example	Athletic training	Aortic stenosis ?Extreme athletic training
Signalling pattern	Pro-survival	Pro-apoptotic Pro-fibrotic
Key signals	IGF-1	P38 MAP kinase TGF-B Angio-II
Fetal gene program	No	Yes, e.g. PPAR- α deactivation
Interstitial fibrosis	No	Yes
Myocyte apoptosis	No	Yes
Systolic contraction	Normal or increased	Decreased
Diastolic relaxation time	Normal or increased	Decreased
Doppler LV filling	Normal	Impaired

Table 1-9 Physiologic versus pathologic hypertrophy.

Abbreviations: IGF= insulin-like growth factor; STAT-3= signal transducer and activator of transcription; MAP kinase = mitogen-activated protein kinase; TGF-B= transforming growth factor- beta; PPAR= peroxisome proliferator-activated receptor alpha. Adapted from ESC Textbook of Cardiology, Chapter 32.³¹⁶

The rate and extent of the remodelling response to exercise is not uniform - only 15% of highly trained athletes have marked LV enlargement,⁸ and the effects of moderate training is largely unknown. Previous work using CMR has suggested that much of the population differences in cardiopulmonary exercise capacity (as measured by peak oxygen uptake, VO_{2max}) can be explained by differences in cardiac morphology rather than function.³¹⁷ Our understanding of the athletic heart has continued to improve with increasingly refined phenotyping. Data using MRI relaxometry reported increased myocyte hypertrophy and decreased extracellular volume (ECV) in athletes training

greater than six hours a week compared to controls. In the same study, athletes with a $\text{VO}_{2\text{max}} > 60\text{mL/kg/min}$ had 17 g/m^2 greater indexed myocyte mass than low-performance athletes, but similar extra cellular matrix mass (ECM).³¹⁸

1.7.1. Recommended exercise dose

Much of this previous work was performed in highly trained athletes, and the dose-response relationship of exercise and remodelling has not been fully sampled. Exercise intensity is typically measured in metabolic equivalents (METs). 1 MET is equivalent to the amount of resting energy expended, such as whilst sitting awake.³¹⁹ Moderate exercise includes walking briskly or playing volleyball. These activities have a MET between 3-6 units. Intense activities have METs >6 units, and include running (depending on intensity) or swimming. Energy expenditure can also be relative, that is, placed in the context of an individual's functional capacity.³²⁰ Because older individuals have lower aerobic capacity than younger individuals, relative intensity compared to that expected for that age group may be a more appropriate measure for them. It is important to quantify the duration and intensity of exercise to measure total exercise activity, but it is unclear what are the clinical implications of a similar overall exercise dose with different contributions of duration and intensity.³²¹

The health benefits of moderate exercise are, however, well accepted on the cardiovascular system,³²² other systems,³²³ on life expectancy and health in general.³²⁴ It is therefore recommended to perform at least 150 minutes of exercise a week of moderate intensity exercise.³²⁵ In the UK it is advised to perform 30 minutes of moderate intensity on at least five days a week, or 75 minutes of vigorous intensity activity over the course of a week.³²⁶ 2018 USA guidelines have also recently recognized the benefit in increasing physical activity by even a small amount can

improve outcomes.^{319,327,328} This is consistent with early work by Jerry Morris in the 1950s describing a 50% reduction in coronary heart disease in more active London bus conductors, compared to their sedentary driver counterparts.³²⁹

1.7.2. Impact of aerobic exercise training on cardiac remodelling

At one extreme, participation in life-long, intense, aerobic exercise is increasingly common, and chronic intense exercise may be “too much of a good thing”.²⁵ Whilst life-long athletes live longer than controls,^{25,330} male master athletes have more coronary calcification than sedentary counterparts, and coronary disease is underestimated by conventional risk scores in frequent marathon runners.³³¹ The presence of myocardial fibrosis identified using late gadolinium enhancement imaging is associated with non-sustained ventricular tachycardia in athletes.²⁴ This adds to a growing area of question as to whether sustained exercise may cultivate maladaptive changes in an otherwise adaptively remodelled heart. A comprehensive understanding of the morphologic remodelling process is therefore needed to identify mechanisms that explain the transition.^{20,36}

At the other end of the spectrum, the effects of starting exercise from sedentary behaviour on the cardiovascular system are less well studied in the real-world. Prospective cohort studies have suggested as little as 15 minutes a day may have a benefit, and the greatest incremental benefit derived from exercise training is from those taking no exercise at baseline to little exercise.^{324,332,333} The Copenhagen Heart Study showed that mortality in runners was 44% less than controls. The greatest risk reduction was at 1 to 2.5 hours of exercise per week, but those running >20 miles per week had similar mortality rates to controls.³³⁴

Prospective longitudinal studies of exercise regimens in trained athletes described changes to LV structure and mechanics.^{335,336} Marathon training is an increasingly popular form of aerobic exercise training, and provides a model for studying real-world exercise training in novices. The New York marathon has reported an increase in total runners by 65% in the 1980s and 25% for the last two decades, with an increasing proportion of female runners.³³⁷ A number of studies have investigated the immediate effects of completing a marathon. There appears to be transient risk as reflected by depressed myocardial function, and increased troponin (but unchanged PWV).^{338–342} The risk of sudden death during vigorous exertion has been estimated at 6 in 100,000 in healthy Finnish men, and is inversely related to leisure time physical activity.³⁴³ In a marathon, this risk is approximately 5-fold lower.³⁴⁴

The cardiovascular benefits of novice real-world exercise training (including for a marathon), has had limited study. Ziliniski et al. enrolled 49 participants training for a marathon. Approximately half had previous marathon running experience (at baseline participants ran 13.6 ± 11.5 miles per week), and approximately one quarter with cardiovascular risk factors or diastolic dysfunction. 45 completed the structured, supervised, training programme with 4 drop-outs due to musculoskeletal injury. Training was not inconsiderable, averaging 24 ± 12 miles per week for 4.5 months. After training, there were small increases in maximal VO_2 . LV wall thickness increased by 0.5mm, LV mass by $\sim 11 \text{ g/m}^2$, and LVEDV by 16mls. LVEF was unchanged. E:A ratio showed an improvement from 1.3 to 1.2. RV and LA dilatation was also observed. 60% exceeded the upper limit of normal wall thickness after training. There were reductions in body mass index, LDL and triglycerides and there was no change in BP or HDL.

1.7.3. Impact of aerobic exercise training on vascular remodelling

The impact of aerobic exercise training on vascular structure and function supports a significant beneficial effect. Non-pharmacological modification is important given that wave reflection by wave intensity analysis, and large artery stiffness are independently associated with stroke and cognitive decline.^{345,346}

A meta-analysis of supervised aerobic training programmes showed an average reduction in brachial SBP by 4.8 (4.3 to 5.6) mmHg over 197 randomised control trials.^{347–349} The effects of endurance and resistance training were similar. The reduction in blood pressure appears mediated by a reduction in vascular resistance, sympathetic tone and the renin-angiotensin system.³⁴⁸ Some studies have correlated the change in arterial stiffening with the reduction in blood pressure,³⁵⁰ whilst others have not demonstrated a correlation.³⁵¹

A systematic review of randomised control trials by Ashor et al. aimed to investigate the effect of exercise training on arterial stiffness and wave reflection.³⁵² Included studies measured arterial stiffness as carotid-femoral, brachial-ankle PWV, and wave reflection as AIx. On average, PWV reduced by 0.63m/s with aerobic exercise, with a tendency to larger reductions in studies lasting greater than 10 weeks. Exercise interventions were mostly running, walking, and cycling and there was no difference between modalities. Overall, resistance training was ineffective at reducing PWV, although there was significant heterogeneity. AIx reduced by 2.63% on average, and this did not differ for older participants with greater AIx at baseline.

Mechanistically, one study measuring AIx during cycling, showed that older men (mean age 73 years) failed to decrease their AIx during exercise. It was suggested that this could be due to an impaired vasodilatory capacity or non-modifiable stiff arteries.³⁵³

These data suggest that an older vasculature may therefore be less modifiable with

exercise. Whilst studies have demonstrated the beneficial effects of exercise in a range of diseases, arterial stiffening may also be less modifiable in some disease groups, including obese adults or those with isolated systolic hypertension.³⁵⁴ The effect of marathon training on arterial structure has only been described by Hafner et al.³⁵⁵ Hafner observed that peripheral arterial dilatation occurred in both trained and non-trained limbs, and that adaptation may be dose-dependent. This study included only 14 runners and did not study the impact on large central arterial stiffening, which is more strongly associated with ageing and outcomes.³⁵⁶ Immediately after running a marathon, central and brachial blood pressure and AIx has been observed to decrease, whilst PWV was not altered.³⁴⁰

2. Research aims and objectives

2.1. Hypothesis

The application of computational analysis techniques to cardiovascular magnetic resonance imaging datasets can extract more detailed cardiovascular phenotyping information than conventional measures from CMR imaging, and that these phenotypes can help to understand the remodelling response to different loading conditions.

2.2. Aims

The feasibility of phenotype extraction from CMR imaging was tested separately for LV bSSFP cine imaging, and aortic phase contrast imaging. The utility of these approaches was tested in health (exercise training) and disease (patients with aortic stenosis), and so my aims are organized by the results chapters:

- To deliver a generalisable scan:rescan resource for use as a tool to measure human and automated LVEF and LVM analysis performance. To then use this resource to identify sources of error in CMR analysis, and to quantify the precision of techniques with varying degrees of automation.
- To create a cardiac atlas of patients with severe aortic stenosis, and compare its sensitivity to regional LV remodelling, against conventional global measures.
- To use non-invasive measures of the central blood pressure (cBP) and velocity waveforms to perform wave intensity analysis in order to assess ventriculo-arterial coupling. To then compare measures of local wave speed with a reference of conventionally calculated PWV, and to evaluate associations between aortic WIA, age and sex in healthy individuals.
- Using a cohort of healthy, first-time marathon runners, to explore the effects of real-world exercise training on age-related aortic stiffening and ventriculo-arterial coupling using aortic WIA.

3. Methods

3.1. Outline and personal contribution

Firstly, the details of the three cohorts used in this thesis are described, Table 3-1.

Secondly, the CMR sequences acquired for each cohort are detailed. Thirdly, details of image analysis are provided. These image analysis details are split for bSSFP cine imaging of the left ventricular short axis, and phase contrast imaging of the aorta.

The first cohort was a cohort of individuals (patients and healthy volunteers) undergoing repeat CMR scanning in a time-frame where biological change was not anticipated. This was used to test the precision of automated analysis for LV structure and function. The other two cohorts were used both to test the feasibility of more detailed ventricular and aortic phenotypes, and their clinical utility. A cohort of patients with severe aortic stenosis represented cardiovascular remodelling to pressure overload, and a cohort of individuals running a first-time marathon represented cardiovascular remodelling to volume overload.

Cohort	<i>n</i>	Loading condition	Timepoints	Sequences used	Analysis techniques
Scan-rescan cohort	110	<i>Validation cohort only</i>	Repeat scanning (96% in one week)	bSSFP SAX cine	Automated LVEF, LV mass
Severe aortic stenosis (RELIEF-AS)	116	Aortic stenosis	Before AVR	bSSFP SAX cine	3D LV modelling
		Aortic valve replacement	One year post AVR		
First-time marathon runners	237	Exercise training	Before training	bSSFP SAX cine	3D LV modelling
			Six months post exercise training (one week after marathon)	Aortic phase-contrast	Aortic WIA
					Regional aortic stiffness

Table 3-1 Cohorts and CMR sequences used in this thesis. Abbreviation: bSSFP= balanced steady state free precession; LV = left ventricle; SAX=short-axis cine stack.

Methods

For chapter 4, related to the scan-rescan cohort, I conceived the idea, designed the study and obtained grant funding. I recruited, and performed the CMR studies of 44 patients on two occasions. I collated, cleaned and anonymised the complete 110 patient multi-centre resource. I collaborated with *Circle* (CVI42, Calgary, Canada) to translate a level-set fractal analysis tool to a semi-automated endocardial volumetric assessment. I contacted MICCAI 2009 and STACOM 2011 challenge winners to test automated analysis strategies. I subsequently developed a training strategy to generalise a neural network developed by Dr Wenjia Bai. I prepared data for neural network analysis, and quality controlled neural network and clinician results. I performed the statistical analysis. I wrote the website (front and back-ends), and made the resource available online.

For chapter 5, I conceived the idea for this analysis of the RELIEF-AS study. Dr Treibel submitted the ethics application, and performed the original patient data collection under separate grant funding. I performed the CMR acquisition for the sensitivity analysis in 24 subjects. I compiled a cardiac atlas by segmenting and labelling CMR data from >300 patients and healthy volunteer datasets. Using the atlas, I applied an approach to create 3D segmentations and co-register studies for patients and matched controls. I summarised 3D model data visually and computationally, and performed the statistical analysis.

Chapters 6 and 7 use data acquired as part of the Marathon Study. I performed the baseline CMR acquisitions (n=237), and the majority of follow-up acquisitions (n=178). I coordinated individual study days and performed some of the data acquisition in other modalities (stress echocardiography, blood pressure, ECG, anthropometrics). I stored and databased blood and urine samples, anthropometric and imaging data. For Chapter 6, I interpolated and processed pressure and velocity waveform signals for wave

intensity analysis. Professor Alun Hughes provided Matlab scripts for individual alignment of waveforms and calculation of wave intensity from pressure and velocity derivatives. For the scale of this analysis, I automated steps of this process. I also wrote scripts to quantify wave intensity peaks, timings and energies automatically, including artefact identification. I manually aligned all waveforms and measured wave speed from pressure-velocity loops. For aortic stiffness data in Chapter 7, I supervised Dr Nadarajan in the phase-contrast CMR data analysis for an MSc thesis, receiving a distinction. I developed the analysis protocols for T1 and volumes (see Chapter 3.7) and performed the inter-observer analysis for clinician CMR LV assessment. I performed the atlas-based LV analysis of all datasets using the approach described in Chapter 5. I performed all statistical analysis. I am grateful to the work of approximately fifty individuals to complete the overall study, and particular Drs D'Silva and Torlasco who provided overall coordination.

3.2. Scan-rescan precision cohort

3.2.1. Study population

Institutions from across the UK were approached to develop a resource that reflects the range of scanning protocols, pathologies and scanners. Principal Investigators were approached with a request as outline in Figure 3-1. In total, paired scans were obtained from five UK institutions (Barts Heart Centre, University Hospitals Bristol, Leeds Teaching Hospitals, University College London Hospital, and University Hospitals Birmingham NHS Trusts) with 6 different MRI scanners of 2 field strengths (1.5T, 3T), 2 manufacturers (Siemens, Philips), and 3 models (Aera, Achieva, Avanto) representing the clinical spectrum (health, dilatation, hypertrophy, regional disease, n=118). The scan-rescan CMR parameters for precision assessment are outlined in Table 3-4.

Inclusion criteria were patients over age 18 years undergoing CMR with balanced steady-state free precession (SSFP) cine imaging on two occasions within a timeframe where biological change was not anticipated. Scans:rescans were acquired either both before or after gadolinium based contrast administration, using the same protocol, as per the international guidelines on scan acquisition.³⁵⁷ Scans acquired on the same day involved removing the patient from the table and performing repeat isocentre positioning. Exclusion criteria included patients with a cardiac implantable electronic device, significant arrhythmia (atrial fibrillation or ectopy) during the scan, claustrophobia or inability to breath-hold.

Each institution obtained local approval via the UK National Research Ethics Service; the study conformed to the principles of the Helsinki Declaration, and all subjects gave written informed consent.



TEST – RETEST VOLUMES STUDY REQUIREMENTS

Thank you for your help with this study. We kindly request the following requirements for the left ventricular volumes studies:

- Anonymised test – retest data within a credible time frame where biological variability is not expected
- 1.5 or 3T
- Any scanner manufacturer
- Standard segmented SSFP
- Paired long axis cine imaging
- Health or disease
- Brief outline of ethical framework
- Age, gender, and underlying diagnosis

We would be grateful if you can upload the dicoms into the T1MES dicom transfer portal through whoever uses this at your institution. If other methods are easier please let us know- we can also provide a cloud based upload.

If there are any queries, please feel free to contact us.

Many thanks

Dr Anish Bhuvu
a.bhuva@ucl.ac.uk

Figure 3-1 Request for imaging data collaborations with UK CMR centres to develop a multi-centre scan-rescan CMR resource.

3.2.2. CMR dataset anonymization and randomization

Each dataset consisted of cine imaging in at least two long-axis orientations and a complete short-axis stack. Because the purposed of the cohort was to quantify human and automated analysis reproducibility, it was necessary to ensure all analysis was performed blinded. Therefore both scans per patient were assigned separate, randomly-generated, four-digit identification codes for blinded scan and rescan assessment. The first scan was also duplicated and assigned a separate identification code for assessment of blinded intra-observer reassessment. Anonymisation took place in Horos, CVI42 or with custom scripts in Matlab 2013b. Randomisation took place using Excel. Datasets were excluded if there were missing slices or unacceptable quality on one or other acquisition judged by an expert observer (JM).

3.3. Patients with severe aortic stenosis

3.3.1. Patient recruitment

Patients were recruited for a prospective observational cohort study in patients with severe, symptomatic AS who underwent AVR between January 2012 and January 2015 in a single tertiary referral cardiac centre, University College London Hospital NHS Trust, London, United Kingdom. Study recruitment and drop-out rates are shown in Figure 3-2, and have been previously published.³⁵⁸ Pre-AVR and post-AVR, the assessment included clinical history, blood pressure, 6-minute walk test (6MWT), blood sampling (for N-terminal pro-B-type natriuretic peptide [NT-proBNP] and high-sensitivity troponin [hsTNT]), electrocardiography, trans-thoracic echocardiography, and CMR. All investigations were performed using the same equipment for all participants. Inclusion criteria were adult patients with severe AS (2 or more of: aortic valve area $<1\text{cm}^2$, peak pressure gradient $>64\text{ mm Hg}$, mean pressure gradient $>40\text{ mm Hg}$, aortic valve velocity ratio <0.25) who were undergoing AVR with or without coronary artery bypass grafting. Exclusion criteria were pregnancy or breastfeeding, estimated glomerular filtration rate $<30\text{ ml/min/1.73 m}^2$, non MRI-conditional implanted devices, inability to complete the protocol, previous valve surgery, or greater than moderate valve disease other than AS. The study was approved by the ethical committee of UK National Research Ethics Service (07/H0715/101) and registered on ClinicalTrials.gov (NCT02174471). This study was performed by Dr Thomas Treibel as part of his doctoral thesis work. I assisted with performing some of the CMR acquisitions, sample storage and data analysis prior to starting and in the early stages of my PhD.

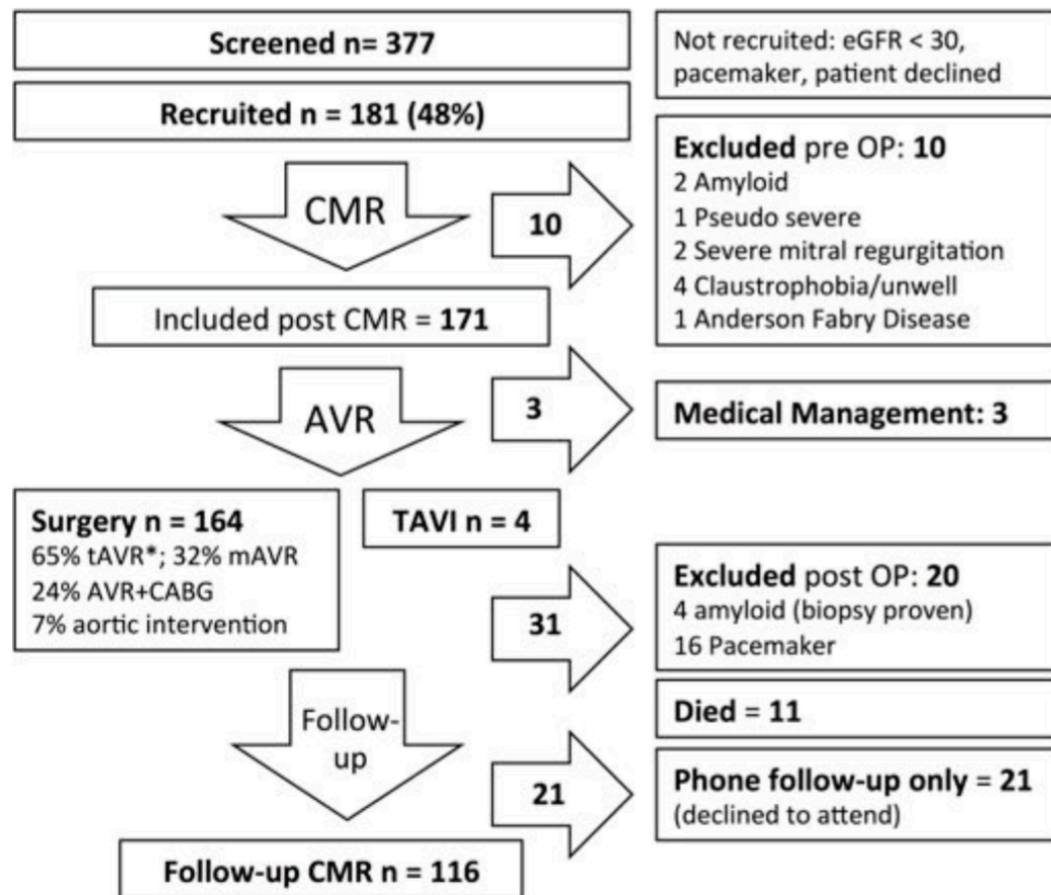


Figure 3-2 RELIEF-AS study flow chart.

From Dr Thomas Treibel doctoral thesis. Abbreviations: tAVR= tissue aortic valve replacement, mAVR= mechanical AVR, CABG= coronary artery bypass graft. CMR = cardiovascular magnetic resonance.

3.3.2. CMR

CMR was performed at 1.5-T (Magnetom Avanto, Siemens Healthcare, Erlangen, Germany) using a standard clinical scan protocol with late gadolinium enhancement (LGE) imaging and T1 mapping before and after a bolus of gadolinium contrast (0.1 mmol/kg of gadoterate meglumine [Dotarem, Guerbet S.A., Paris, France]). Cine imaging in long and short axis was acquired using a standard balanced steady-state free precession pulse sequence (SSFP) with parameters detailed in Methods-3.5.

3.3.3. Echocardiography

Clinical transthoracic echocardiography was performed using a GE Vivid E9 system (GE Healthcare, Wauwatosa, Wisconsin) with a 4-MHz transducer, following the guidelines for assessment of AS severity and diastolic function as recommended by the American and European Societies of Echocardiography.²⁹⁷

3.3.4. Other investigations

6MWT was performed at the Heart Hospital along a flat corridor in accordance with current guidelines.³⁵⁹ Patients were asked to walk a 30-metre length of the corridor at their own pace while attempting to cover as much ground as possible in the 6-minute period. Participants had blood tests taken prior to the CMR scan. NT-proBNP and hsTnT were measured by ELISA (Roche Diagnostics). The inter-assay coefficients of variation were less than 7% for both of them. The lower limit of detection was 5 pg/mL for NT- proBNP and 3 ng/L for hsTnT.

3.4. Novice marathon runners

3.4.1. Patient recruitment

Healthy participants were recruited into a prospective longitudinal observational study to investigate the effect of first-time marathon training on cardiovascular function. The timeline of investigations performed are described below and illustrated in Figure 3-3. Participants were recruited over the 2016 and 2017 London Marathons (Virgin Money). Details of the muscle oxygen consumption sub-study have been reported previously.³⁶⁰ After receiving confirmation of a ballot place, individuals received an email with details of the study. Individuals interested in participation contacted a call centre and if they satisfied inclusion criteria, were booked into an assessment day. Inclusion criteria were: no significant past medical history; no previous marathon-running experience (approximately half of ~50,000 receiving ballot places each year); and current participation in running for <2 hours per week. In 2016, participants of age 18-35 years were included and in 2017, adults of all ages were included. Exclusion criteria were: pre-existing cardiovascular disease during preliminary investigations, or contraindication to CMR. All procedures were in accordance with the principles of the Helsinki declaration, all participants gave written informed consent and the study was approved by the London-Queen Square National Research Ethics Service Committee (15/LO/0086).

All assessments were conducted before training started, immediately after the release of the results from the ballot entry system six months prior to the marathon. These were repeated within 3 weeks after completion of the London Marathon, but not earlier than one week after completion to avoid the acute effects of exercise.

Methods

At both time points, participants attended Barts Heart Centre (Barts Health NHS Trust) for all assessments on a single visit. Assessments included CMR, blood pressure, trans-thoracic echocardiography, electrocardiography, anthropometrics, body composition, and cardio-pulmonary exercise testing (CPET) with concurrent stress echocardiography. Due to the number and variety of assessments, these were performed by a large team who have made the Marathon Study possible (listed in individual chapter acknowledgements).

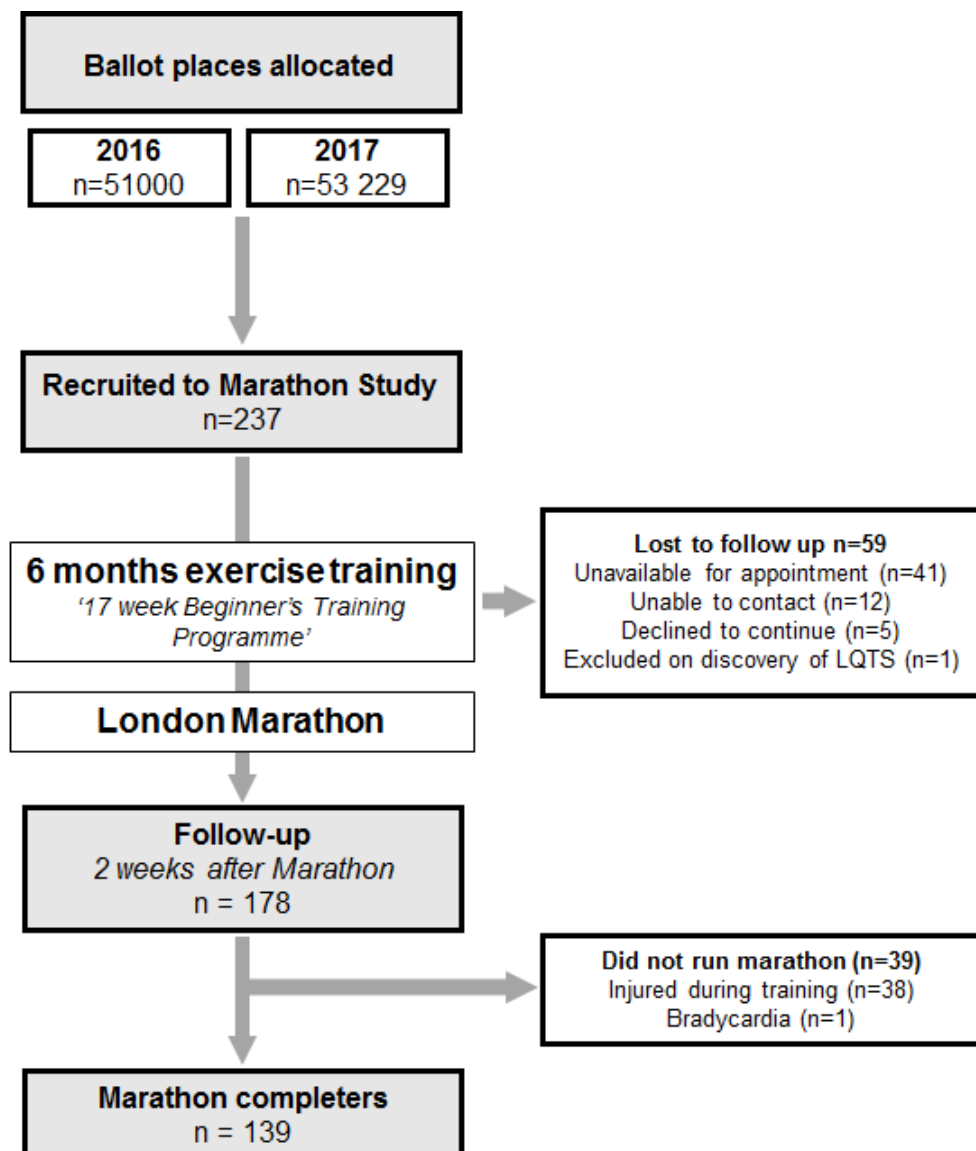


Figure 3-3 Marathon Study flow chart.

Within two weeks of receipt of a ballot place for the London Marathon, participants underwent pre-training assessment followed by six-months of exercise training.

3.4.2. Six-month exercise training

Participants were recommended to follow the “Beginner’s Training Plan” provided by the marathon organizers with the aim of achieving marathon completion rather than improvement in cardiovascular fitness. This consists of approximately 3 runs per week, increasing in difficulty for a 17-week period leading into the London Marathon race (<https://bit.ly/1UOPwiN>), Figure 3-4.³⁶¹ Those who wished to follow alternative, higher intensity or longer training plans were however not discouraged from doing so.

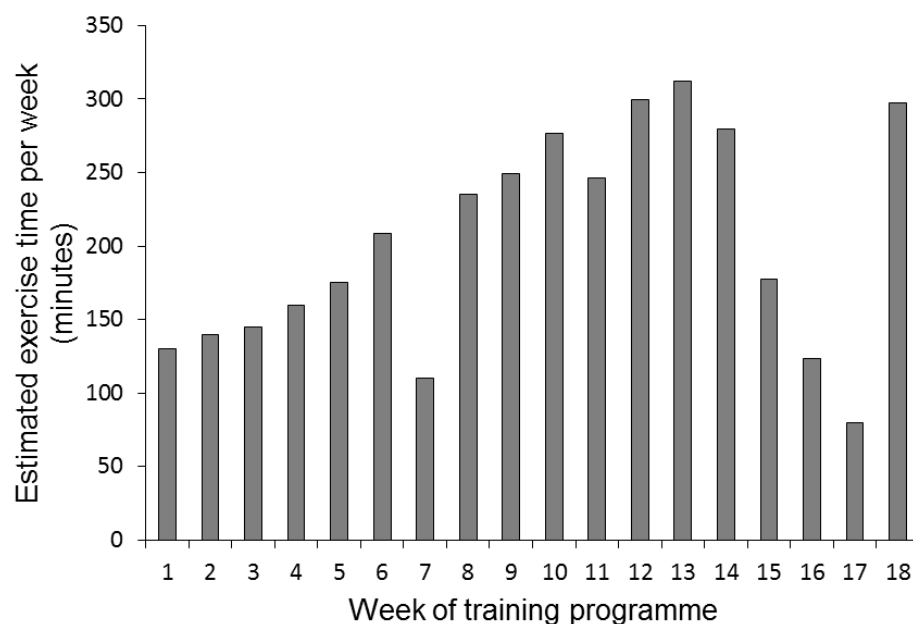


Figure 3-4 “Beginner’s Training Programme” for first time marathon runners.

Total exercise includes walking, running and runs of a target distance. Times for runs of a target distance were estimated from the average marathon pace for the cohort. Week 18 is the Marathon itself, presented for comparison.

3.4.3. CMR acquisition and blood sample timing

CMR with gadolinium based contrast agent was performed at 1.5T (Aera, Siemens Healthcare, Erlangen, Germany) with a 30 channel phased array receiver coil. The protocol is summarised in

Table 3-2 and phase contrast sequence parameters are summarised in Table 3-5.

Immediately prior to CMR, serum and plasma samples were acquired at cannulation and frozen at -80°C.

3.4.4. Blood pressure acquisition

Prior to CMR, brachial and derived central (aortic) blood pressure were acquired after a period of rest in the semi-supine position using a validated supra-systolic oscillometric cuff sphygmomanometer (BP+, USCOM, Australia). Supra-systolic oscillometric blood pressure was measured over ten seconds in duplicate at 200Hz after a period of rest in the semi-supine position, as per international guidelines (Cardioscope II BP+, Uscom Ltd, Sydney, Australia).³⁶²

3.4.5. Allometric and body composition measurements

Height was recorded using a standard stadiometer. Weight, body fat mass and percentage were measured using bioimpedance (BC-418, Tanita, USA).

3.4.6. Echocardiography

Trans-thoracic echocardiography was performed using a standard protocol with images acquired by a British Society of Echocardiographer accredited sonographer or physician on GE Vivid E9 system (GE Healthcare, Wauwatosa, Wisconsin) with a 4-MHz transducer.

3.4.7. Cardiopulmonary exercise testing and stress-echocardiography

The CPET was carried out on a cycle ergometer (Ergoselect1200, Ergoline, Germany) using an incremental protocol standardized by bodyweight and gender. Expired gases were analyzed throughout using a metabolic cart system (Quark CPET, COSMED, Italy). The study was performed in the semi-supine position to enable concurrent tissue

Methods

Doppler stress echocardiography at incremental workloads. The individual participant protocol planned for CPET after CMR, however, due to the busy nature of the study days, this was occasionally changed to ensure efficient workflow for all participants.

3.5. CMR protocols used across all studies

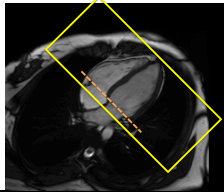
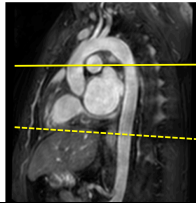
Sequence	Notes as per scanning protocol card	Used for automated analysis in this thesis
Localiser		
White & black blood transverse stack		
HepaFat, PancreaFat scan* (Resonance Health Ltd, Australia) ³⁶³	Modified Dixon approach	
2CH (VLA), 4CH (HLA) and 3CH cines		
RV 2CH cine*	Through TV and RV apex	
SA stack cine		3.8 Methods - 3D ventricular phenotyping using a cardiac atlas approach
LV 3D cine (single breath-hold)* 	Fov as per 2D; can vary slices c. 36-44. Capture cycle. Copy central slice from SAX stack so same orientation Slices should extend slightly beyond the mitral valve plane/apex and antero-posteriorly- wrap can be in all directions. Repeat if artefacts. Breathhold c. 20s	3.8 Methods - 3D ventricular phenotyping using a cardiac atlas approach
Native T1 [MOLLI 5s(3s)5s] T2 mapping - Mid SAX slice and 4CH slice	Repeat if artefacts or gating error	
Frequency (off-resonance) map	Same FoV, phase encoding as T1 map	
Inject contrast		
Time stamp image (mid SAX)	Time stamp at point of injection	
LVOT cine		
Aortic valve cine		
TI scout (mid SA slice)		
3 x Long Axis LGE (2CH, 4CH and 3CH)		
SAX stack LGE	Slices match SAX cine	
Pulse wave velocity		
Aortic view ("candy cane" view) fast pilot* (to measure aortic length)	Use 3 points plan: Aortic arch, ascending; & lower thoracic descending aorta- descending arch does not need to be in view if not possible.	3.9 Methods - Measurement of aortic stiffness
Free-breathing aortic flows: 1 slice of ascending aorta, at level of PA bifurcation (<i>solid line</i>). Try and copy from black blood, keeping round circles for ascending & descending 1 slice of descending aorta*, just below central peak of diaphragm (<i>dotted line</i>).	Slices should be perpendicular to both flow "Candy cane" slice and the aortic wall to form a perfect circle . 	3.9 Methods - Measurement of aortic stiffness 6 Results – Feasibility and validation of aortic wave intensity analysis
At 15 mins post injection:		
Post contrast T1 mapping: MOLLI 4s(1s)3s(1s)2s, mid SAX slice and 4CH	Same FOV size as pre contrast T1 map- check for synthetic ECV output*	

Table 3-2 CMR protocol cards for the Marathon and RELIEF-AS studies. * = sequences acquired in the Marathon Study not in the RELIEF-AS Study.

Methods

The overall study protocols for the RELIEF-AS and Marathon studies are presented in Table 3-2, highlighting the particular sequences used for more detailed analysis in this thesis. The sequence parameters for cine sequences were different for each study, and so are split by study cohorts in Table 3-3 and Table 3-4. A 3D cine-SSFP sequence was acquired in a single breath-hold in the Marathon Study. This encoded a 3D volume for every phase using frequency, phase and (additionally) slice encoding, with the data reconstructed using a 3D Fourier transform. Breath-hold duration varied between 15-20 seconds depending on the heart rate. Whilst cardiac phases were fewer than conventional 2D sequences, it was hypothesized the acquisition would facilitate smooth 3D modeling and reduce basal slice variability.

Phase-contrast imaging in the RELIEF-AS studied was piloted perpendicular to the forward jet. In the Marathon study, phase-contrast imaging was piloted to represent a uniform aortic cross-section at the level of the pulmonary artery. The spoiled gradient echo phase-contrast sequence used was free-breathing, ECG-gated, Table 3-5.

SSFP cine parameter	RELIEF-AS (2D)	Marathon (2D)	Marathon (3D)
Manufacturer	Siemens	Siemens	Siemens
Model	Avanto (1.5T)	Aera (1.5T)	Aera (1.5T)
Slice thickness/ mm	7	8	3
Gap/ mm	3	2	0
Gating	Retrospective	Retrospective	Prospective
Cardiac phases	25	30	15
Field of view/ mm ²	280x360	300x360	300x380
Acquisition matrix	320x154	240x198	114x116
Acquired voxel size/ mm ²	2.3x1.4	1.25x1.8	2.6x3.3
Reconstructed voxel size/ mm ²	-	-	3x3
Echo time (TE) (ms)	1.35	1.19	1.08
Temporal resolution/ ms)	31.7	42	55.9
Flip angle/ degrees	88	71	35
Acceleration factor	-	-	4

Table 3-3 Cine sequence parameters for the RELIEF-AS and Marathon studies.

VOLUMES Study					
SSFP cine parameter	Centre 1	Centre 2	Centre 3	Centre 4	Centre 5
n	24	35	31	15	5
Manufacturer	Siemens	Siemens	Siemens	Phillips	Siemens
Model	Avanto	Aera	Avanto	Achieva	Avanto
Strength/ Tesla	1.5	1.5	1.5	3.0	1.5
Slice thickness/ mm	7	8	8	10	7
Gap/ mm	3	2	0	0	3
Cardiac phases	25	25	25	30	25
FoV/ mm	270 x 360	340 x 420	308 x 380	288 x 288	270 x 340
Acquisition matrix	320 x 168	208 x 153	256 x 208	153 x 158	208 x 170
Echo time/ ms	1.43	1.07	1.21	1.28	1.17
Temporal resolution/ ms	50.3	33.2	51.7	36.6	46.6
Flip angle/ °	80	74	78	40	67

Table 3-4 Cine sequence parameters for the multi-centre scan-rescan CMR resource (the VOLUMES study).

Further details are in Chapter-4. *Abbreviations: FoV = field of view.*

Phase-contrast sequence parameter	Configuration
Typical field of view (FOV) (mm)	340 x 191
Acquisition matrix	192 x 97
Acquired voxel size (mm ²)	1.97 x 1.77
Reconstructed voxel size (mm ²)	1.77 x 1.77
Slice thickness (mm)	6
Flip angle (degrees)	20
Repetition time (TR) (ms)	9.24
Echo time (TE) (ms)	2.46
Parallel imaging acceleration factor	2
Acquired temporal resolution/ ms	9.24
Calculated cardiac phases	100
Number of signal averages	2
Velocity encoding (cm/s)	150

Table 3-5 CMR Phase- contrast sequence parameters in the Marathon Study.

3.6. Haemodynamic measurements

Estimation of central blood pressure is detailed as follows, and performed by the BP+ device. The blood pressure is measured directly in the brachial artery using the oscillometric device to obtain ten seconds of BP waveforms. All the beats in a ten second waveform recording are aligned by the wavefoot, and any beats with poor quality or artefact are removed. An average waveform is then created by taking the average of all the acceptable beats at each sample. The supra-systolic blood pressure waveform is then converted to a central pressure waveform using a model based on the tube law to reconstruct the central pressure waveform, Introduction-1.5.3.²⁵⁰ Central systolic and pulse pressure (PP) were measured from this waveform which was calibrated using brachial systolic and diastolic pressures according to manufacturer's recommendations. Blood pressure was measured in duplicate, and so two ensemble-averaged central pressure waveforms were obtained for each patient and analysed for systolic, diastolic and mean arterial pressure. Final measurements were taken as the average of both waveform measurements, after excluding any readings with a signal-to-noise ratio of <6dB to maintain high quality. The heart rate was calculated from the number of waveforms in each ten second recording, and then taken as the average of both measurements.

3.7. CMR analysis

3.7.1. Global ventricular volumetric analysis by clinicians (manual analysis)

Volumetric analysis of left ventricular mass and volume was performed manually for each cohort including papillary muscle in ventricular mass (CVI42, Circle, Calgary Canada), based on international post-processing guidelines.⁹⁵ Manual measures were used for validation of automated analysis techniques applied to the RELIEF-AS.

A local standard operating procedure was developed for analysis of left ventricular mass and volume analysis, Chapter-0 (https://youtu.be/n_7Wfs3G_xg). This was used for analysis in Chapter-4, and for the Marathon Study. As part of Chapter-4, a training programme was designed for two junior observers (Dr Y.Y, and Dr C.L.). This consisted of analysis of 15 scans, including patients and healthy volunteers to identify methodology to reduce intra-observer and inter-observer error including valve plane tracking, papillary muscles and varying degrees of automation. A range of semi-automated techniques were also studied including the development of a level-set approach to endocardial border delineation (used in the test-retest cohort), previously validated for trabeculae analysis, was incorporated into CVI42 (5.3.8, build 659). Its use is described here: <https://youtu.be/F0unF19YzxA>.

3.7.2. Standard Operating Procedure for left ventricular mass and volume analysis in CVI42.

Settings

1. Open 'Short 3D'
2. In Settings > Preferences> Contours>
 - a. Sub pixel matrix 4 x 4, subpixel weight SD On
 - b. 'Detect left ventricular papillary muscle' = On
 - c. 'Rounded Contour' = Off
3. Image contrast, pre-defined setting of 2. Adjust slightly if any borders are not clear.
4. Exclude basal and apical slice gaps = Off

Valve plane

1. Zoom so LV is centre of screen
2. Toggle valve plane on and import 2 x long axis views [LAX]
3. Using LAX, choose systole and diastole.
 - a. Diastole= The largest blood volume.
 - b. Systole = The smallest volume.
 - c. If dyssynchrony, preference towards basal volume.

Endocardium

1. Follow CVI42 user manual for selected method (Version 5.2). Free-hand correction of large errors is permitted for the more semi-automated methods.
2. Manually adjust papillary muscles
 - a. Ensure systolic papillary muscles are similar to diastolic papillary muscle mass.

Basal slice selection

1. Include any slice where there is over 50% of myocardium surrounding blood-pool
2. Atria can be excluded if there is systolic expansion

LVOT

1. Include LVOT

Epicardium

1. Use CVI42 automated tool and manually adjust on each slice
2. If this fails, use manual tool of personal preference.
3. When the most basal slice contains only a small crescent of basal lateral myocardium and no discernible ventricular blood-pool, an epicardial contour for the visible myocardium is included for LV mass only. Similarly, when the most apical slice contains only a circle of myocardium without cavitory blood-pool, an epicardial contour without an endocardial contour should be drawn for LV mass calculations.

3.8. 3D ventricular phenotyping using a cardiac atlas approach

3.8.1. Automated analysis: initialisation and segmentation

LV balanced SSFP (bSSFP) short axis imaging were analyzed using a cardiac atlas machine learning approach. This permits automated image segmentation and construction of 3D models of wall thickness and geometry. The technique also provides image co-registration, which is necessary for prospective image analysis, and to understand regional changes on follow-up imaging in the clinical studies. Image processing was performed in R (R foundation, Vienna, Austria) using RStudio Server version 0.98 (Boston, Mass, USA) and Matlab R2013a (The MathWorks, Inc., Natick, Mass, USA). To create a cardiac atlas specific to aortic stenosis, twenty patients with aortic stenosis were segmented manually by labelling each voxel as myocardium, LV and RV blood pool using ITK-SNAP (US National Institutes of Health³⁶⁴), Figure 3-5.¹⁶⁰

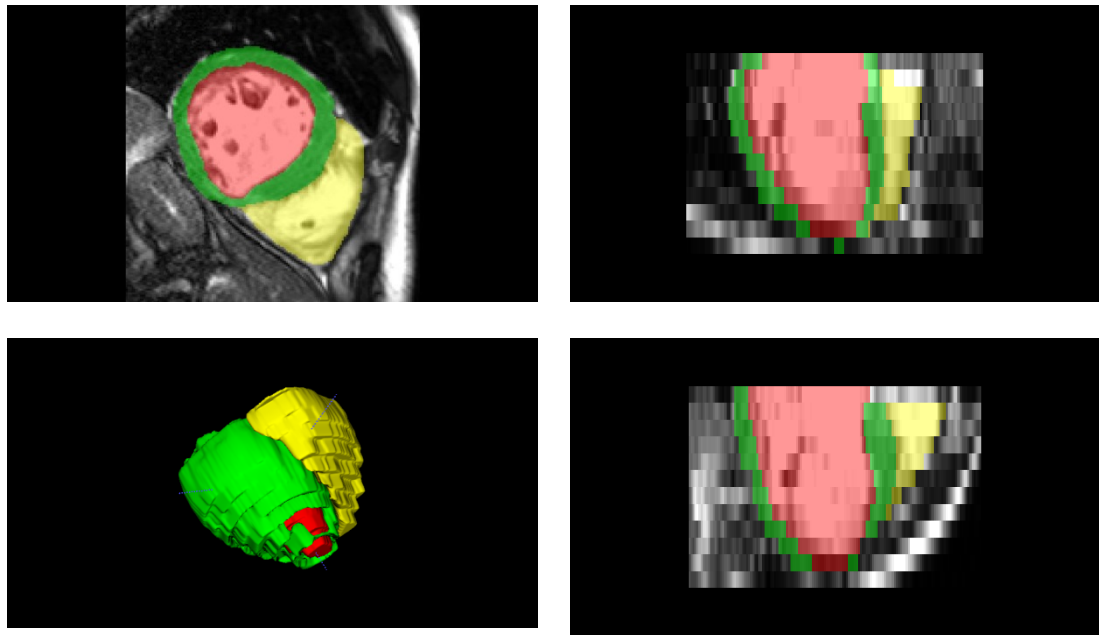


Figure 3-5 Manual labelling of a cardiac atlas from a patient with aortic stenosis in the RELIEF-AS study.

Voxels are labelled separately for LV blood pool (red), LV myocardium (green) and RV blood pool (yellow). Top left- mid ventricular short axis (also demonstrating an inferior infarction); Top and bottom right- long axis reconstructions; Bottom left- 3D volume rendered reconstruction. Step artefact due to 2D breath-hold slice misregistration is more pronounced at the apex.

The segmentation process was then applied to unseen LV SAX dicom datasets (“targets”). The segmentation required initialisation by placing six anatomical landmarks manually on each data set (left ventricular apex, mitral valve annulus, left and right ventricular free walls, superior and inferior right ventricular insertion points), Figure 3-6. This allows for image registration by firstly scaling, rotating and translating the image to a template space (“affine” registration), and then accounting for local deformations using a B spline non-rigid registration.¹⁶⁰

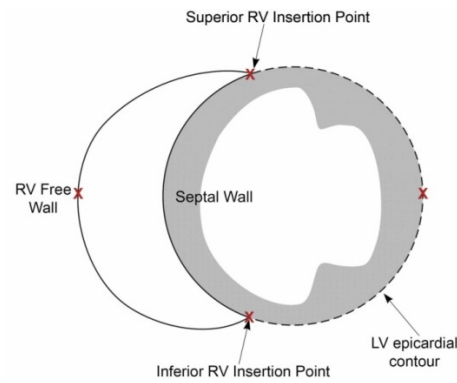


Figure 3-6 Location of six landmarks on a mid left ventricular short axis representation.

The knowledge of the voxel labels within the original atlas pool is then used to guide segmentation, using a multi-atlas “PatchMatch” algorithm.³⁶⁵ After intensity normalisation, similar patches are sought within the target image and each paired image and segmentation within the atlas population, accounting for voxel intensity and context of surrounding regions. Each target voxel is then labelled with a confidence weight to form the segmentations. Volumetric data is extracted from these segmentations to calculate global mass (assuming a myocardial density of 1.05g/mL) and cavity volume. In order to perform standardized comparisons across the population, segmentations need to be co-registered. The segmentations are transformed to a template space using the previous non-rigid transformations. Surface meshes for LV myocardium, RV and LV cavities are created from the transformed segmentation by choosing the most likely anatomical label for each voxel which is then smoothed using a Laplacian filter to highlight regions of rapid intensity change as edges.¹⁶⁰ This process takes approximately 12 hours for 24 segmentations run in parallel on a high performance cluster with 24 cores (Precision R7610 Rack workstation, Dell, UK)

Segmentations were then directly overlaid onto the target image and manually inspected using Rview, part of the IRTK software package, Figure 3-7.¹⁷³ If errors were noted in the segmentation (Figure 3-8), the target segmentation was manually re-labelled and

Methods

placed within the atlas pool. This augments the variation encoded within the atlas population before the target is re-segmented. This process reiterated with an increasing atlas pool until all targets were segmented satisfactorily.

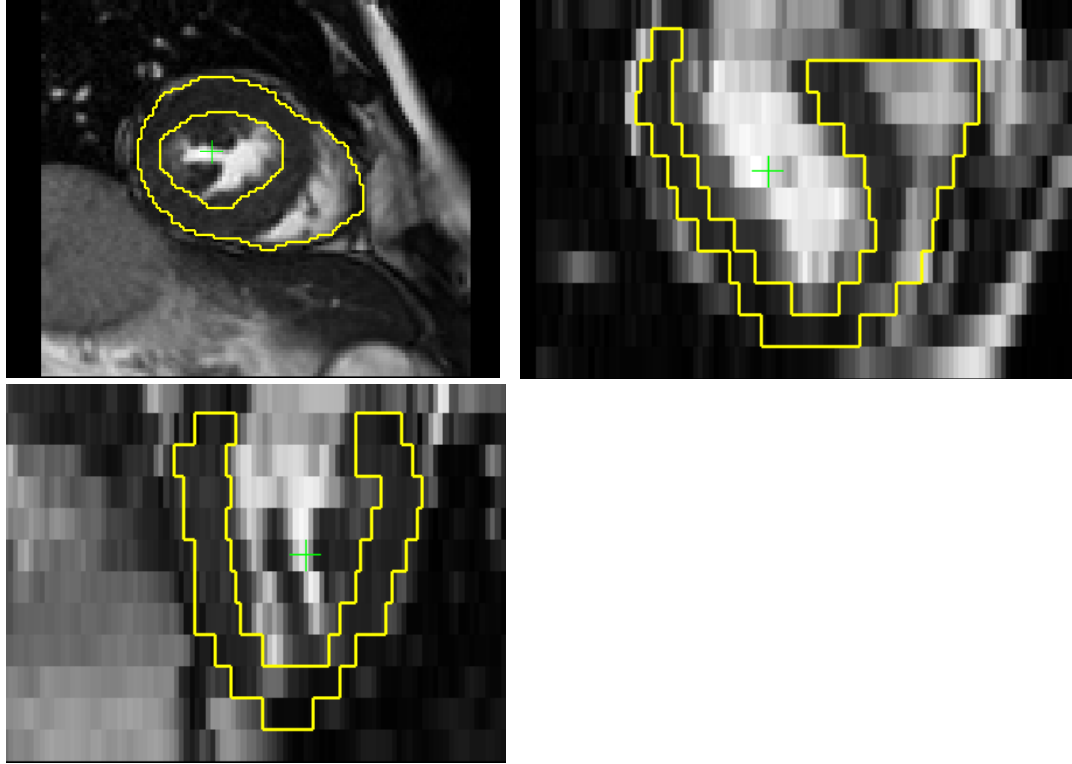


Figure 3-7 Example of a good target segmentation overlaid onto original dicom data.

Yellow contours represent the left ventricular endocardium, and the right and left ventricular epicardium. Top left – mid ventricular short axis; top right and bottom left – long axis reconstructions.

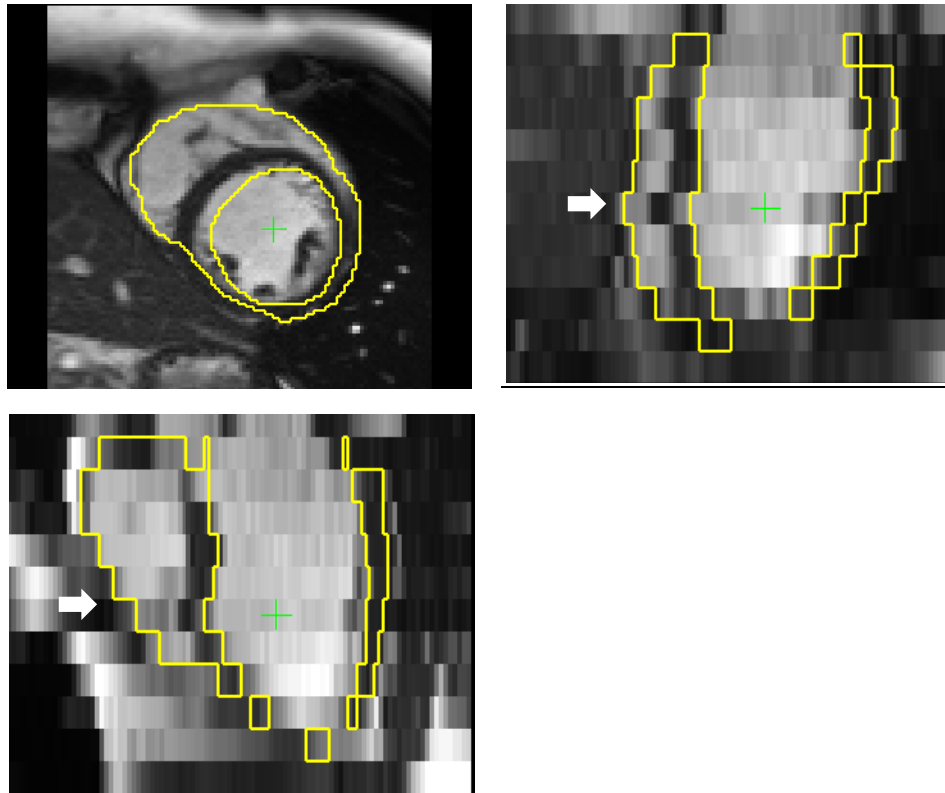


Figure 3-8 Example of an unacceptable segmentation with slice-misregistration.

Yellow contours represent the left ventricular endocardium, and the right and left ventricular epicardium (the RV septal contour is not displayed). Top left – mid ventricular short axis; top right and bottom left – long axis reconstructions. White arrows highlight the slice-misregistration which results in step artefact and imprecision in three dimensional phenotypes.

Statistical analysis was performed using a mass-univariate framework by analysis of covariates or group comparison. Because each surface mesh is co-registered into common template space, phenotypes can be compared for each vertex across the population. At each vertex (“mass”), a statistical test takes place to create a 3D statistical map of the heart. Threshold-free cluster enhancement of contiguous regions and permutation testing take place to derive p values associated with each vertex following adjustment to control for false discovery rate.^{366–369}

Previous work using this technique has shown that 72 (interquartile range [IQR]: 49–104) subjects would be needed to detect a 1mm difference in wall thickness in healthy

controls.⁷⁶ This was repeated for this thesis in patients with left ventricular hypertrophy, and inter-observer and scan-rescan reproducibility is presented in Chapter-5.3.1.

3.8.2. Three-dimensional left ventricular phenotypes

The surface mesh for each patient is assigned a phenotypic measurement for each of 19,185 endocardial and 27,623 epicardial points. This can be inspected visually and allows for statistical analysis as it is represented in a common template space (ParaView by Ahrens et al.)³⁷⁰. The following three-dimensional phenotypes were used:

Left ventricular wall thickness

At each vertex, wall thickness was calculated by measuring the distance between the endocardium and epicardium perpendicular to the midwall plane, Figure 3-9.

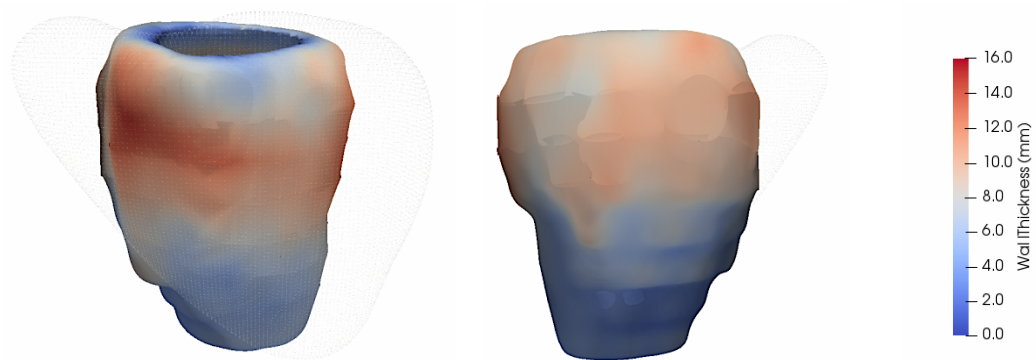


Figure 3-9 3D wall thickness for one patient with aortic stenosis represented across the ventricle.

Red represents greater wall thickness, here showing maximal hypertrophy in the anterior septum at the basal to mid ventricular level. En-face septal (left) and lateral (right) wall views are presented. The RV is depicted for reference as a light grey point cloud.

Surface geometry

Endocardial and epicardial volume is described as a positive or negative displacement relative to a template shape, Figure 3-10. The template shape is the average of 1053 healthy volunteers free of cardiovascular disease from the UK Digital Heart Study population.³⁶⁵ A negative displacement therefore means that there is inward displacement relative to the template, and positive displacement means there is outwards relative displacement.

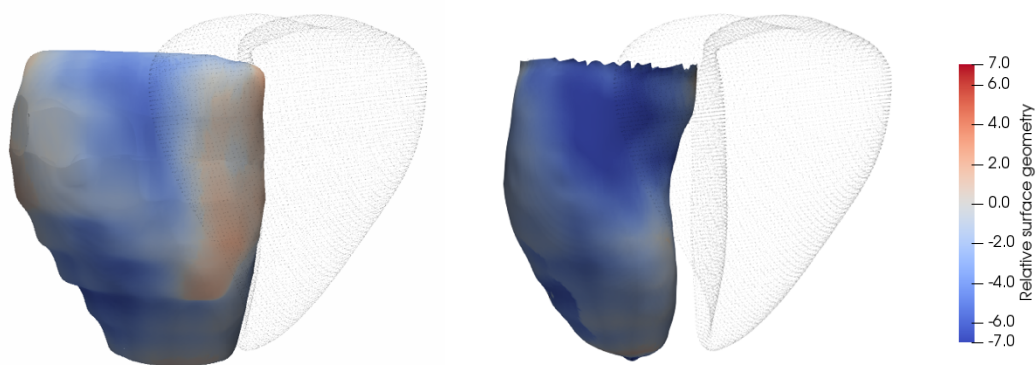


Figure 3-10 3D surface displacement relative to an average cardiac shape.

Blue represents inward displacement (smaller) and red represents outward displacement in the epicardium (right) and endocardium (left). The RV is depicted for reference as a light grey point cloud.

3.8.3. Attempted approaches to develop wall smoother 3D models

3D wall stress measurements

The remodelling response to a loading condition is associated with changes in myocardial wall stress and mechanics. 3D ventricular models provide the opportunity for a detailed assessment of active fibre stress that does not rely on 2D analysis or simpler geometric models. These require accurate measurements of curvature to incorporate into measures of wall stress. Radius of Gaussian curvature and wall thickness (Section 3.8.2) can be calculated for each point on the surface. It is possible to estimate active fibre stress with additional knowledge of LV pressure, as described by Zhong et al.:^{371–373}

$$WS = 0.133 \times SP \times \frac{R}{2T \times \left(1 + \frac{T}{2R}\right)}$$

Equation 3-1 Wall stress calculated by Zhong et al.

WS= peak systolic wall stress; R = inner radius of curvature; T= end systolic wall thickness. SP = systolic pressure. 0.133 is a conversion factor to express the results in 1000N/m².

The current cardiac atlas technique however results in step artefact which is accentuated when describing curvature, Figure 3-11. After exploring a number of approaches, a modification of the current cardiac atlas approach¹⁸⁰ was used to estimate smoother 3D models from 2D datasets, Figure 3-18 and Figure 3-19. Due to time limitations, wall stress measurements using this technique have not been incorporated into this thesis.

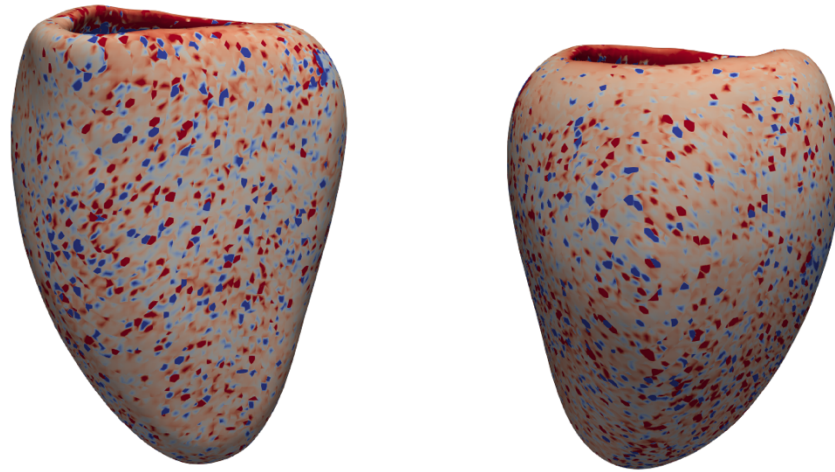


Figure 3-11 Mean wall stress in patients with aortic stenosis.

Due to step artefact, extremes in curvature result in inaccurate measurement of wall stress (dark red and dark blue are extreme values)

Use of 3D-cine SSFP CMR imaging

3D-cine imaging using a 1.5T Philips Achieva system has previously shown to improve statistical power in LV mass studies.⁷⁶ A 3D sequence was successfully acquired in all individuals in the Marathon Study, with sequence parameters in Table 3-3. The 3D-cine voxel size was isotropic at 3mm³, compared to a 2D-cine voxel size of 1.25x1.8mm with a slice thickness of 8mm. Additionally, there was no slice gap between 3D-cine slices, and it could be acquired in a single breath-hold, compared to 7-8 breath-holds for a 2D-cine. The benefit of the 3D-cine therefore was greater, smooth, sampling of base to apical geometry. However, approximately 15 phases were acquired per cardiac cycle (depending on the heart rate) compared to 25-30 phases in a conventional 2D-cine. The reduced temporal resolution may lead to an underestimation of LVEF. Unlike other 3D-cine sequences using Philips systems and SENSE acceleration in two spatial directions, acceleration was in one spatial direction. Therefore, imaging was limited by low blood-myocardial contrast, acceleration artefact and wrap. To minimize wrap, a larger field of

Methods

view was often needed, reducing true voxel size, Figure 3-12. Manual analysis in CVI42 of 3D data sets suggested improved 3D modelling was possible, Figure 3-13.

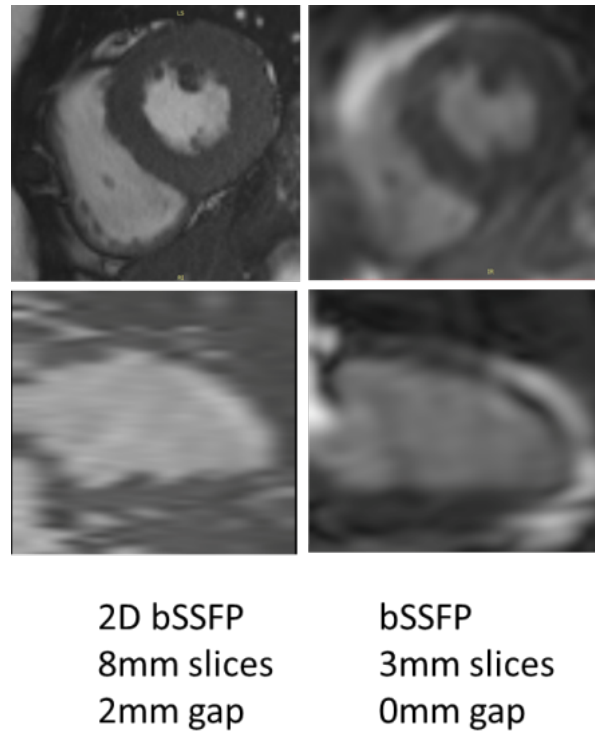


Figure 3-12 2D (left) vs 3D (right) cine imaging.

Top row: Short-axis views **Bottom Row:** Long-axis views. *Abbreviations: bSSFP=balanced steady-state free precession.*

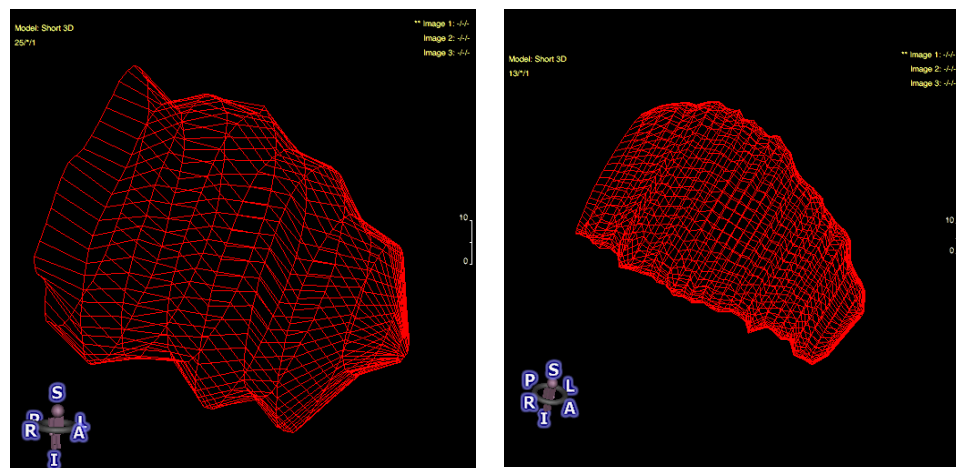


Figure 3-13 Segmentations from 2D (left) and 3D (right) cine imaging in the same patient at end - diastole.

Because manual analysis required unfeasible segmentation of 40-60 slices per individual, the atlas-based approach described above was used. The atlas was trained with manually labelled 3D-CMR data. However, segmentations lacked sufficient accuracy, Figure 3-14. This was because of large errors due to imaging artefact and a large field of view.

A similar atlas-based segmentation approach was also tested.¹⁸⁷ A segmentation process was applied by Dr Benedetta Biffi using the knowledge of a separate 3D cardiac atlas. This atlas was derived from a different 3D-CMR sequence and resulted in failed segmentations, Figure 3-15.¹¹³

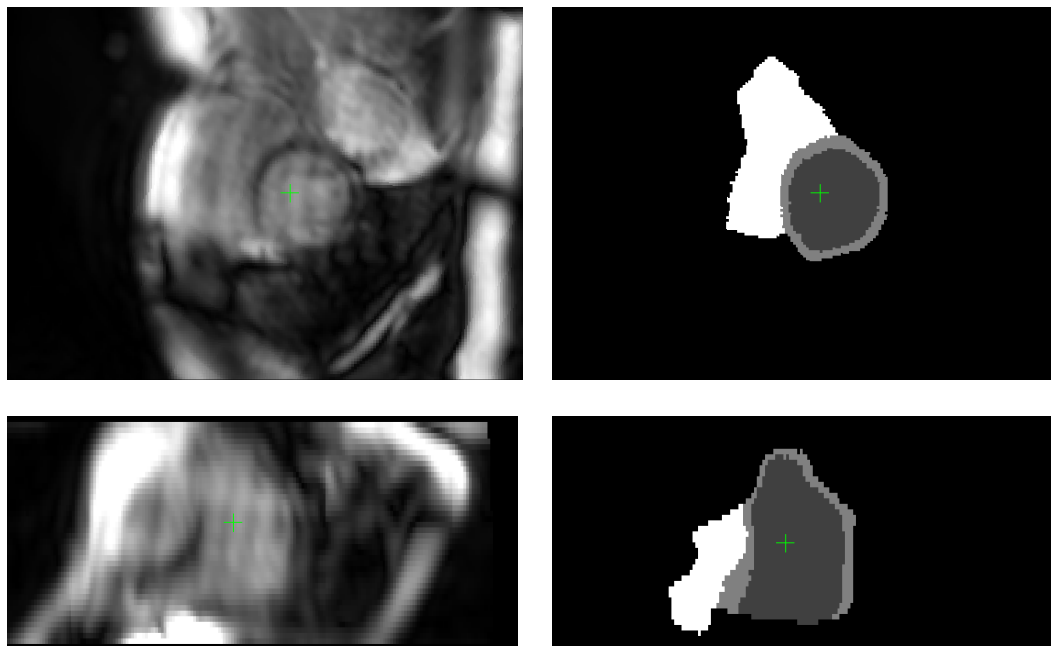


Figure 3-14 Inaccurate atlas-based segmentations 3D-cine imaging

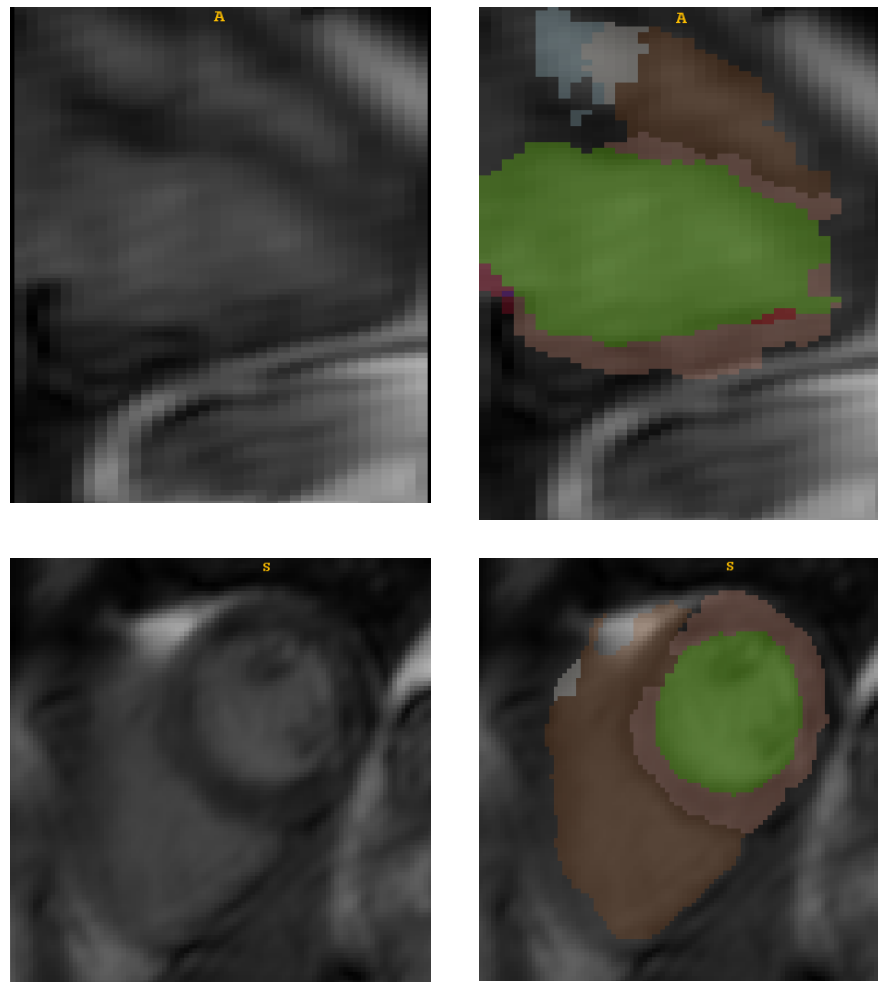


Figure 3-15 Failed segmentations using an atlas trained on 3D-cine data, but using a different 3D cine sequence.

Smoothing atlas-derived 3D models

The principle source of extreme changes in the ventricular surface was due to changes at the 2D slice boundaries due to breath-hold misregistration. A kernel smoother function was applied to the segmentation (*ksmooth* package, R), by taking a non-parametric average of the surrounding points. Whilst this appeared to smooth the models, it did not do so selective to slice boundaries, or sufficiently at slice boundaries even with extreme smoothing (1000 surrounding points), Figure 3-16.

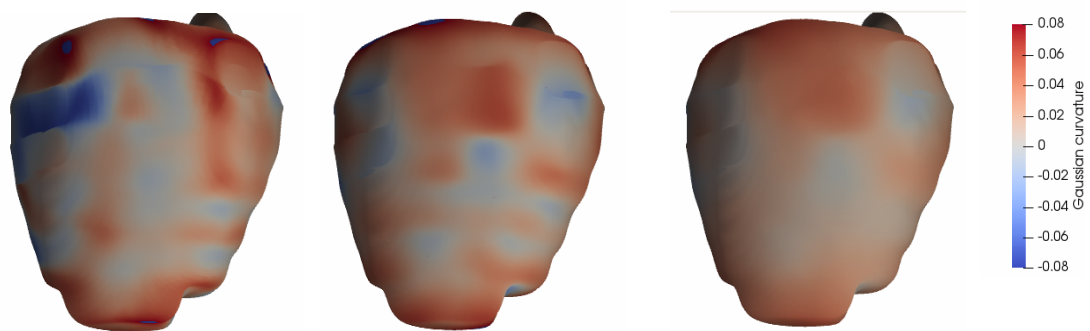


Figure 3-16 One attempt to refine models of curvature using different degrees of smoothing.

Gaussian curvature is calculated from the original segmentation (left) at each point. Smoothing is demonstrated using a non parametric estimate from 100 (centre), and 1,000 surrounding points (right). Curvature is represented as blue (negative) or red (positive) showing extreme curvature changes accentuated at 2D slice boundaries despite smoothing.

A further attempt to smooth models was made using a Savistky-Golay filter.³⁷⁴ The segmentations were split into single plane representations on the y axis (the base to apical length of the heart), representing approximately 93 slices, each of 500 points. However, as each x variable contains more than one z value, each quadrant of the image must be smoothed separately. Models would then require subsequent reconstruction and smoothing for final 3D segmentations.

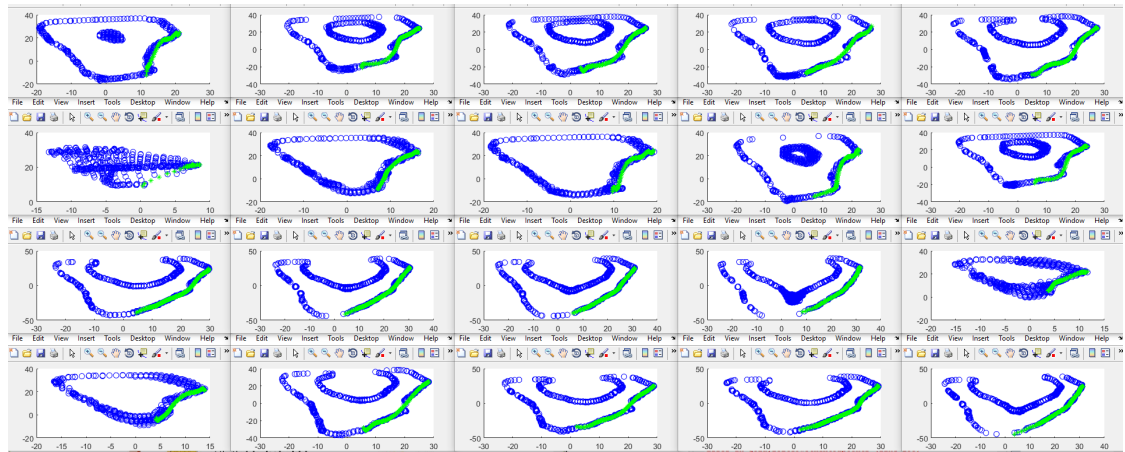


Figure 3-17 Application of a Savitsky-Golay smoothing filter to the inferolateral wall of a left ventricular segmentation.

Blue points represent the original segmentation x and z coordinates of 20 slices in the y plane. Green points represent the smoothed epicardium after the application of a Savitsky-Golay filter to data points representing the infero-lateral wall. Smoothing performed in conjunction with Bo Song (UCL).

Cardiac atlas approach using shape representations

A modified version of the original atlas approach was subsequently deployed. The different approach incorporated “spectral matching” into a multi-atlas PatchMatch methodology.¹⁸⁰ Atlases are represented as both image segmentations and, additionally, shape representations which allow a segmentation to be applied to each slice and between slices to deal with respiratory motion and large slice thickness. Two atlases were therefore constructed - the original atlas plus an additional shape atlas containing smoothed 3D segmentations from successful 3D cine segmentations. The shape atlas was augmented prospectively by adding further successful 3D models to it.

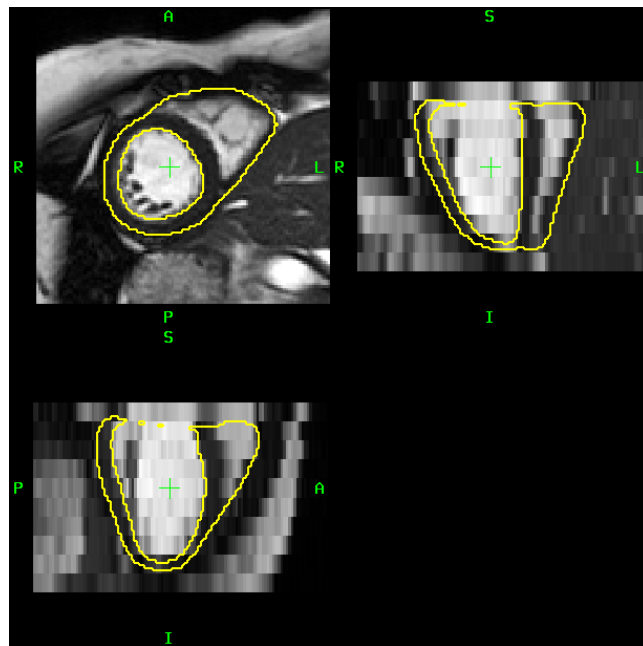


Figure 3-18 Example of a smoothed target segmentation overlaid onto original dicom data.

Yellow contours represent the left ventricular endocardium, and the right and left ventricular epicardium (the RV septal contour is not displayed). Top left – mid ventricular short axis; top right and bottom left – long axis reconstructions. Unlike Figure 3-7 there is limited step artefact between slices allowing for more precise representation of curvature and apical wall thickness and geometry.

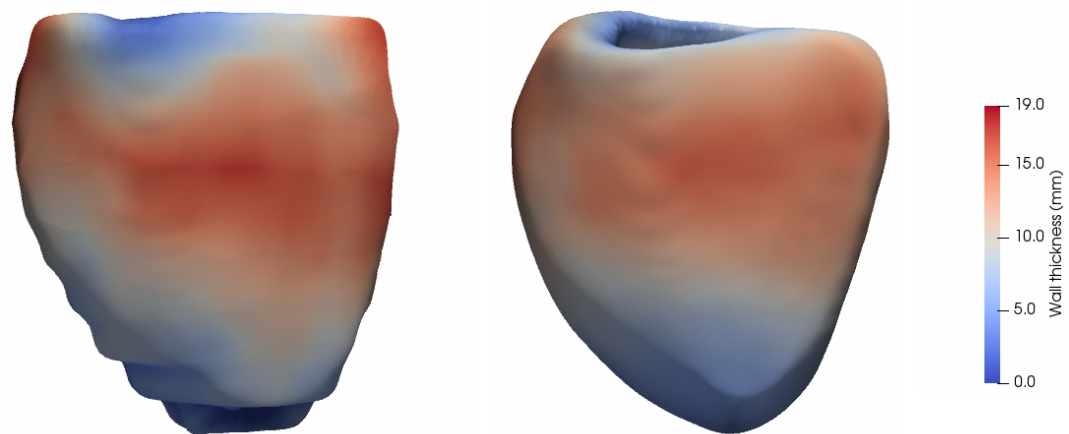


Figure 3-19 Successfully smoothed ventricular geometry and wall thickness.

Ventricular models of wall thickness and geometry in the same patient are shown using a cardiac atlas based segmentation approach with (left) and without (right) perturbations in cardiac shape isometry.

3.9. Aortic stiffness analysis

Flow velocity waveforms from phase contrast CMR imaging were analysed to calculate distensibility and transit times for the aortic arch, descending and whole aorta (ArtFun, University Pierre Marie Curie–INSERM), Figure 3-20.^{375,376}

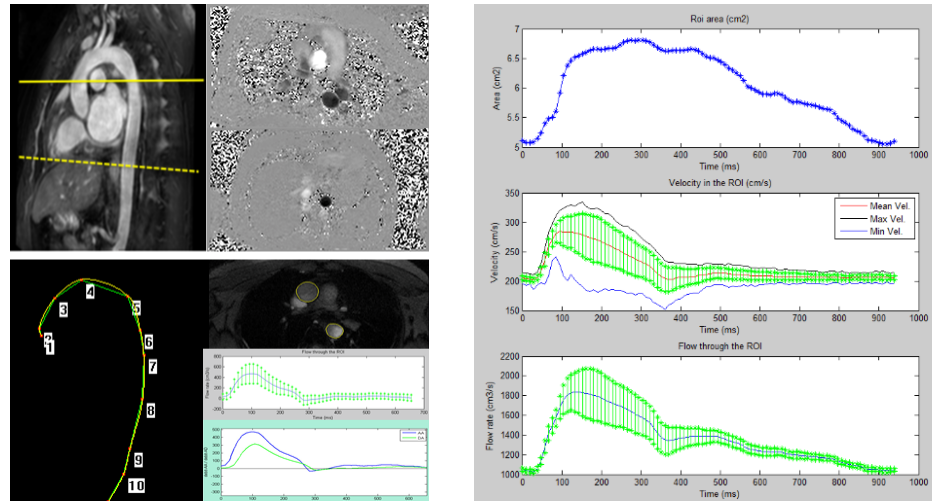


Figure 3-20 Phase contrast CMR analysis.

Top left: sagittal slice orientation to measure aortic length and pilot cross-sectional aortic phase-contrast imaging. **Bottom left:** measured aortic length and semi-automated segmentation of the aorta to obtain transit time. **Right:** Area (top), velocity (middle), and flow (bottom) profiles over an RR interval.

3.9.1. Measurement of aortic stiffness

PWV was calculated as the 3D distance between the ascending and descending aortic locations of the phase-contrast imaging divided by the transit time between velocity profiles, Equation 3-2.

$$PWV \left(\frac{cm}{s} \right) = \frac{3D \text{ distance}}{transit \text{ time}}$$

Equation 3-2 Pulse wave velocity (PWV).

Distance travelled was measured in a 3D coordinate system combining the sagittal and axial imaging using at least 14 markers placed in the centreline of the aorta. For transit

time, the only user interaction was to select the centre and border of the lumen on the modulus imaging.³⁷⁷ A circular cross-sectional aortic lumen region of interest (ROI) was then contoured automatically and propagated to each velocity-encoded phase; automatic contours were checked and modified manually if necessary. Mean aortic velocity within each ROI was then calculated for every phase to plot a velocity-time profile.^{375,376} The transit time was calculated using the least squares estimate between the systolic upslopes, which has shown to be most reproducible and accurate for CMR.^{264,378}

Distensibility was calculated as the change in aortic area relative to the central pulse pressure, Equation 3-3. This was measured on the ascending aorta, and the descending aorta at the level of the pulmonary artery and diaphragm.

$$Distensibility = \frac{A_{max} - A_{min}}{A_{min} \times cPP \times 1000} 10^{-3}.mmHg^{-1}$$

Equation 3-3 Aortic distensibility.

A_{max} and A_{min} are the maximum and minimum aortic areas across the cardiac cycle.

For distensibility and PWV, repeated measures by a second observer in 11 cases showed excellent reproducibility. Intra- and inter-observer ICCs were 0.99 and 0.99 for distensibility; and 0.93 and 0.95 for PWV.

Results, Chapters 4-7

4. Generalizability and precision of automated LV structure and function

This chapter is based on the published manuscript:

A multi-centre, scan-rescan, human and machine learning CMR study to test generalizability and precision in imaging biomarker analysis. Bhuvana AN, Bai W, Lau C, Davies RH, Ye Y, Bulluck H, McAlindon E, Culotta V, Swoboda PP, Captur G, Treibel TA, Augusto JB, Knott KD, Seraphim A, Cole GD, Petersen SE, Edwards NC, Greenwood JP, Bucciarelli-Ducci C, Hughes AD, Rueckert D, Moon JC, Manisty CH
Circulation: Cardiovascular Imaging Aug 2019 [Epub ahead of print]

Hypothesis:

Greater clinician experience and semi-automated contouring would improve human precision, and an automated technique would have superior performance overall.

Contribution:

I conceived the idea, designed the study and obtained grant funding. I recruited, and performed the CMR studies of 44 patients on two occasions. I collated, cleaned and anonymised the complete 110 patient multi-centre resource. I collaborated with *Circle* (CVI42, Calgary, Canada) to translate a level-set fractal analysis tool to a semi-automated endocardial volumetric assessment. I contacted MICCAI 2009 and STACOM 2011 challenge winners to test automated analysis strategies. I subsequently developed a training strategy to generalise a neural network developed by Dr Wenjia Bai. I prepared data for neural network analysis, and quality controlled neural network and clinician results. I performed the statistical analysis. I wrote the website (front and back-ends), and made the resource available online.

4.1. Introduction

Left ventricular ejection fraction (LVEF) and mass (LVM) remain key imaging biomarkers and are used daily for clinical decision-making and as clinical trial outcome measures.^{64,379} Absolute values guide pharmacotherapy, device therapy and surgical intervention. Although it is important that measurement is accurate against some putative reference - or at least that any bias is known, it is measurement precision (repeatability) that determines the clinical smallest detectable difference with time or treatment and, in conjunction with the minimally importance clinical difference, the sample size of clinical trials.⁸⁵ Cardiovascular magnetic resonance (CMR) imaging is the reference standard imaging modality to assess LV structure and function, and image acquisition is largely standardized through international consensus guidelines.³⁵⁷ In contrast, there is less agreement regarding analysis techniques where significant variation exists between inclusion/exclusion of papillary muscles, trabeculae and use of edge detection methods despite the CMR community desire for consistency and precision.

LVEF and LVM measurement variation arise from many sources including “on-target” changes with disease or intervention, “off-target” unavoidable biological variation (e.g. heart rate, volume status), and avoidable intra-observer, inter-observer, inter-study, inter-centre variation. These include random noise (e.g. intra-observer variation) and bias (one observer may systematically detect an edge differently to another),^{89,90} but relative contributions of each error source are not known.

Training programs and semi-automated contouring speed up segmentation and improve inter-observer agreement but techniques vary considerably.^{96–98} Automated analysis via machine learning (ML) approaches using deep learning neural networks show potential,^{103,147} and could remove this intra- and inter-observer variation. Currently ML

algorithms are tested by direct comparison with human expert observers as the reference standard, however this ignores sources of human error and means that ML techniques are unable to demonstrate superiority over human techniques. Precision can only be properly assessed using a test:retest dataset - this requires an adequately sized patient cohort to be scanned twice in an identical fashion within an interval short enough to effectively exclude variation in disease biology.^{89,94,380} For generalizability, this should be done across multiple sites and platforms.

A multi-scanner, multi-centre, health and disease precision (scan:rescan) CMR dataset resource for use as a tool to measure human and ML LVEF and LVM analysis performance was collated. This resource was then used to quantify CMR precision and different sources of human error (scan acquisition, observer experience, level of automation) using multiple analysis techniques. Having understood error sources from human approaches, a deep learning convolutional neural network was trained on a large multi-scanner multi-centre disease cohort and explored human and ML performance. It was hypothesized that greater clinician experience and semi-automated contouring would improve human precision and that an automated technique would have superior performance overall.

4.2. Methods

4.2.1. Study population

Institutions from across the UK were approached to develop a resource that reflects the range of scanning protocols, pathologies and scanners. Principal Investigators were approached with a request as outlined in Figure 3-1. In total, paired scans were obtained from five UK institutions (Barts Heart Centre, University Hospitals Bristol, Leeds Teaching Hospitals, University College London Hospital, and University Hospitals Birmingham NHS Trusts) with 6 different MRI scanners of 2 field strengths (1.5T, 3T), 2 manufacturers (Siemens, Philips), and 3 models (Aera, Achieva, Avanto); diseases represented the clinical spectrum (health, dilatation, hypertrophy, regional disease, n=118). The scan-rescan CMR parameters for precision assessment are outlined in Table 3-4. Further details on inclusion criteria are stated in the Methods 0. Each institution obtained local approval via the UK National Research Ethics Service; the study conformed to the principles of the Helsinki Declaration, and all subjects gave written informed consent.

Allometric data were collected before the scan and body surface area (BSA) was calculated using the Mosteller formula, $(\frac{Height \times Weight}{3600})^{1/2}$. Diagnoses were provided by the recruiting centre. Eight datasets were excluded because there were missing slices or unacceptable quality on one or other acquisition judged by an expert observer (JM).

4.2.2. Clinician analysis

Images were analyzed by an expert (JM) with greater than fifteen years' experience and two cardiology trainees (YY, CL) with less than one year of experience reporting CMR. With five human analysis techniques, variation in performance was expected. A three stage process was therefore designed, Figure 4-1.

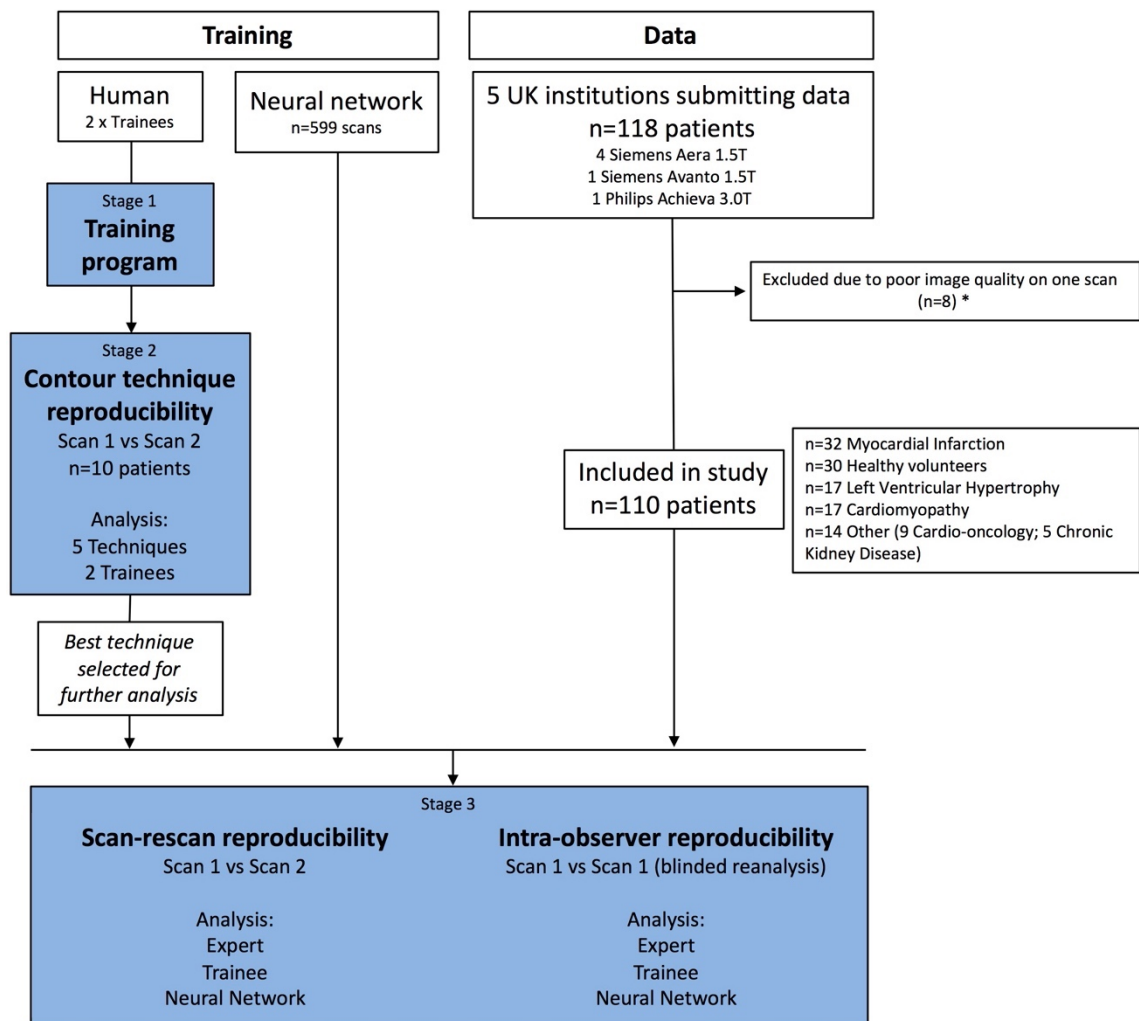


Figure 4-1 Flow diagram illustrating study recruitment and analysis.

Shaded blue boxes represent study outcome measures. *missing slices or significant breathing artefact on one scan.

Stage one: Two trainees undertook a training/standardization program over one month. Both were initially SCMR level 1 accredited and they had contoured approximately 100 and 700 scans with senior clinicians respectively for the two observers. Contouring feedback was provided by two experts (JM, CM) and standardized instructions created (consensus – based on local practice and informed by known international standard operating procedures within UK Biobank and MESA),⁹⁵ - see tutorial video (https://youtu.be/n_7Wfs3G_xg). Fifteen (different) studies ranging in difficulty were contoured and then re-contoured a month later to assess training impact.

Stage two: The two trainees each analyzed ten scan:rescans of patients representing different pathologies using five techniques (total 200 complete LVs contoured, Figure 4-2). Techniques were: [1] free-hand fully manual contouring; [2] visual thresholding of the blood-myocardial border; [3] curve fitting between points on the endocardium (“click-draw”); [4] level-set segmentation initialized by a mid-myocardial contour; and [5] semi-automated contouring after manual centering of the LV blood-pool. To minimize the impact of learning, at least 24 hours were left between analysis using the separate techniques and scans were analyzed blinded to participant identity in a random order for each technique.

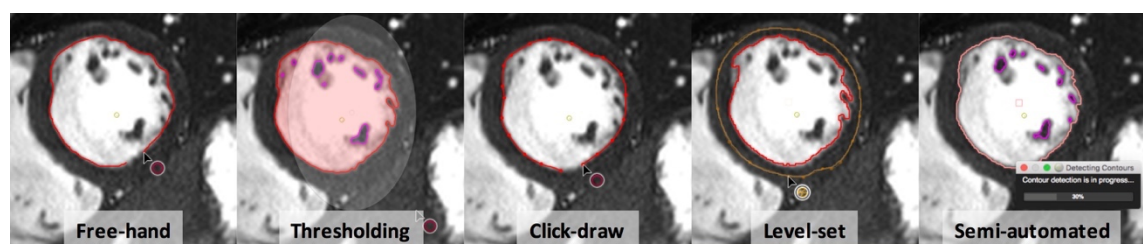


Figure 4-2 Manual and semi-automated techniques used to segment the endocardial border.

From left to right segmentation techniques become increasingly semi-automated: fully manual; visual signal intensity-based thresholding; manual point series; mid-myocardial contour to initialize level-set segmentation; and blood-pool centreing to initialize semi-automated segmentation.

Stage three: This transitioned the most precise technique from stage two for both the expert and trainees to analyze the entire dataset of 101 patients (scan A, scan B, blinded scan A again). This totalled 303 LV volumes by expert; 303 by trainees – by this time the trainees were indistinguishable in performance so they acted as one observer, dividing work; and 303 by the automated neural network). Analysis time was measured for a sample of 50 scans for one trainee and for all automated analyses.

All analysis took place using a bespoke prototype of *CVI42* (Release 5.3.8 [720], Circle, Calgary, Canada) to include a novel level-set segmentation technique previously developed and implemented for fractal analysis and modified in this study for endocardial contouring.³⁸¹ Details of the bespoke tool in *CVI42* are at <https://youtu.be/F0unF19YzxA>. End diastolic (ED) and end systolic (ES) phases were defined as the largest and smallest long-axis ventricular volumes visually. Contiguous short-axis slices were delineated in ED (endocardium first then epicardium) and ES (endocardium) to derive LV end diastolic volume (EDV), end systolic volume (ESV), stroke volume (SV), ejection fraction (LVEF) and LVM, with allometric scaling using BSA. To address basal slice variability, blood volume was included if there was over 50% of LV myocardium surrounding blood-pool, and a long-axis atrioventricular plane correction was used. The left ventricular outflow tract was included in the blood volume.

4.2.3. Developing collaborations for automated analysis approaches

In 2016, there were no approaches available in commercial software for fully automated analysis of CMR LV structure and function. Previous successful entrants in ventricular segmentation challenges were therefore contacted for collaboration, Figure 4-3. In total 16 entrants were contacted, Table 1-7. 6 replied including the top 3 competitors from the latest challenge, the Kaggle 2016 Data Bowl. Code was available online for these competitors, but competitors were unable to offer an active collaboration. This was necessary to understand errors and ensure any approach was generalisable to the real-world resource, and performed optimally.

The VOLUMES Study:
Cardiac volumetric analysis - a roadmap for improved precision

Dr Arsh Shah
Dr Gaby Caputo
Dr Charlotte Morley
Professor James Moon

Department of Cardiovascular Magnetic Resonance, Barts Heart Centre, London UK
Institute of Cardiovascular Sciences, University College London, UK

Background

- Volumetric analysis is fundamental to clinical cardiac imaging and research studies
- Increasing reliance on *reproducible* accurate serial imaging for clinical decision-making
- Little improvement seen in the past 10 years, despite huge computational advances
- Multiple analysis techniques available with little standardisation.

Has this patient's cardiac function worsened?

LV Ejection Fraction 54% → LV Ejection Fraction 49%

Confidence in our analysis technique is essential for clinical decision making.

Requirements

- An optimal technique would give the same result irrespective of the person analysing and consistently between scans:
 - Accurate
 - Good Intraobserver reproducibility
 - Good Interobserver reproducibility
 - Good Interstudy reproducibility
- Interstudy has not been looked at for over 10 years and is important for planning sample sizes and follow up scans.

Aims

- To identify sources of measurement error with current techniques and the impact of automation on test-retest precision
- To define current optimal analysis technique
- To produce an online open source library of test-retest scans for future validation work
- To develop an open access training program to improve clinical standards

Methods

- Test-retest datasets in 100 subjects with repeat scans acquired on same day
 - Across a wide range of pathologies;
 - Multiple MRI scan vendors;
 - Multiple clinical sites (UK, Europe, USA);
 - 1.5 and 3T.
- Investigation of multiple manual, semi automated and automated segmentation techniques.
- We will incorporate the most precise techniques into an online training module for clinicians.

Our request for collaboration

- We are contacting all successful entrants in previous segmentation challenges as well as using a commercial clinical analysis platform.
- We are hoping to incorporate your method into our project.
- If you are willing to participate, we ask for your script to be made available, ideally in C++, for the purposes of this research.

Data available

'Real world' cardiovascular magnetic resonance scan-rescan data:

- Multi-center
- Multi-disease
- Multi-vendor
- Multi-field strength

Thank you

- We are excited to move forward with this work and development for the CMR community.
- Please contact a.bhuva@ucl.ac.uk

Figure 4-3 Request for analysis technique collaborations with grand challenge winners for automated analysis approaches.

4.2.4. Automated neural network training and analysis

A collaboration was established with Dr Wenjia Bai and Professor Rueckert (Imperial College London). An automated two-dimensional deep fully convolutional neural network was previously developed to predict LV endocardial and epicardial contours at ED and ES from an input CMR SSFP short-axis stack.¹⁴⁷ The network was previously trained on 4,875 subjects from the UK Biobank. On initial testing, the trained network was not generalisable to the multi-centre, multi-disease data, and did not initialize segmentations even on some healthy volunteer scans.

A separate training dataset was therefore collated to reflect more real-world CMR imaging. The network was trained on multi-centre, multi-scanner datasets of patients with severe aortic stenosis, as described elsewhere.³⁸² Data were acquired at 1.5T and 3T. 1.5T scanners were Siemens Sonata, Avanto; and Philips Intera. 3T scanners were Siemens Verio, Skyra, Trio; and Philips Achieva TX. Although this cohort represents one primary disease, extensive comorbidity (hypertension ~53%, diabetes ~22%, coronary artery disease ~29%), and the ventricular response (~50% with focal scar, ~60% with hypertrophy (3 different subtypes), ~20% with impairment) made it representative of human cardiac disease in general. Scans (comprising ~ 13 cines, each 25 frames, 195,000 images) were annotated at ED and ES by an expert observer (JM). Annotations were performed following the standardized post-processing guidelines above. Papillary muscles and trabeculations were included in the LV blood-pool. After segmentation of ~300 datasets, performance was not generalizable to all multi-centre, multi-disease data, Figure 4-4, and in some cases failed to initialize. The failures did not appear to be related to specific scanning protocols, institutions or pathologies. The total training cohort consisted of 599 scans, and after training on this total training

dataset, there were no segmentation failures, Figure 4-5. Final training of the network took 8 hours 40 minutes on a Nvidia Titan X GPU.

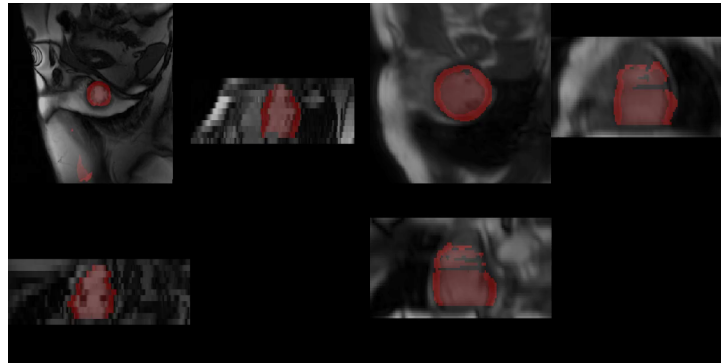


Figure 4-4 Segmentations after training on ~300 annotated datasets.

This shows extra-cardiac segmentations (left) or incomplete left ventricular segmentations (right).

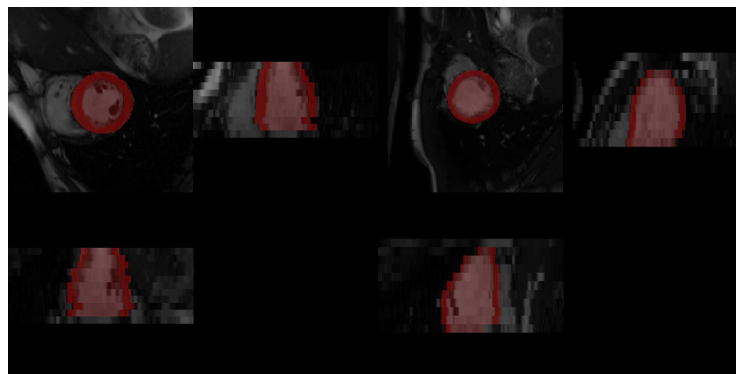


Figure 4-5 Improved segmentations after training on the complete training dataset (599 scans).

4.2.5. Statistics

Data were analyzed in R (R foundation, Vienna, Austria) using RStudio Server version 0.98 (Boston, Mass, USA). All continuous variables are expressed as mean \pm SD or median (interquartile range [IQR]) for skewed data. Categorical variables are expressed as percentages. Multiple groups were compared using one-way analysis of variance. Linear mixed effects regression models were used which account for multiple observers analyzing multiple measures per subject. Models were run separately for each LV metric (EDV, ESV, SV, LVEF or LVM) as the dependent variable. To assess training, the dependent variable was the difference between expert and trainee, and the fixed effect was training category (before/after). To assess technique, the dependent variable was the LV metric, and the fixed effects were technique and scan-rescan category (1 or 2). An interaction between technique and scan category was used to assess scan-rescan precision for each technique.³⁸³ To assess scan-rescan precision between different operators, the dependent variable was the LV metric, and the fixed effects were operator, scan-rescan category and the interaction term of operator and scan-rescan category. To assess the effect of LV impairment, a fixed effect of Scan 1 LVEF was included. Random effects included study subject in all models, and operator when assessing training and effect of semi-automated technique.

To quantify reproducibility in the whole cohort, three metrics were used: the absolute difference between scans, Bland-Altman limits of agreement (LoA), and within-subject Coefficient of Variation (CV). The within-subject variance was bootstrapped (1000 bootstraps) to estimate a 95% confidence interval of the CV. For inter-observer agreement in the whole cohort, an intra-class correlation coefficient (ICC, Lin's concordance correlation coefficient) was used as a summary measure; this reflects both

agreement and deviation from the line of perfect concordance; <0.2 =poor, >0.8 =excellent agreement.

Sample size required to detect a clinical change was calculated from the standardized difference (d) in each LV metric with a power of 90% and α of 0.05, where d is the desired clinical change divided by the standard deviation of scan-rescan differences.

The standard error of measurement (SEM) was calculated as the square root of the mean squared error obtained from one-way analysis of variance. The minimal detectable change between two scans considered to be different was calculated as $2 \times \text{SEM}$. All tests were two-tailed and $p < 0.05$ was considered statistically significant.

4.3. Results

4.3.1. Scan-rescan cohort

The final dataset of 110 scan-rescans represented patients with myocardial infarction (n=32), left ventricular hypertrophy (n=17, including hypertrophic cardiomyopathy), cardiomyopathy (n=17, dilated, arrhythmogenic right ventricular [ARVC] and left ventricular non-compaction [LVNC] cardiomyopathies), other pathology (n=14, cardio-oncology follow-up and chronic kidney disease), and healthy volunteers (n=30). All LV metrics differed between diagnostic sub-groups ($p < 0.05$ for all), Table 4-1. 106 rescans (96%) were performed within one week (82% on the same day); 4 scans in healthy volunteers were performed between 1 week and 3 months.

Baseline characteristic	MI	LVH	CM	Other	Healthy volunteers	P
<i>n</i>	32	17	17	14	30	
Male	26 (81%)	14 (82%)	9 (53%)	5 (36%)	22 (73%)	-
BSA/ m ²	1.94 ±0.4	1.99 ±0.4	2.00 ±0.4	1.88 ±0.5	1.82 ±0.5	-
Age/ years	60 ±11	60 ±12	49 ±13	50 ±15	31 ±9	<0.001
LVMi/ g/m ²	77 ±22	92 ±19	93 ±33	61 ±16	61 ±10	<0.001
EDVi/ ml/m ²	75 ±22	73 ±15	122 ±45	76 ±23	88 ±13	<0.001
ESVi /ml/m ²	34 ±17	24 ±7	72 ±51	28 ±13	33 ±9	<0.001
SVi/ ml/m ²	41 ±9	49 ±12	49 ±12	48 ±12	55 ±7	<0.001
EF / %	56 ±8	68 ±8	45 ±17	64 ±7	63 ±5	<0.001

Table 4-1 Study participant characteristics.

Patients with left ventricular hypertrophy had diagnoses of hypertrophic cardiomyopathy (n=11), aortic stenosis (n=3), hypertensive heart disease (n=2), Anderson-Fabry disease (n=1). Patients with other cardiomyopathies had diagnoses of dilated cardiomyopathy (n=13), arrhythmogenic right ventricular cardiomyopathy (n=1) and left ventricular non-compaction (n=3). Other pathologies include chronic renal failure (n=5) and patients under cardio-oncology follow-up (n=9). Groups were compared using one-way analysis of variance. Abbreviations: BSA = body surface area; LVM(*i*) = (indexed) left ventricular mass; LVEDV(*i*) = (indexed) left ventricular end diastolic volume; LVESV(*i*) = (indexed) left ventricular end systolic volume; LVSV(*i*) = (indexed) left ventricular stroke volume; EF = left ventricular ejection fraction.

4.3.2. Impact of initial training on trainee-expert agreement

Training and implementation of a standard operating procedure improved agreement between trainees and an expert for all LV metrics ($p < 0.05$ in linear mixed effect models for each LV metric), Table 4-2.

	Improvement in agreement	CI	<i>p</i>
EDV/ ml	4.0	1.5, 6.6	<i>0.003</i>
ESV/ ml	2.2	0.2, 4.2	<i>0.034</i>
SV/ ml	3.2	0.9, 5.6	<i>0.009</i>
EF/ %	1.6	0.5, 2.7	<i>0.008</i>
LVM/ g	4.9	2.2, 7.5	<i><0.001</i>

4-2 Inter-observer improvement in agreement after training.

Data presented is for the fixed effect of training in separate linear mixed models for each LV metric. Abbreviations: CI= confidence interval; EDV= end diastolic volume; ESV= end systolic volume; SE= standard error; SV= stroke volume; EF= ejection fraction; LVM= left ventricular mass.

4.3.3. Impact of techniques on human accuracy (bias) and precision

The thresholding and semi-automated techniques did not show a difference in accuracy with reference to manual contouring. As expected, the other two techniques showed over/under-estimation in EDV, ESV and LVM; but not LVEF or SV: the click-draw technique measured the LV as larger and showed a trend to lower LVM (EDV 6.0 ± 2.9 mls, $p=0.04$; ESV 5.0 ± 2.0 mls, $p=0.01$; LVM -6.7 ± 3.6 g, $p=0.07$); the level-set technique measured the LV as smaller and LVM as higher (EDV -8.3 ± 2.9 mls, $p=0.06$; ESV -5.8 ± 2.0 mls, $p=0.004$; LVM 15 ± 4.3 g, $p<0.001$).

For precision, however, there was no difference between techniques for either observer ($p > 0.05$ for each LV metric), Table 4-3. This included both techniques that included papillary muscles in the blood-pool and those that included them within the myocardial mass, Figure 4-2. Given the similar precision between techniques, subsequent analysis

of the complete dataset by the expert and trainee used the thresholding technique because it showed fewer large mistakes requiring manual correction.

Contribution of technique to scan- rescan difference		CI		<i>p</i>
Manual				
EDV/ ml	-0.39	-6.19	5.42	<i>0.87</i>
ESV/ ml	1.18	-2.77	5.15	<i>0.56</i>
SV/ ml	-1.57	-6.60	3.46	<i>0.54</i>
EF/ %	-0.51	-2.36	1.33	<i>0.58</i>
LVM/ g	6.18	-0.84	13.21	<i>0.08</i>
Thresholding				
EDV/ ml	-0.47	-8.69	7.75	<i>0.91</i>
ESV/ ml	-1.78	-7.39	3.82	<i>0.53</i>
SV/ ml	1.31	-5.80	8.42	<i>0.72</i>
EF/ %	0.87	-1.74	3.48	<i>0.51</i>
LVM/ g	3.13	-6.81	13.07	<i>0.54</i>
Click-draw				
EDV/ ml	2.34	-5.88	10.55	<i>0.58</i>
ESV/ ml	-1.68	-7.29	3.92	<i>0.55</i>
SV/ ml	4.02	-3.10	11.13	<i>0.27</i>
EF/ %	1.41	-1.20	4.02	<i>0.29</i>
LVM/ g	3.25	-6.75	13.25	<i>0.52</i>
Level-set				
EDV/ ml	-2.78	-10.99	5.44	<i>0.51</i>
ESV/ ml	-3.90	-9.51	1.70	<i>0.17</i>
SV/ ml	1.13	-5.99	8.24	<i>0.76</i>
EF/ %	1.35	-1.26	3.97	<i>0.31</i>
LVM/ g	3.09	-8.91	15.09	<i>0.61</i>
Semi-automated				
EDV/ ml	0.23	-7.99	8.45	<i>0.96</i>
ESV/ ml	-0.54	-6.15	5.06	<i>0.85</i>
SV/ ml	0.77	-6.34	7.89	<i>0.83</i>
EF/ %	0.09	-2.52	2.70	<i>0.95</i>
LVM/ g	0.90	-9.08	10.80	<i>0.86</i>

Table 4-3 Comparison of scan-rescan reproducibility between manual and semi-automated endocardial contouring techniques.

Data presented is for the fixed effect interaction between each technique and the scan category (scan A or B) in separate linear mixed models for each LV metric. Abbreviations: EDV= end diastolic volume; ESV= end systolic volume; SV= stroke volume; EF= ejection fraction; LVM= left ventricular mass.

4.3.4. Expert, trainee and automated accuracy (bias), precision and speed

There was good agreement between expert and trainee (ICCs 0.92, 0.98) and automated analysis (ICCs 0.90, 0.98) for all LV metrics, Figure 4-6 and Figure 4-7. Compared to expert analysis, trainee analysis measured the LV as slightly smaller, and LVEF and LVM as slightly higher. Automated analysis, conversely, measured the LV as slightly larger, and LVEF and LVM as slightly lower, Table 4-4.

	Bias	CI		p
Trainee vs Expert				
EDV/ ml	-3.12	-5.50	-0.75	0.01
ESV/ ml	-4.76	-6.63	2.89	<0.001
SV/ ml	1.70	-0.72	4.12	0.68
EF/ %	2.22	1.20	3.25	<0.001
LVM/ g	3.72	1.25	6.19	0.003
Neural network vs Expert				
EDV/ ml	6.69	4.32	9.07	<0.001
ESV/ ml	7.31	5.44	9.18	<0.001
SV/ ml	-0.55	-2.97	1.87	0.66
EF/ %	-2.95	-3.97	-2.95	<0.001
LVM/ g	-8.06	-10.53	-5.59	<0.001

Table 4-4 Bias between trainee and neural network observers compared to an expert.

Data presented is for the fixed effect of observer in separate linear mixed models for each LV metric. Abbreviations: EDV= end diastolic volume; ESV= end systolic volume; SV= stroke volume; EF= ejection fraction; LVM= left ventricular mass.

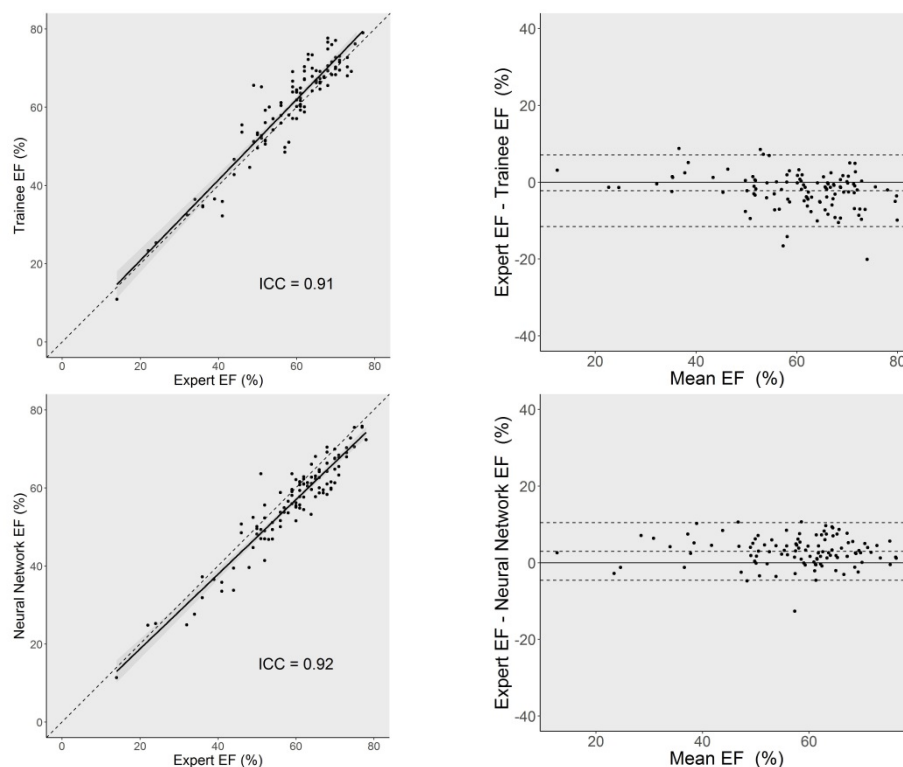


Figure 4-6 Correlation plots and Bland-Altman bias and limits of agreement for left ventricular ejection fraction (EF) between observers for scan A.

Abbreviations: ICC= intra-class correlation coefficient.

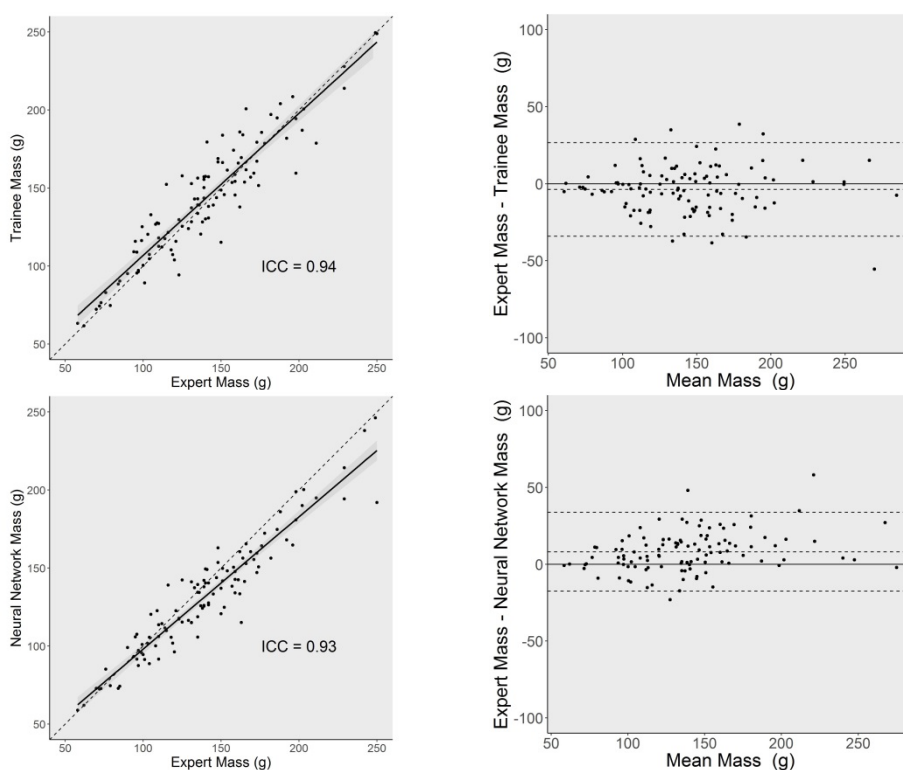


Figure 4-7 Correlation plots and Bland-Altman bias and limits of agreement for left ventricular mass between observers for scan A.

Abbreviations: ICC= intra-class correlation coefficient; g= grams.

For precision, there was no difference between expert, trainee and automated analysis ($p>0.05$ for each LV metric),

Table 4-5. Table 4-6 and Figure 4-8 detail scan-rescan and intra-observer differences, Bland-Altman LoA and CV.

Human analysis time was 13(IQR: 9, 19) minutes per scan. Automated analysis time of a 25-phase short-axis stack was approximately 0.07 minutes.

Contribution of observer to scan-re-scan difference				
	Estimate	CI		<i>p</i>
Expert				
EDV/ ml	-1.89	-4.38	0.61	0.14
ESV/ ml	0.37	-1.50	2.24	0.70
SV/ ml	-2.42	-4.84	0.003	0.0503
EF/ %	-0.59	-1.61	0.43	0.26
LVM/ g	0.02	-2.44	2.49	0.98
Trainee				
EDV/ ml	-0.10	-3.63	3.43	0.96
ESV/ ml	-0.58	-3.22	2.06	0.67
SV/ ml	0.65	-2.78	4.07	0.71
EF/ %	0.67	-0.78	2.12	0.37
LVM/ g	0.84	-2.65	4.33	0.64
Neural network				
EDV/ ml	0.56	-3.29	4.36	0.75
ESV/ ml	0.49	-3.80	3.73	0.71
SV/ ml	0.24	-3.57	3.47	0.89
EF/ %	-0.06	-1.73	1.32	0.86
LVM/ g	1.01	-3.28	4.09	0.70

Table 4-5 Scan-rescan reproducibility comparison between human and automated neural network techniques.

Data presented is for the fixed effect interaction between observer and the scan category (scan A or B) in separate linear mixed models for each LV metric. Abbreviations: EDV= end diastolic volume; ESV= end systolic volume; SV= stroke volume; EF= ejection fraction; LVM= left ventricular mass.

	Scan-rescan reproducibility					Intra-observer reproducibility				
	EDV (ml)	ESV (ml)	SV (ml)	EF (%)	Mass (g)	EDV (ml)	ESV (ml)	SV (ml)	EF (%)	Mass (g)
Expert										
Cohort Mean	159 ±51	69 ±46	90 ±23	59 ±12	142 ±44	160 ±51	69 ±45	91 ±24	59 ±12	143 ±44
Difference	9 ±8	6 ±6	9 ±8	4 ±3	7 ±7	5 ±4	5 ±5	6 ±5	3 ±3	4 ±3
CV/ %	5.7 (4.7,6.8)	10.0 (8.1,11.8)	9.4 (7.8,11.0)	6.1 (5.2,7.1)	4.8 (4.1,5.6)	3.1 (2.5,3.7)	7.4 (6.1,8.9)	6.4 (5.1,7.8)	5.4 (3.9,6.9)	3.8 (3.25,4.29)
BA limits	-23,26	-18,17	-20,25	-9,10	-19,19	-12.5,12.2	-13,13	-16,15	-8,8	-16,15
Trainee										
Mean	156 ±51	64 ±47	92 ±26	61 ±14	146 ±45	157 ±51	64 ±45	92 ±26	61 ±13	144 ±43
Difference	10 ±9	7 ±7	10 ±9	5 ±4	9 ±8	5 ±6	5 ±5	6 ±6	3 ±3	8 ±7
CV/ %	7.0 (5.8,8.2)	13.8 (11.4,16.2)	11.7 (9.4,13.9)	8.3 (5.6,10.3)	6.1 (5.2,6.9)	3.6 (2.9,4.3)	9.6 (7.4,11.8)	6.8 (5.5,8.2)	5.2 (4.2,6.2)	5.5 (4.2,6.7)
BA limits	-25,29	-19,20	-25,28	-12,12	-25,23	-15,16	-14,14	-17,18	-8,9	-22,20
Automated										
Mean	166 ±53	77 ±47	89 ±26	56 ±12	135 ±40					
Difference	10 ±9	8 ±8	10 ±9	4 ±4	6 ±6					
CV/ %	6.5 (5.2,7.8)	11.8 (8.5,14.6)	11.7 (9.1,14.1)	8.8 (6.1,11.1)	4.7 (4.0,5.6)					
BA limits	-25,28	-22,20	-24,29	-11,12	-17,16					

Table 4-6 Scan-rescan and intra-observer reproducibility stratified by observer.

Data are presented cohort mean± standard deviation; absolute difference between scans ± standard deviation of difference; Coefficient of variation (CV) and 95% confidence interval; and Bland-Altman limits of agreement (BA limits). *Abbreviations: CV= within-subject coefficient of variation; BA limits= Bland-Altman limits of agreement; other abbreviations as per Table 4-1.*

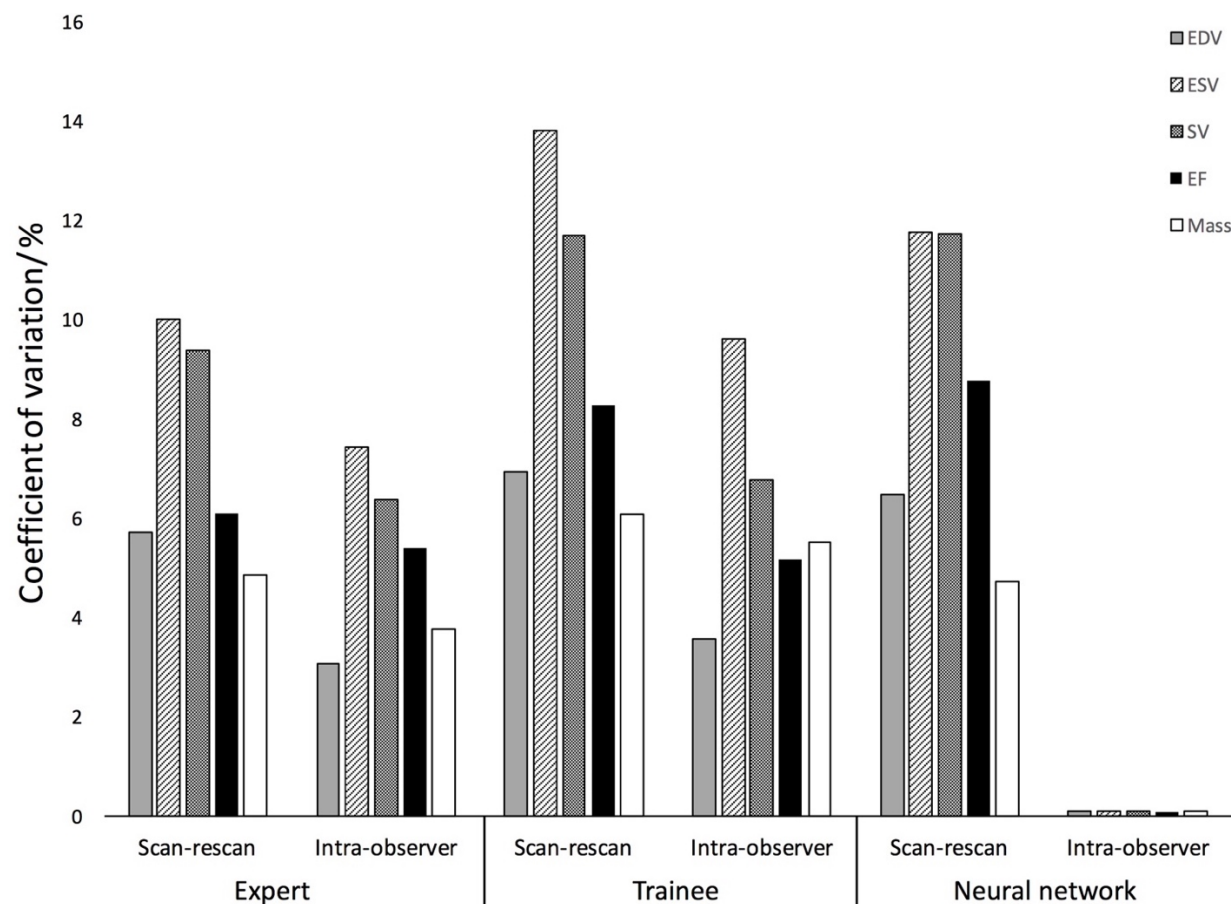


Figure 4-8 Scan-rescan coefficient of variation for expert, trainee and automated neural network analysis.

All comparisons are $p > 0.05$ (Table 4-5). Abbreviations: EDV = left ventricular end diastolic volume; ESV = left ventricular end systolic volume; SV = left ventricular stroke volume; EF = left ventricular ejection fraction

4.3.5. Sources of error for human and automated techniques

Average human CV for intra-observer, inter-observer and scan-rescan reproducibility were, for LVEF: 5.3%, 6.3% and 7.2%, and for LVM: 4.6%, 7.6% and 5.5% respectively, Figure 4-9 and Figure 4-10. For all LV metrics, human intra-observer CV was greater than half of the scan-rescan CV. For humans, scan-rescan CV was the greatest source of error for EDV, ESV, SV and LVEF, whilst inter-observer error was the greatest source of error for LVM. For automated analysis, there was zero intra-observer error as this technique was non-stochastic, that is, with the same image, the network would always generate an identical result. For all observers, precision was not influenced by the degree of impairment in LVEF.

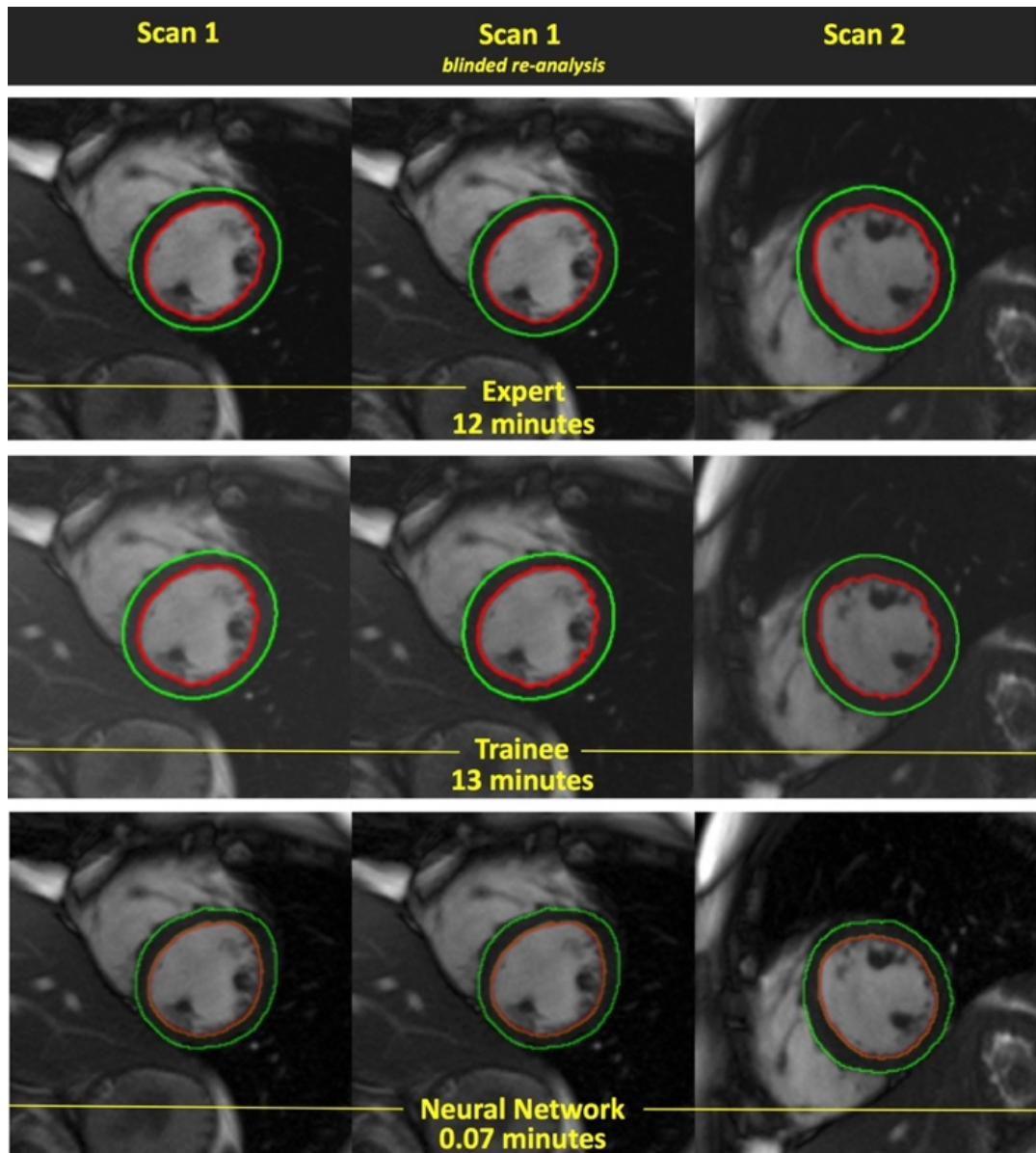


Figure 4-9 Examples of different contours for one cardio-oncology patient.

Analysis is by three observers (rows) over three datasets (columns), with average analysis timing per scan per observer reported. Left column: original scan 1, middle column: blinded scan 1 re-analysis; right column: repeat scan 2. Note this is one phase of one slice of ~10 in each short-axis stack; that all human contours differ whereas the automated neural network scan 1 blinded reanalysis contours are identical. Note also the similar position but different piloting and orientation of the repeat scan 2.

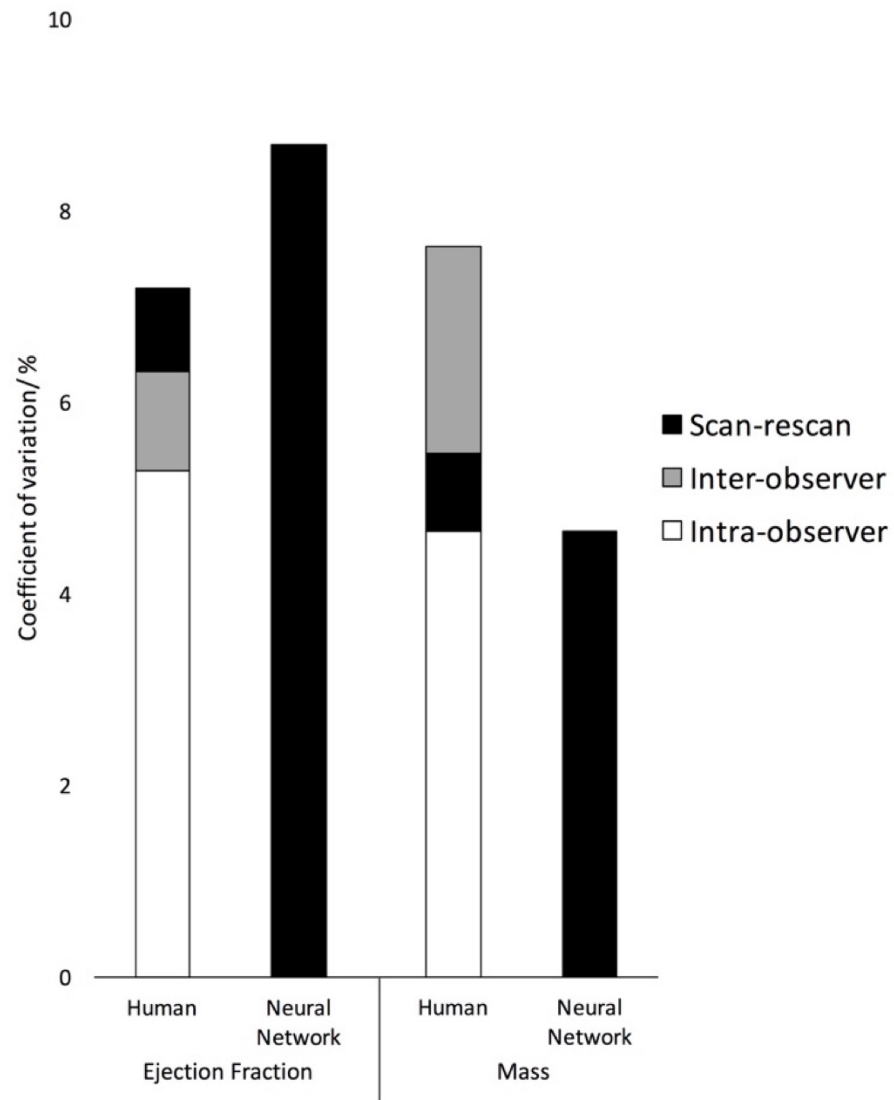


Figure 4-10 Contributions of intra-, inter-observer and scan-rescan error to human measurement variability.

For ejection fraction, human error (coefficient of variation) is incremental from intra-observer, inter-observer (on the same scan), to inter-scan. For mass, human inter-observer error is greatest. Scan-rescan error is similar for human and automated neural network analysis, however the majority of error for human analysis is related to the observer suggesting that automated techniques have other sources that can be addressed in order to surpass human performance. Human error is the average of both human observers.

4.3.6. Sample size estimates and minimal detectable change

Calculation of sample size from these data shows that CMR requires 28 patients to detect a 3% change in LVEF; 12 patients to detect a 10g change in LVM; and 17, 10 and 16 patients to detect a 10 ml change in EDV, ESV and SV respectively, Table 4-7.

The percentage change in sample size of an expert for all LV metrics was similar to a trainee (x1.2-1.5) and automated analysis (x0.8-1.5). Sample size requirements were largest for patients with left ventricular hypertrophy.

For an individual patient, the minimal detectable change was 8.7% in LVEF or 20g in LVM, based on expert analysis (with no difference when compared with automated analysis).

	Sample size estimates (n), $\alpha = 0.05$, 90% power									
	EDV		ESV		SV		EF		Mass	
	sd	n	sd	n	sd	n	sd	n	sd	n
<i>Whole cohort</i>										
Expert	12	17	9	10	11	16	5	28	10	12
Trainee	14	x1.3	10	x1.2	14	x1.3	6	x1.5	12	x1.5
Automated	13	x1.2	11	x1.4	13	x1.3	6	x1.5	8	x0.8
<i>Sub-groups (expert only)</i>										
MI	12	18	7	7	11	15	5	31	11	14
LVH	13	20	9	11	13	20	5	36	8	9
CM	12	17	10	12	9	10	4	19	13	20
Other pathology	14	23	6	6	12	17	3	15	6	7
HV	9	11	10	13	11	16	5	26	9	11

Table 4-7 Sample size estimates stratified by observer and pathology.

For Trainee and Automated Neural Network analysis, sample size is represented as a proportional change to Expert analysis. Sample size estimates stratified by pathology are presented for expert analysis only. The detectable change in volumes is 10mls; mass is 10g, and EF is 3%. Abbreviations: CM= cardiomyopathy; HV= healthy volunteers; LVH= left ventricular hypertrophy; MI= myocardial infarction; sd = standard deviation; other abbreviations as per Table 4-1.

4.4. Discussion

Despite reliance on measurements of LVEF and LVM for clinical decision-making and as endpoints in research studies, analysis is often not standardized and the relative contributions of error sources are imperfectly known. These data show that using current standardized image acquisition and multi-centre, multi-vendor, multi-field strength, multi-disease, scan:rescan data at scale, measurement error was largely due to inconsistency in the human observer rather than variation in modifiable factors - clinician experience, scan acquisition, or human contouring strategy (here performed using 5 techniques). This study also demonstrated for the first time that an automated analysis technique using deep learning has equivalent precision (scan:rescan reproducibility) to an expert, and yielded approximately 13 minutes time-saving per scan, tested head-to-head on variable pathologies from multiple institutions. Clinicians can be confident in detecting a 9% change in LVEF or a 20g change in LVM, this was similar if using an automated ML technique. Because the resource has the potential to test superiority of automated over human analysis, data and training videos/standard operating procedures have been made available.

Previous studies investigating LV analysis by CMR have largely focused on inter-observer and intra-observer differences, using datasets from healthy individuals in single centres, including older gradient echo cine acquisitions.^{89,90} Clinical practice relies on scan-rescan precision, and includes sources of variation not previously captured in most datasets such as the scan acquisition, differences between institution, and disease states. This study looked at the efficacy of a number of potential strategies (decided a priori) that might reduce or maintain variability with time-saving through

automation: clinician experience, training, human contouring methods, and deployment of an automated neural network segmentation approach.

4.4.1. Benefits of automated analysis

The adoption of ML can offer comparable precision with clinicians, with the time saving and global standardization that would ensue. Training of junior clinicians required a month-long program (excluding previous CMR experience and level 1 accreditation), compared to approximately nine hours for a neural network (excluding contour annotation time). Once trained, clinicians required an average of 13 minutes for analysis per scan, compared to approximately 4 seconds for a neural network. In the UK, an estimated 2275 scans per million adults are needed annually, performed in 61 centres.³⁸⁴ Automating this one aspect of CMR analysis alone would therefore potentially translate into a saving of 54 clinician-days per centre. Accurate automated segmentation is a bridge to reliable extraction of more information from the same imaging beyond established imaging biomarkers, Chapter 5. In combination with time saving, this maximizes use of acquired data in a value-based manner.

4.4.2. ML techniques can surpass human precision

Given that the greatest sources of measurement error were human factors (i.e. non-modifiable intra- and inter-observer variability), with improvement, it is only a matter of time before automated approaches are super-human, with cascading consequences in clinical (confidence, smallest detectable difference) and research (trial size) domains of increased precision. Improvement could be related to either training data or the network itself, and comparison of scan:rescan precision against that of an expert offers the

ability to show superior performance, and provides an important validation step towards real-world scalability.

Similar performance of automated techniques to humans has previously been shown by comparing the degree of inter-observer agreement between two clinicians and clinician-network agreement in typically healthy subjects.^{103,147} Use of measurement precision between techniques using test-retest methodology provides a direct comparison, and this cohort enables identification of methods that are both generalizable and superior to humans.

Superior performance will require potentially larger and more variable pathology datasets facilitated by adversarial training, or transfer learning.^{146,385} However, if training is performed by one expert annotating each dataset, neural networks will be trained to minimize between subject differences but not differences between or within observers. Training on repeated measures may minimize these errors. This could also be surmounted by the use of stronger priors,³⁸⁶ three-dimensional neural networks or even limiting the reliance on annotation through deeper, more intelligent pixel classification. Neural network approaches however do show limitations. Data must be standardized prior to analysis, and neural networks are computationally expensive to train and require clinician-facing interfaces before widespread implementation. Biologically implausible segmentations are also possible and therefore results require human review.¹⁰³ In this study, each segmentation was reviewed by a clinician using automated printouts for rapid quality control. Image quality assessment, in combination with detection of erroneous segmentations, will need to be incorporated into any clinically robust workflow.

4.4.3. Sample size estimates

This study provides benchmark precision metrics that reflect a range of pathologies and institutions. Required sample sizes to detect a standardized difference was greatest for patients with left ventricular hypertrophy who had increased LVM and small systolic cavity volumes. The sample size required to detect a clinically important change was between 10 and 28 patients for different LV metrics, which is higher than previous estimates.^{89,94,380} This dataset however is different due to its high variability, and should these results be considered for future study design, there may be reasons that these results either over- or under-represent anticipated performance for a specific real-world task. Factors that make precision higher here include: excellent training/standardization and operator selection; bias from using only the best 110 studies from 118 with (by definition) no further dropout; scan:rescan at short time intervals; a few expert centres only. Factors that make precision lower here include: inclusion of multiple diseases; multiple centres; multiple scanners and blinded analysis. Whilst follow-up studies may be analyzed consecutively in clinical practice, we ensured that the two scans acquired for each subject were assigned different randomized study numbers to minimize bias in this study. There was no review of study data at study completion, with all analysed datasets included in the results.

4.4.4. Sources of human measurement error

It is generally accepted that there is incremental variation from intra-observer, inter-observer and scan-rescan (physiological and technical) differences.³⁸⁷ These data demonstrated that human (intra-observer) error (CV) was greater than half of scan-rescan error, an effect that was not minimized when an expert was compared with junior

clinicians after appropriate training, despite fifteen years' additional experience. A training program combined with standard operating procedures was an effective approach to improve inter-observer agreement, by standardizing basal blood volume and papillary muscles, as previously reported.^{96,97} Semi-automated techniques, including a novel level-set approach with minimal user interaction also did not improve precision over manual techniques, a finding replicated in two observers. However, human contouring strategies resulted in potentially clinically relevant differences for an individual patient, emphasizing the need to interpret reference ranges in the context of the technique from which they were derived.

In order to improve human measurement precision, an improved focus on unifying a systematic approach to analysis and greater acquisition standardization appears important. This would require investigating piloting of the short-axis cine stack, loading conditions, or sequence improvements that improve myocardial contrast with epicardial fat.⁹⁹

4.4.5. Why is reproducibility best for mass?

Across all operators, the scan-rescan reproducibility error (CV) was highest for ESV and lowest for LVM. Variance of measurements derived from other measurements (EF, SV, LVM) showed better reproducibility than simply the sum of their components (EDV, ESV), similar to other studies.^{89,380,388} This is because the error of the components propagate to the derived measurement as the square root of their summated CVs ("law of propagation of errors").³⁸⁹ CV of EF for the expert observer is therefore related to the CV of SV (9.4%) and of EDV (5.7%) = $\sqrt{9.4^2 + 5.1^2} = 10.7\%$.

Table 4-6 however shows that expert CV of EF is 6.1%, which is lower than expected because EDV and SV correlate strongly. This also applies to the reproducibility of SV which is derived from EDV and ESV. Error propagation weights towards the larger source of uncertainty, and the reproducibility error of ESV is more than double EDV. Therefore the CV of SV tends towards the CV of ESV. Figure 4-8 shows this, with real-world data within the expected confidence limits. LVM similarly shows very similar reproducibility to EDV. Because endocardium was drawn before epicardium, epicardial segmentation is weighted to a strong prior (endocardial contour) and so to the reproducibility of EDV.

4.4.6. Study limitations

We measured variability using a relatively small number of observers, however by including both trainees and an international expert as the gold standard observer, the errors measured are likely to be representative. Both scans for each patient were acquired in the same institution using the same protocol, and therefore we have not assessed scan-rescan precision between institutions. The scan-rescan interval was short (with 82% of studies acquired on the same day), and we are therefore unable to assess the contribution of physiological variability across months or years. The precision of right ventricular assessment was not within the scope of this study. We analyzed the performance of a ML approach but not its prospective clinical application.

4.5. Conclusion

Automated machine learning techniques for LV analysis match human precision and perform substantially faster. Based on multi-centre, multi-vendor, multi-field strength, multi-disease data, a 9% change in ejection fraction can be detected confidently by expert clinicians, and this is similar using automated analysis. Given that a major source of measurement variability is attributable to the observer, automated approaches offer the future potential to surpass human experts, demonstrable using this scan:rescan resource.

4.5.1. Acknowledgements

The authors thank the patients and healthy volunteers for taking part in this study. The authors acknowledge all research staff at each site for their contribution to recruitment. They also acknowledge the contribution of the British Society for Cardiovascular Magnetic Resonance Valve Consortium for developing, acquiring and making available the training dataset segmentations.

5. Utility of 3D LV modelling in patients with aortic stenosis

This chapter is based on the published manuscript:

Sex and regional differences in myocardial plasticity in aortic stenosis are revealed by 3D model machine learning. Bhuva AN, Treibel TA, De Marvao A, Biffi C, Dawes TJW, Doumou G, Bai W, Patel K, Boubertakh R, Rueckert D, O'Regan DP, Hughes AD, Moon JC, Manisty CH.

Eur Heart J Cardiovasc Imaging. 2019 Jul 5 [epub ahead of print]

doi: 10.1093/ehjci/jez166

Hypothesis:

A 3D machine learning approach would provide new insights into left ventricular remodelling in patients with aortic stenosis, including sex dimorphism and reverse remodelling one year post-aortic valve replacement.

Contribution:

I conceived the idea for this analysis. Dr Treibel submitted the ethics application, and performed the original patient data collection under separate grant funding. I performed the CMR acquisition for the sensitivity analysis in 24 subjects. I compiled a cardiac atlas by segmenting and labelling CMR data from >300 patients and healthy volunteer datasets. Using the atlas, I applied an approach to create 3D segmentations and co-register studies for patients and matched controls. I summarised 3D model data visually and computationally, and performed the statistical analysis.

5.1. Introduction

Aortic stenosis (AS) is the most common valvular heart disease in the developed world and is associated with high mortality once symptoms develop.³⁹⁰ Aortic valve replacement (AVR) improves survival but risk stratification and timing is difficult because symptoms are hard to elucidate and current grading criteria focus largely on echocardiographic valvular parameters which may be discordant.²⁸⁶ Outcome is however also known to be determined by left ventricular (LV) remodelling, encompassing changes to geometry and hypertrophy (LVH), which may be asymmetrical and varies in extent between individuals.^{291,391,392} In response to pre-coronary pressure overload, ventricular remodelling may be initially adaptive but later maladaptive and associated with adverse consequences of diastolic dysfunction, ischemia, fibrosis, heart failure and eventually death.^{290,291} Following intervention, reverse remodelling is also variable,³⁰⁸ and linked to re-hospitalization rates.³⁹³ These changes appear to be at macro- and microscopic levels and have sex specific features,^{297,314,394–396} and impact.³⁰⁷

Conventional metrics of remodelling using left ventricular mass indexed (LVMI) to body surface area (BSA) and concentricity (global LV mass to end-diastolic volume ratio [MVR]) provide broad insight into the myocardial response to AS,³¹ however may mask early changes or regional differences. By capturing asymmetry in LV remodelling, it is possible to add incremental value for identification of early disease, different disease pathways and outcome prediction.³⁹⁷ Advances in atlas approaches utilizing machine learning for robust automated segmentation and co-registration now permit unbiased appreciation of three-dimensional (3D) ventricular architecture (local myocardial wall thickness and shape) and comparison with health and change over

time.¹⁶⁰ 3D phenotyping delivers deeper insights into the complex structural patterns in cardiac imaging data, moving closer towards personalized imaging biomarkers for risk assessment.³⁹⁸ But before 3D machine learning can be incorporated into predictive models, it should demonstrably deliver a more sensitive marker of LV remodelling than conventional metrics. We hypothesized that such a 3D machine learning approach would provide new insights into AS remodelling, including sex dimorphism and reverse remodelling one year post-AVR.

5.2. Methods

5.2.1. Study population

A prospective observational cohort study was conducted in patients with severe, symptomatic AS who underwent AVR between January 2012 and January 2015 in a single tertiary referral cardiac centre, University College London Hospital NHS Trust, London, UK. The study was approved by the ethical committee of the UK National Research Ethics Service (07/H0715/101). The study conformed to the principles of the Helsinki Declaration, and all subjects gave written informed consent.

Full details of study design and methodology have been previously published, and are described in Methods-3.1.^{297,315} Controls were matched to balance for age, sex, BSA and African Caribbean ethnicity covariate distributions from a prospective observational study of 1,968 healthy adult volunteers free of cardiovascular disease for the United Kingdom Digital Heart Project (www.digital-heart.org), Table 5 1.

	Patients with aortic stenosis	Matched controls	<i>p</i>
<i>n</i>	116	40	
LVM (g)	161 ±43	120 ±27	<0.001
LVEDV (ml)	154 ±61	156 ±34	0.92
LVESV (ml)	61 ±47	49 ±13	0.02
EF (%)	64 ±12	68 ±3	<0.001
	Patients with normal pre-operative geometry	Matched controls	
<i>n</i>	19	17	
LVM (g)	122 ±27	107 ±22	0.11
LVEDV (ml)	128 ±33	136 ±23	0.41
LVESV (ml)	42 ±21	43 ±9	0.85
EF (%)	68 ±8	69 ±3	0.96
	Patients with normal post-operative geometry	Matched controls	
<i>n</i>	45	19	
LVM (g)	114 ±26	117 ±28	0.69
LVEDV (ml)	126 ±30	141 ±26	0.06
LVESV (ml)	42 ±17	45 ±9	0.43
EF (%)	67 ±8	69 ±3	0.46

Table 5-1 Comparison of global LV metrics in patients with aortic stenosis and healthy matched controls free of cardiovascular disease.

Abbreviations: EDV = end diastolic volume; EF = ejection fraction; ESV = end systolic volume; LVM= Left ventricular mass; SV = stroke volume.

5.2.2. CMR and manual analysis

CMR was performed at 1.5 T (Magnetom Avanto, Siemens Healthcare, Erlangen, Germany), using a standard clinical scan protocol, see Methods-3.5.³¹⁵ Extracellular volume fraction (ECV) calculation for matrix and cell volumes were performed as previously described.³¹⁵

Volumetric analysis of left ventricular mass and volume was performed manually by an observer (TT) with greater than six years' experience (CVI42, Circle, Calgary Canada). Left ventricular hypertrophy was defined as an LVMi $>95^{\text{th}}$ percentile of the widely-used normal range, corrected for age and gender.³⁹⁹ AS patients were categorized into four patterns of LV geometric adaption: “normal geometry”, “concentric remodelling”, “concentric hypertrophy” and “eccentric hypertrophy”. Categories were defined by BSA-indexed LV mass (LVMi), indexed LV end-diastolic volume (LVEDVi) and mass-volume ratio (MVR). Normal geometry: normal LVMi and $\text{MVR} \leq 1.15$; Concentric remodelling: normal LVMi and $\text{MVR} > 1.15$; Eccentric hypertrophy: increased LVMi and $\text{MVR} \leq 1.15$; Concentric hypertrophy: increased LVMi and $\text{MVR} > 1.15$.

5.2.3. Global and regional (3D) atlas-based assessment of LV structure

3D analysis was performed as previously described using an atlas-based machine learning approach for image segmentation to produce global LV metrics and 3D models of wall thickness and geometry, co-registered in the same space.^{160,194} Image processing was performed using Matlab R2013a (The MathWorks, Inc., Natick, Mass, USA) and ITK-SNAP (US National Institutes of Health). Each voxel was segmented based on a reference atlas of over one thousand individuals.¹⁶⁰ In brief, this was initialized by

manually placing six anatomical landmarks (left ventricular apex, mitral valve annulus, left and right ventricular free walls, superior and inferior right ventricular insertion points). This produced a patient-specific mesh of ~40,000 vertices aligned within a common reference space. At each vertex, wall thickness was calculated by measuring the distance between the endocardium and epicardium perpendicular to the midwall plane. Changes in end-diastolic chamber and epicardial volume were measured as a positive or negative displacement from an average healthy volunteer template shape. By 3D geometric analysis, regional concentric remodelling was defined as chamber volume reduction due to inward displacement of the endocardium; and conversely, regional eccentric remodelling was defined as cavity dilatation due to outward endocardial expansion. If either of these processes was associated with outward epicardial expansion, this resulted in concentric hypertrophy and eccentric hypertrophy respectively (Figure 5-4). For a 3D assessment of function, fractional wall thickening (FWT) was calculated as the percentage change between end-diastolic and end-systolic wall thickness. For baseline comparison to matched controls, all 116 patients with AS were analyzed.³¹⁵ At follow-up, two patients (one male, one female) were excluded due to significant slice misregistration precluding 3D model construction.

5.2.4. Accuracy and precision of atlas-based assessment

For accuracy of global parameters, inter-observer agreement was performed between manual and atlas-based measures of global LV metrics using an intraclass correlation coefficient (ICC, mixed model).

For precision of 3D parameters, twenty-four patients (12 patients with left ventricular hypertrophy, 12 healthy volunteers) separate to the RELIEF-AS study underwent CMR SSFP cine imaging on two occasions consecutively after removing the patient from the table and performing a repeat isocentre. 3D models were constructed and co-registered to obtain repeat measurements of wall thickness at each vertex, Figure 5-1.

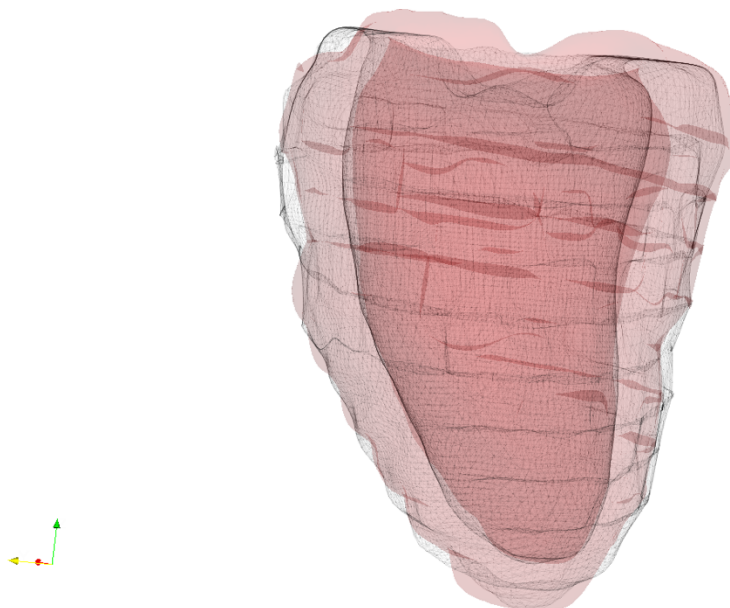


Figure 5-1 Co-registration of LV models from a CMR scan and a consecutive rescan from the same individual.

5.2.5. Statistical analysis

Data were analyzed in R (R foundation, Vienna, Austria) using RStudio Server version 0.98 (Boston, Mass, USA). All continuous variables are expressed as mean \pm SD or median(IQR) for skewed data. Normality was checked using the Shapiro-Wilk test. Categorical variables are expressed as percentages. Groups were compared using independent-samples Student's t-tests for normally distributed continuous variables or Mann-Whitney U test and the Chi-square tests for non-normally distributed and categorical variables respectively. A regression sensitivity analysis was performed using an allometric adjustment of height^{1.7} instead of BSA, which did not alter interpretation of results. Standardized beta coefficients (β) from regression models were calculated to permit comparison of strengths of association. Changes between pre-AVR and post-AVR visits were compared using paired Student's t-tests for continuous variables or using Wilcoxon signed rank tests for ordinal variables. As previously described in 3D datasets, group comparisons applied threshold-free cluster enhancement to optimize sensitivity to significant signal in "clusters" of adjacent LV vertices. P values were derived from permutation testing at each vertex after control for false discovery rate (FDR).^{76,368} To describe the changes in 3D parameters, the summary variables reported are the mean and standard deviation across the percentage area of ventricular surface that achieved statistical significance (p values are therefore not reported given that all reported comparisons and associations are $p < 0.05$ after correction for FDR).

For precision data, a sensitivity analysis was performed by calculating the sample size required to detect a 1 mm change in wall thickness. Power was 90%, $\alpha = 0.05$, and $d = 0.54$, where d is the desired clinical change (1mm) divided by the standard deviation of

scan-rescan differences. A Bonferroni correction was used to minimize type 1 error. This provides a more conservative sensitivity analysis than the use of threshold-free cluster enhancement and control of FDR used for the primary analysis.

5.3. Results

5.3.1. Accuracy and scan–rescan precision of clinician and 3D assessment

For clinician LV and right ventricular structure and function, inter-observer comparison in 15 subjects showed good reproducibility, with intra-class correlation coefficients (ICCs) between 0.88-0.98. The lowest ICC of 0.88 was for RV EF.

The ICCs between clinician and atlas analysis for structure and functional parameters were between 0.93 and 0.96, Table 5-2. Bland-Altman and correlations are in Figure 5-3.

LV metric	ICC	<i>p</i>	95 % CI
LV mass	0.96	<0.001	(0.95, 0.98)
End diastolic volume	0.95	<0.001	(0.93, 0.97)
End systolic volume	0.95	<0.001	(0.93, 0.97)
Ejection fraction	0.93	<0.001	(0.90, 0.95)

Table 5-2 Intra class correlation coefficients comparing manually and atlas analyses of left ventricular metrics ICC= intra class correlation coefficient using a two–way random model for absolute agreement.

The sensitivity analysis showed that in a 100 pair study, 54% ventricular surface is powered to detect a 1mm change in wall thickness; increasing to 88% ventricular surface with 200 pairs. The power was greatest at the mid ventricular level where co-registration was most accurate, but sufficient circumferentially, Figure 5-2. An example of a scan-rescan co-registration for one individual is above in Figure 5-1.

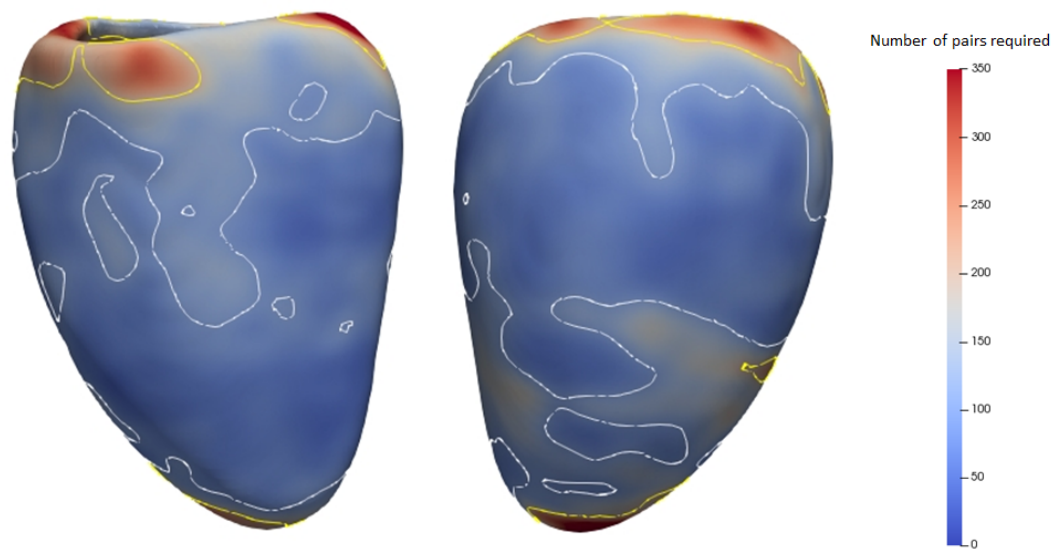


Figure 5-2 Number of pairs needed to detect a 1mm change in wall thickness.

Contours enclose ventricular surface with power to detect a 1mm change using 100 paired subjects (white contour) and 200 paired subjects (yellow contour).

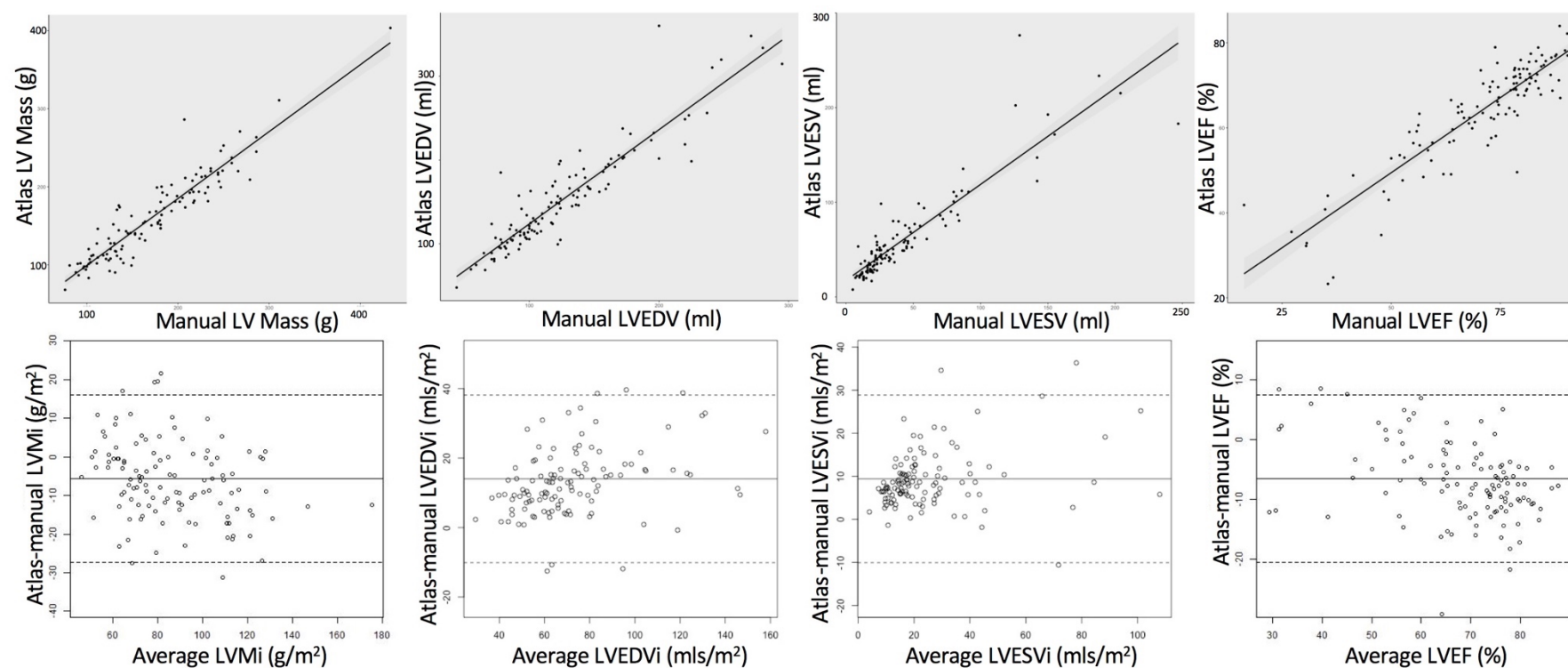


Figure 5-3 Correlations and Bland-Altman analyses of LV metrics analysed by atlas and manual techniques. There was good correlation for all metrics, and a small bias to underestimating indexed left ventricular mass (LVMi) and ejection fraction (EF), and overestimating cavity volume using the atlas based technique compared with manual measurements. *Abbreviations: EDVi = indexed end-diastolic volume; ESVi= indexed end-systolic volume.*

5.3.2. Patients

One hundred and sixteen patients (54% male) with severe, symptomatic AS were assessed at baseline. There were no sex differences in patient age or echocardiographic severity of aortic stenosis, but males had lower systolic blood pressure (129 ± 17 vs 137 ± 16 mmHg, $p=0.004$) and had greater functional capacity (6MWT: 533 ± 163 vs 399 ± 183 m, $p<0.001$). Demographic, clinical, and imaging characteristics are shown in Table 5-3.

5.3.3. Global and regional (3D) LV shape: AS versus matched controls

Patients had increased LVM compared to matched controls (161 ± 43 vs 120 ± 27 g, $p<0.001$) with similar EDV (154 ± 61 vs 155 ± 34 ml, $p=0.92$), Table 5-1. By 3D analysis, patients had significantly greater wall thickness across 83% of the ventricular surface (wall thickness averaged across the whole myocardium: 9.1 ± 2.3 vs 6.9 ± 1.3 mm). This was most pronounced in the septum, Figure 5-4, with a maximal wall thickness of 16 ± 2.5 mm in patients versus 12 ± 1.8 mm in matched controls. There was inward displacement of the septal endocardium, whilst in the lateral wall there was outward expansion of the endocardium, compared to controls. The epicardium expanded outwards globally, meaning that there was overall septal concentric hypertrophy and lateral eccentric LV hypertrophy, Figure 5-4.

	AS cohort	Males	Females	p	Matched controls
N	116	63 (54%)	53 (46%)		40
Male sex	63 (54%)				23 (58%)*
Age	70 ±9	68 ±11	71 ±8	0.13	65 ±7
BSA (m ²)	1.90 ±0.22	2.00 ±0.20	1.77 ±0.16	<0.001	1.86 ±0.20*
African Caribbean	1 1%	0 0%	1 2%		1 (3%) †
Bicuspid	33 (28%)	23 (37%)	10 (17%)	0.06	-
Hemodynamics					
SBP (mmHg)	133 ±17	129 ±17	137 ±16	0.004	126 ±17
DBP (mmHg)	76 ±10	74 ±9	77 ±12	0.17	80 ±8
Heart rate (bpm)	73 ±13	71 ±12	75 ±12	0.08	-
Comorbidities					
Hypertension (%)	75%	79%	71%	0.45	0%
Hypercholesterolemia (%)	64%	65%	64%	0.99	0%
Diabetes (%)	20%	21%	19%	0.98	0%
Coronary artery disease	29%	35%	21%	0.14	0%
Clinical status					
NYHA Functional Class	2.3 ±0.7	2.1 ±0.6	2.4 ±0.7	0.07	-
Six minute walk test (m)	472 ±184	533 ±163	399 ±183	<0.001	-
NT-proBNP (ng/L)	50 (26-173)	91 (31-286)	40 (25-105)	0.059	-
hs-TnT (pmol/L)	13 (9-20)	15 (11-24)	11 (7-16)	<0.001	-
Echocardiography					
AVA (cm ²)	0.75 ±0.26	0.77 ±0.29	0.72 ±0.22	0.24	-
AVAi (cm/m ²)	0.4 ±0.13	0.39 ±0.13	0.41 ±0.13	0.36	-
MPG (mmHg)	47.9 ±14.2	48.6 ±15.3	46.9 ±13	0.92	-
Vmax (m/s)	4.4 ±0.58	4.4 ±0.56	4.3 ±0.59	0.51	-
Mean E/E' ratio	13.2 ±5.8	12.8 ±5.8	13.8 ±5.7	0.41	-
E/A ratio	0.94 ±0.49	1.00 ±0.61	0.87 ±0.29	0.17	-
Cardiovascular magnetic resonance					
LA volume indexed (mls)	54 ±19	56 ±21	51 ±17	0.14	-
Aortic Regurgitation (%)	10 (3-29)	13.5 (4-46)	9 (2-23)	0.21	-

Table 5-3 Baseline clinical characteristics.

* no significant difference ($p > 0.05$) between matched controls and patients with aortic stenosis. † No statistical comparison between controls and patients due to low frequencies. p values are for sex differences in patients with aortic stenosis, in bold are less than 0.05. Abbreviations: AVA(i) = Aortic valve area (indexed to BSA); BSA = Body surface area; DBP = diastolic blood pressure; hs-TnT = high-sensitivity troponin T; LA = Left atrium volume indexed to BSA; NT-proBNP = N-terminal pro-brain natriuretic peptide; NYHA = New York Heart Association; MPG = mean pressure gradient; SBP = systolic blood pressure; Vmax = peak velocity through the aortic valve

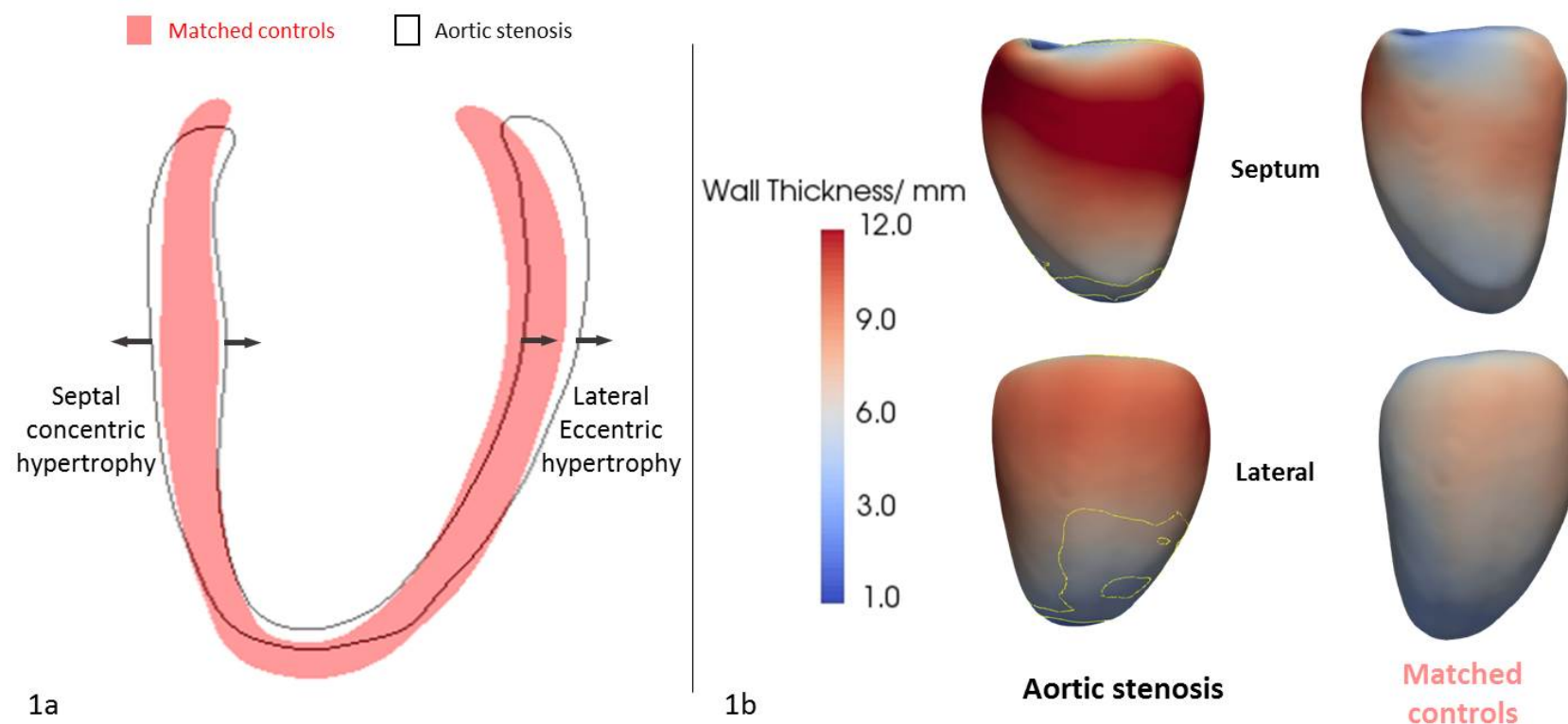


Figure 5-4 Left ventricular end-diastolic shape (1a) and wall thickness (1b) in patients with aortic stenosis versus matched controls.

1a Ventricular four chamber cross-cut showing a regional response of septal concentric and lateral eccentric hypertrophy (black contour = AS; red= matched controls).

1b Mean shape and wall thickness are represented in en-face septal (top row) and lateral (bottom row) views for patients with aortic stenosis (left) and matched controls (right). Red= thicker wall (mostly septal). Yellow contour encloses 83% of the ventricular surface with $p < 0.05$ after correction for multiple testing.

5.3.4. Sex differences in regional shape: AS versus matched controls

Males demonstrated greater outward expansion of the lateral endocardium (β 0.53, 33% ventricular surface), whilst females had greater inward displacement of the septal endocardium (β -0.77, 4% ventricular surface) compared to sex-matched controls. Both sexes demonstrated circumferential outward expansion of the epicardium (males: β 0.88, 76% ventricular surface, females: β 0.74, 33% ventricular surface). Overall this represents septal concentric hypertrophy in both males and females and lateral eccentric hypertrophy in males.

5.3.5. Sex differences in wall thickness and function in AS

Male sex was positively associated with LVM when adjusting for age, BSA, hypertension and aortic valve area (β 0.22; 95% CI: 0.05, 0.38), Table 5-4 and Table 5-5. By 3D analysis, male sex was positively associated with wall thickness across 56% of the ventricular surface - most pronounced in the septum, Figure 5-5. Males had lower FWT both in the septum and lateral walls when compared to females (58 ± 20 versus $77 \pm 23\%$, 18% ventricular surface).

Outcome:	Univariate			Multivariate		
LV mass	Beta	95% CI	p	Beta	95% CI	p
Dependent:						
Age	-0.25	-0.44, -0.08	0.005	-0.22	-0.37, -0.07	0.004
Male gender	0.54	0.39, 0.70	<0.001	0.22	0.05, 0.38	0.01
BSA*	0.63	0.49, 0.78	<0.001	0.47	0.30, 0.64	<0.001
AVA	0.12	-0.07, 0.31	0.2	-0.03	-0.16, 0.11	0.71
Hypertension	0.13	-0.04, 0.32	0.14	0.14	-0.00, 0.29	0.06
Adjusted R ²				0.48		

Table 5-4 Linear regression model showing the association of gender with LV mass and age, body surface area (BSA), aortic valve area (AVA) and a diagnosis hypertension.

Beta are standardized coefficients. * Repeating analysis with height^{1.7} demonstrated similar association patterns.

Baseline characteristics	Total cohort		Males		Females		p
LVM (g)	161.3	±55.1	188.6	±51.0	128.9	±40.6	<0.001
LVMi (g/m ²)	84.1	±23.5	93.8	±22.0	73.2	±21.5	<0.001
LVM/height ^{1.7} (g/m ^{1.7})	67.9	±19.9	75.0	±19.2	59.4	±17.4	<0.001
LVEDV (ml)	153.7	±61.2	177.6	±59.2	125.2	±50.8	<0.001
LVEDVi (ml/m ²)	80.3	±28.4	88.5	±27.6	70.5	±26.4	<0.001
LVESV (ml)	60.7	±47.3	73.9	±47.0	45.0	±43.1	<0.001
LVESVi (ml/m ²)	31.5	±23.4	36.7	±22.6	25.2	±23.0	<0.001
LVEF (%)	63.9	±12.2	60.9	±12.1	67.5	±11.5	<0.001
MVR	1.44	±0.37	1.50	±0.42	1.33	±0.29	0.02
ECV (%)	28.2	±2.9	28.6	±3.2	27.6	±2.4	0.08
Matrix volume (g/m ²)	25.3	±9.0	29.1	±8.7	20.5	±6.8	<0.001
Cell volume (g/m ²)	64.4	±17.6	73.0	±16.7	54.6	±12.8	<0.001

Table 5-5 Global left ventricular (LV) metrics at baseline, stratified by gender.

Abbreviations: ECV = extracellular volume fraction; EDV = end diastolic volume; EF = ejection fraction; ECV = extracellular volume fraction; ESV = end systolic volume; LVM= Left ventricular mass; LVMi = LVM indexed to body surface area; MVR = mass to volume ratio; SV = stroke volume. Data presented are global measures calculated from atlas-based segmentation.

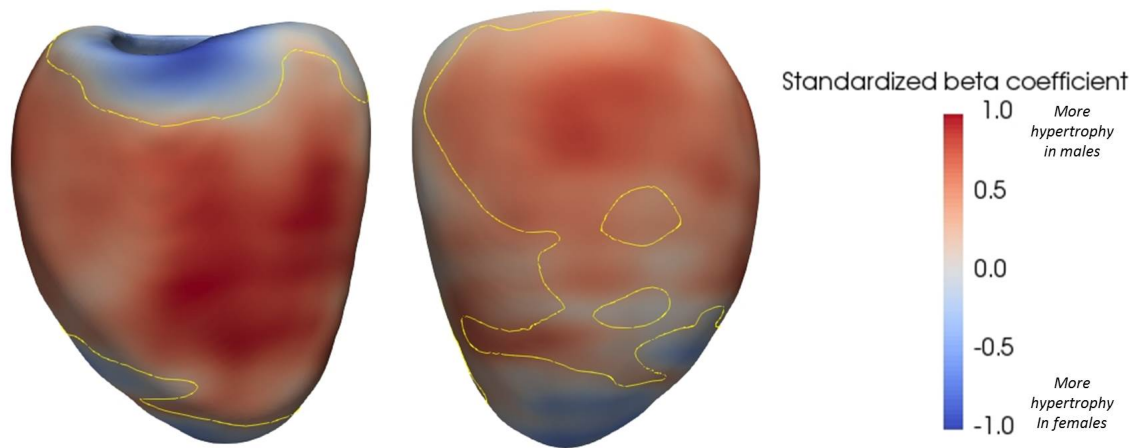


Figure 5-5 Sex difference in regional wall thickness in patients with aortic stenosis, septal (left) and lateral (right) en-face views.

More positive standardized beta coefficients (red) demonstrate a more extensive remodelling response in males compared to females in the septum (β 0.55, 56% ventricular surface). Yellow contour encloses 56% of the ventricular surface (positive beta coefficients, red region), $p < 0.05$. Models adjusted for covariates.

5.3.6. Sex differences in reverse remodelling and clinical measures one year post-AVR

One year post-AVR, LVMi was lower ($-12.2 \pm 16 \text{ g/m}^2$, $p < 0.001$, Table 5-6 and Figure 5-6) with a significant reduction in wall thickness across 77% of the ventricular surface by 3D analysis (average over this region: $-1.0 \pm 0.6 \text{ mm}$, most pronounced in the septum). Males had similar percentage LVM reduction to females (-15.4 ± 13.8 vs $-9.6 \pm 18.2\%$, $p = 0.07$), but a greater reduction in 3D percentage wall thickness (-13 ± 3.6 vs $-6 \pm 1.9\%$, 8% ventricular surface), with significant differences between sexes confined to the septum, Figure 5-7. In the septum, males increased contractility, and females showed a reduction from more hyperdynamic contractility (FWT: $+10 \pm 5$ vs $-4 \pm 10\%$ respectively, 11% of the ventricular surface), with no sex differences at follow-up (FWT males: $68 \pm 59\%$, females: $70 \pm 44\%$, $p = 0.47$).

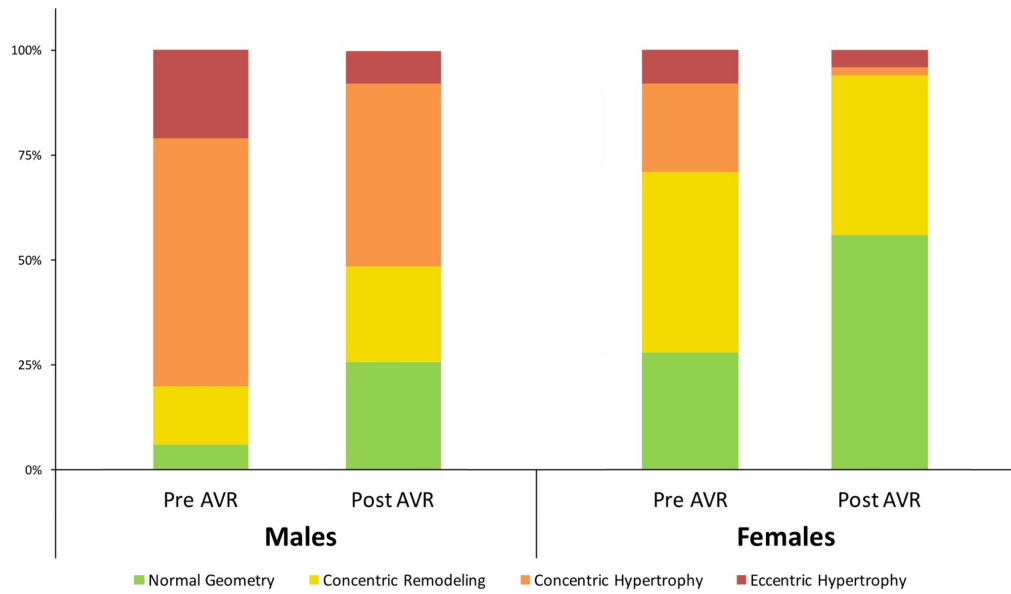


Figure 5-6 Changes in remodelling categories at one year after aortic valve replacement (AVR), stratified by sex.

All male versus female comparisons both before and post-AVR are statistically significant, $p < 0.05$.

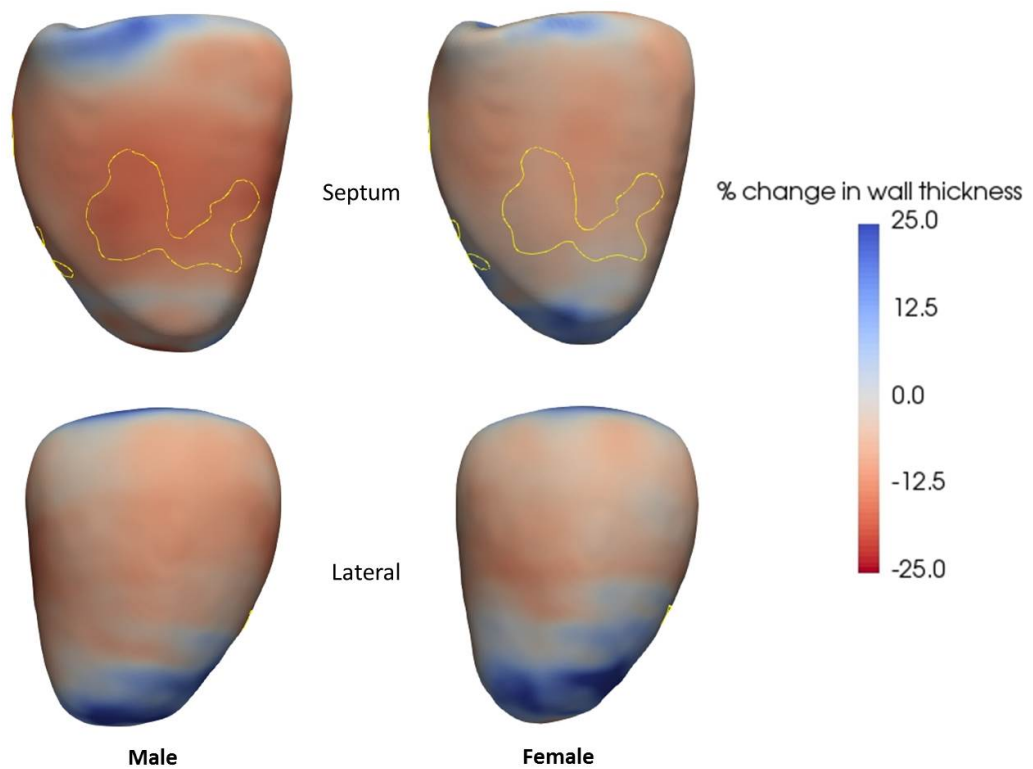


Figure 5-7 Percentage change in wall thickness at one year after aortic valve replacement in males (left) and females (right). The greatest percentage regression in wall thickness is in the mid septum for both sexes and it is more pronounced in males. Yellow contour encloses 8% of the ventricular surface with statistically significant greater wall thickness regression in males than females, $p < 0.05$.

Changes in global LV metrics one year after aortic valve replacement									
	Total AS cohort		<i>p</i>	Males		<i>p</i>	Females		<i>p</i> (sex difference)
LVM (g)	-24.0	±31.9	<0.001	-31.8	±34.6	<0.001	-14.7	±25.7	<0.001 0.003
LVMi (g/m ²)	-12.2	±16.0	<0.001	-15.7	±16.2	<0.001	-8.1	±14.9	<0.001 0.01
% LVM	-12.7	±16.2		-15.4	±13.8		-9.6	±18.2	0.07
LVEDV (ml)	-12.9	±37.4	<0.001	-19.3	±41.0	0.001	-5.3	±31.2	0.22 0.04
LVEDVi (ml/m ²)	-6.2	±19.1	<0.001	-9.4	±19.2	<0.001	-2.4	±18.3	0.39 0.05
% LVEDV	-4.1	±21.6		-7.6	±18.5		0.2	±24.2	0.06
LVESV (ml)	-9.9	±29.6	<0.001	-15.0	±34.9	0.001	-3.8	±20.3	0.38 0.04
LVESVi (ml/m ²)	-4.9	±14.9	<0.001	-7.2	±16.5	0.002	-2.0	±12.2	0.25 0.06
% LVESV	-3.1	±39.6		-8.8	±36.2		3.7	±42.7	0.10
LVEF (%)	2.0	±10.0	0.03	3.2	±11.2	0.03	0.7	±8.4	0.37 0.17
MVR	-0.22	(-0.4,-0.05)	<0.001	-0.22	(-0.4,-0.04)	<0.001	-0.21	(-0.3,-0.07)	<0.001 0.90
ECV (%)	1.4	(-0.5,3.1)	<0.001	1.5	(-0.5,3.3)	0.002	1.1	(-0.7,3.0)	0.003 0.34
% ECV	4.8	(-1.9,11.9)		5.5	(-1.9,12.5)		4.1	(-2.6,11.1)	0.41
Matrix volume (g/m ²)	-3.3	(-0.6,-6.1)	<0.001	-4.0	(-1.5,-7.5)	<0.001	-1.9	(0.2,-4.8)	<0.001 0.04
% Matrix volume	-15.5	(-4.8,-24.3)		-16.6	(-6.6,-24.5)		-14.4	(-3.3,-23.9)	0.41
Cell volume (g/m ²)	-11.9	(-7.2,-19.2)	<0.001	-14.9	(-9.8,-22.2)	<0.001	-10.0	(-5.5,-15.1)	<0.001 0.001
% Cell volume	-19.8	(-13,-26.8)		-20.8	(-14,-29.6)		-18.6	(-12,-24.8)	0.12

Table 5-6 Changes in global left ventricular metrics one year after aortic valve replacement, stratified by sex. Changes in CMR parameters derived from atlas analysis, represented as mean±standard deviation or median (IQR). Abbreviations: ECV = extracellular volume fraction; EDV = end-diastolic volume; EF = ejection fraction; ESV = end-systolic volume; LVM(i)= Left ventricular mass (indexed to body surface area); MVR = mass to volume ratio; SV = stroke volume.

One year post-AVR, NT-proBNP reduced only in males ($-37[-88,-2]$ vs $-1[-24,11]$ ng/L, $p=0.008$), with no sex differences at follow-up ($38[17-130]$ vs $38[26-79]$ ng/L, $p=0.96$).

Males also had a greater increase than females in systolic blood pressure (SBP) (12.9 ± 23 vs 2.1 ± 17 mmHg respectively, $p=0.009$) and diastolic blood pressure (DBP) (5 ± 14 vs -1 ± 14 mmHg respectively, $p=0.04$) post-AVR, with no sex differences at follow-up (SBP: 140 ± 16 vs 139 ± 19 mmHg, $p=0.69$; DBP: 79 ± 11 vs 76 ± 11 mmHg, $p=0.12$). Changes in clinical measures are summarized in Table 5-7.

In men, percentage change in 3D septal wall thickness correlated more strongly than global LVM with the change in hs-TnT (β 0.37, $p=0.006$ versus 0.3, $p=0.03$ respectively). Conversely, percentage change in LVM correlated more strongly than percentage change in 3D septal wall thickness with the change in NT-proBNP (β 0.32, $p=0.02$ versus 0.23, $p=0.08$ respectively). There was no correlation in females, with only 4 (8%) having elevated NT-proBNP at baseline. For either sex, there was no correlation with the change in NYHA class, 6MWT or SBP.

Outcome	Change in outcome one year after aortic valve replacement			<i>P</i> sex difference
	Total Cohort	Male	Female	
<i>n</i>	114	62 (54%)	52 (46%)	
Hemodynamics				
SBP	7.9±21***	12.9±23***	2.1±17	0.009
DBP	2.2±14	5±14**	-1±14	0.04
Heart rate	-4±11***	-3±11*	-5±11***	0.35
Clinical status				
NYHA	-0.8±0.77***	-0.7±0.79***	-0.9±0.75***	0.18
Six minute walk test (m) †	90 (0, 165)***	75 (0,144)***	90 (20,430)***	0.16
NT-proBNP (ng/L)	-14 (-67, 9)***	-37 (-88,-2)***	-1 (-24,11)	0.008
hs-TnT (pmol/L)	-1 (-4,1)**	-2 (-7,1)	-1 (-2,1)	0.27
Echocardiography				
AVA (cm ²)	0.8±0.56***	1±0.55***	0.6±0.51***	<0.001
AVAi (cm/m ²)	0.44±0.29***	0.5±0.27***	0.4±0.30***	0.013
MPG (mmHg)	-35±15.5***	-37±16.0***	-33±14.8***	0.19
Vmax (m/s)	-1.9±0.78***	-2.1±0.72***	-1.8±0.82***	0.55
Mean E/e' ratio	-1.1 (-5.2,1.9)**	-1.1 (-5.3,2.0)*	-1.6 (-5.1,1.7)	0.87
E/A ratio	-0.06 (-0.3,0.2)	-0.06 (-0.3,0.2)	-0.04 (-0.3,0.2)	0.17
CMR				
LA volume (mls)	-6 (-22,12)	-13 (-22,15)	-3 (-25,2)	0.67
Aortic regurgitation (%)	-7.5 (-21,0.01)***	-7.8(-30,0.2)***	-3.8 (-19,-0.4)**	0.47

Table 5-7 Changes (post – pre) in clinical characteristics one year after aortic valve replacement.

Paired comparison vs baseline, represented as mean±standard deviation or median (IQR): * p< 0.05; **p <0.01; *** p<0.001 † n = 85. Abbreviations as per Table 5-3.

5.3.7. Wall thickness in patients with severe AS and normal geometry versus matched controls

There were 19 patients with normal LVM and geometry at baseline (n=19, 79% female, mass:end-diastolic volume<1.15). Echocardiographic severity of AS was similar to patients with abnormal LV geometry, but NT-proBNP was lower and hypertension less frequent, Table 5-8.

Although global measures of LVM were fairly similar in this group to matched controls (122 ± 27 vs 107 ± 22 g, $p=0.11$), Table 5-1, by 3D analysis patients had greater inferior and septal wall thickness (8.8 ± 1.6 vs 6.6 ± 1.2 mm, 46% ventricular surface), Figure 5-8.

One year post-AVR, these patients had some equivocal evidence of a reduction in LVMi (-5 ± 11 g/m², $p=0.054$) and no convincing evidence of a change in LVEDVi (-0.5 ± 15 mls/m², $p=0.59$). 3D analysis however revealed a reduction in wall thickness in the inferior and septal walls (-1.6 ± 0.3 mm, 0.8% ventricular surface) that remained hypertrophied compared to matched controls (7.8 ± 1.9 vs 6.5 ± 1.4 mm, 29% ventricular surface).

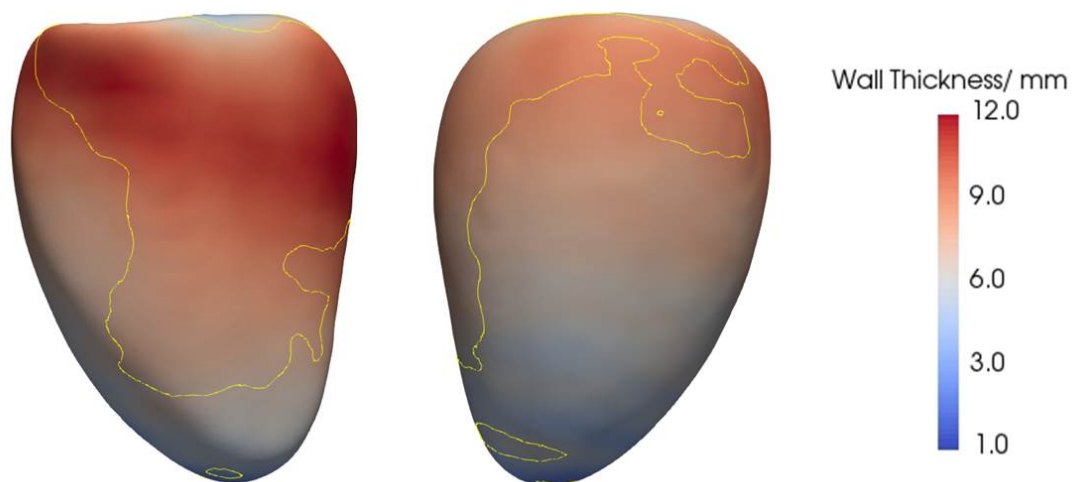


Figure 5-8 Left ventricular wall thickness in patients with aortic stenosis and normal baseline geometry, septal (left) and lateral (right) en-face views.

There is relative inferior and septal hypertrophy compared to controls (red= thicker wall). Yellow contour encloses 46% of the ventricular surface, $p<0.05$.

Baseline characteristics stratified by LV geometry					
	Normal Geometry		Abnormal Geometry		p
n	19	16%	97	84%	
Age	71	±9.8	69	±9.7	0.37
Bicuspid	1	5%	32	33%	-
BSA (m ²)	1.79	±0.19	1.92	±0.22	0.02
Hemodynamics					
SBP	135	±14.5	132	±17.5	0.39
DBP	78	±9.6	75	±10.6	0.35
Heart rate (bpm)	71	±9	73	±13	0.32
Comorbidities					
Hypertension (%)	53%		79%		0.048
Hypercholesterolemia	71%		63%		0.04
Diabetes (%)	18%		21%		0.44
Coronary Artery Disease	18%		31%		0.19
Clinical status					
NYHA Functional Class	2.4	±0.5	2.2	±0.7	0.35
Six minute walk test (m)	439	±170	478	±187	0.44
NT-proBNP (ng/L)	39	(26-66)	69	(24-199)	0.03
Echocardiography					
AVA (cm ²)	0.72	±0.17	0.75	±0.27	0.6
AVAi (cm/m ²)	0.41	±0.09	0.393	±0.14	0.58
MPG (mmHg)	45	±10.7	48	±14.6	0.22
Vmax (m/s)	3.9	±0.51	4.3	±0.59	0.57
Cardiovascular magnetic resonance					
Aortic Regurgitation (%)	5.19	(1-12)	12	(4-32)	0.28

Table 5-8 Baseline characteristics split by LV remodelling category.

Abbreviations: AVA(i)= Aortic valve area (indexed to BSA); DBP = diastolic blood pressure; NT-proBNP = N-terminal pro-brain natriuretic peptide; MPG = mean pressure gradient; NYHA = New York Heart Association; SBP = systolic blood pressure; Vmax= peak velocity through the aortic valve.

5.4. Discussion

This study shows that in patients with severe symptomatic AS the septum is the most adaptive myocardium compared to other regions - it hypertrophies to a greater extent and regresses the most one year post-AVR. Men had twice the percentage wall thickness regression in this region than women, correlating with improvements in serum biomarkers, suggesting functionally significant, sex-specific responses to aortic stenosis and its correction. Even in patients without overt LVH by global parameters, inferior and septal hypertrophy was present compared to controls. Whilst males did not recover normal LV geometry by conventional measures following AVR as often as females, even females with normal geometry at baseline showed wall thickness regression, but not normalization, post-AVR. The 3D machine learning approach highlights regional reverse remodelling and sex differences in patients with AS that are not detectable using global measures. These findings show that cardiac remodelling is an asymmetric continuous spectrum challenging conventional categorization. Because 3D machine learning provides a more sensitive measure of LV remodelling, this may permit enhanced risk stratification in patients with AS.

5.4.1. Asymmetric remodelling in aortic stenosis

3D machine learning enables co-registration, shape changes and unbiased whole-heart coverage that are not possible with conventional wall thickness analysis. Our findings are consistent with previous data showing that asymmetric septal hypertrophy is a common structural variant in 22-27% of patients with AS.³¹ In addition we demonstrate that there is a septal preponderance to remodelling across all patients with severe AS, rather than a characteristic specific to predisposed patients.^{31,297} 3D analysis also shows that patients with normal conventional global measures of LVM and volume display

relative inferior and septal hypertrophy compared to matched controls. This may represent a region of early adaptation to pressure overload providing functional advantages.

5.4.2. Regional sex differences before and after AVR

We observed the greatest sex difference in hypertrophy in the basal to mid septum, independent of other drivers of asymmetric remodelling, including hypertension and AS severity. The regions are similar to where Dobson et al. found males had more focal fibrosis, measured regionally using late gadolinium enhancement.³¹⁴ This suggests males have greater hypertrophy and matched fibrosis in response to AS, highlighting the complex regional interplay of these processes. The association between change in hs-TnT and change in septal wall thickness was stronger than with the change in global LVM, potentially related to regional variations in wall stress. Recently we have shown that fibrosis is also plastic, and a regional comparison of fibrosis regression between sexes may also contribute to our understanding of remodelling post-AVR.³¹⁵

We previously described that CMR detects more concentric remodelling in women compared to echocardiography.²⁹⁷ We build on this by using a more detailed phenotype to show that the female concentric remodelling response is predominantly septal, and the eccentric hypertrophy observed in males is predominantly lateral.

We additionally observed small but significant sex differences in percentage wall thickness regression in the septum. Greater relative regression of hypertrophy in males has not been previously reported, but greater absolute LVM regression was observed in one other CMR study.³¹⁴

5.4.3. Greater sensitivity to AS remodelling using machine learning

imaging biomarkers

Current decision-making regarding intervention in AS includes an assessment of myocardial structure and function, however this relies on waiting for a reduction in global EF – an insensitive and late marker of myocardial remodelling. These data show that a 3D atlas-based approach for assessment of remodelling provides visually and clinically intuitive insights into the complex changes in response to AS over time. These data support the notion that there are sex-specific biological pathways that may require separate intervention thresholds.^{314,394} Importantly, this was only detectable using a 3D machine learning approach, as were myocardial changes in patients classified with overall normal geometry by reference standard global measures. Because 3D approaches are able to maximize information from a dataset, these may offer scope to identify additional biomechanical risk components, moving closer to more personalized decision-making. The 3D approach used in this study showed sufficient precision to detect changes circumferentially. This suggests that the septal predominance in myocardial plasticity is not due to more imprecise segmentation in the lateral wall. The sensitivity analysis demonstrating this is a conservative approach, because it employs a Bonferroni approach rather than TFCE.

5.4.4. Sex differences: what constitutes adaptive remodelling?

The LV remodelling phenotype described in males is associated with a depressed contractile state, higher levels of NT-proBNP and lower blood pressure, which may indicate a maladaptive response. Consistent with this, we have previously reported that males have more focal fibrosis.²⁹⁷ Following AVR however there appears to be greater septal reverse remodelling in males, an improvement in contractility, with a greater

reduction in NT-proBNP, and increases in blood pressure. Both inappropriately high LVM in response to AS, and the extent of reverse remodelling response post-AVR, particularly in women, have been associated with worse prognosis.^{291,307,400} The observation of greater myocardial plasticity in males therefore supports a less favourable remodelling response to AS but one which is more modifiable with AVR. Conversely, remodelling in women, whilst less pronounced, is less likely to be reversed with AVR. This suggests that rather than a transition from concentric remodelling to a decompensated eccentric hypertrophic phenotype, there are different biological pathways between sexes.³⁹⁵

5.4.5. Mechanisms of sex differences in reverse remodelling

Greater hypertrophy, interstitial and focal fibrosis in males with AS^{290,297,401} may be attributed to a different cardio-metabolic environment modulated by deregulation of muscle contraction genes,⁴⁰² less favourable cardiac metabolism,⁴⁰¹ background atherosclerosis, and the effect of sex hormones, itself modulated by ACE I/D polymorphism.²⁹⁸ Given the females in our cohort were post-menopause, androgens may have a more important effect than oestrogen. Testosterone is considered to have deleterious effects on cardiac remodelling resulting in excessive hypertrophy and increased fibrosis.^{297,401} We however describe greater, potentially beneficial, ventricular plasticity in men than women post-AVR. This suggests that remodelling in men may be a more adaptive response to a more unfavourable cardio-metabolic environment. There are several genetic, animal and cell culture models that describe such beneficial hypertrophy to pressure overload,⁴⁰³ and whilst testosterone promotes LV hypertrophy⁴⁰⁴ it exerts a protective effect against apoptosis and necrosis.⁴⁰⁵ Consistent

with this, it has been reported that men are less likely to develop symptoms in AS but display a greater remodelling response.^{396,406}

Differences in remodelling post-AVR have also been explained by aortic regurgitation,³¹⁴ patient prosthesis mismatch, and ACE I/D polymorphism. In our cohort, aortic regurgitation was similar between sexes and both mean and peak forward pressure gradients at baseline and follow-up were similar. There was a greater increase in indexed effective orifice area at follow-up in men, however area change is not linearly associated with LVM regression, and significant hemodynamic relief resulted in improved pressure gradients at follow-up in both sexes.

5.4.6. Why do we observe regional shape differences in aortic stenosis?

In all patients with AS compared to matched controls, concentric septal hypertrophy and eccentric lateral hypertrophy were noted, contributing to visually greater sphericity. Greater sphericity may increase wall stress and has been associated with mortality after myocardial infarction. Asymmetric septal hypertrophy has been observed for over forty years yet adequate explanations have still not been provided. In part this is because historically it has been difficult to quantify regional geometry accurately. Advanced 3D phenotyping of CMR data has shown that the septum appears to be particularly plastic in response to obesity and SBP.^{194,407} The regional pattern of remodelling of concentric septal hypertrophy and eccentric lateral dilatation in AS has also been observed in response to pressure overload associated with rising SBP.¹⁹⁴ Sex differences in regional remodelling have also been observed in association with increased body fat, with women demonstrating more lateral eccentric hypertrophy.⁴⁰⁷ This suggests either that the mechanical influences on LV remodelling are more complex than envisaged, or that there are non-mechanical mechanisms which modulate the myocardial response to

mechanical load.⁴⁰⁸ This work supports that of Becker in 1982 who noted that “the part of the septum underneath the aortic valve shows a very different fibre orientation”,⁵¹ namely a greater proportion of mid-wall circumferential fibres may contribute to a greater mechanical transduction of LV pressure, compounded by late electrical activation (which itself may be exaggerated in conduction disease present in AS). Adequate myocardial perfusion may also be necessary for hypertrophy,⁴⁰⁹ and this also appears to show regional differences in AS and changes differentially in association with LV regression post-AVR.⁴¹⁰

5.4.7. Study limitations

The differences we observed are in patients with severe symptomatic aortic stenosis and so do not reflect mild or moderate AS, where females have been noted to demonstrate greater plasticity.²⁹⁰ Given that all patients recruited had severe AS and were awaiting AVR, further work validating the prognostic power of this approach will require expanding the population to include mild or moderate AS and incorporating motion analysis. Genetic, downstream metabolic variants, and medication were not accounted for and may contribute to the differences. Whilst aortic regurgitation was similar between sexes, aortic root morphology is different between sexes and subsequent variation in regurgitant flow pattern and direction may influence septal remodelling. Controls were healthy volunteers free of cardiovascular disease and prescription medication which may introduce bias. Whilst our approach is adequately powered,⁷⁶ short axis stack cine imaging requires base to apical smoothing to represent 3D geometry. We did not look at the association of 3D LV remodelling and clinical outcomes because permutation testing was limited to 3D LV metrics as the dependent variable.

5.5. Conclusion

In severe symptomatic AS, the septum is the most adaptive myocardium with greatest hypertrophy and regression one year post-AVR, even when global LV mass is normal. LV remodelling is greater in males than females and tracks clinical parameters, suggesting sex-specific responses to AVR. Changes are only detectable using a 3D phenotyping approach with machine learning, and may offer a more sensitive risk assessment in severe AS.

6. Feasibility and validation of aortic wave intensity analysis

This chapter is based on the following manuscript:

Non-invasive assessment of ventriculo-arterial coupling using aortic wave intensity analysis combining central blood pressure and phase-contrast cardiovascular magnetic resonance. Bhuvu AN, D'Silva A, Torlasco C, Nadarajan N, Jones S, Boubertakh R, Van Zalen J, Scully P, Knott K, Benedetti G, Augusto JB, Rachel Bastiaenen, Lloyd G, Sharma S, Moon JC, Parker KH, Manisty CH, Hughes AD

Eur Heart J Cardiovasc Imaging. 2019 Sep 9. doi: 10.1093/ehjci/jez227. [Epub ahead of print]

Hypothesis:

Estimation of local wave speed and wave intensities can be performed in the aorta non-invasively combining CMR velocity and BP data, and these measures can be used to determine influences on healthy ventriculo-arterial coupling.

Contribution:

I performed the CMR acquisition in all subjects. I processed pressure and velocity waveform signals for analysis. Professor Alun Hughes provided Matlab scripts for individual alignment of waveforms and calculation of wave intensity from pressure and velocity derivatives. For the scale of this analysis, I automated steps of this process. I also wrote scripts to quantify wave intensity peaks, timings and energies automatically, including artefact identification. I manually aligned all waveforms and measured wave speed from pressure-velocity loops. I performed all statistical analysis.

6.1. Introduction

An integrated assessment of the cardiovascular system is clinically and mechanistically important, yet ventricular and arterial function are often considered in isolation. Wave intensity analysis (WIA) is a technique that characterizes flow generated by the heart and the afterload imposed by the vasculature in terms of wave propagation.^{411,412} It also calculates wave reflection and wave speed which predict coronary and cardiac events, independently of conventional cardiovascular risk factors.^{215,227,263,280,413,414} The relationship of local wave speed and the reference standard of regional pulse wave velocity measured from transit time (PWV_{tt}) has not been established. Aortic wave reflection can provide insight into energy transfer between the left ventricle and the aorta, and therefore may provide a useful measure of ventriculo-arterial coupling in health and disease.⁴¹⁵

Traditionally, WIA has been derived invasively using simultaneous catheter measures of pressure and flow or velocity.⁴¹⁶ It has offered insights into a range of diseases but because of feasibility, understanding of healthy ageing and sex differences in the aorta has been limited.^{256,275,282,283} Phase-contrast cardiovascular magnetic resonance imaging (CMR) allows non-invasive assessment of aortic flow, and CMR is the gold-standard for anatomically standardized cross-sectional measurements. CMR distensibility has successfully been used as a central pressure surrogate to perform WIA, but the method does not provide a direct measure of wave energy and can be technically challenging.^{275,284} Cuff based devices simplify the acquisition of central blood pressure waveform data and show good agreement with invasive measures.²⁵³

The aims of this study were (1) to use non-invasive measures of the central blood pressure (cBP) and velocity waveforms to perform wave intensity analysis, (2) to compare measures of local wave speed with a reference of conventionally calculated

PWV_{tt}, and (3) to evaluate associations between aortic WIA and age and sex in healthy individuals.

6.2. Methods

6.2.1. Study population

237 healthy participants were recruited from the pre-training assessment of the Marathon Study. This is an observational study recruiting healthy volunteers to investigate the effects of first-time marathon training on cardiovascular function, as detailed in Methods-3.4.³⁶⁰ Acquisition of data for WIA did not add extra time to the standard tests performed. Inclusion criteria were: age over 18 years, no past significant medical history, no previous marathon-running experience, and current participation in running for <2 hours per week. All procedures were in accordance with the principles of the Helsinki declaration, all participants gave written informed consent and the study was approved by the London Queen Square National Research Ethics Service Committee (15/LO/0086).

At baseline, a total of 211 participants underwent paired phase-contrast CMR and central blood pressure waveform recording, and so were included in this analysis. Five participants were excluded due to noisy blood pressure profiles, leaving a total 206 participants for this analysis.

6.2.2. Central blood pressure and heart rate estimation

As detailed in Chapter 3, supra-systolic oscillometric brachial blood pressure was measured over ten seconds with a sampling frequency of 200Hz in duplicate after a period of rest in the semi-supine position. (Cardioscope II BP+, Uscom Ltd, Sydney, Australia). A single ensemble averaged central pressure estimate (P) was derived from the second ten-second measurement of the brachial supra-systolic arterial waveform, as

previously described.²⁵¹ Heart rate (HR) was taken as the average of the HR during the recording.

6.2.3. CMR acquisition and analysis

After BP acquisition, CMR was performed at 1.5T (Magnetom Aera, Siemens AG Healthcare, Erlangen, Germany), Methods-3.5. Participants were supine for approximately half an hour of scanning before the sequence acquisitions used for this analysis. Single-shot ECG-gated white blood sagittal aortic (“candy cane”) views were acquired first, to allow 3D aortic arch length measurement and standardized cross-sectional imaging. This was used to pilot axial aortic blood flow-velocity maps at the level of the pulmonary artery bifurcation. The spoiled gradient echo phase-contrast sequence used was free-breathing, ECG-gated and segmented, Methods-3.5. Images were analyzed using validated software to obtain velocity-time profiles for the ascending and descending aorta, Methods-3.9 (ArtFun, University Pierre Marie Curie–INSERM).^{375,376} Visual Abstract 3 provides a flow chart of data acquisition and analysis.

6.2.4. Pulse wave velocity calculation using transit time (PWV_{tt})

Aortic arch PWV was calculated from the 3D distance between the ascending and descending aortic locations of the phase-contrast imaging and the transit time between velocity profiles, Equation 3-2.

Distance travelled was measured in a 3D coordinate system combining the sagittal and axial imaging using at least 14 markers placed in the centreline of the aorta. The transit time was calculated using the least squares estimate between the systolic upslopes, which has shown to be most accurate and reproducible.^{264,378} Reproducibility of aortic stiffness measures are described in the Methods-3.9.1.

6.2.5. Interpolation and alignment of pressure and velocity waveforms

It is necessary to combine ascending aortic velocity-time profiles (U) with BP waveforms for WIA, Figure 6-4. First, the central pressure waveform (P) was linearly interpolated to the same sample frequency as the ascending aorta velocity data (U) (R foundation, Vienna, Austria). Both cubic and linear spline interpolations were tested. A cubic spline was felt to give a slightly better visual interpolation, and so this was used for all pressure waveforms.

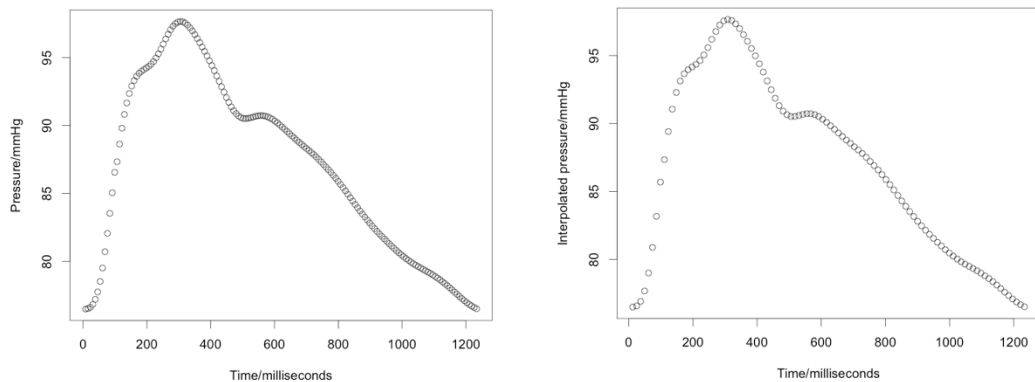


Figure 6-1 Original ensemble-averaged (left) and cubic spline interpolated (right) waveforms to one hundred samples over the R-R interval.

Pressure and velocity waveforms were then aligned manually. Alignment of physiological signals was performed using custom written software in Matlab R2016a provided by Professor Alun Hughes (The MathWorks, Inc., Natick, Mass, USA). Accurate alignment is important because it has subsequent impact on measurement of wave speed (c) and WIA and results in artefact, Figure 6-2.

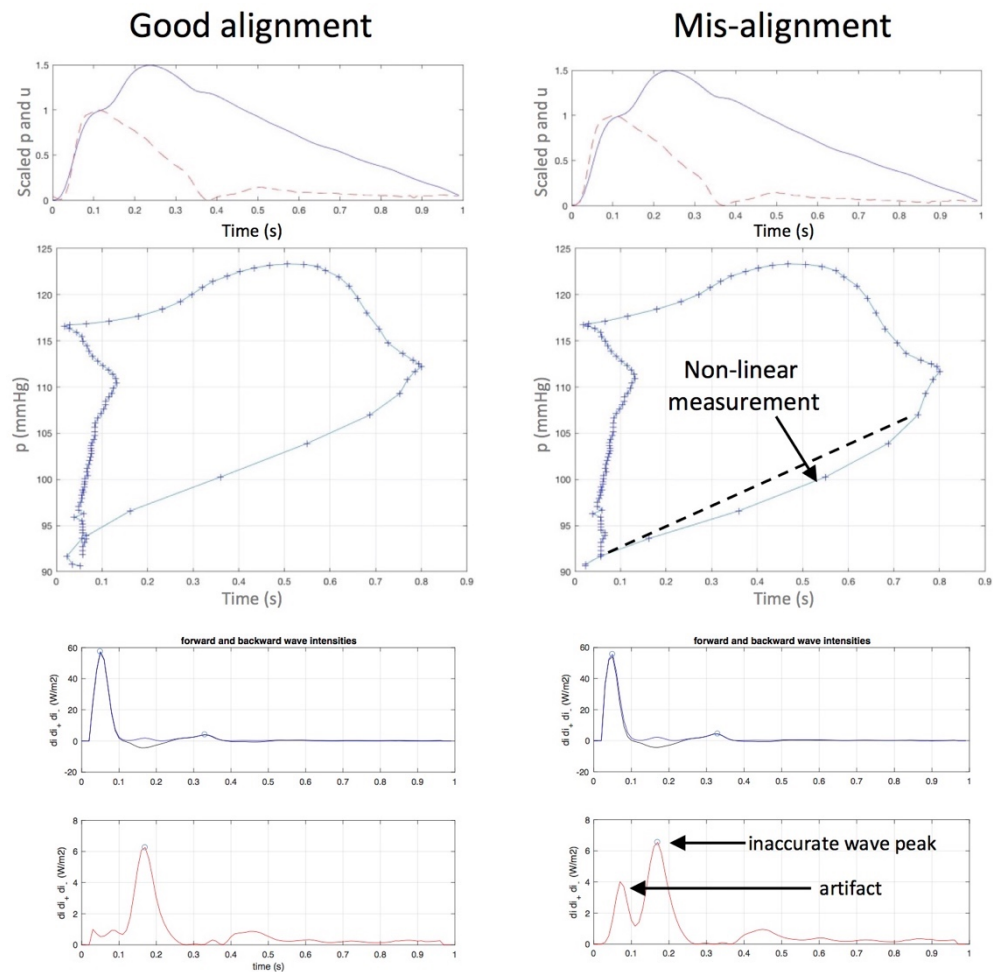


Figure 6-2 Waveform alignment. Slight waveform mis-alignment (right column, top row) leads to subsequent inaccuracies in wave speed (middle row) and wave reflection (bottom row).

For reference, data from the same individual with good alignment in early systole is provided on the left. The time lag results in a non-linear pressure-velocity loop measurement (middle row), making estimation of wave speed inaccurate. Artefact is also introduced in early systole that can be mistaken for a wave reflection peak. There is also a ~10% inaccuracy in backward wave intensity (red waveform), even with only slight mis-alignment error in this example. *Abbreviations: p = pressure; u = velocity.*

Waveforms were therefore aligned at early systole, rather than at the wave foot to avoid these errors. This is because it corresponds to where the PU loop is subsequently measured. It is still however possible for some residual time lag to remain, which should be accounted for in analysis of both c and WIA, as explained below.

6.2.6. Local wave speed estimation

Based on the conservation of mass and momentum, wave speed, c , is a function of the change in pressure and velocity described by the water-hammer equation, Equation 6-

1.²⁶⁹

$$dP_{\pm} = \pm \rho c dU_{\pm}$$

Equation 6-1 Water-hammer equation.

+ refers to waves moving away from the heart, – to waves moving towards the heart, and ρ is the density of blood (1050kg/m³).

It is assumed that reflected waves are absent in early systole. After waveform alignment, c was therefore estimated as the gradient of the PU-loop at this time,

Equation 6-2.

$$c = \frac{1}{\rho} \frac{dP}{dU}$$

Equation 6-2 Wave speed using the pressure velocity loop

Measurements were made by fitting a straight line to the part of the PU-loop that corresponds to early systole using a graphical interface operated by a computer mouse, Figure 6-3. As described by experiments performed by Khir et al., in instances of time lag that cannot be corrected by manual alignment, the PU-loop shows convex or concave deviation.²⁶⁹ In these cases, a linear gradient was estimated after visually correcting for the deviation. This was necessary in only a small proportion of total cases.

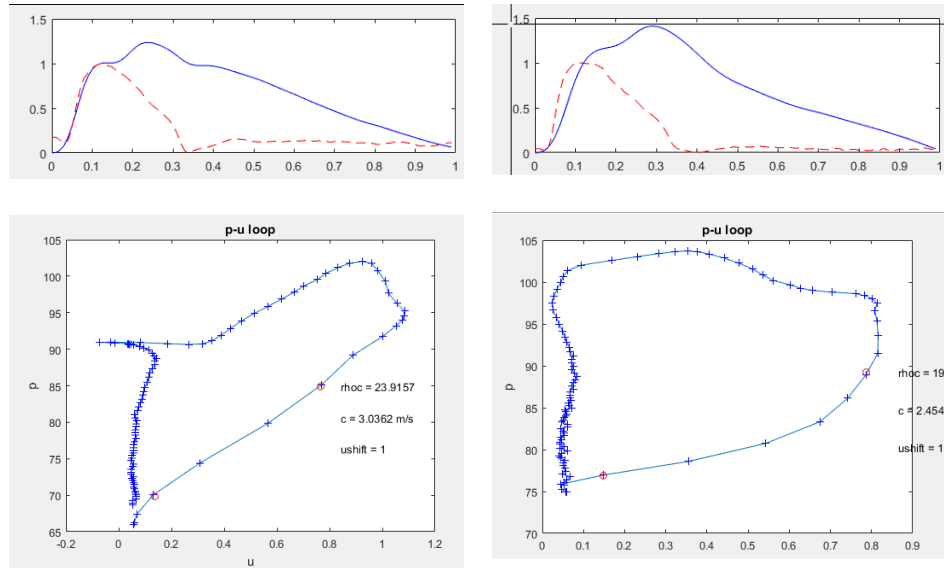


Figure 6-3 Measurement of ρc with good (left) and poor (right) waveform alignment in two different individuals.

Top row: waveform alignment. **Bottom row:** PU-loops showing manually annotated points (red circles) fitted to a straight line. The gradient of the straight line is equivalent to ρc (rhoc).

Wave speed can also be estimated by assuming that net wave energies are minimized over a complete cardiac cycle. This is known as the sum of squares method (c_{SS}),²⁷⁰ and was calculated as Equation 6-3:

$$c_{SS} = \frac{1}{\rho} \sqrt{\frac{\sum dP^2}{\sum dU^2}}$$

Equation 6-3 Wave speed estimated from the sum of squared differences

6.2.7. Wave intensity analysis

For WIA and c_{SS} , the P and U waveforms were filtered using a standard 7 point, 2nd order polynomial Savitzky-Golay filter to smooth data and calculate derivatives.³⁷⁴ Net wave intensity (dI) was calculated as the product of the derivative of pressure (dP) and velocity (dU) over the cardiac cycle.²⁶⁸

$$dI = dP \cdot dU$$

Equation 6-4 Net wave intensity

When wave speed is known (c), forward and backward wave intensity can be separated using the water-hammer equation:

$$WI_+ = \frac{1}{4\rho c} (dP + \rho c \cdot dU)^2$$

$$WI_- = -\frac{1}{4\rho c} (dP - \rho c \cdot dU)^2$$

Equation 6-5 Forward and backward wave intensities. WI_+ is the forward wave intensity, WI_- is the backward wave intensity, and c is wave speed estimated using the PU-loop method.

Wave intensity was quantified using the magnitude and timing of the peak of three waves:²⁴⁰ the initial forward compression (FCW), backward compression (BCW) and forward protodiastolic decompression (expansion) (FDW) waves, Figure 6-4.

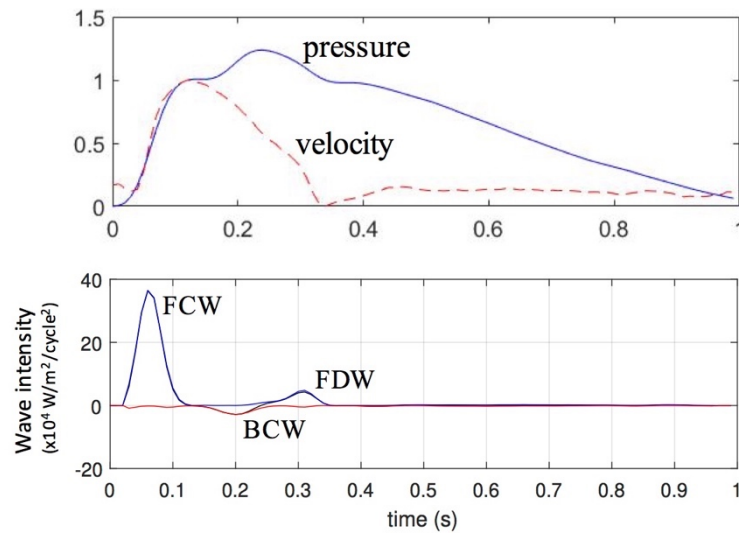


Figure 6-4 Aortic wave intensity analysis.

Top: Alignment of scaled pressure (blue) and velocity (red) waveforms. **Bottom:** Wave intensity analysis example showing initial compression (FCW), backward compression (BCW) and protodiastolic decompression (FDW) waves.

Artefact can occur even with optimal waveform alignment. This can be particularly pronounced for backward wave intensities. This was evident as an early backward wave intensity peak (

Figure 6-2, bottom row). This can be present prior to the FCW which is not physiologically possible. Therefore, any backward peaks occurring prior to the peak of the FCW were automatically discarded prior to waveform quantification. Any prominences that were less than 0.05 W/m^2 were considered fluctuations due to noise. Wave energy was then calculated as the area under each wave. Waveforms were assumed to conform to a gaussian distribution for this purpose, because any deviations from this are likely to be attributable to noise, Figure 6-5. Therefore, area under the curve estimates from the integral or multiple trapezoid measurements were not used.

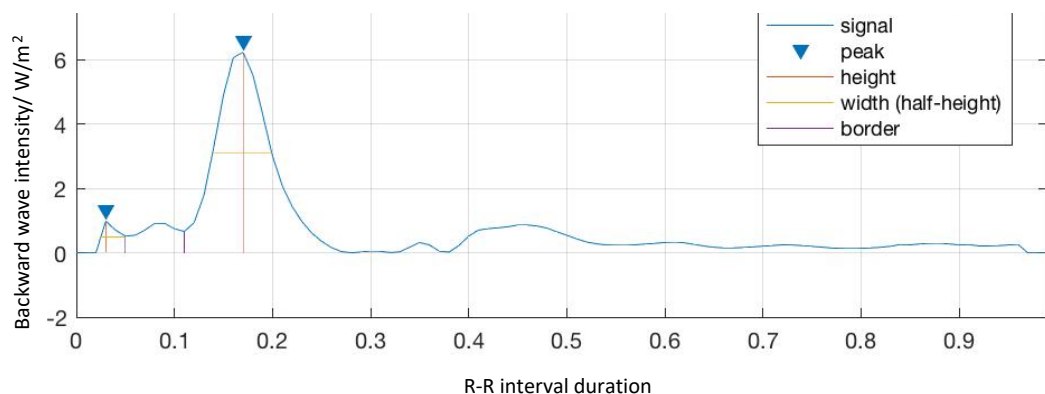


Figure 6-5 Quantification of wave area.

The largest peak was taken as the BCW peak. The early portion of the BCW (the first peak) is continuous with apparent artefact. By assuming a gaussian wave distribution of the BCW, it is possible to reasonably estimate wave area whilst excluding these inaccuracies due to artefact.

Area was calculated as the multiple of the local prominence peak (h), the width (w) at half the peak, and a gaussian constant. A higher width could be used if overlapping waves exist Figure 6-6. The constant was taken as 1.07 that has been used for the

calculation of area from Gaussian type peaks in chromatographic analysis, Equation 6-6.

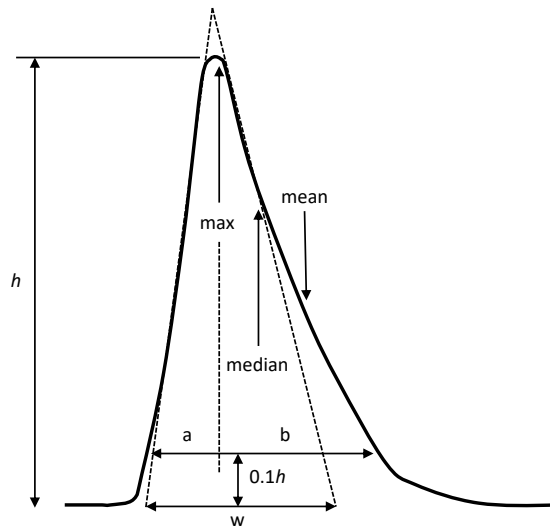


Figure 6-6 Quantification of an asymmetric peak.

Abbreviations as per Equation 6-6. Adapted from *Data and signal processing in Chromatography*, edited by Attila Felinger. [https://doi.org/10.1016/S0922-3487\(98\)80019-1](https://doi.org/10.1016/S0922-3487(98)80019-1)⁴¹⁷

$$Peak\ area = 1.07\ hw_{0.5} \left(\frac{b}{a}\right)^{0.235}$$

Equation 6-6 Integration of a gaussian peak area. a, b are the half-widths of the peak measured at a given height used for an asymmetry factor.⁴¹⁷ Wave intensity peaks are assumed to be symmetrical so $a=b$.

To enable comparisons between subjects, the sample period was normalised by the duration of the cardiac cycle,²⁸² but can be converted into $W/m^2/s^2$ simply by multiplying by the heart rate per second. The reflection index was taken as the ratio of BCW/FCW.²⁸³ For comparison, wave separation analysis was performed to calculate the reflection magnitude, taken as the ratio of the backward to the forward wave amplitudes.⁴¹²

6.2.8. Anthropomorphic and other assessments

Height was recorded using a standard stadiometer. Weight and body fat percentage were measured using digital bioimpedance scales (BC-418, Tanita, USA). Body surface area was calculated using the Mosteller formula. Maximal oxygen consumption (peak VO_2) was estimated by a cardio-pulmonary exercise test (CPET) on a semi-supine ergometer (Ergoselect1200, Ergoline, Germany) using an incremental protocol standardized by bodyweight and gender, as previously described.³⁶⁰

6.2.9. Statistics

Data were analyzed in R (R foundation, Vienna, Austria) using RStudio Server version 0.98 (Boston, Mass, USA). All continuous variables are expressed as mean \pm SD or median(interquartile range, (IQR)) for skewed data. Normality was checked using the Shapiro-Wilk test. Categorical variables are expressed as percentages. Characteristics are stratified by age decile and gender. Groups were compared using independent-samples Student's t-tests for normally distributed continuous variables or Mann-Whitney U test and the Chi-square tests for non-normally distributed and categorical variables respectively. For trends over age deciles, the non-parametric Mann-Kendall monotonic trend test was used. Pearson's correlation coefficient (r) and Bland-Altman limits of agreement (LoA) were used to assess correlation and agreement respectively. Multivariable linear regression models for the association between age and WIA parameters were adjusted for covariates that a priori could confound the relationship; these were sex, heart rate, and height; similarly, sex was adjusted for age, heart rate and height. Mean arterial pressure was not included as a potential confounder as it may be dependent on wave generation rather than the converse.²⁴¹ Regression diagnostics were performed and data were log-transformed if appropriate. All tests were two tailed, and

$p < 0.05$ was considered statistically significant.

Participant characteristics	Males					Females				
	20-30	30-40	40-50	50-60	60+	20-30	30-40	40-50	50-60	60+
<i>n</i>	31	31	22	9	3	33	35	30	9	3
Age/ years	26 ±2	32 ±2	44 ±3	54 ±2	66 ±4	26 ±2	33 ±3	45 ±3	54 ±2	67 ±6
Height/ cm	181 ±7	181 ±7	180 ±6	177 ±9	172 ±4	167 ±5	167 ±5	167 ±6	169 ±5	160 ±5
Weight/ kg	78 ±8	82 ±15	85 ±9	81 ±15	76 ±7	63 ±9	69 ±11	69 ±15	71 ±13	70 ±16
BMI/ kg.m ⁻²	24 ±3	25 ±4	26 ±3	26 ±4	26 ±2	22 ±3	25 ±4	25 ±5	25 ±5	27 ±5
BSA/ m ²	2.0 ±0.1	2.0 ±0.2	2.0 ±0.1	2.0 ±0.2	1.9 ±0.1	1.7 ±0.1	1.8 ±0.1	1.8 ±0.2	1.8 ±0.1	1.7 ±0.2
Body Fat/ %	15 ±5	20 ±6	23 ±5	22 ±6	23 ±2	28 ±6	32 ±7	32 ±8	33 ±8	35 ±7
Peak VO ₂ / ml/kg/min	43 ±6	38 ±6	33 ±6	34 ±7	25 ±3	35 ±4	32 ±6	29 ±7	24 ±4	24 ±3
Resting Heart Rate/ bpm	70 ±15	70 ±15	72 ±14	67 ±14	64 ±4	74 ±15	71 ±10	69 ±12	67 ±12	67 ±11
Brachial SBP/ mmHg	124 ±11	124 ±12	128 ±10	133 ±18	146 ±19	113 ±8	113 ±10	117 ±13	127 ±20	136 ±33
Brachial DBP/ mmHg	75 ±4	75 ±6	79 ±5	79 ±7	79 ±10	72 ±5	73 ±6	74 ±7	80 ±10	76 ±18
Aortic SBP/ mmHg	113 ±10	113 ±10	117 ±9	124 ±19	136 ±23	104 ±8	106 ±10	109 ±11	122 ±19	129 ±31

Table 6-1 Study participant characteristics stratified by sex and age decile.

Abbreviations: BMI: body mass index; BSA: body surface area; DBP: diastolic blood pressure; MAP: mean arterial pressure; SBP: systolic blood pressure; peak V02: maximal oxygen consumption.

6.3. Results

6.3.1. Baseline characteristics

In 206 healthy volunteers, the median age was 37 years (range 21-73 years), 189 (92%) were normotensive (<140/90mmHg) on assessment; and mean aortic arch PWV_{tt} was 4.7 ± 1.5 m/s, Table 6-1. The peak intensity of the initial compression wave, backward compression wave and forward decompression wave were 69.5 ± 28 , -6.6 ± 4.2 and $6.2 \pm 2.5 \times 10^4$ W/m²/cycle² respectively; reflection index was 0.10 ± 0.06 .

6.3.2. Local wave speed compared to PWV_{tt}

There was a moderate correlation between PWV_{tt} and c , and this was stronger with c_{SS} ($r=0.60$ and 0.68 respectively, $p<0.01$ for both). PWV_{tt} was greater than c , and this difference was reduced for c_{SS} (difference: -1.3 [LoA: -3.8 to 1.2] versus -0.64 [LoA: -3.0 to 1.7] m/s respectively), Figure 6-7.

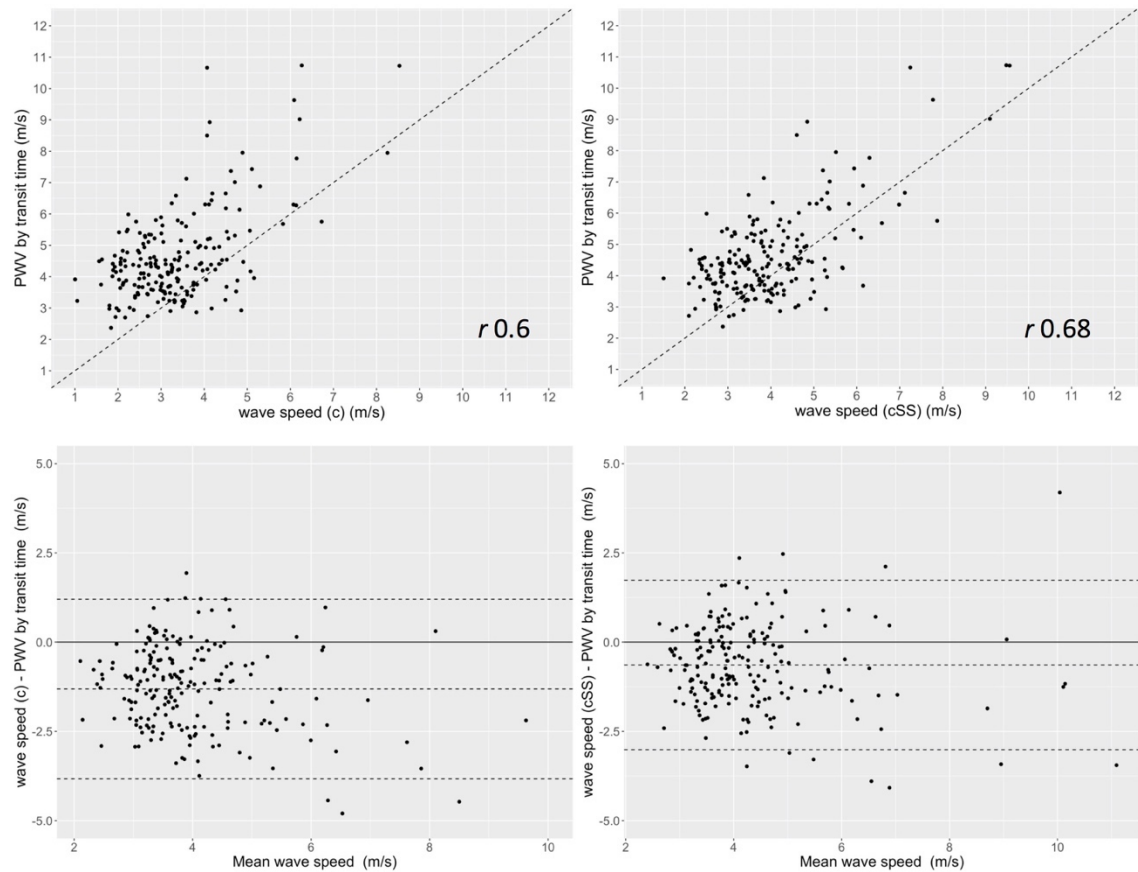


Figure 6-7 Correlation (top row) and Bland-Altman analysis (bottom row) of wave speed and pulse wave velocity (PWV) measured by transit time.

Left: wave speed calculated from the pressure-velocity slope during early systole (c) **Right:** wave speed calculated from the sum of squares method (cSS).

6.3.3. Wave speed and wave intensity by age decade

Both c and cSS increased from youngest (20-30 year-olds) to oldest (≥ 60 year-olds) age decade, Figure 6-8, although cSS tended to be higher than c . Table 6-2 displays all WIA measures stratified by age decade and sex.

FCW decreased progressively with age up to 50-60 year-olds, but rose in ≥ 60 year-olds.

The BCW increased steadily from youngest to oldest age decade. This resulted in a steady increase in reflection index with age decade. There was no convincing trend in FDW with age. Age-related trends were not modified by sex, so data for both sexes are pooled in Figure 6-8.

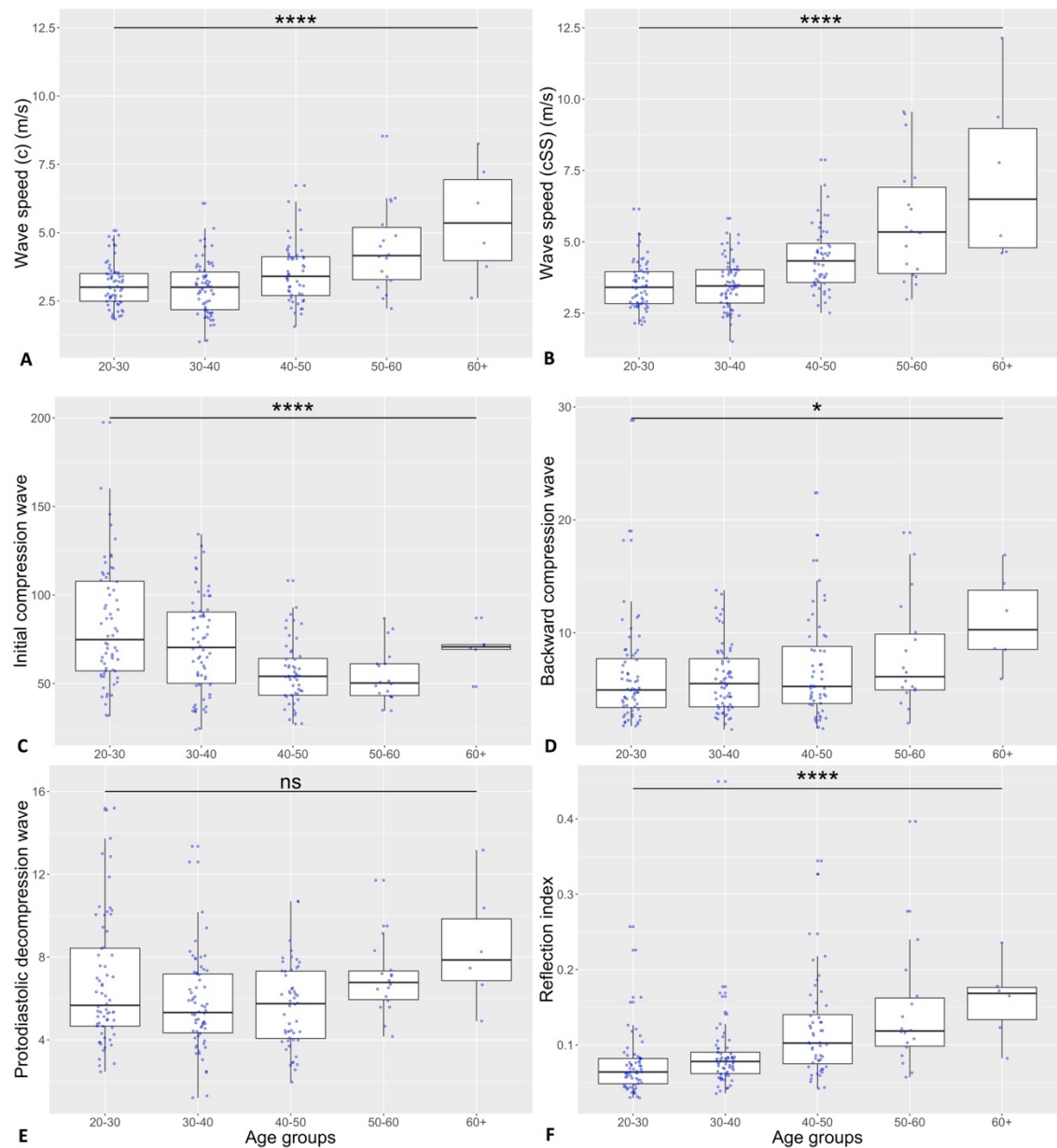


Figure 6-8 Influence of age on wave speed and wave intensity indices.

(A) wave speed (c) measured by PU-loop. **(B)** wave speed measured by sum of squares method (cSS). **(C)** Forward compression wave. **(D)** Backward compression wave. **(E)** Forward decompression wave. **(F)** Reflection index. Abbreviations: ns: $p > 0.05$, * $p < 0.05$, **** $p < 0.0001$.

Wave intensity measures	Males										Females									
	20-30		30-40		40-50		50-60		60+		20-30		30-40		40-50		50-60		60+	
Wave speed/ ms ⁻¹																				
<i>c</i>	3.4	±0.9	3.3	±1.1	3.9	±1.2	4.9	±2.0	5.7	±1.8	2.7	±0.6	2.7	±0.8	3.3	±1.0	4.0	±1.0	5.2	±2.9
<i>c</i> SS	3.4	±0.9	3.6	±0.9	4.6	±1.2	5.8	±2.3	7.3	±2.4	3.0	±0.7	3.5	±0.8	4.3	±1.1	5.5	±2.0	7.3	±4.2
Pulse wave velocity/ m/s	4	±0.7	4	±0.7	5	±1.1	7	±1.8	9	±3.4	4	±0.6	4	±0.6	5	±0.9	8	±2.1	7	±1.6
Wave peak/ 10 ⁴ W/m ² /cycle ²																				
FCW	99	±35	84	±27	61	±23	62	±17	71	±1	67	±22	61	±24	52	±14	47	±9	68	±19
BCW	7.0	±4	5.9	±3	6.1	±4	8	±5	11.6	±6	5.3	±5	6.0	±4	7.4	±5	7.7	±5	10.5	±3
FDW	8.4	±3	6.7	±2	6.2	±2	7.5	±3	10.3	±3	5.2	±2	4.8	±2	5.2	±2	6.5	±1	6.6	±2
Wave timing/ ms																				
FCW	50	±5	50	±7	52	±4	53	±3	56	±3	49	±5	48	±4	51	±5	53	±2	53	±2
BCW	152	±32	163	±24	169	±14	164	±11	162	±8	158	±19	154	±28	157	±32	167	±8	164	±6
FDW	258	±38	268	±40	275	±26	303	±48	303	±19	272	±40	272	±45	296	±27	311	±25	306	±33
Reflection index	0.06	±0.03	0.07	±0.02	0.10	±0.04	0.12	±0.05	0.16	±0.08	0.07	±0.05	0.10	±0.07	0.14	±0.07	0.17	±0.11	0.16	±0.03
Reflection magnitude	0.54	±0.1	0.55	±0.1	0.58	±0.1	0.56	±0.1	0.59	±0.1	0.55	±0.1	0.57	±0.1	0.61	±0.1	0.59	±0.1	0.61	±0.1
Wave energy/ J																				
Forward wave	5.6	±1.6	4.6	±1.4	3.6	±1.0	3.5	±0.7	4.6	±0.5	3.5	±1.1	3.5	±1.2	3.0	±0.6	2.9	±0.4	4.3	±1.0
Backward wave	0.74	±0.4	0.67	±0.2	0.65	±0.3	0.70	±0.4	1.05	±0.4	0.58	±0.4	0.67	±0.3	0.71	±0.4	0.73	±0.3	1.13	±0.4

Table 6-2 Wave intensity analysis stratified by sex and age decile.

Pulse wave velocity was measured conventionally in the aortic arch from transit time. *Abbreviations: c: wave speed measured by the pressure-velocity loop; cSS: wave speed measured by the sum of squares method; BCW: backward compression wave; FCW: forward compression wave; FDW: forward decompression wave; J: joules.*

6.3.4. Associations of wave intensity after adjustment for confounders

In multivariable analysis including age, sex, heart rate and height as covariates, older age was associated with a smaller FCW, a larger BCW and a larger reflection index.

Male sex was associated with a higher FCW, no difference in BCW and consequently a lower reflection index, and a higher FDW compared with females. Higher heart rate was associated with a lower FCW, a lower BCW, a lower reflection index and a lower

FDW. Height was not associated with any WIA parameter in adjusted models, Table 6-3.

Outcome:	Multivariate		
FCW peak	β	95% CI	<i>p</i>
Age (years)	-0.96	-1.26,-0.65	<0.001
Male sex	20.7	11.7,29.7	<0.001
Heart Rate (bpm)	-0.80	-1.0,-0.56	<0.001
Height (cm)	-0.02	-0.53,0.49	0.94
<i>R</i> ² 0.38			
BCW peak	β	95% CI	<i>p</i>
Age (years)	0.06	0.01,0.11	0.02
Male sex	0.61	-0.91,2.12	0.43
Heart Rate (bpm)	-0.12	-0.16,-0.08	<0.001
Height (cm)	-0.03	-0.12,0.06	0.49
<i>R</i> ² 0.20			
Reflection index	β	95% CI	<i>p</i>
Age (years)	0.002	0.0015,0.0029	<0.001
Male sex	-0.03	-0.05,-0.003	0.02
Heart Rate (bpm)	-0.001	-0.002,-0.0005	<0.001
Height (cm)	0.000	-0.001,0.001	0.84
<i>R</i> ² 0.26			
FDW peak	β	95% CI	<i>p</i>
Age (years)	0.01	-0.02,0.04	0.44
Male sex	1.86	0.94,2.78	<0.001
Heart Rate (bpm)	-0.02	-0.05,-0.0005	0.045
Height (cm)	0.02	-0.03,0.07	0.49
<i>R</i> ² 0.17			

Table 6-3 Linear regression models showing the association of wave intensity peaks with age when adjusted for pre-specified covariates.

6.4. Discussion

This is the first study to determine wave intensity and local wave speed by combining direct non-invasive measures of central blood pressure and velocity data from phase contrast cardiovascular magnetic resonance. This straightforward method allows aortic WIA to be performed at scale, here in the largest cohort reported to date. This technique was validated by showing good agreement between local wave speed (calculated from combined non-invasive pressure and phase contrast CMR-derived flow data) and conventionally measured pulse wave velocity using transit time. WIA patterns and magnitude appeared similar to invasive data,^{224,273,416} but the non-invasive nature of testing used in this study permitted exploration of healthy ventriculo-arterial coupling. The resolution was sufficient to detect that ageing and female sex were independently associated with decreased forward compression wave energy and an increased proportion of wave reflection, suggesting a less energy efficient cardiovascular system.

6.4.1. WIA at scale using central measures

Whilst central hemodynamics have most impact on the ventricle, previous non-invasive studies of WIA have typically been in peripheral arteries because they are easier to interrogate using ultrasound doppler and tonometry.^{272,280} The approach developed in this study uses measures of central pressure and velocity rather than surrogates such as distensibility, which are dependent on aortic stiffness. Like other methods,²⁵⁶ these were acquired sequentially, but simultaneous acquisition is feasible in future studies using longer tubing for the central blood pressure cuff measurement. This would enable the oscillometric device to be situated in the MRI control room for pressure measurement, whilst the patient has flow measured in the MRI scanner.

6.4.2. Local wave speed estimation

The validity of two single-point methods of wave speed were tested by comparing with a conventional regional estimate extending across the aortic arch (PWV_{tt}).²⁷⁵ We used two previously described single-point methods, one based on the pressure-velocity loop,²⁶⁹ and the other using the sum-of-squares method.²⁷⁰ Both showed acceptable agreement with the transit time based method which was assumed to be the reference, although agreement was slightly better for *c*SS which is consistent with the findings of a previous in-vitro study.⁴¹⁸ Because wave speed increases distally, both measures of ascending aortic local wave speed were expectedly lower than regional PWV_{tt} which extends to the aortic arch.

6.4.3. Associations between sex or age and aortic WIA

These data show that females have a greater wave reflection index in the aorta and lower FDW magnitude, which has not been reported previously, to our knowledge. Consistent with Li et al., females also demonstrated a smaller FCW.²⁷⁵ Borlotti et al. found a sex difference in the reflection index in carotid but not femoral arteries, however wave reflection in the aorta is different to that seen in the carotid.²⁸³ Differences in wave reflection may provide a substrate for the development of heart failure.⁴¹⁵

The increase in wave speed and arterial stiffness with age are well recognized, however age-related changes in aortic WIA measures have only previously been described in one study, which used diameter rather than pressure measurements to derive an alternative index of wave intensity.²⁷⁵ The study also reported a decrease in FCW, BCW and an increase in reflection index but reported a decrease in FDW rather than the lack of change seen in this cohort. Differences with these data may be due to different study

populations, or the use of diameter as a surrogate measure of pressure in the previous study, which itself is inversely related to wave speed. The proportion of reflection increased with age whether measured by wave separation or wave intensity analysis. The contribution of higher intensity waves appears more pronounced at older ages and higher degrees of overall reflection. This suggests that the greater reflection that occurs with healthy ageing presents a more adverse load on the heart.⁴¹⁹

6.4.4. Study limitations

Because data were ensemble averaged, the average cycle is truncated leading to a slight shortening of the duration of diastole; however since wave intensity in end-diastole is negligibly small this is unlikely to affect findings. Participants were recruited based on intention to participate in a first marathon, and while they were not engaged in training at the time of study it is unlikely that they are truly representative of the general population. Older participants were under represented and are selective recruited as more healthy individuals. Patients were excluded with any known significant medical problems including hypertension or diabetes mellitus. We used a free-breathing phase-contrast CMR sequence which provides sufficient spatio-temporal resolution for the velocity profile. A similar sequence has been used to measure CMR distensibility as a surrogate for pressure, but because it is free-breathing this may compromise accuracy for measures of compliance due to through-plane motion.²⁷⁴ Breath-held sequences are possible using an accelerated spiral sequence but can be difficult to analyze due to artefact.⁴²⁰ Hematocrit differences between sexes were not accounted for, although this is unlikely to affect blood density significantly.

6.5. Conclusion

This paper describes a novel non-invasive method for wave intensity analysis, using central blood pressure and CMR velocity data. Local wave speed measured by this technique showed good agreement with regional pulse wave velocity and the method has straightforward application for large sample sizes. In healthy individuals, women had a smaller forward compression wave, and poorer overall ventriculo-arterial coupling than men. In both sexes, older age was associated with higher wave speed and poorer ventriculo-arterial coupling as assessed by WIA.

7. Application of automated analysis techniques to assess cardiovascular remodelling in novice marathon runners

This chapter is based on the following submitted manuscript:

Training for a first-time marathon reverses age-related aortic stiffening: a prospective longitudinal cohort study. Bhuva AN, D'Silva A, Torlasco C, Jones S, Nadarajan N, Van Zalen J, Chaturvedi N, Lloyd G, Sharma S, Moon JC, Hughes AD, Manisty CH
Currently under second review by the Journal of the American College of Cardiology

Hypothesis:

Age-related vascular decline in health may be reversible with real-world exercise training for a first-time marathon.

Contribution:

I performed the baseline CMR acquisitions (n=237), and the majority of follow-up acquisitions (n=178). I coordinated individual study days and performed some of the data acquisition in other modalities (stress echocardiography, blood pressure, ECG, anthropometrics). I stored and databased blood and urine samples, anthropometric and imaging data. I supervised Dr Nadarajan in the phase-contrast CMR data analysis for an MSc thesis, receiving a distinction. I developed the analysis protocols for T1 and volumes (see Chapter 3.7) and performed the inter-observer analysis for clinician CMR LV assessment. I performed the atlas-based LV analysis of all datasets using the approach described in Chapter 4. I performed all statistical analysis. I am grateful to the work of approximately fifty individuals to complete the overall study, and particular Drs D'Silva and Torlasco who provided overall coordination.

7.1. Introduction

Ageing is a major risk factor for cardiovascular disease beyond simple cumulative conventional risk factor exposure. In large arteries, advancing age is associated with biochemical and histological changes that result in vessel stiffening. The aorta buffers pulsatile stroke volume and translates this to steady peripheral flow, therefore progressive stiffening increases pulse pressure and ventricular afterload. Such changes in hemodynamics are associated with dementia, cardiovascular and kidney disease,^{421–423} even in the absence of atherosclerosis,⁴²⁴ suggesting that age-related arterial stiffening is detrimental to health. Anti-hypertensive agents can modify arterial stiffness once established in disease, but more cardiovascular events occur in individuals without diagnosed hypertension,⁴²⁵ providing an opportunity for early lifestyle modification in health.^{263,354}

One potential beneficial strategy is regular aerobic exercise.³²⁷ Mass participation running is an increasingly popular form of non-prescribed exercise, with 18 million finishers in the USA in 2018.⁴²⁶ Cross-sectional studies have shown that lifelong athletes possess more distensible peripheral arteries,⁴²⁷ and relatively brief (< 3 months) supervised aerobic exercise interventions benefit brachial blood pressure (BP) and peripheral artery stiffness.^{351,428} The dose of exercise needed to preserve or even rejuvenate the central (aortic) arterial system in a real-world setting is not known. Using cardiovascular magnetic resonance, it is now possible to assess local arterial stiffness by distensibility in the aorta rather than peripheral vessels. This is a stronger prognostic marker, and is more closely associated with the natural ageing process, even though associations vary regionally with aortic composition.^{378,429,430}

We hypothesized that age-related aortic stiffening in health would be reversible with real-world exercise training. To explore this, we used a large cohort of healthy, first-time marathon runners investigated before training initiation, and after completion of the London Marathon.

7.2. Methods

7.2.1. Study population and assessment timing

Healthy participants were recruited into a prospective longitudinal observational study to investigate the effect of first-time marathon training on cardiovascular function.

Participants were recruited over the 2016 and 2017 London Marathons (Virgin Money).

Details of the study have been reported previously, and detailed in Methods-3.4.³⁶⁰ All procedures were in accordance with the principles of the Helsinki declaration, all participants gave written informed consent and the study was approved by the London-Queen Square National Research Ethics Service Committee (15/LO/0086).

All measurements were conducted before training started, immediately after the release of the results from the ballot entry system six months prior to the marathon. These were repeated within 3 weeks after completion of the London Marathon, but not earlier than one week after completion to avoid the acute effects of exercise.

In this analysis, participants were included if they had successfully completed the marathon and attended both baseline and follow-up assessments. 237 participants were recruited, 71 did not run the Marathon (52 due to injury), and 139 completers attended follow-up. One participant started anti-hypertensive medication after the baseline assessment and was excluded from subsequent analysis.

7.2.2. Data acquisition and analysis

Peripheral BP, central BP, anthropomorphic, and cardio-pulmonary exercise test assessments are described in the Methods-3.4. After BP acquisition, CMR was performed at 1.5T (Magnetom Aera, Siemens AG Healthcare, Erlangen, Germany).

Single-shot ECG-gated white blood sagittal aortic (“candy cane”) views were acquired

first to measure 3D aortic length and to standardize cross-sectional imaging. This was used to pilot axial aortic blood flow-velocity maps at the level of the pulmonary artery bifurcation and the level of the diaphragmatic descending thoracic aorta. The spoiled gradient echo phase-contrast sequence used was free-breathing, ECG-gated and segmented, with parameters described in Methods-3.5. The contours for the ascending, proximal and distal (diaphragmatic) descending aorta were traced semi-automatically using validated software (ArtFun) on the phase-contrast modulus for area analysis, and velocity images to derive velocity profiles.³⁷⁷ Analysis was performed with the operator blinded to the scan timing (baseline or follow up), and with the paired scans analysed independently.

7.2.3. Local aortic stiffness

Because the aorta is known to have varying regional tissue composition, arterial stiffness was measured by distensibility at three levels of the thoracic aorta. Arterial stiffness may mechanistically reflect either intrinsic changes in the arterial wall or the functional effect of loading conditions, therefore, beta (β)-stiffness index was also calculated. This is a pressure-independent measure of intrinsic arterial stiffness because it accounts for the non-linear compliance to pressure relationship, Equation 7-1.

$$\beta = \frac{\ln (cSBP / cDBP)}{(d_s / d_d) - 1} - \ln \left(\frac{cDBP}{P_{ref}} \right)$$

Equation 7-1 Beta-stiffness (a pressure independent measure, β). d_s and d_d are the maximum and minimum aortic diameters calculated from the areas and P_{ref} is a reference BP, here 100mmHg.

Measurement of global aortic stiffness using pulse wave velocity, and reproducibility of aortic stiffness measures are described in the Methods-3.9.1.

7.2.4. Biological aortic age

Biological aortic age was determined from the relationship between age and local aortic stiffness at each level of the aorta using the baseline cross-sectional data. Aortic stiffness is strongly correlated with chronological age, and so any deviations from expected values may reflect between-subject susceptibility to accelerated ageing, or conversely, vascular adaptation.

First, linear regression models of chronological age and distensibility at each level of the aorta were constructed using the baseline cross-sectional data. As this relationship was non-linear for β -stiffness, data were log-transformed. Biological aortic age was then determined by an inverse function of the regression model, with aortic stiffness as the input (distensibility or β -stiffness). Using the same baseline model, biological aortic age was then determined at follow-up, with the difference between time points reflecting the change in estimated biological age with exercise training.

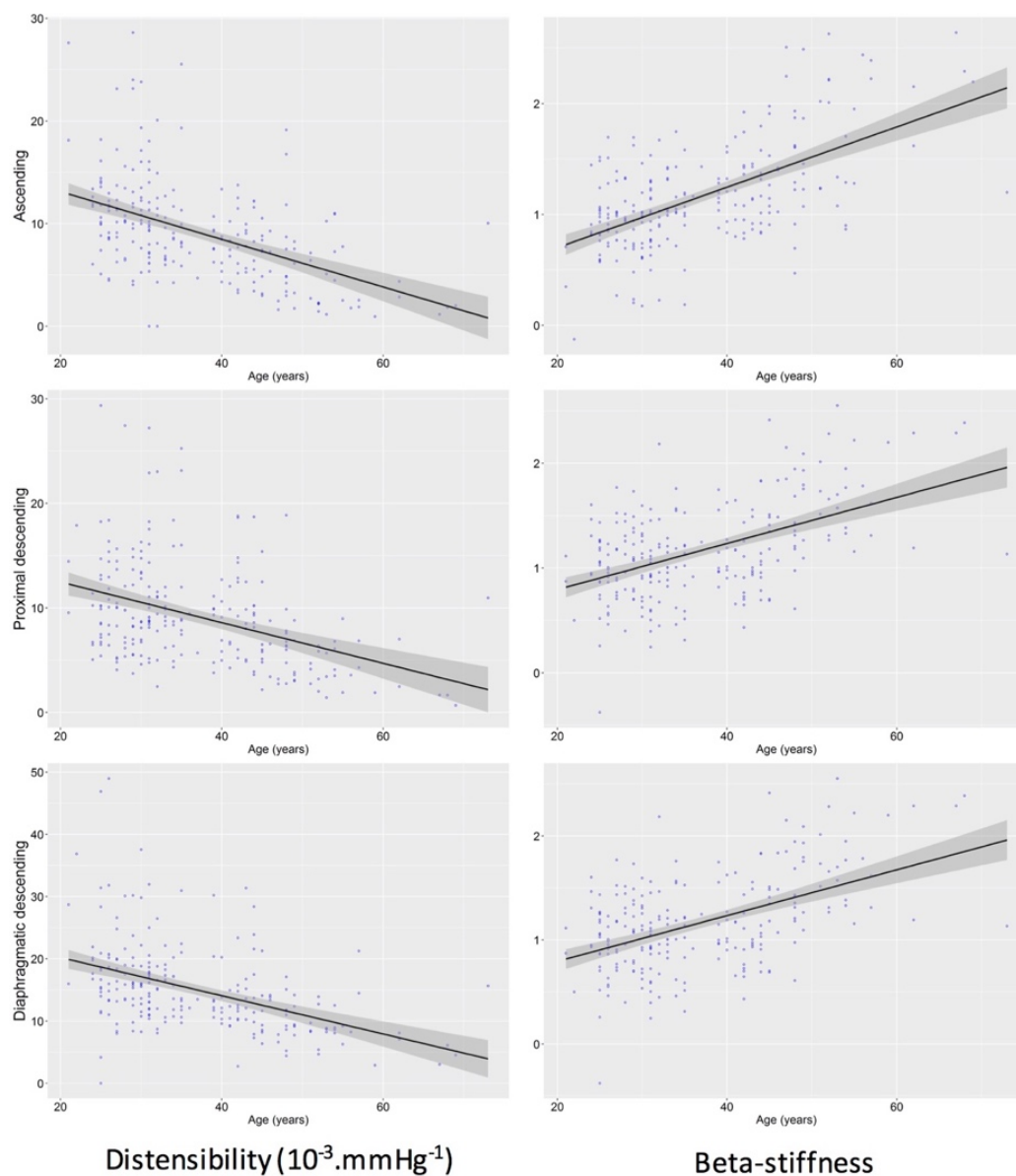


Figure 7-1 Baseline associations of age and aortic stiffness measures at different levels of the aorta.

Beta-stiffness is log-transformed. Regression line and 95% confidence intervals are displayed.

7.2.5. Global and regional assessment of LV structure

Three-dimensional analysis was performed as previously described using an atlas-based machine learning approach for image segmentation. This produced global LV metrics and 3D models of wall thickness and geometry, co-registered in the same space. Further details can be found in Methods-3.8. Example of individual participant co-registrations are in Figure 7-2.

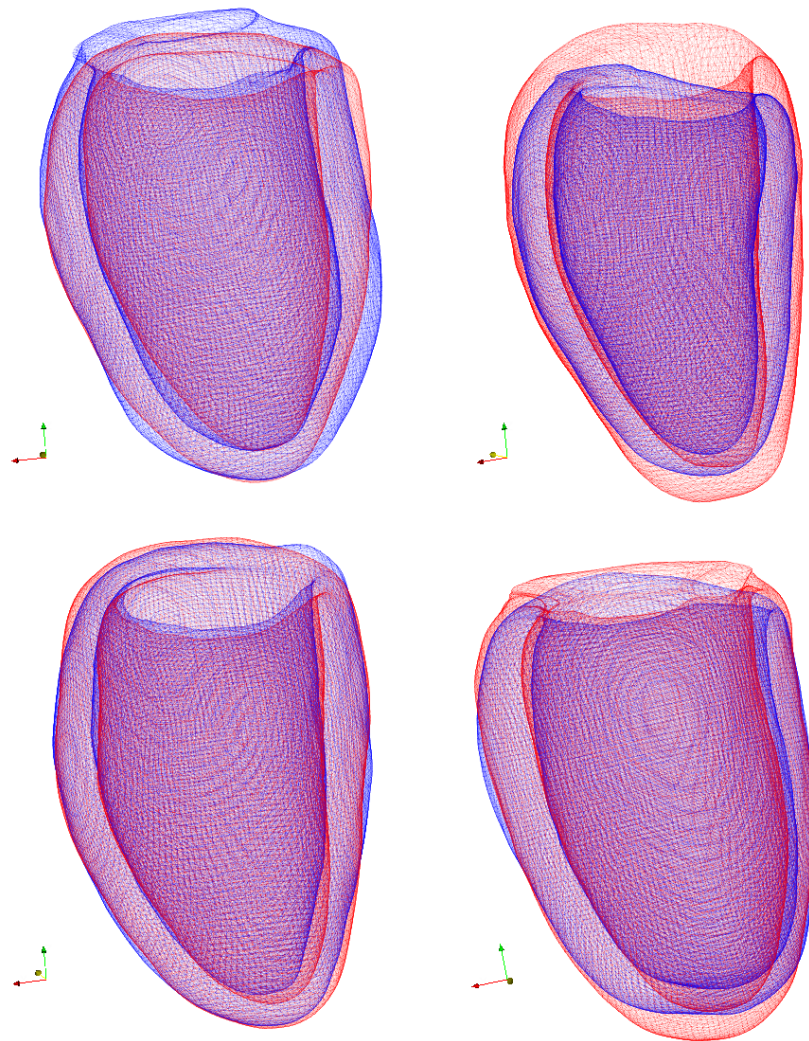


Figure 7-2 Three-dimensional models for four individuals before (blue) and after (red) six-months training for and completion of a first-time marathon.

Representations are standardized to an anterior en-face view, so the septum is on the right and the free wall on the left. Qualitatively, the changes for each individual can be interpreted as follows: top left individual: septal hypertrophy and cavity contraction; top right: global, concentric hypertrophy and cavity dilatation; bottom left: no convincing change; bottom right: cavity elongation and apical hypertrophy.

7.2.6. Assessment of ventriculo-arterial coupling

WIA was performed by combining standard CMR flow-velocity and non-invasive central BP waveforms, as described in Chapter 6. Wave intensity was quantified using the magnitude and timing of the initial forward compression wave (FCW), and the backward compression wave (BCW).²⁴⁰ The reflection index was taken as the ratio of BCW/FCW, as a measure of left ventricular-arterial coupling.^{256,415}

7.2.7. Statistical analysis

Data were analysed in R (R foundation, Vienna, Austria) using RStudio Server version 1.0.153 (Boston, Mass, USA). All continuous variables are expressed as mean \pm SD or median (interquartile range [IQR]) for skewed data, and the 95 percent confidence interval of the changes with exercise training. Baseline and follow-up data were compared using paired Student's t-tests for normally distributed continuous variables or Mann-Whitney U test and the Chi-square tests for non-normally distributed and categorical variables respectively. Because the study was designed to look at older and younger participants, age groups were a priori stratified by the mean age of the cohort (37 years), similar to Tanaka et al.(14) To minimize the influence of outliers, extreme data points (greater than six interquartile ranges below the first or above the third quartile) were removed (8 out of 1668 data points in aortic stiffness measures pre- and post- training).

Multivariable linear regression was used to assess relationships after adjusting for covariates, and strengths of association were summarised as partial correlation coefficients (r_{partial}) i.e. the correlation having controlled for other variables.

Associations between aortic stiffness and baseline BP, heart rate, weight, body fat, marathon completion time and peak VO_2 were adjusted for age and sex. Associations

between aortic stiffness and sex were adjusted for age and peak VO_2 . Because aortic stiffness is partly dependent on loading conditions, the association between the change in aortic distensibility and change in systolic blood pressure (SBP) was adjusted for the “operating” BP (baseline mean central arterial pressure). Changes between aortic stiffness and other dependent variables at follow-up were adjusted for the baseline measurement of the covariate. To determine whether the change in aortic stiffness was attributable to a change in intrinsic structure, the change in distensibility was adjusted for the change in operating BP, and the change in β -stiffness was examined. Linear regression model diagnostics were inspected, and data were power transformed if appropriate to satisfy the assumptions of constant variance and normality of residuals. All tests were two-tailed and a p value of <0.05 was considered statistically significant.

7.3. Results

7.3.1. Participants

138 first-time marathon completers attended assessment 176 ± 11 days before and 16 ± 4 days after marathon completion. The mean age was 37 ± 10 years (range: 21-69 years) and 49% were male. Participant characteristics at baseline and follow-up are summarized in Table 7-1. Average marathon running time was 5.4 ± 1.0 hours for women and 4.5 ± 0.8 hours for men, Figure 7-3. Based on weekly training data and marathon completion times from 27,000 runners, these timings are consistent with a training schedule of between 6 and 13 miles per week.⁴³¹

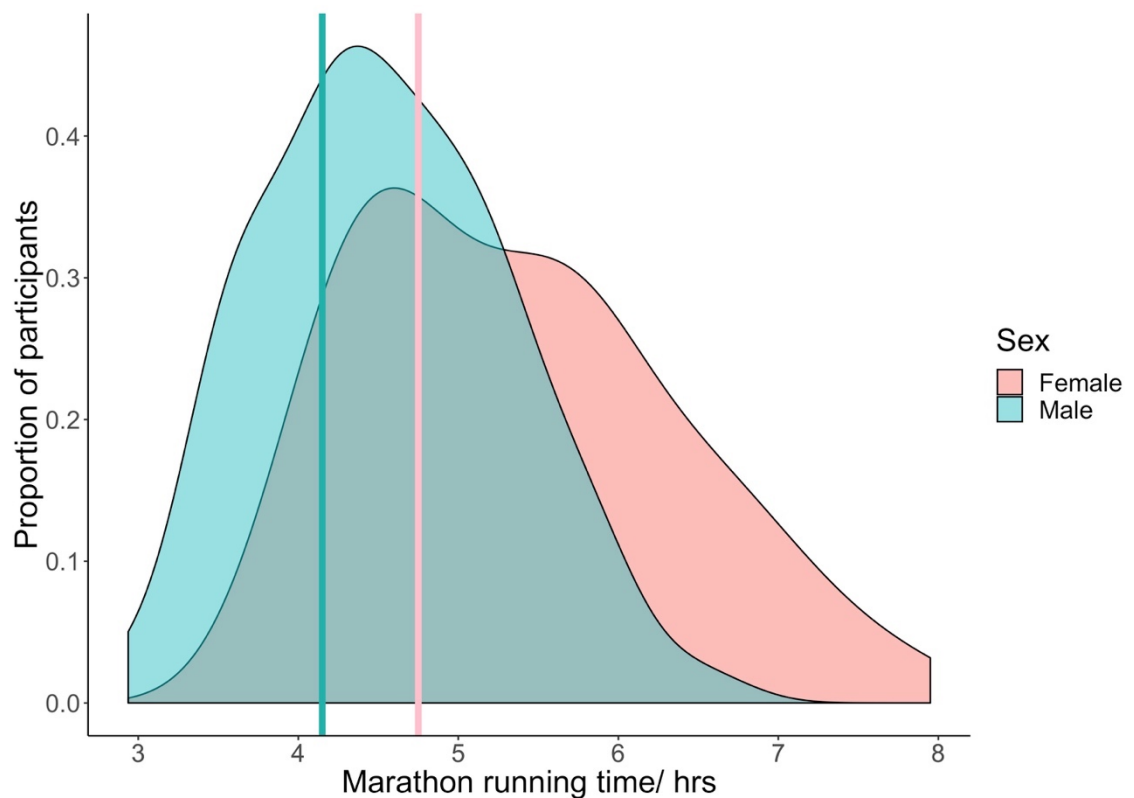


Figure 7-3 London Marathon running times for study participants.

Vertical lines represent the average of the median running times for the 2016 and 2017 London Marathons.

	Whole cohort			<i>p</i>	Older (>37 years)			<i>p</i>	Younger (≤37 years)			<i>p</i>
	Baseline	Follow-up			Baseline	Follow-up			Baseline	Follow-up		
<i>n</i>	138				59				79			
Age (years)	37 (21-69)				47 ±7				30 ±4			
Male	68 (49%)				28 (47%)				40 (51%)			
Running Time (hrs)	4.96 ±0.98				5.37 ±1.05				4.65 ±0.80			
Weight (kg)	73 ±13	72 ±12	0.002		75 ±14	73 ±13	<0.001		72 ±13	71 ±12	0.59	
Body Fat (%)	25 ±8	24 ±9	0.009		28 ±7	26 ±8	0.01		23 ±8	23 ±9	0.34	
Peak V02 (ml/kg/min)	34.5 ±7.5	35.6 ±8.3	0.02		31 ±6.5	32.0 ±6.7	0.048		37 ±7.0	39 ±8.3	0.06	
Heart Rate (bpm)	69 (61,77)	67 (61,75)	0.07		69 (61,78)	67 (58,77)	0.29		69 (61,76)	67 (62,75)	0.14	
Blood Pressure (mmHg)												
Brachial SBP	120 (111,128)	116 (108,124)	<0.001		124 (114,132)	120 (109,127)	<0.001		118 (110,124)	114 (108,122)	0.004	
Brachial DBP	75 (70,79)	72 (68,76)	<0.001		78 (74,82)	74 (67,77)	<0.001		73 (70,77)	71 (68,76)	0.016	
Brachial MAP	90 (85,95)	88 (81,92)	<0.001		94 (87,98)	89 (82,93)	<0.001		88 (83,92)	86 (81,90)	0.005	
Brachial PP	45 (40,51)	44 (40,50)	0.004		46 (42,54)	44 (40,52)	0.03		45 (40,49)	43 (40,47)	0.053	
Central SBP	110 (102,121)	106 (100,114)	<0.001		116 (109,123)	109 (101,119)	<0.001		108 (100,114)	104 (100,111)	0.002	
Central DBP	76 (72,81)	74 (69,78)	<0.001		79 (75,83)	75 (69,79)	<0.001		74 (71,78)	73 (69,77)	0.02	
Central MAP	87 (82,94)	85 (79,90)	<0.001		92 (87,96)	86 (80,92)	<0.001		85 (82,90)	83 (79,88)	0.007	
Central PP	35 (31,41)	33 (30,39)	0.02		39 (33,43)	35 (32,41)	0.056		33 (29,39)	33 (30,37)	0.19	
Augmentation index (%)	53 ±29	52 ±4	0.98		67 ±31	62 ±24	0.158		42 ±22	46 ±22	0.17	

Table 7-1 Baseline characteristics and follow-up response to exercise, stratified by older (>37 years) and younger (≤37 years) participants.

Data are mean (±standard deviation; full age range for whole cohort) or median (inter-quartile range). 1 participant did not have follow-up cardiovascular magnetic resonance due to pregnancy; 3 participants had partial aortic phase contrast acquisition due to scanner crashes; 1 participant imaging data was not saved successfully at one time-point. 5 participants did not have cardiopulmonary exercise testing data due to either machine crashes or injury at follow-up. *Abbreviations: SBP= systolic blood pressure, DBP= diastolic blood pressure; MAP= mean arterial pressure; PP= pulse pressure.*

7.3.2. Baseline ageing and aortic stiffness

For the ascending, proximal descending and diaphragmatic descending aorta, a decade of ageing corresponded to a decrease in distensibility of 2.3, 1.9, and 3.1 $\times 10^{-3} \text{mmHg}^{-1}$ and an increase in β -stiffness by 27, 22, and 16% respectively, Figure 7-1.

7.3.3. Effect of training on blood pressure and heart rate

Brachial SBP and DBP decreased with training by 4 (2.8, 5.5) and 3 (1.6, 3.5) mmHg respectively, $p < 0.01$ for both. Central SBP and DBP decreased with training by 4 (2.5, 5.3) and 3 (1.6, 3.5) mmHg respectively, $p < 0.001$ for both, Figure 7-4. There was no significant change in heart rate with training (-2.3 (0.3, -4.3) beats per minute), $p = 0.07$.

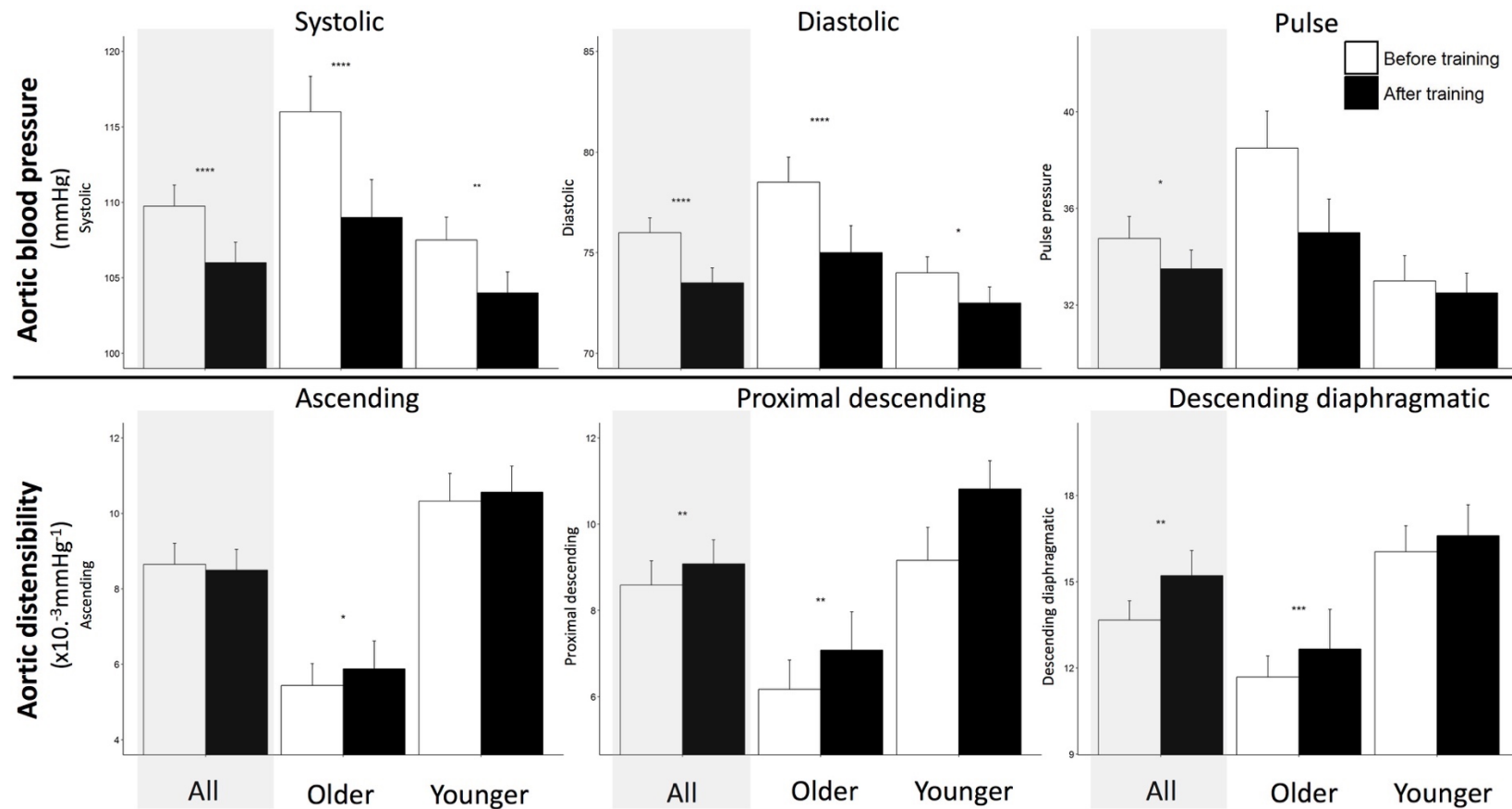


Figure 7-4 Greater change with exercise training in aortic blood pressure (top) and distensibility (bottom) in older age category (>37 years old).

Data are medians and bars representing standard errors. The standard error the median was taken as 1.253 times the standard error of the mean. Abbreviations: * $p < 0.05$; ** $p < 0.01$; *** $p < 0.001$; **** $p < 0.0001$.

7.3.4. Effect of training on aortic stiffness

Training was associated with a reduction in aortic stiffness, which was more pronounced in the distal aorta, Table 7-2. Distensibility did not change discernibly in the ascending aorta ($p=0.14$), but increased by 9% and 16% in the proximal descending and diaphragmatic descending aorta, $p=0.009$ and 0.002 respectively. The change in distensibility was independent of the change in mean arterial pressure ($p<0.001$ for the descending aorta). β -stiffness showed less pronounced but similar regional trends. β -stiffness did not change in the ascending ($p=0.60$) or proximal descending aorta ($p=0.08$), but decreased by 6% in the diaphragmatic descending aorta ($p=0.04$), Figure 7-5. The change in β -stiffness did not correlate with the change in distensibility in the ascending ($R^2=0.009$, $p=0.13$) or proximal descending aorta ($R^2=0.01$, $p=0.11$), but explained 42% of the change in distensibility in the diaphragmatic descending aorta ($p<0.001$).

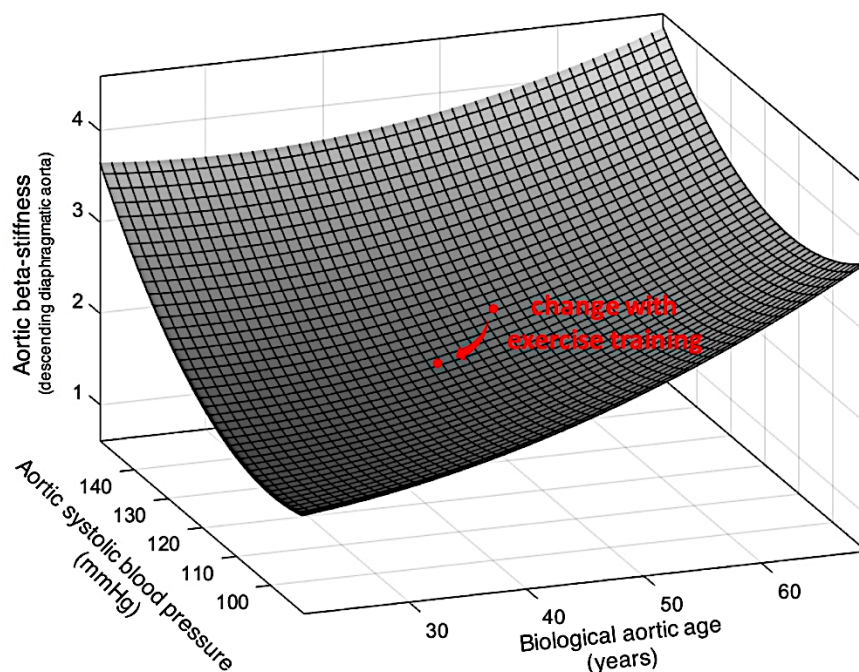


Figure 7-5 Baseline central (aortic) systolic blood pressure, aortic stiffness and estimated aortic age; and the change (red arrow) with exercise training for the average older marathon completer.

	Whole cohort					Older (>37 years)					Younger (≤37 years)				
	Baseline		Follow up		<i>p</i>	Baseline		Follow up		<i>p</i>	Baseline		Follow up		<i>p</i>
<i>n</i>	138					59					79				
Distensibility (×10 ⁻³ .mmHg ⁻¹)															
Ascending	8.6	(5,11)	8.5	(6,12)	0.16	5.4	(3,8)	5.9	(4,9)	0.04	10.3	(8,13)	10.6	(8,13)	0.80
Proximal Descending	8.6	(6,12)	9.1	(6,13)	0.009	6.2	(4,10)	7.1	(5,10)	0.02	9.2	(8,14)	10.8	(8,14)	0.13
Diaphragmatic Descending	13.7	(11,18)	15.2	(12,21)	0.002	11.7	(9,14)	12.7	(10,17)	<0.001	16.0	(13,20)	16.6	(14,23)	0.32
Beta-stiffness															
Ascending	2.9	(2.5,4.2)	3.1	(2.4,4.2)	0.60	4.2	(3.3,6.8)	4.1	(3.1,6.0)	0.42	2.7	(2.1,2.9)	2.6	(2.2,3.3)	0.72
Proximal Descending	3.1	(2.4,4.3)	2.9	(2.3,4.0)	0.08	3.9	(2.7,5.6)	3.9	(2.7,4.9)	0.15	2.7	(2.2,3.4)	2.6	(2.1,3.2)	0.43
Diaphragmatic Descending	2.0	(1.7,2.3)	1.9	(1.6,2.3)	0.04	2.3	(2.0,2.7)	2.1	(1.9,2.5)	0.051	1.8	(1.6,2.1)	1.8	(1.5,2.2)	0.68
Vascular age (Distensibility)															
Ascending	39.3	(28,53)	39.9	(24,52)	0.16	53.1	(43,63)	51.2	(37,59)	0.04	32.0	(20,40)	31.0	(19,44)	0.80
Proximal Descending	40.0	(22,55)	37.5	(19,51)	0.009	53.4	(34,63)	48.0	(35,59)	0.02	28.1	(10,44)	28.6	(12,42)	0.13
Diaphragmatic Descending	41.4	(28,51)	36.4	(19,48)	0.002	47.8	(41,57)	44.6	(32,53)	<0.001	33.6	(20,44)	31.8	(12,41)	0.32
Vascular age (Beta-stiffness)															
Ascending	38.3	±17.9	38.6	±16.8	0.99	50.1	±17.7	48.5	±17.2	0.99	29.4	11.9	30.9	±11.6	0.99
Proximal Descending	37.1	±20.5	34.8	±19.0	0.11	46.3	±22.0	43.2	±20.4	0.15	30.3	16.4	28.4	±15.2	0.40
Diaphragmatic Descending	37.2	±17.5	33.6	±18.6	0.04	46.1	±17.4	40.4	±20.0	0.051	30.4	14.4	28.4	±15.5	0.37
Pulse wave velocity (m/s)															
Arch	4.4	(4,5)	4.2	(4,5)	0.21	5.4	(5,6)	5.3	(4,6)	0.09	3.9	(3,4)	3.9	(4,4)	0.95
Descending Aorta	7.9	(6,10)	7.4	(6,9)	0.06	8.1	(7,10)	7.7	(7,10)	0.41	7.6	(6,10)	7.1	(6,9)	0.08
Whole Aorta	5.7	(5,7)	5.5	(5,6)	0.03	6.3	(6,7)	6.1	(5,8)	0.17	5.1	(5,6)	5.0	(5,6)	0.10
Diameter (mm)															
Ascending	28	±4	28	±4	0.83	30	±4	30	±4	0.94	26	±3	26	±3	0.59
Proximal Descending	21	±3	20	±3	0.10	21	±3	21	±3	0.70	20	±3	19	±3	0.04
Diaphragmatic descending	17	±2	17	±3	0.18	18	±2	18	±3	0.27	16	±2	16	±2	0.32
Reflection index	10.2	±0.6	9.1	±0.45	0.04	13.0	±0.6	11.6	±0.5	0.15	8.3	±0.6	7.2	±0.3	0.14

Table 7-2 Aortic stiffness and reflection index before and after exercise training, stratified by older (>37 years) and younger (≤37 years) participants. Data are mean (±standard deviation) or median (inter-quartile range).

7.3.5. Effect of training on biological aortic age

After training, the increase in distensibility translated to a reduction in biological aortic age by 1.5 (-0.9, 5.4; $p=0.16$), 3.9 (1.1, 7.6; $p=0.009$) and 4.0 (1.7, 8.0; $p=0.002$) years in the ascending, proximal descending and diaphragmatic descending aorta respectively. When estimated from β -stiffness, biological aortic age reduced by 0 (-2.8, 2.8; $p=0.99$), 2.4 (-0.5, 5.3; $p=0.11$) and 3.2 (0.1, 6.2; $p=0.04$) years in the ascending, proximal descending and diaphragmatic descending aorta respectively.

7.3.6. Associations with the training-related change in aortic stiffness

Increasing age was associated with greater reduction in either measure of aortic stiffness in the descending aorta (greatest r_{partial} 0.27, $p=0.002$), Table 7-3 and Figure 7-4. Males had a greater reduction than females in descending aorta β -stiffness (r_{partial} 0.19 and 0.16, $p=0.03$ and $p=0.03$ respectively) when adjusted for peak VO_2 . This was equivalent to a median 1.4 year greater benefit in men.

Higher baseline central SBP was associated with a greater reduction in β -stiffness of the proximal and diaphragmatic descending aorta (r_{partial} 0.23 and 0.21, $p=0.006$ and 0.02 respectively). The strength of these associations were reduced when adjusted for age and sex (r_{partial} 0.16 and 0.20, $p=0.06$ and 0.02 respectively). There was no association between baseline central SBP and the change in distensibility with training. With training, a greater reduction in either measure of aortic stiffness was associated with a greater reduction in SBP, adjusted for loading conditions (greatest r_{partial} -0.31, $p<0.001$), Table 7-3.

Slower marathon running time was associated with a greater increase in proximal descending aortic distensibility with exercise training (r_{partial} -0.20, $p=0.02$), Table 7-3. There was no association between the change in β -stiffness and marathon performance.

Baseline peak VO_2 , heart rate, body fat, and weight or alterations in these parameters with training were not associated with the change in either measure of aortic stiffness after training.

	Age	Male sex	Baseline cSBP	Change in cSBP	Marathon performance	Baseline peak VO ₂	Change in peak VO ₂
Change in Distensibility							
Ascending	-0.08	0.22*	0.03	-0.29‡	-0.08	0.02	0.06
Proximal descending	-0.07	-0.01	-0.14	-0.18*	-0.20*	0.12	0.17
Diaphragmatic descending	-0.17*	-0.02	-0.02	-0.31‡	-0.12	0.13	0.16
Change in Beta-stiffness							
Ascending	0.20*	-0.03	0.01	0.11	0.05	0.05	-0.05
Proximal descending	0.19*	0.19*	0.16	0.13	0.10	0.07	0.07
Diaphragmatic descending	0.27†	0.16*	0.20*	0.18*	0.04	0.03	0.06

Table 7-3 Associations of the change in aortic stiffness after exercise training (pre-post) with age, sex, blood pressure, marathon performance and aerobic fitness.

Associations are r_{partial} . Associations with male sex are adjusted for age and peak VO₂; associations with baseline central systolic blood pressure (cSBP), baseline V02, and marathon performance, are adjusted for age and sex; and associations between distensibility and change in cSBP are adjusted for baseline operating pressure (mean central arterial pressure). *p<0.05; †p<0.01; ‡p<0.001. Abbreviations: cDBP=central diastolic blood pressure; peak VO₂= maximal oxygen consumption.

7.3.7. Effect of training on LV wall thickness

LV mass increased with training by 2.9 (0.4, 5.1) grams, $p=0.02$. There was no change in cavity volumes or LVEF. By 3D analysis, the increase in mass was a global process, Figure 7-6, but the distribution of wall thickness across the LV changed, with a redistribution of mass from the septum to other regions, Figure 7-7. Age, baseline peak VO_2 , aortic stiffness, and marathon performance were not associated with the change in LV mass after training.

7.3.8. Effect of training on ventriculo-arterial coupling

Using wave intensity analysis, there was no change in the FCW (-0.50, 95%CI: -3.8, 3.48; $p=0.93$) and weak evidence of a reduction in BCW (-0.73, 95%CI: 0.13, -0.95; $p=0.07$) with training. Reflection index decreased by 1.2 (0.1, 2.3) with training ($p=0.04$), Table 7-2.

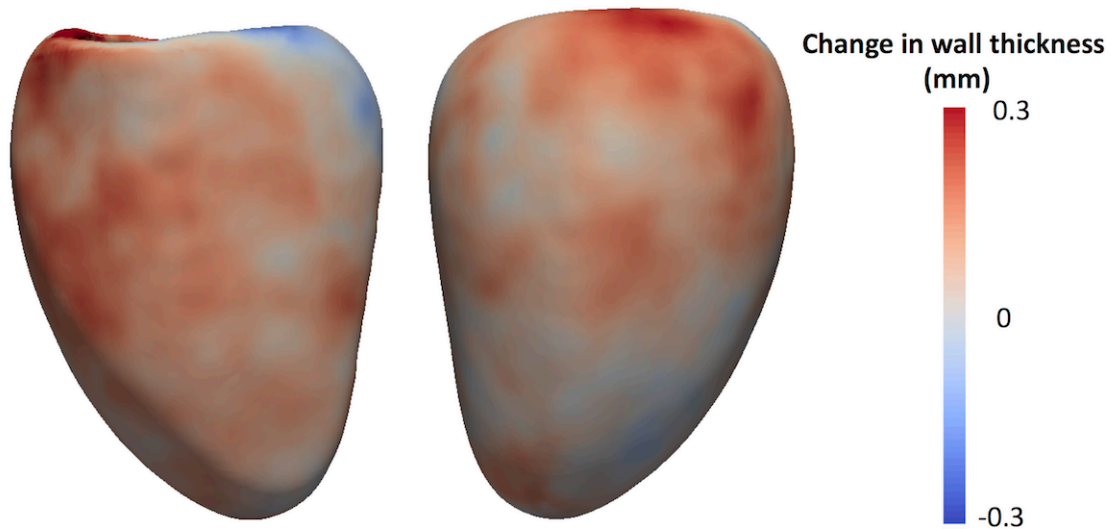


Figure 7-6 Increase in left ventricular (LV) wall thickness with exercise training.

The increase in LV mass with exercise training is a global, but modest process. The average wall thickness across the whole LV surface increased from 6.9 ± 1.5 to 7.0 ± 1.5 mm. The colour represents the mean change in wall thickness (red = thicker, blue = thinner) with exercise training in septal (left) and lateral (right) views.

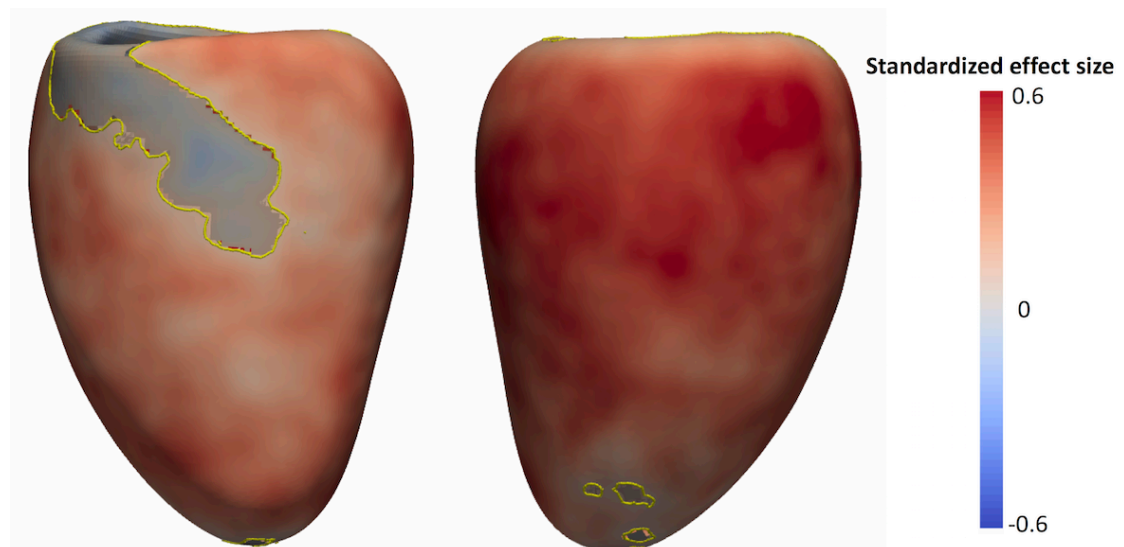


Figure 7-7 Redistribution of LV mass with exercise training is away from the septum.

The colour represents the standardized effect size between the change in LV mass and the change in wall thickness at each vertex with exercise training. The change in LV mass with exercise training is correlated with the change in wall thickness, except for the septal region enclosed within the yellow contour. The yellow contour encloses the shaded, smaller area at the septum which shows a negative correlation, but is not statistically significant (p values greater than 0.05 after correction for multiple testing). Views are septal (left) and lateral (right) en-face.

7.4. Discussion

This prospective longitudinal cohort study shows that six-months of training and completion of a first-time marathon is sufficient to achieve reductions in blood pressure, wave reflection and aortic stiffness. It was possible to reverse the consequences of ageing on vessel stiffening by the equivalent of approximately four years, as measured in the aorta rather than more peripheral vessels. Both brachial and aortic SBP reduced by 4 mmHg, a magnitude comparable to first line anti-hypertensive medications.⁴³²

Benefits were observed in healthy individuals across a broad age range, and were greater in older, slower, male marathon runners with higher baseline BP. Performance times were suggestive of achievable exercise doses in real-world novice participants – approximately thirty minutes slower than the average completion time for the London Marathon. Based on completion times, participants trained for 6-13 miles a week, in line with the suggested 17-week training program and within the recommendations of the 2018 USA Physical Activity Guidelines.³¹⁹

In healthy individuals, chronological ageing leads to a gradual increase in aortic stiffness and elevated cardiovascular risk. However, chronological age is not the same as the biological process which captures life course influences and frames how we make choices that can accelerate or rejuvenate the vasculature.⁴³³ Cross-sectional studies have shown that moderate intensity exercise at 4-5 days a week preserves “youthful” compliance of the carotid artery.⁴³⁴ However it is important to know both the effect of exercise on aortic rather than peripheral arterial stiffening given its greater prognostic importance, and the mechanism of changes in stiffness.²⁶³ Cross-sectional findings may be attributable to genetic or confounding influences, and vascular capacitance itself may determine exercise capacity. Several studies have demonstrated the efficacy of

supervised training programmes that prescribe the type, dose and frequency of exercise.^{428,435} Examining the consequences of first-time marathon training helps to understand the benefits from real-world exercise behaviour that people enjoy and may continue. A goal-orientated exercise training recommendation (“*sign-up for a marathon*” or “*run a fun-run*”) can be a good motivator to keep active and may increase the likelihood of sustaining benefits. This study emphasizes the importance of lifestyle to modify the ageing process, particularly as it appears “never too late” to gain the benefit as seen in older, slower runners.³⁴³ For this cohort, the average exercise per week estimated from the training programme recommendations was 203 ± 74 minutes. Adults are recommended to do at least 150 to 300 minutes for substantial health benefits.³¹⁹

In this context, this study contributes a number of findings in a large real-world cohort comprising both sexes. The relative reduction in SBP observed is comparable to antihypertensive medication, given the participants in this study were normotensive and a greater improvement was observed in those with higher SBP.³⁴⁹ Persistent reductions in SBP of this magnitude reduce stroke mortality by over 10% and avoid large numbers of premature deaths in the general population.⁴³⁶ Both the observed reduction in aortic stiffness and BP are in keeping with the magnitude of benefit from other aerobic exercise interventions.³⁵² There was a small change in peak VO_2 which did not explain the change in stiffness, contrary to expectation but also observed in other studies.^{351,355} The training program was designed to habituate individuals to sustained running rather than augment fitness,³⁶¹ and this is supported by a previous study in this cohort showing greater improvements in skeletal muscle peak VO_2 than cardio-pulmonary peak VO_2 .³⁶⁰ Changes in stiffness were also not associated with changes in other measures (heart rate,

weight or adiposity), suggesting that the hemodynamic impact of more frequent exercise sessions and lifestyle modification has a direct effect on intrinsic aortic remodelling.

The improvement in aortic stiffness was both functional due to blood pressure lowering, as well as intrinsic due to structural changes in the descending aorta, Figure 7-8.

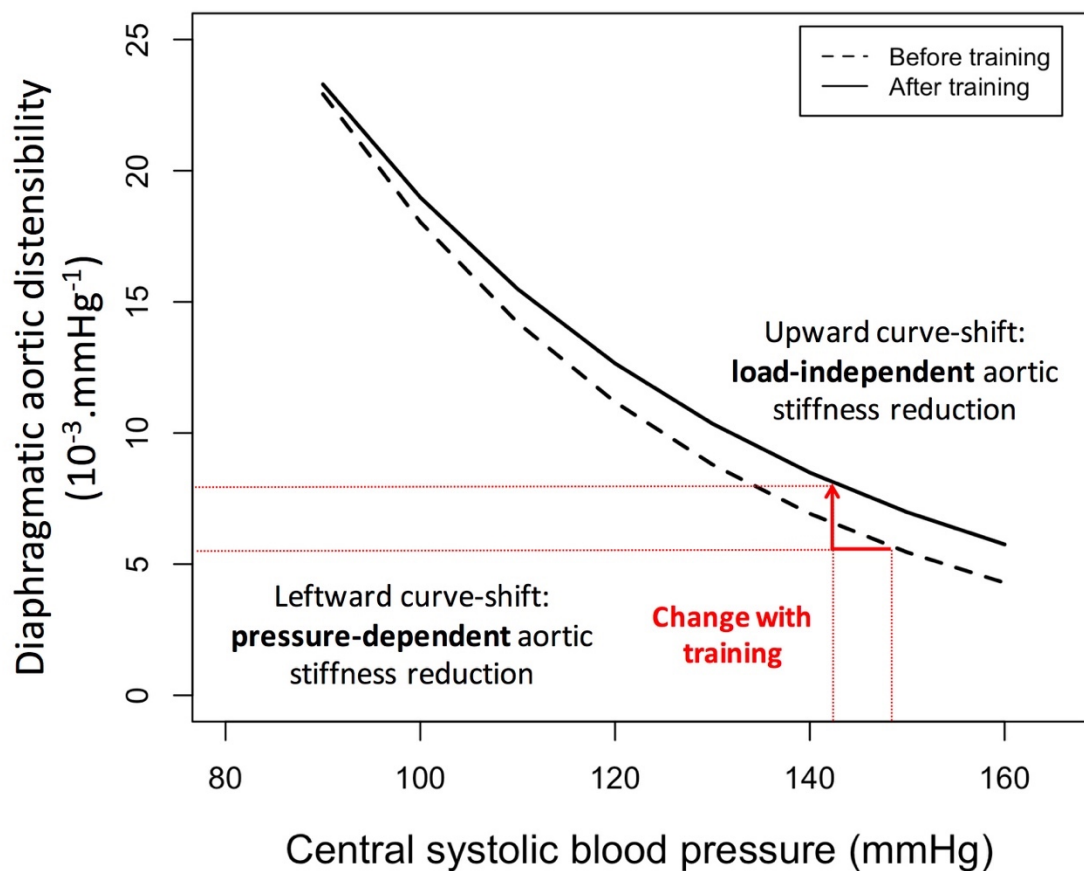


Figure 7-8 Reduction in aortic stiffness with exercise stiffness is due to both intrinsic structural (load-independent) and functional (pressure-dependent) changes.

At higher arterial pressure, the aorta is functionally stiffer, but this relationship is not linear. Exercise training results in a reduction in pressure-dependent distensibility (leftward shift along the curve), and additionally a reduction in intrinsic β -stiffness (upward shift of the curve), contributing to a greater reduction in stiffness (red arrows and lines). In this schematic, data are fitted to an exponential for the cohort both before and after exercise training.

One study of 13 males observed similar benefits after just four weeks of training,⁴³⁷ but other studies of two to four months duration observed that the reduction in stiffness was predominantly functional.^{438,439} Unlike previous studies, we used direct CMR assessment of the aorta and over a longer duration of training for aortic remodelling. Differences in intrinsic stiffness may be due to endothelial function, smooth muscle tone or extracellular matrix changes, but were beyond the measurement scope of this study.³⁵⁵ Older, male runners had a greater reduction in aortic stiffness, attributable to greater baseline BP and aortic stiffness. Whilst aortic stiffening increases markedly after the age of 50, these data suggest that this is in part modifiable in non-hypertensive individuals.⁴⁴⁰ Slower marathon runners also had a greater reduction in distensibility from higher baseline measures of stiffness, although directionality can only be assumed in this study.

Structural properties may explain the preferential effect of exercise on the descending thoracic aorta. The proximal aorta media has a higher elastin:collagen ratio to maintain high compliance.²¹⁰ Conversely, the distal aorta media contains a higher proportion of smooth muscle that may be more readily modifiable within a six-month period.⁴³⁰ The effect of both exercise and combination medication have previously been noted to have an effect on the arterial tree that can vary by 25% depending on the branch.^{439,441}

There was only a modest increase in left ventricular mass, suggesting that real-world marathon training is not sufficient to induce LV hypertrophy to the same extent as that observed in pathological conditions. These changes appeared to be symmetrical, in contrast to the asymmetrical hypertrophy observed in aortic stenosis.

7.4.1. Study limitations

This study was conducted in healthy individuals, therefore our findings may not apply to patients with hypertension who have stiffer arteries that may be less modifiable.⁴⁴² From these data, however, those with higher SBP at baseline appeared to derive greater benefit. Since this was not a randomized double blind controlled trial (RCT) the possibility of unobserved confounding cannot be excluded. However, this study was not designed to provide structured training in the context of a RCT, but rather to observe the consequences of real-world preparation for a marathon, a setting in which randomized control trials are difficult to implement. Nevertheless, more information on the intensity and frequency of exercise training would have been valuable to understand further the beneficial effects on aortic stiffness. The modest change in peak VO_2 may be related to exercise training intensity or low adherence, which reflects the real-world. Peak VO_2 was performed semi-supine to allow concurrent echocardiography and this may also have reduced sensitivity to changes due to running, or running efficiency. We assessed only marathon finishers – plausibly, non-finishers could have had different vascular responsiveness. The causal link of exercise to measured changes is only inferred - marathon training may lead to other lifestyle modifications (dietary, other behavioral factors), or alterations in lipid profiles and glucose metabolism – although these have not been previously associated with changes in aortic stiffness.³⁵¹ We did not examine the effect of exercise on peripheral arteries or endothelial dysfunction. Whilst individual participants served as internal controls, there may have been run-in bias for the initial blood pressure measurement. This appears unlikely as blood pressure changes would not have been age-related nor correlated with the change in separate measures (e.g. aortic stiffness) with training. The exercise dose-response curve here is not sampled –

only training for a first-time marathon with single timepoint assessment. This area warrants further study. We measured distensibility on modulus imaging acquired at 1.5T rather than steady-state free precession imaging. This has previously been shown to correlate well and show similar associations with ageing.³⁷⁷ Diaphragmatic descending aortic distensibility data reported here were however higher than expected, although there is limited literature for comparison.⁴⁴³ Unlike Voges et al. central rather than brachial PP was used which would explain greater distensibility, and the use of 1.5T phase-contrast modulus may accentuate image contrast differences between 3T gradient echo sequences. Nevertheless, associations with age and changes with training were similar to more proximal distensibility.

7.5. Conclusion

Training and completion of a first-time marathon result in beneficial reductions in blood pressure and intrinsic aortic stiffening in healthy participants. These changes are equivalent to approximately a four-year reduction in vascular age. Greater benefit was observed in older, slower, male marathon runners with higher baseline blood pressure.

7.5.1. Acknowledgements

I thank the study participants for voluntarily giving their time and taking part in the study. I am also grateful to Virgin London Marathon for their support in recruitment of participants. I am particularly grateful to the entire marathon study team performing investigations. In addition to the authors of this manuscript, The Marathon Study group included the following staff from St George's University of London, University College London, Bart's Health Trust and other organisations: Andrew D'Silva, Camilla Torlasco, Siana Jones, Jet Van Zalen, Amna Abdel-Gadir, Thomas Treibel, Stefania Rosmini, Manish Ramlall, Gabriella Captur, Katia D Menacho Medina, Joao Augusto, Yang Ye, Niromila Nadarajan, Nabila Mughal, Sunita Chauhan, Shino Kiriakose, Tolu Akinola, Cheelo Simaanya, Lizette Cash, James Willis, David Hoare, James Malcolmson, Pamela de la Cruz, Annabelle Freeman, Delfin Encarnacion, Lesley Hart, Jack Kaufman, Frances Price, Rueben Dane, Karen Armado, Gemma Cruz, Lorna Carby, Tiago Fonseca, Fatima Niones, Zeph Fanton, Jim Pate, Joe Carlton, Sarah Anderson, Rob Hall, Sam Liu, Sonia Bains, Claire Kirkby, Pushpinder Kalra, Raghuveer Singh, Bode Ensam, Tee J Yeo, Rachel Bastiaenen, Della Cole, Jacky Ah-Fong, Sue Brown, Sarah Horan, Ailsa McClean, Kyle Conley, Paul Scully, Luke Horsfield, Mark McLaren, Elizabeth Clough, Daniel Key, Riyaz Patel and Sanjeev Bhattacharyya. We are grateful to Virgin Money London Marathon, particularly Hugh Brasher and Penny Dain, for their support with study advertisement and participant recruitment. From our funders Cardiac Risk in the Young we are particularly grateful to Steve Cox and Azra Loncarevic-Srmic for their additional support with administration and transport.

8. Discussion

8.1. Summary of key contributions

Cardiovascular remodelling in health and disease show great variation to the same apparent stressors. Both blood pressure and LV ejection fraction are influenced by these remodelling changes, and clinical decisions are based on their absolute cut-offs. It is well appreciated that variation exists between subjective categorization, and that more detailed measurements of LV geometry, and of the blood pressure waveform, improve risk prediction. Biomarkers that can quantify the phenotypic spectrum could offer better targeting of therapies and greater insight into disease processes. Information that is obtained during routine clinical measurements, but usually discarded, may be able to provide more detailed cardiovascular biomarkers.

The primary hypothesis in this work was that it is possible to quantify more detailed cardiovascular phenotypes than conventional measures from CMR imaging, and that these phenotypes can provide additional clinical and physiological insights. The feasibility of cardiovascular phenotype extraction from CMR imaging was tested separately for LV bSSFP cine imaging, and aortic phase contrast imaging. The utility of these approaches were tested in health (exercise training) and disease (patients with aortic stenosis).

The following contributions are related to defining the most precise clinician-derived measurements of LV structure and function from bSSFP cine imaging:

- A training programme improves inter-observer agreement with an expert. The absolute improvement however is relatively modest. After completing this training programme, the precision of junior trainees is equivalent to that of more senior clinicians.

- A large proportion of precision error is attributable to the human observer, rather than other factors such as scan acquisition or physiological variation.
- Semi-automated techniques, whilst quick, do not show superior precision to manual analysis. The choice of semi-automated technique introduces bias in the absolute values, and so reference ranges should be interpreted in the context of the technique used to derive them.
- A novel level-set endocardial border detection technique was developed. This was fast, but showed similar precision to other techniques. It showed greater mass and smaller volumes, but similar EF compared to fully manual analysis.
- Clinicians can be confident in detecting a 9% change in EF, or a 20g change in LVM for follow-up scans. This will be hard to improve because of a large contribution of human error to overall precision error.
- Sample sizes for future clinical trials are presented, and stratified by pathology.

The following contributions are related to testing a convolutional neural network based approach for the analysis of real-world bSSFP cine imaging:

- A convolution neural network (CNN) analysis approach can be generalisable to real-world (multi-disease, multi-centre, multi-field strength, multi-scanner) CMR imaging.
- A training strategy using single pathology, but multi-centre, CMR data, can be used to generalize to multi-disease, multi-centre CMR data.
- The precision of automated CNN analysis is comparable to the most precise clinician analysis techniques. After training and data preparation, CNN analysis takes place in the fraction of the time of a clinician.
- A real-world benchmarking resource is made available to test future automated analysis techniques, and for human training.

The following contributions are related to the use of an atlas-based approach to LV three-dimensional modelling:

- The first cardiac atlas of patients with severe aortic stenosis was created to quantitatively describe regional LV wall thickness, shape and function. Using the atlas, a pipeline to segment and co-register new scans of patients with AS was developed. This approach is able to detect a 1mm difference in WT using 100 patients (a conservative estimate) across the majority of the ventricular surface.
- An atlas-based analysis approach to changes in regional LV remodelling is more sensitive than conventional analysis, potentially helping to personalize risk stratification.

The following contributions are related to the development of a novel approach to measure ventriculo-arterial coupling using phase-contrast CMR velocity waveforms:

- Using WIA, it is possible to combine phase-contrast CMR velocity with non-invasive measures of central BP (rather than a surrogate), to provide an integrated assessment of the cardiovascular system.
- Local wave speed estimates show good agreement with other validated measures of wave speed. The sum of squares estimate shows less bias and better correlation than a pressure-velocity loop method with a reference standard (aortic arch pulse wave velocity). This may be due to difficulty in aligning waveforms.
- In healthy ageing, wave reflection increases, with an increasing contribution of earlier, more adverse waves reflected back to the heart. There is also greater wave reflection in women. These associations are independent of potential

confounders. There is no association between cardio-pulmonary fitness and wave reflection after adjustment for potential confounders.

The following contributions are related to patients with severe aortic stenosis (AS):

- The septum is the most plastic myocardium, compared to other regions. In response to AS, hypertrophy is most pronounced in the septum. One year after AVR, regression of hypertrophy is also greatest in the septum.
- The LV in patients with AS is more spherical, consistent with an increase in wall stress. Septal hypertrophy is accompanied by a smaller septal cavity (concentric hypertrophy), whilst lateral hypertrophy is accompanied by lateral cavity dilatation (eccentric hypertrophy).
- The LV remodelling response to AS in men is less favourable, but more modifiable with AVR.

Male patients demonstrate greater septal hypertrophy, and greater lateral eccentric hypertrophy. This is after adjustment for hypertension, and associated with a more unfavourable biochemical and haemodynamic response. At one year after AVR, males show greater regression of hypertrophy than females in the septum, as well as greater biochemical and haemodynamic improvement.

- In men, septal plasticity may be an important adaptation to wall stress. This is because regression of septal wall thickness is more strongly related to changes in troponin-T, than global LV mass.
- In patients with AS and normal global mass and geometry, there is relative hypertrophy of the infero-septum and regression at one year post-AVR. This may represent a region of early adaptation to pressure overload providing functional advantages.

The following contributions are related to individuals training for and completing a first-time marathon:

- Increased aortic stiffness and central aortic blood pressure, both strong predictors of cardiovascular mortality, are lower in healthy individuals after six-months training for and completion of a first-time marathon. Lifestyle advice to partake in unsupervised, popular forms of exercise training that people enjoy and are likely to continue may be an effective strategy to reduce the effects of age-related arterial stiffening.
- The reduction in blood pressure is comparable to first-line anti-hypertensive medication. If sustained over a lifetime, this reduction is equivalent to a 10% reduction in stroke risk.
- The reduction in aortic stiffening is equivalent to four chronological years of aortic ageing, as measured by aortic stiffness. The reduction was greatest on older, male, slower runners and with higher baseline BP.
- The decrease in aortic stiffness is partly due to an intrinsic change in stiffness, and partly due to a blood pressure-dependent effect.
- There is a modest increase in non-septal LV mass (opposite to severe AS).
- There is an improvement in ventriculo-arterial coupling, which is due to decreased wave reflection. This may be due to greater peripheral small vessel recruitment, vasodilatation, or decreased arterial stiffening.
- To achieve these benefits, an estimated 6-13 miles of training are required over a 17-week period, plus marathon completion.

8.2. Future directions

Current clinical measurements are well validated for use as biomarkers to stratify patients into pathophysiological diagnoses, provide risk assessment, and guide treatments.^{85,211,444} Ejection fraction, for example, will always remain important to identify systolic dysfunction. Similarly, since the Framingham Study in 1965, elevated blood pressure was no longer thought of as an appropriate physiological response, but rather a recognized risk factor for cardiovascular disease.⁴⁴⁵ The requirements for biomarkers have however gradually evolved. There is a decline in systolic dysfunction due to myocardial infarction, whilst at the same time the prevalence of heart failure with preserved ejection fraction (HFpEF) is on the rise. Because these biomarkers have provided such utility, their use has been adapted to other circumstances. They are increasingly relied on to detect serial changes in disease status, and there is a growing focus on screening or detection of early stage disease.^{9,85,193} Absolute measurement of LVEF guides pharmacotherapy, device implantation and surgical decision-making.^{84–86} Measurement of LV cavity volumes can prompt intervention for valvular heart disease or necessitate the cessation of chemotherapeutic agents for cancer treatment.⁴⁴⁶ Examples of current limitations are common in cardiology. For example, whilst early trials showing the benefit of ICD implantation did not have a standardized definition for EF measurement, this has subsequently contributed to part of the difficulty in identifying responders to therapy.^{447,448} To meet these requirements, tests should be precise and personalised.^{1,2,449}

This work demonstrates that the most important imaging biomarker of LVEF lacks sufficient precision for absolute numbers to hold clinical importance beyond the nearest decile. According to current clinical guidelines, absolute values must be incorporated for clinical decision-making. These data suggest that measurements of LVEF should be

reported as a maximal likelihood point estimate with a 95% confidence interval - a patient with a point estimate LVEF of 33%, could be reported instead, as a patient with an LVEF between 24 and 42%. Whilst clinical guidelines require absolute numbers, imprecision is inadequately acknowledged, and decision-making is deferred to multi-disciplinary consensus or a post-hoc review of imaging data with the knowledge of other variables.

The collated real-world benchmarking resource (the VOLUMES resource) will be made available for training, validating new clinical measures and automated analysis techniques. This will include a built-in web application to provide online precision analysis, and comparison against other observers. Currently, the imaging and analysis data are being used to validate a new clinical measure (“global wall thickness”), and other automated approaches. A more precise automated technique than clinician analysis has not yet been described, but such a method is not out of reach. This may provide a useful tool for detecting changes in serial scanning if combined with co-registration strategies used in this work. The generalisability, speed and precision of automated techniques demonstrated in this work suggest they can be now applied to Corelabs and clinical workflows. Further work would require testing the ability to predict outcomes, and the application of more refined segmentation algorithms. This requires translation into the computer vision domain, and so discussions have begun to develop a MICCAI challenge using the resource. Despite the advent of automated technologies, our understanding of human error can be further explored. Sample sizes have been presented for different pathologies, but it is uncertain what structural features contribute to precision variability. Additionally human factors beyond training and experience (such as basal slice selection) could be explored. Right ventricular analysis

is recognized as more difficult than LV analysis, but real-world precision of human or automated techniques remains unknown.

A cardiac-atlas based approach to 3D LV modelling in aortic stenosis is also sufficiently precise. Precision here refers to the Metrological definition, as defined in the Introduction (Section 1.2.3). Different interpretations do exist, and are equally relevant to future work. “Precision medicine” refers to treatment decisions that factor in individual variability, typically related to molecular medicine.⁴⁴⁹ For computer scientists, precision may be interpreted as the positive predictive value for a test. Whilst an atlas approach captures more personalised, detailed phenotyping, it must also be demonstrably precise- in both other senses of the definition- to translate to clinical practice. Future work will therefore require the application of a cardiac-atlas analysis approach for outcome prediction in AS. This has recently been demonstrated as a superior approach to outcome prediction in pulmonary hypertension.³⁹⁸ Deeper phenotypes incorporating motion analysis and wall stress may be required, and would also help to provide mechanistic insights into the spectrum of LV adaptation-maladaptation in AS (is it more regional, longitudinal or circumferential motion that contributes to overall function?). Preliminary work (not presented in this thesis) has described an association between lower systemic vascular resistance and a larger, thicker walled ventricle except for the septum.⁴⁵⁰ This suggests that there may be other influences in AS LV remodelling in the septum. Changes in cardiac metabolism may be useful to determine whether structural changes are adaptive or maladaptive. Serum samples have been processed for metabolomic analysis, and future work will require linking this with imaging phenotypes. Serum metabolomic analysis may also contribute changes in cardiovascular risk-profiles with exercise training.

HFpEF requires more advanced phenotypes than either blood pressure or ejection fraction currently offer. Patients may be sub-stratified through detailed phenotyping from aortic wave intensity analysis. Coronary WIA has successfully stratified patients with AS into those with failing and non-failing ventricles.⁴⁵¹ As demonstrated here in health and exercise training, WIA may be able to provide mechanistic insight into drug mechanisms, or other diseases. The technique is currently being used in trials of inorganic nitrates for the treatment of hypertension; Anderson-Fabry disease; obesity and life-long exercise. The data presented in this thesis suggests increased wave reflection in ageing and female sex. Both are associated with increased risk of developing HFpEF.^{277,452}

There is an increasing focus on preventative Cardiology and lifestyle medicine. As described in this thesis, changes in sub-clinical phenotypes of arterial stiffness and ventriculo-arterial coupling may be useful to inform healthy risk-reduction behaviour. Whilst vascular benefits were observed at relatively low exercise doses in real-world training programmes, the exercise-dose response curve is not yet completely known. Studies have been completed in veteran athletes using phase-contrast CMR sequence to derive measurement of aortic stiffness and ventriculo-arterial coupling. Whilst the data in this thesis suggests training has a direct impact on aortic remodelling, the mechanisms of these changes is not yet known, and measures such as diet or endothelial function may provide further insight.

8.3. Limitations

This work demonstrated that it is possible to extract more detailed cardiovascular phenotypes from clinical CMR sequences. This was performed in retrospective and prospective clinical studies, but was not applied in a prospective workflow. Application in this work required data acquisition, collation, standardisation, preparation for analysis. For data analysis itself, techniques required adequate computing power, and refinement through curation of training databases, weighting of automated approaches, and artefact detection strategies.

Clinical application was studied in health and disease, but great variation exists on the spectrum between novice exercise training and aortic stenosis. These studies demonstrated mechanistic and sub-clinical insights. To avoid the fallacy of computer assisted detection software in the 1990s (Figure 1-15), studies of major cardiovascular events should demonstrate the clinical utility of more detailed phenotyping, rather than observational studies as described here.

This study elected to use CMR data rather than other imaging modalities. This is because of the cross-sectional nature of the technique permits standardized assessment of cardiac and aortic function. Whilst CMR is relatively expensive and time-consuming compared to other imaging modalities, automated approaches may help to extract more information in a value-based manner.

8.4. Conclusions

This thesis describes the feasibility of using automated analysis approaches to develop more detailed cardiovascular phenotypes than current clinical assessments. Automating analysis of clinical cardiovascular phenotypes is precise with significant time-saving. Complex data that is usually discarded can be used efficiently to identify new biology. Clinically, deeper phenotypes can inform risk reduction behaviour in healthy individuals, and demonstrably deliver a more sensitive marker of LV remodelling, potentially enhancing risk prediction in severe aortic stenosis.

9. Academic Outputs

9.1. Awards during this studentship

2019

President's Medal Winner, Royal Society of Medicine, for the best UK Cardiology PhD.

Young Investigator Runner-up, EuroCMR, Venice, Italy.

Young Investigator Runner-up, British Society of Cardiovascular Magnetic Resonance, Oxford, UK.

British Cardiovascular Society Hackathon third place, "CPR for schools" seed funding, Manchester, UK.

National Cardiac Benchmarking Collaborative Service Improvement Award – Shortlisted (submitter), Manchester, UK.

2018

Young Investigator Winner, International Artery Society, Guimaraes, Portugal.

Health Service Journal "Improving the value of diagnostics" – Winner (submitter, presenter), Manchester, UK.

British Medical Journal Diagnostic Team of the Year Award - MRI for pacemaker patients (submitter, presenter), London, UK.

Moderated Poster Finalist, Society for Cardiovascular Magnetic Resonance, Barcelona, Spain.

Barts Health Heroes award for contributions to the department of Cardiac Imaging, London, UK.

Travel Scholarship, Artery Conference, , Guimaraes, Portugal.

2017

Young Investigator Finalist, Society for Cardiovascular Magnetic Resonance, Los Angeles, USA.

Walking Poster Finalist, Society for Cardiovascular Magnetic Resonance, Los Angeles, USA.

Travel Scholarship, Society for Cardiovascular Magnetic Resonance, Los Angeles, USA.

9.2. Publications during this studentship

** denotes first author publication in full manuscript * denotes first author publication in abstract

Published papers, letters and abstracts

2019

26. ****Non-invasive assessment of ventriculo-arterial coupling using aortic wave intensity analysis combining central blood pressure and phase-contrast cardiovascular magnetic resonance**
Bhuva AN, D'Silva A, Torlasco C, Nadarajan N, Jones S, Boubertakh R, Van Zalen J, Scully P, Knott K, Benedetti G, Augusto JB, Rachel Bastiaenen, Lloyd G, Sharma S, Moon JC, Parker KH, Manisty CH, Hughes AD
Eur Heart J Cardiovasc Imaging. 2019 Sep 9. [Epub ahead of print]
25. ****A multi-center, scan-rescan, human and machine learning CMR study to test generalizability and precision in imaging biomarker analysis.**
Bhuva AN, Bai W, Lau C, Davies RH, Ye Y, Bulluck H, McAlindon E, Culotta V, Swoboda PP, Captur G, Treibel TA, Augusto JB, Knott KD, Seraphim A, Cole GD, Petersen SE, Edwards NC, Greenwood JP, Bucciarelli-Ducci C, Hughes AD, Rueckert D, Moon JC, Manisty CH
Circulation: Cardiovascular Imaging Aug 2019. [Accepted, in press]
24. ****Cardiovascular magnetic resonance: a promising method for detecting myocardial scar in patients with cardiac implantable devices. Response to Editor.**
Bhuva AN, Manisty CH
IJC 2019 Nov 1;294:60 [Epub ahead of print]
23. ****Sex and regional differences in myocardial plasticity in aortic stenosis are revealed by 3D model machine learning**
Bhuva AN, Treibel TA, De Marvao A, Biffi C, Dawes TJW, Doumou G, Patel K, Boubertakh R, Bai W, Rueckert D, O'Regan DP, Hughes AD, Moon JC, Manisty CH
EHJ Cardiovascular Imaging 2019 Jul 5 [Epub ahead of print]
22. ****MRI for patients with cardiac implantable electronic devices: simplifying complexity with a 'one-stop- service model**
Bhuva AN, Feuchter P, Hawkins A, Cash L, Boubertakh R, Evanson J, Schilling R, Lowe, M, Moon JC, Manisty CH
BMJ Qual Saf 2019 Feb 13
21. **Quantitative myocardial perfusion in coronary artery disease: A perfusion mapping study**
Knott KD, Camaioni C, Ramasamay A, Augusto JA, Bhuva AN, Xue H, Manisty C, Hughes RK, Brown LAE, Amersey R, Bourantas C, Kellman P, Plein S, Moon JC
J Magn Reson Imaging. 2019 Jan 25

20. ****Clinical impact of cardiovascular magnetic resonance with optimized myocardial scar detection in patients with cardiac implantable device**
Bhuva AN, Kellman P, Graham A, Ramlall M, Boubertakh R, Feuchter P, Hawkins A, Lowe M, Lambiase PD, Sekhri N, Schilling RJ, Moon JC, Manisty CH
IJC 2019 Mar 15; 279:72-78

19. **INCA (Peru) Study: Impact of non-invasive cardiac magnetic resonance assessment in the develop world**
 Menacho K, Ramirez S, Segura P, Nordin S, Abdel-Gadir A, Illatopa V, Bhuva A, Benedetti G, Boubertakh R, Abad P, Rodriguez B, Medina F, Treibel T, Westwood M, Fernandes J, Walker JM, Litt H, Moon JC
J Am Heart Assoc. 2018 Sept 4;7(17):e008981

- 2018**
18. **Reverse Myocardial Remodelling Following Valve Replacement in Patients With Aortic Stenosis.**
 Treibel TA, Kozor R, Schofield R, Benedetti G, Fontana M, **Bhuva AN**, Sheikh A, Lopez B, Gonzalez A, Manisty C, Lloyd G, Kellman P, Diez J, Moon JC
JACC. 2018;71(8):860-871

17. **Myocardial native T1 and extracellular volume (ECV) with healthy ageing and gender.**
 Rosmini S, Bulluck H, Captur G, Treibel TA, Abdel-Gadir A, **Bhuva AN**, Culotta V, Merghani A, Fontana M, Maestrini V, Herrey A, Piechnik S, Kellman P, Manisty CH, Moon JC
EHJ Cardiovascular Imaging 2018; Mar 30

16. ****MRI for patients with cardiac implantable electronic devices**
Bhuva AN, Feuchter P, Moon JC , Manisty CH
RAD Magazine 2018;44(516):11-12

15. ***Feasibility of aortic wave intensity analysis from cardiac MRI and non-invasive central blood pressure.**
Bhuva AN, Nadarajan N, D'Silva A, Torlasco C, Jones S, Boubertakh R, Scully P, Bastiaenen R, Lloyd G, Sharma S, Moon JC, Parker K, Manisty CH, Hughes AD
Artery Research 2018;24:71

14. ***MRI- conditionality has no impact on pacemaker and defibrillator lead parameter changes with MRI at 1.5T**
Bhuva AN, Lascelles K, Patel K, Lowe M, Sekhri N, Alpendurada F, Pennell D, Boubertakh R, Schilling R, Moon JC, Baksi JA, Mansity CH
Heart 2018;104:A14

13. ***Proximal but not distal aortic stiffness explains blood pressure reduction associated with exercise training for a first time marathon**
Bhuva AN, D'Silva A, Torlasco C, Nadarjan N, Jones S, Knott KD, Benedetti G, Scully P, Bastiaenen R, Kellman P, Lloyd G, Chaturvedi N, Sharma S, Moon JC, Hughes AD, Manisty CH
Heart 2018;104:A13

2017

12. **Redefining viability by cardiovascular magnetic resonance in acute ST-segment elevation myocardial infarction.**
Bulluck H, Rosmini S, Abdel-Gadir A, **Bhuva AN**, Treibel TA, Fontana M, Knight DS, Nordin S, Sirker A, Herrey AS, Manisty C, Moon JC, Hausenloy DJ
Scientific Reports. 2017;7:14676.

11. **Improved Exercise-Related Skeletal Muscle Oxygen Consumption Following Uptake of Endurance Training Measured Using Near-Infrared Spectroscopy.**
Jones S, D'Silva A, **Bhuva AN**, Lloyd G, Manistyh C, Moon JC, Sharma S, Hughes AD
Frontiers in Phys 2017;8:1018

10. ***Decreased systemic vascular resistance is associated with a larger, thicker walled ventricle except for the septum in aortic stenosis.**
Bhuva AN, Treibel TA, Doumou G, De Marvao A, Biffi C, Dawes T, Jones S, O'Regan D, Moon JC, Hughes AD, Manisty CH
Artery Research 2017;20:107

9. ***Wideband MOCO LGE changes patient care in patients with implanted cardiac devices.**
Bhuva AN, Ramlall M, Boubertakh R, Knott K, Feuchter P, Sekhri N, Schilling R, Kellman P, Moon JC, Manisty CH
Heart 2017;103:A11-A12

8. **Defining left ventricular remodelling following acute ST-segment elevation myocardial infarction using cardiovascular magnetic resonance.**
Bulluck H, Go YY, Crimi G, Ludman AJ, Rosmini S, Abdel-Gadir A, **Bhuva AN**, Treibel TA, Fontana M, Pica S, Raineri C, Sirker A, Herrey A, Manisty C, Groves A, Moon JC, Hausenloy D.
JCMR 2017;19:26.

7. **Diagnostic performance of T_1 and T_2 mapping to detect intramyocardial hemorrhage in reperfused ST-segment elevation myocardial infarction (STEMI) patients.**
Bulluck H, Rosmini S, Abdel-Gadir A, **Bhuva AN**, Treibel TA, Fontana M, Gonzalez-Lopez E, Ramlall M, Hamarneh A, Sirker A, Herrey A, Manisty C, Yellon DM, Moon JC, Hausenloy DJ
JMRI 2017;46(3):877-886.

6. **Impact of microvascular obstruction on semiautomated techniques for quantifying acute and chronic myocardial infarction by cardiovascular magnetic resonance.**
Bulluck H, Rosmini S, Abdel-Gadir A, **Bhuva AN**, Treibel TA, Fontana M, Weinmann S, Sirker A, Herrey AS, Manisty C, Moon JC, Hausenloy DJ
Open Heart. 2016;3(2):e000535.

2016

5. **Residual Myocardial Iron Following Intramyocardial Hemorrhage During the Convalescent Phase of Reperfused ST-Segment–Elevation Myocardial Infarction**
Bulluck H, Rosmini S, Abdel-Gadir A, White SK, **Bhuva AN**, Treibel TA, Fontana M, Ramlall M, Hamarneh A, Sirker A, Herrey AS, Manisty C, Yellon D, Kellman P, Moon JC, Hausenloy DJ
Circ Cardiovasc Imaging. 2016;9:e004940.

4. **Left ventricular remodelling after reperfused myocardial infarction: insights from automated ECV mapping.**
Bulluck H, White SK, Rosmini S, Abdel-Gadir A, **Bhuva AN**, Treibel TA, Fontana M, Reant P, Ramlall M, Hamarneh A, Sirker A, Herrey AS, Manisty C, Kellman P, Moon JC, Hausenloy DJ
Journal of Cardiovascular Magnetic Resonance. 2016;18(Suppl 1):Q67.

3. **Automated Extracellular Volume Fraction Mapping Provides Insights Into the Pathophysiology of Left Ventricular Remodelling Post-Reperfused ST-Elevation Myocardial Infarction.**
Bulluck H, Rosmini S, Abdel-Gadir A, White SK, **Bhuva AN**, Treibel TA, Fontana M, Gonzalez-Lopez E, Sirker A, Herrey AS, Manisty C, Yellon DM, Kellman P, Moon JC, Hausenloy DJ
J Am Heart Assoc. 2016 Jul 11;5(7). PMID: 27402229

2. **Intracoronary ethanol ablation of ventricular premature contractions in patients with preserved left ventricular function**
Lellan AJA, **Bhuva A**, Sporton S, Knight C, O'Mahony C, Dhinoja MB
Indian Pacing and Electrophysiology Journal. 2016;16(5):165-168.

1. **Automatic Measurement Of The Myocardial Interstitium: Synthetic Extracellular Volume Quantification without Hematocrit Sampling.**
Treibel TA, Fontana M, Maestrini V, Castelletti S, Rosmini S, Nasir A, **Bhuva A**, ...Manisty C, Spottiswoode BS, Wong TC, Piechnik SK, Kellman P, Robson MD, Schelbert EB, Moon JC.
JACC Cardiovasc Imaging. 2016 Jan;9(1):54-63.

Submitted manuscripts under review

4. ****Training for a first-time marathon reverses age-related aortic stiffening: a prospective longitudinal cohort study**
Bhuva AN, D'Silva A, Torlasco C, Jones S, Nadarajan N, Van Zalen J, Chaturvedi N, Lloyd G, Sharma S, Moon JC, Hughes AD, Manisty CH

3. **Improving the generalisability of convolutional neural network-based segmentation on cardiac MR images**
Chen C, Bai W, Davies RH, **Bhuva AN**, Manisty C, Moon JC, Aung N, Lee AM, Sanghvi MM, Fung J, Paiva JM, Petersen SE, Lukaschuk E, Piechnik SK, Neubauer S, Rueckert D

2. Myocardial inflammation and edema in People living with Human Immunodeficiency Virus

Menacho K, Seraphim A, Ramirez S, Falcon L, **Bhuva AN**, Alave J, Banda C, Mejia F, Salazar D, Putri A, Mosto F, Gonzales P, Culotta V, Menacho J, Herrey AS, Ntobeko ABN, Walker JM, Moon JC

1. Left ventricular mass and global wall thickness- characterization of left ventricular hypertrophy and prognostic utility

Lundin M, Heiberg E, Nordlund D, Gyllenhammar T, Steding-Ehrenborg K, Engblom H, Carlsson M, Atar D, van der Pals J, Erlinge D, Borgquist R, Khoshnood A, Ekelund U, Nickander J, Themudo R, Nordin S, Kozor R, **Bhuva AN**, Moon JC, Maret E, Caidahl K, Sigfridsson A, Sörensson P, Schelbert E, Arheden H, Ugander M

Review articles

4. **Advanced Imaging Modalities to Monitor for Cardiotoxicity**
Seraphim A, Westwood M, **Bhuva AN**, Crake T, Moon JC, Menezes LJ, Lloyd G, Ghosh AK, Slater S, Oakervee H, Manisty C
Curr. Treat. Options in Oncol. 2019;20:73
3. **Quantitative cardiac MRI**
Seraphim A, Knott KD, Augusto J, **Bhuva AN**, Manisty C, Moon JC
J Magn Reson Imaging. 2019 May 20
2. ****Imaging fibrosis in heart failure with preserved ejection fraction**
Bhuva AN, Schofield R, Lumbers T, Manisty CH, Moon JC
Heart Metab. 2016; 71:18-22
1. **Cardiovascular Magnetic Resonance frontiers: tissue characterisation with mapping**
Schofield R, **Bhuva AN**, Manacho K, Moon JC
S Afr J Rad. 2016;20(2), a1019.

9.3. Presentations

2019

Deep phenotyping approaches to cardiovascular magnetic resonance imaging, Cardiology President's Medal winner, Royal Society of Medicine

Cardiovascular benefits of first-time marathon training, Young Investigator Runner- up, EuroCMR,

Safety of MRI-conditional and legacy leads undergoing MRI, Late Breaking Registry (first author), EuroCMR

Head to head: Automated vs Clinician LV analysis, Oral Presentation, EuroCMR

Training for a first-time marathon reverses vascular ageing, Young Investigator Runner- up, British society of Cardiac MRI

2018

Feasibility of aortic wave intensity analysis from cardiac MRI and non-invasive central blood pressure, Young Investigator Award winner Artery Society.
Artery Research 2018;24:71

MRI- conditionality has no impact on pacemaker and defibrillator lead parameter changes with MRI at 1.5T
Young Investigator Poster Finalist British Society of Cardiovascular Magnetic Resonance
Heart 2018;104:A14

Aortic stenosis septal hypertrophy and its regression post AVR is more plastic in males than females: insights from a 3D cardiac atlas
Poster presentation Society for Cardiovascular Magnetic Resonance

Proximal but not distal aortic stiffness explains blood pressure reduction associated with exercise training for a first time marathon
Young Investigator Poster Finalist British Society of Cardiovascular Magnetic Resonance
Heart 2018;104:A13.

Blood pressure reduction with six months exercise training is mediated by changes in proximal but not distal aortic stiffness as assessed by CMR
Moderated Poster Finalist Society for Cardiovascular Magnetic Resonance

Blood pressure reduction with six months exercise training is mediated by changes in proximal but not distal aortic stiffness as assessed by CMR
Medical Research Council presentation at the Institute of Cardiovascular Sciences, UCL

2017

Wideband free breathing MOCO LGE changes patient care in patients with CIEDs

Poster presentation, British Society of Cardiovascular Magnetic Resonance
Heart 2017;103:A11-A12.

In severe aortic stenosis, decreased systemic vascular resistance is associated with a larger, thicker walled ventricle except for the septum.

Poster presentation Artery Society
Artery Research 2017;20;107

Wideband late gadolinium enhancement gives important insights in patients with implanted cardiac devices.

Early Career Award Finalist Society for Cardiovascular Magnetic Resonance
Resonance

Off resonance error correction to improve myocardial T1 mapping in patients with implanted cardiac devices

Oral Moderated Poster Finalist Society for Cardiovascular Magnetic Resonance

9.4. Invited presentations during this studentship

2019

MRI for patients with cardiac devices

Invited Lecture Royal Society of Medicine (Cardiology SpR training day)

MRI for patients with cardiac devices: time to tear up the rule-book?

Invited Lecture UK Imaging & Oncology Conference

Service development - Implantable cardiac devices and MRI

Invited Webinar Royal College of Radiology

Managing artefact from implanted devices

Invited Lecture British Society of Cardiovascular Magnetic Resonance

Cardiac MRI for patients with cardiac devices

Invited Lecture, Havana, Cardiology Society of Cuba

2018

CMR to guide Cardiac Resynchronization Therapy

Invited Lecture International Society of Cardiovascular Magnetic Resonance

Getting to the heart of the matter – an unusual case of LVH due to Conn's Syndrome

Grand Round, St Bartholomew's Hospital

Cardiac imaging in cancer treatment

Grand Round, University College London Hospital

Barriers to setting up an MRI Cardiac Device service

Grand Round, Brighton General Hospital

2017

MRI for cardiac device patients

Grand Round, St Bartholomew's Hospital

2016

Imaging guided ventricular tachycardia ablation

Invited Lecture Royal Society of Medicine (Cardiology SpR training day).

9.5. Co-authored presentations and abstracts

The value of scar mapping by cardiac magnetic resonance imaging pre ablation for ventricular tachycardia: should an implantable cardioverter defibrillator put you off?

Seraphim A, **Bhuva AN**, Moon JC, Manisty CH
Poster Presentation, EuroCMR 2019

General anaesthesia: a stress on the heart?

Seraphim A, Bhuva AN, Moon JC, Manisty CH
Poster Presentation, EuroCMR 2019

Left ventricular ejection fraction quantification for cardiotoxicity, measurement precision differs between modalities

Menacho K, Culotta V, **Bhuva A**, Davies R, Ferreira A, Carneiro O, Gosh A, Westwood M, Menezes L, Lloyd G, Moon G, Manisty C
Poster Presentation, EuroCMR 2019

Aortic stenosis. the role of aortoseptal angulation as a predictive factor for asymmetrical septal hypertrophy

Jenkins A, **Bhuva AN**, Hughes AD, Manisty CH, Moon JC, Treibel TA
Poster Presentation, EuroCMR 2019

Left Ventricular Mechanics Reveals a Benign Reduction in Ejection Fraction After Valve Replacement in Aortic Stenosis

Patel K, Eiros R, Boubertakh R, Moir S, Kozor R, Davies R, **Bhuva AN**, Scully PR, Herrey AS, Manisty C, Moon JC, Treibel TA
Abstract EuroCMR 2019

Extracellular Volume Expansion Predicts Mortality in Aortic Stenosis

Treibel TA, Patel K, Kozor R, Scully P, **Bhuva AN**, Schofield R, White SK, Herrey A, Fontana M, Manisty CH, Moon JC
Quick Fire Abstract SCMR 2019

Primary aldosteronism is associated with regional and whole aortic stiffness

Nadarajan N, **Bhuva AN**, Lau C, Torlasco C, D'Silva A, Hughes AD, Moon JC, Drake W, Manisty CH
Poster Presentation SCMR 2019

Exercise-induced left ventricular trabeculation: real entity or fake news?

D'Silva A, **Bhuva AN**, Jones S, van Zalen J, Bastiaenen R, Menacho K, Abdel-Gadir A, Treibel TA, Rosmini S, Ramlal M, Scully PR, Liu S, Yeo T, Ensam B, Conley K, Ah-Fong J, Della C, Augusto J, Ye Y, Captur G, Gati S, Torlasco C, Sharma R, Patel R, Bhattacharyya S, Hughes A, Lloyd G, Manisty C, Moon J, Sharma S
Poster Presentation, ESC 2018

Age matters: differences in cardiac response to training in young and middle aged first-time marathon runners

C Torlasco, A D'silva, J Augusto, A Faini, K Knott, **A Bhuva**, G Benedetti, P Scully, S Jones, I Lobascio, G Parati, G Lloyd, C Manisty, JC Moon, S Sharma
Poster presentation, ESC 2018

Defining the effects of genetic variation using machine learning analysis of CMRS: a study in hypertrophic cardiomyopathy and in a healthy population

Marvao AD, Biffi C, Walsh R, Doumou G, Dawes T, Shi W, Bai W, Berry A, Buchan R, Pierce I, Tokarczuk P, Statton B, Francis C, Duan J, Quinlan M, Felkin L, Le Thu, **Bhuva A**, Tang H, Barton P, Chin C, Rueckert D, Ware J, Prasad S, O'Regan DP, Cook SA.
Heart 2018;104:A7-A8.

Validation of ultrasound determination of local pulse wave velocity in the human ascending aorta against MRI measurements.

Negoita M, Manisty C, **Bhuva A**, Hughes A, Parker K, Khir A.
Artery Research, 2018(24):62

Myocardial perfusion is influenced by age, gender, diabetes, myocardial fibrosis and the use of beta-blockers: a perfusion mapping study

Knott KD, Camaioni C, **Bhuva AN**, Brown L, Xue H, Manisty CH, Plein S, Kellman P, Moon JC
Heart 2018;104:A13-A14.

Exercise-induced cardiac remodelling in novice marathon runners

D'Silva A, **Bhuva AN**, Jones S, van Zalen J, Bastiaenen R, Menacho K, Abdel-Gadir A, Treibel TA, Rosmini S, Ramlal M, Scully PR, Liu S, Yeo T, Ensam B, Conley K, Ah-Fong J, Della C, Augusto J, Ye Y, Captur G, Gati S, Torlasco C, Sharma R, Patel R, Bhattacharyya S, Hughes A, Lloyd G, Manisty C, Moon J, Sharma S
Oral presentation, SCMR 2018

A Bi-ventricular atlas for machine learning analysis of hypertrophic cardiomyopathy CMR

Doumou G, De Marvao A, Biffi C, Walsh R, Shi W, Dawes T, Bai W, Pierce I, Tokarczuk P, Le T, **Bhuva A**, Tang J, Chin C, Rueckert R, Ware JS, Prasad S, O'Regan D, Cook S
Oral presentation, SCMR 2018

We don't know how to measure wall thickness in HCM- Time for a guideline?

Captur G, Manisty C, Ariga R, Lobascio I, Camaioni C, Ofori J, Nakamori S, **Bhuva AN**, Zaha V, Wong TC, Nasis A, Al-Mallah M, Valentin S, Arenaza DP, Olivotto I, Kwong RY, Neubauer S, Lloyd G, Nihoyannopoulos P, Moon J
Oral presentation, SCMR 2018

Stop drawing circles! Deep learning for automating volumetric analysis

Davies R, Treibel T, Bhuva AN, Captur G, Manisty C, Xue H, Kellman P, Moon JC
Poster presentation, SCMR 2018

Myocardial perfusion reserve falls in diabetes and with increasing age – a perfusion mapping study

Academic Outputs

Knott K, Camaioni C, **Bhuva A**, Captur G, Xue H, Manisty CH, Bourantas C, Plein S, Kellman P, Moon JC
Heart 2017;103:A19-A20.

Perfusion mapping in hypertrophic cardiomyopathy: microvascular dysfunction occurs regardless of hypertrophy

Camaioni C, Knott K, Captur G, **Bhuva A**, Lops L, Xue H, Brown L, Mohiddin S, Manisty C, Plein S, Kellman P, Moon JC
Heart 2017;103:A4.

9.6. Collaborations

1. Imperial College London, MRC Clinical Sciences Centre.

Dr Declan O'Regan, MRC Senior Clinical Scientist.

2. Imperial College London, Department of Computing, Biomedical Image Analysis Group.

Professor Daniel Rueckert, Professor of Visual Information Processing.

3. St George's University, Sports Cardiology Unit.

Professor Sanjay Sharma, Professor of Cardiology.

4. Kings College London , Imaging and Biomedical Engineering Clinical Academic Group.

Jorge Mariscal Harana, PhD student.

Dr Jordi Alastruey, Senior Lecturer.

5. Kings College London and University of Auckland, Department of Biomedical Engineering.

Professor Alistair Young, Professor of machine learning.

6. Circle, Cardiovascular Imaging Incorporated. Calgary, Canada.

7. University College London, Institute of Cardiovascular Sciences, Translational Mass Spectrometry Group.

Dr Kevin Mills, Head of Department.

9.7. Teaching

Course Director –

MRI for patients with cardiac devices (>100 delegates, 7 countries)

Course Faculty –

Level 1 CMR course, St Thomas' Hospital

Level 1 CMR course, Lima, Peru

Regular tutor –

MRCP PACES examinations “Pass PACES course”

London Deanery Medical Registrar Refresher Course- ECG workshop

CMR for Radiographers- Improver's Course, Barts Heart Centre

MSc Supervision, Institute of Cardiovascular Sciences, University College London

Niromila Nadarajan - Distinction, 2017

Alice Jennings – Distinction, 2018

Kristina Thompson – Merit, 2018

Cardiometabolic Pathway Tutor, UCL Medical School, 2017-2019

9.8. Funding enabling this work

I am grateful to the following funders:

1. British Heart Foundation Clinical Research Training Fellowship award 2016-2019.
2. Development of a semi-automated, level set algorithm for improved quantification of ventricular function Academic Support Grant, Barts Hospital Charity, 2015-2018.
3. Research Grant, Abbott Laboratories 2019.

10. References

1. Topol E. The Topol Review: Preparing the Healthcare Workforce to Deliver the Digital Future; 2019.
2. HM GoIndustrial Strategy: Building a Britain Fit for the Future; 2017.
3. Townsend N, Williams J, Bhatnagar P, Wickramasinghe K, Rayner M. Cardiovascular Disease Statistics 2014.; 2014.
4. Scarborough P, Wickramasinghe K, Bhatnagar P, Rayner M. Trends in coronary heart disease , 1961-2011. *Hear Dis*. 2011;1961-2011.
5. Hill J a, Olson EN. Cardiac plasticity. *N Engl J Med*. 2008;358(13):1370-1380. doi:10.1056/NEJMr072139
6. Lawrence C. Moderns and ancients: the “new cardiology” in Britain 1880-1930. *Med Hist Suppl*. 1985;(5):1-33.
7. Osler W. The Principles and Practice of Medicine.; 1892. doi:10.1007/s13398-014-0173-7.2
8. Maron BJ, Pelliccia A. The heart of trained athletes: Cardiac remodeling and the risks of sports, including sudden death. *Circulation*. 2006;114(15):1633-1644. doi:10.1161/CIRCULATIONAHA.106.613562
9. The SPRINT Research Group. A Randomized Trial of Intensive versus Standard Blood-Pressure Control. *N Engl J Med*. 2015;373(22):2103. doi:10.1056/NEJMoa1511939
10. Konstam M a, Kramer DG, Patel AR, Maron MS, Udelson JE. Left ventricular remodeling in heart failure: current concepts in clinical significance and assessment. *JACC Cardiovasc Imaging*. 2011;4(1):98-108. doi:10.1016/j.jcmg.2010.10.008
11. Buckberg GD, Hoffman JIE, Coghlan HC, Nanda NC. Ventricular structure-function relations in health and disease: Part I. The normal heart. *Eur J Cardiothorac Surg*. 2014;47(August 2014):1-15. doi:10.1093/ejcts/ezu278
12. Keith A. The Functional Anatomy of the Heart. *Bmj*. 1918;361-363.
13. Sallin EA. Fiber orientation and ejection fraction in the human left ventricle. *Biophys J*. 1969;9(7):954-964. doi:10.1016/S0006-3495(69)86429-5
14. Hall ME, George EM, Granger JP. The heart during pregnancy. *Rev Esp Cardiol*. 2011;64(11):1045-1050. doi:10.1016/j.recesp.2011.07.009
15. Lorell BH CB. Left Ventricular Hypertrophy. *Circulation*. 2000;102:470-479.
16. Allen DG, Kentish JC. The cellular basis of the length-tension relation in cardiac muscle. *J Mol Cell Cardiol*. 1985;17(9):821-840.
17. Gulati J, Ruf T, Goldstein DJ, et al. Length-sensing function of troponin C and Starling’s law of the heart. *Circulation*. 1992;85(5):1954-1955. doi:10.1161/01.cir.94.4.683
18. Andersen JB, Rourke BC, Caiozzo VJ, Bennett AF, Hicks JW. Physiology: Postprandial cardiac hypertrophy in pythons. *Nature*. 2005;434(7029):37-38. doi:10.1038/434037a
19. Eghbali M, Deva R, Alioua A, et al. Molecular and functional signature of heart hypertrophy during pregnancy. *Circ Res*. 2005;96(11):1208-1216. doi:10.1161/01.RES.0000170652.71414.16
20. Dorn GW. The fuzzy logic of physiological cardiac hypertrophy. *Hypertension*. 2007;49(5):962-970. doi:10.1161/HYPERTENSIONAHA.106.079426

References

21. Major RJ, Poss KD. Zebrafish Heart Regeneration as a Model for Cardiac Tissue Repair. *Drug Discov Today Dis Models*. 2007;4(4):219-225. doi:10.1016/j.ddmod.2007.09.002
22. Riquelme CA, Magida JA, Harrison BC, et al. Fatty acids identified in the Burmese python promote beneficial cardiac growth. *Science*. 2011;334(6055):528-531. doi:10.1126/science.1210558
23. Cohn JN, Ferrari R, Sharpe N. Cardiac remodeling concepts and clinical implications: a consensus paper from an international forum on cardiac remodeling. Behalf of an International Forum on Cardiac Remodeling. *J Am Coll Cardiol*. 2000;35(3):569-582.
24. Merghani A, Maestrini V, Rosmini S, et al. Prevalence of Subclinical Coronary Artery Disease in Masters Endurance Athletes With a Low Atherosclerotic Risk ProfileClinical Perspective. *Circulation*. 2017;136(2):126-137. doi:10.1161/CIRCULATIONAHA.116.026964
25. Merghani A, Malhotra A, Sharma S. The U-shaped relationship between exercise and cardiac morbidity. *Trends Cardiovasc Med*. 2016;26(3):232-240. doi:10.1016/j.tcm.2015.06.005
26. Frey N, Katus H a., Olson EN, Hill J a. Hypertrophy of the Heart: A New Therapeutic Target? *Circulation*. 2004;109(13):1580-1589. doi:10.1161/01.CIR.0000120390.68287.BB
27. Grossman W, Jones D, McLaurin LP. Wall stress and patterns of hypertrophy in the human left ventricle. *J Clin Invest*. 1975;56(1):56-64. doi:10.1172/JCI108079
28. Woods RH. A few applications of a physical theorem to membranes in the human body in a state of tension. *Trans R Acad Med Irel*. 1892;10(1):417-427. doi:10.1007/BF03171228
29. Niederer SA, Smith NP. The Role of the Frank–Starling Law in the Transduction of Cellular Work to Whole Organ Pump Function: A Computational Modeling Analysis. Nash M, ed. *PLoS Comput Biol*. 2009;5(4):e1000371. doi:10.1371/journal.pcbi.1000371
30. Uretsky S, Supariwala A, Nidadovolu P, et al. Quantification of left ventricular remodeling in response to isolated aortic or mitral regurgitation. *J Cardiovasc Magn Reson*. 2010;12:32. doi:10.1186/1532-429x-12-32
31. Dweck MR, Joshi S, Murigu T, et al. Left ventricular remodeling and hypertrophy in patients with aortic stenosis: insights from cardiovascular magnetic resonance. *J Cardiovasc Magn Reson*. 2012;14(1):50. doi:10.1186/1532-429X-14-50
32. Gerdes AM. Cardiac myocyte remodeling in hypertrophy and progression to failure. *J Card Fail*. 2002;8(6):S264-S268. doi:10.1054/jcaf.2002.129280
33. Grossman W, Paulus WJ. Myocardial stress and hypertrophy : a complex interface between biophysics and cardiac remodeling. 2013;123(9):3701-3703. doi:10.1172/JCI69830.wall
34. Delhaas T, Arts T, Prinzen FW, Reneman RS. Regional fibre stress-fibre strain area as an estimate of regional blood flow and oxygen demand in the canine heart. *J Physiol*. 1994;477 (Pt 3):481-496.
35. Hein S, Arnon E, Kostin S, et al. Progression from compensated hypertrophy to failure in the pressure-overloaded human: Heart structural deterioration and compensatory mechanisms. *Circulation*. 2003;107(7):984-991. doi:10.1161/01.CIR.0000051865.66123.B7
36. Bernardo BC, Weeks KL, Pretorius L, McMullen JR. Molecular distinction between physiological and pathological cardiac hypertrophy: experimental findings and therapeutic strategies. *Pharmacol Ther*. 2010;128(1):191-227.

- doi:10.1016/j.pharmthera.2010.04.005
37. Levy D, Garrison RJ, Savage DD, Kannel WB, Castelli WP. Prognostic implications of echocardiographically determined left ventricular mass in the Framingham Heart Study. *N Engl J Med*. 1990;322(22):1561-1566. doi:10.1056/NEJM199005313222203
38. Gardin JM, McClelland R, Kitzman D, et al. M-mode echocardiographic predictors of six- to seven-year incidence of coronary heart disease, stroke, congestive heart failure, and mortality in an elderly cohort (the Cardiovascular Health Study). *Am J Cardiol*. 2001;87(9):1051-1057.
39. Koren MJ, Devereux RB, Casale PN, Savage DD, Laragh JH. Relation of left ventricular mass and geometry to morbidity and mortality in uncomplicated essential hypertension. *Ann Intern Med*. 1991;114(5):345-352.
40. Shenasa M, Shenasa H, El-Sherif N. Left ventricular hypertrophy and arrhythmogenesis. *Card Electrophysiol Clin*. 2015;7(2):207-220. doi:10.1016/j.ccep.2015.03.017
41. Bikkina M, Levy D, Evans JC, et al. Left ventricular mass and risk of stroke in an elderly cohort. The Framingham Heart Study. *JAMA*. 1994;272(1):33-36.
42. Spirito P, Bellone P, Harris KM, Bernabo P, Bruzzi P, Maron BJ. Magnitude of left ventricular hypertrophy and risk of sudden death in hypertrophic cardiomyopathy. *N Engl J Med*. 2000;342(24):1778-1785. doi:10.1056/NEJM200006153422403
43. Haider AW, Larson MG, Benjamin EJ, Levy D. Increased left ventricular mass and hypertrophy are associated with increased risk for sudden death. *J Am Coll Cardiol*. 1998;32(5):1454-1459.
44. Ghali JK, Liao Y, Cooper RS. Influence of left ventricular geometric patterns on prognosis in patients with or without coronary artery disease. *J Am Coll Cardiol*. 1998;31(7):1635-1640.
45. Lavie CJ, Milani R V, Shah SB, et al. Impact of left ventricular geometry on prognosis-a review of ochsner studies. *Ochsner J*. 2008;8(1):11-17.
46. Verdecchia P, Schillaci G, Borgioni C, et al. Adverse prognostic significance of concentric remodeling of the left ventricle in hypertensive patients with normal left ventricular mass. *J Am Coll Cardiol*. 1995;25(4):871-878. doi:10.1016/0735-1097(94)00424-O
47. Ganau A, Devereux RB, Roman MJ, et al. Patterns of left ventricular hypertrophy and geometric remodeling in essential hypertension. *J Am Coll Cardiol*. 1992;19(7):1550-1558. doi:10.1016/0735-1097(92)90617-V
48. Hill JA, Karimi M, Kutschke W, et al. Cardiac hypertrophy is not a required compensatory response to short-term pressure overload. *Circulation*. 2000;101(24):2863-2869.
49. Esposito G, Rapacciuolo A, Prasad SVN, et al. Genetic Alterations That Inhibit In Vivo Pressure-Overload Increased Wall Stress. *Circulation*. 2002;105:85-92. doi:10.1161/hc0102.101365
50. Torrent-Guasp F, Kocica MJ, Corno AF, et al. Towards new understanding of the heart structure and function. *Eur J Cardiothorac Surg*. 2005;27(2):191-201. doi:10.1016/j.ejcts.2004.11.026
51. Becker AE, Caruso G. Myocardial disarray. A critical review. *Heart*. 1982;47(6):527-538. doi:10.1136/hrt.47.6.527
52. Greenbaum RA, Ho SY, Gibson DG, Becker AE, Anderson RH. Left ventricular fibre architecture in man. *Heart*. 1981;45(3):248-263. doi:10.1136/hrt.45.3.248

References

53. Hexeberg E, Homans DC, Bache RJ. Interpretation of systolic wall thickening. Can thickening of a discrete layer reflect fibre performance? *Cardiovasc Res.* 1995;29(1):16-21. doi:10.1016/0008-6363(96)88540-3
54. Mulvany M. Vascular remodelling of resistance vessels: can we define this? *Cardiovasc Res.* 1999;41(1):9-13. doi:10.1016/S0008-6363(98)00289-2
55. Devereux RB, Bella JN, Palmieri V, et al. Left ventricular systolic dysfunction in a biracial sample of hypertensive adults: The HyperGEN study. *Hypertension.* 2001;38(3):417-423. doi:10.1161/01.HYP.38.3.417
56. Sadler DB, Aurigemma GP, Williams DW, Reda DJ, Materson BJ, Gottdiener JS. Systolic function in hypertensive men with concentric remodeling. *Hypertension.* 1997;30(4):777-781. doi:10.1161/01.HYP.30.4.777
57. Tadic M, Ivanovic B. Left ventricular geometry and aortic stenosis: The intriguing association. *Arch Cardiovasc Dis.* January 2017. doi:10.1016/j.acvd.2016.12.003
58. de Simone G, Daniels SR, Devereux RB, et al. Left ventricular mass and body size in normotensive children and adults: assessment of allometric relations and impact of overweight. *J Am Coll Cardiol.* 1992;20(5):1251-1260.
59. Ries M, Gupta S, Moore DF, et al. Pediatric Fabry Disease. *Pediatrics.* 2005;115:344-355. doi:10.1542/peds.2004-1678
60. Muiesan ML, Lupia M, Salvetti M, et al. Left ventricular structural and functional characteristics in Cushing's syndrome. *J Am Coll Cardiol.* 2003;41(12):2275-2279. doi:10.1016/S0735-1097(03)00493-5
61. Kuch B, Von Scheidt W, Peter W, et al. Sex-specific determinants of left ventricular mass in pre-diabetic and type 2 diabetic subjects: The Augsburg diabetes family study. *Diabetes Care.* 2007;30(4):946-952. doi:10.2337/dc06-2123
62. Gottdiener JS, Reda DJ, Materson BJ, et al. Importance of obesity, race and age to the cardiac structural and functional effects of hypertension. The Department of Veterans Affairs Cooperative Study Group on Antihypertensive Agents. *J Am Coll Cardiol.* 1994;24(6):1492-1498.
63. Krumholz HM, Larson M, Levy D. Prognosis of left ventricular geometric patterns in the Framingham Heart Study. *J Am Coll Cardiol.* 1995;25(4):879-884. doi:10.1016/0735-1097(94)00473-4
64. Bluemke DA, Kronmal RA, Lima JAC, et al. The relationship of left ventricular mass and geometry to incident cardiovascular events: the MESA (Multi-Ethnic Study of Atherosclerosis) study. *J Am Coll Cardiol.* 2008;52(25):2148-2155. doi:10.1016/j.jacc.2008.09.014
65. Muiesan ML, Salvetti M, Monteduro C, et al. Left Ventricular Concentric Geometry during Treatment Adversely Affects Cardiovascular Prognosis in Hypertensive Patients. *Hypertension.* 2004;43(4):731-738. doi:10.1161/01.HYP.0000121223.44837.de
66. Verma A, Meris A, Skali H, et al. Prognostic Implications of Left Ventricular Mass and Geometry Following Myocardial Infarction. *JACC Cardiovasc Imaging.* 2008;1(5):582-591. doi:10.1016/j.jcmg.2008.05.012
67. Gerds E, Cramariuc D, de Simone G, Wachtell K, Dahlöf B, Devereux RB. Impact of left ventricular geometry on prognosis in hypertensive patients with left ventricular hypertrophy (the LIFE study). *Eur J Echocardiogr.* 2008;9(6):809-815. doi:10.1093/ejehocardi/jen155
68. Galderisi M, Henein MY, Dhooge J, et al. Recommendations of the European Association of Echocardiography How to use echo-Doppler in clinical trials: Different

References

- modalities for different purposes. *Eur J Echocardiogr.* 2011;12(5):339-353. doi:10.1093/ejehocard/jer051
69. Mor-Avi V, Sugeng L, Weinert L, et al. Fast measurement of left ventricular mass with real-time three-dimensional echocardiography: comparison with magnetic resonance imaging. *Circulation.* 2004;110(13):1814-1818. doi:10.1161/01.CIR.0000142670.65971.5F
70. Khouri MG, Peshock RM, Ayers CR, De Lemos J a., Drazner MH. A 4-tiered classification of left ventricular hypertrophy based on Left ventricular geometry the dallas Heart study. *Circ Cardiovasc Imaging.* 2010;3(2):164-171. doi:10.1161/CIRCIMAGING.109.883652
71. Bang CN, Gerds E, Aurigemma GP, et al. Four-group classification of left ventricular hypertrophy based on ventricular concentricity and dilatation identifies a low-risk subset of eccentric hypertrophy in hypertensive patients. *Circ Cardiovasc Imaging.* 2014;7(3):422-429. doi:10.1161/CIRCIMAGING.113.001275
72. Bang C, M R, Best L, et al. A new four-group classification of left ventricular hypertrophy based on left ventricular geometry located a new high-risk group within eccentric hypertrophy in a population-based study: the strong heart study. *J Am Coll Cardiol.* 2013;61(10 Suppl):E1-2126.
73. Baltabaeva A, Marciniak M, Bijnens B, et al. Regional left ventricular deformation and geometry analysis provides insights in myocardial remodelling in mild to moderate hypertension. *Eur J Echocardiogr.* 2008;9(4):501-508. doi:10.1016/j.euje.2007.08.004
74. Florian A, Masci PG, De Buck S, et al. Geometric assessment of asymmetric septal hypertrophic cardiomyopathy by CMR. *JACC Cardiovasc Imaging.* 2012;5(7):702-711. doi:10.1016/j.jcmg.2012.03.011
75. Seiler C, Jenni R. Severe aortic stenosis without left ventricular hypertrophy: prevalence, predictors, and short-term follow up after aortic valve replacement. *Heart.* 1996;76(3):250-255.
76. de Marvao A, Dawes TJW, Shi W, et al. Population-based studies of myocardial hypertrophy: high resolution cardiovascular magnetic resonance atlases improve statistical power. *J Cardiovasc Magn Reson.* 2014;16(1):16. doi:10.1186/1532-429X-16-16
77. Mann DL. Left ventricular size and shape: determinants of mechanical signal transduction pathways. *Hear Fail Rev.* 2005;10(2):95-100. doi:10.1007/s10741-005-4636-y
78. Linzbach AJ. Heart Failure from the Point of View of Quantitative anatomy. *Am J Cardiol.* 1960;5(3):370-382.
79. Bonow RO. Chapter 25. In: Braunwald's Heart Disease: A Textbook of Cardiovascular Medicine. 9th Editio. Elsevier; 2012.
80. Mannaerts HFJ, Van Der Heide JA, Kamp O, et al. Quantification of left ventricular volumes and ejection fraction using freehand transthoracic three-dimensional echocardiography: comparison with magnetic resonance imaging. *J Am Soc Echocardiogr.* 2003;16(2):101-109. doi:10.1067/mje.2003.7
81. Wong SP, French JK, Lydon AM, et al. Relation of left ventricular sphericity to 10-year survival after acute myocardial infarction. *Am J Cardiol.* 2004;94(10):1270-1275. doi:10.1016/j.amjcard.2004.07.110
82. Opie LH, Commerford PJ, Gersh BJ, Pfeffer MA. Controversies in ventricular remodelling. *Lancet (London, England).* 2006;367(9507):356-367. doi:10.1016/S0140-

- 6736(06)68074-4
83. Mitchell GF, Lamas GA, Vaughan DE, Pfeffer MA. Left ventricular remodeling in the year after first anterior myocardial infarction: A quantitative analysis of contractile segment lengths and ventricular shape. *J Am Coll Cardiol.* 1992;19(6):1136-1144. doi:10.1016/0735-1097(92)90314-D
84. McMurray JJ V, Adamopoulos S, Anker SD, et al. ESC Guidelines for the diagnosis and treatment of acute and chronic heart failure 2012: The Task Force for the Diagnosis and Treatment of Acute and Chronic Heart Failure 2012 of the European Society of Cardiology. Developed in collaboration with the Heart. *Eur Heart J.* 2012;33(14):1787-1847. doi:10.1093/eurheartj/ehq278
85. Marwick TH. Ejection Fraction Pros and Cons: JACC State-of-the-Art Review. *J Am Coll Cardiol.* 2018;72(19):2360-2379. doi:10.1016/j.jacc.2018.08.2162
86. Vahanian A, Alfieri O, Andreotti F, et al. Guidelines on the management of valvular heart disease (version 2012). *Eur Heart J.* 2012;33(19):2451-2496. doi:10.1093/eurheartj/ehs109
87. Kellman P, Hansen MS. T1-mapping in the heart: accuracy and precision. *J Cardiovasc Magn Reson.* 2014;16(1):2. doi:10.1186/1532-429X-16-2
88. Sullivan DC, Obuchowski NA, Kessler LG, et al. Metrology Standards for Quantitative Imaging Biomarkers. *Radiology.* 2015;277(3):813-825. doi:10.1148/radiol.2015142202
89. Bellenger NG, Davies LC, Francis JM, Coats a J, Pennell DJ. Reduction in sample size for studies of remodeling in heart failure by the use of cardiovascular magnetic resonance. *J Cardiovasc Magn Reson.* 2000;2(4):271-278. doi:10.3109/10976640009148691
90. Suinesiaputra A, Bluemke DA, Cowan BR, et al. Quantification of LV function and mass by cardiovascular magnetic resonance: Multi-center variability and consensus contours. *J Cardiovasc Magn Reson.* 2015;17(1):1-8. doi:10.1186/s12968-015-0170-9
91. de Vet HCW, Terwee CB. The minimal detectable change should not replace the minimal important difference. *J Clin Epidemiol.* 2010;63(7):804-805. doi:10.1016/j.jclinepi.2009.12.015
92. Popović ZB, Thomas JD. Assessing observer variability: a user's guide. *Cardiovasc Diagn Ther.* 2017;7(3):317-324. doi:10.21037/cdt.2017.03.12
93. Suinesiaputra A, Cowan BR, Al-Agamy AO, et al. A collaborative resource to build consensus for automated left ventricular segmentation of cardiac MR images. *Med Image Anal.* 2014;18(1):50-62. doi:10.1016/j.media.2013.09.001
94. Moody W, Edwards NC, Chue CD, et al. Variability in cardiac MR measurement of left ventricular ejection fraction, volumes and mass in healthy adults: defining a significant change at 1 year. *Br J Radiol.* 2015;88(1049):20140831. doi:10.1259/bjr.20140831
95. Schulz-Menger J, Bluemke D a., Bremerich J, et al. Standardized image interpretation and post processing in cardiovascular magnetic resonance: Society for Cardiovascular Magnetic Resonance (SCMR) Board of Trustees Task Force on Standardized Post Processing. *J Cardiovasc Magn Reson.* 2013;15(1):35. doi:10.1186/1532-429X-15-35
96. Miller C a, Jordan P, Borg A, et al. Quantification of Left Ventricular Indices From SSFP Cine Imaging : Impact of Real-World Variability in Analysis Methodology and Utility of Geometric Modeling. *J Magn Reson Imaging.* 2013;1222(5):1213-1222. doi:10.1002/jmri.23892
97. Karamitsos TD, Hudsmith LE, Selvanayagam JB, Neubauer S, Francis JM. Operator induced variability in left ventricular measurements with cardiovascular magnetic

References

- resonance is improved after training. *J Cardiovasc Magn Reson*. 2007;9(5):777-783. doi:10.1080/10976640701545073
98. Petitjean C, Dacher JN. A review of segmentation methods in short axis cardiac MR images. *Med Image Anal*. 2011;15(2):169-184. doi:10.1016/j.media.2010.12.004
99. Marchesseau S, Ho JXM, Totman JJ. Influence of the short-axis cine acquisition protocol on the cardiac function evaluation: A reproducibility study. *Eur J Radiol Open*. 2016;3:60-66. doi:10.1016/j.ejro.2016.03.003
100. Papavassiliu T, Kühl HP, Schröder M, et al. Effect of Endocardial Trabeculae on Left Ventricular Measurements and Measurement Reproducibility at Cardiovascular MR Imaging. *Radiology*. 2005;236(1):57-64. doi:10.1148/radiol.2353040601
101. Miller C a, Jordan P, Borg A, et al. Quantification of left ventricular indices from SSFP cine imaging: impact of real-world variability in analysis methodology and utility of geometric modeling. *J Magn Reson Imaging*. 2013;37(5):1213-1222. doi:10.1002/jmri.23892
102. Bai W, Sinclair M, Tarroni G, et al. Automated cardiovascular magnetic resonance image analysis with fully convolutional networks. *arXiv:171009289 [csCV]*. 2017. doi:arXiv:1710.09289
103. Bernard O, Lalande A, Zotti C, et al. Deep Learning Techniques for Automatic MRI Cardiac Multi-structures Segmentation and Diagnosis: Is the Problem Solved? *IEEE Trans Med Imaging*. 2018;0062(c):1-12. doi:10.1109/TMI.2018.2837502
104. Rabi I, Zacharias J, Millman S, Kusch P. A new method of measuring intensities of magnetization. *Phys Rev*. 1938;53:318. doi:10.1016/S0031-8914(39)80004-0
105. Bloch F, Hansen WW, Packard M. The Nuclear Induction Experiment. *Phys Rev*. 1946;70(7-8):474-485. doi:10.1103/PhysRev.70.474
106. Damadian R. Tumor detection by nuclear magnetic resonance. *Science*. 1971;171(3976):1151-1153.
107. LAUTERBUR PC. Image Formation by Induced Local Interactions: Examples Employing Nuclear Magnetic Resonance. *Nature*. 1973;242(5394):190-191. doi:10.1038/242190a0
108. Twieg DB. Generalized Fourier Nuclear Magnetic Resonance (NMR) Imaging Methods. *Appl Opt Instrum Med*. 1982;0347(December):354-364. doi:10.1117/12.933854
109. Kumar A, Welti D, Ernst RR. NMR Fourier zeugmatography. *J Magn Reson*. 1975. doi:10.1016/0022-2364(75)90224-3
110. Twieg DB. The k-trajectory formulation of the NMR imaging process with applications in analysis and synthesis of imaging methods. 1982.
111. Mezrich R. A perspective on K-space. *Radiology*. 2014. doi:10.1148/radiology.195.2.7724743
112. Paschal CB, Morris HD. K-Space in the Clinic. *J Magn Reson Imaging*. 2004. doi:10.1002/jmri.10451
113. Uribe S, Muthurangu V, Boubertakh R, et al. Whole-heart cine MRI using real-time respiratory self-gating. *Magn Reson Med*. 2007;57(3):606-613. doi:10.1002/mrm.21156
114. Jeong D, Schiebler ML, Lai P, Wang K, Vigen KK, François CJ. Single breath hold 3D cardiac cine MRI using kat-ARC: preliminary results at 1.5T. *Int J Cardiovasc Imaging*. 2015;31(4):851-857. doi:10.1007/s10554-015-0615-0
115. Kido T, Kido T, Nakamura M, et al. Compressed sensing real-time cine cardiovascular

- magnetic resonance: Accurate assessment of left ventricular function in a single-breath-hold. *J Cardiovasc Magn Reson*. 2016. doi:10.1186/s12968-016-0271-0
116. Kustner T, Wurslin C, Gatidis S, et al. MR Image Reconstruction Using a Combination of Compressed Sensing and Partial Fourier Acquisition: ESPReSSo. *IEEE Trans Med Imaging*. 2016. doi:10.1109/TMI.2016.2577642
117. Pruessmann KP, Weiger M, Scheidegger MB, Boesiger P. SENSE: Sensitivity encoding for fast MRI. *Magn Reson Med*. 1999. doi:10.1002/(SICI)1522-2594(199911)42:5<952::AID-MRM16>3.0.CO;2-S
118. Lotz J, Meier C, Leppert A, Galanski M. Cardiovascular Flow Measurement with Phase-Contrast MR Imaging: Basic Facts and Implementation. *RadioGraphics*. 2002;22(3):651-671. doi:10.1148/radiographics.22.3.g02ma11651
119. Kondo C, Caputo GR, Semelka R, Foster E, Shimakawa A, Higgins CB. Right and left ventricular stroke volume measurements with velocity-encoded cine MR imaging: In vitro and in vivo validation. *Am J Roentgenol*. 1991. doi:10.2214/ajr.157.1.2048544
120. Evans AJ, Iwai F, Grist TA, et al. Magnetic resonance imaging of blood flow with a phase subtraction technique: In vitro and in vivo validation. *Invest Radiol*. 1993. doi:10.1097/00004424-199302000-00004
121. Houle D, Govindaraju DR, Omholt S. Phenomics: the next challenge. *Nat Rev Genet*. 2010;11(12):855-866. doi:10.1038/nrg2897
122. Lewin R. Proposal to sequence the human genome stirs debate. *Science*. 1986;232(4758):1598-1600.
123. Markram H, Meier K, Lippert T, et al. Human Brain Project EU report. *Procedia Comput Sci*. 2012;(April). doi:10.1016/j.procs.2011.12.015
124. Wanichthanarak K, Fahrman JF, Grapov D. Genomic, Proteomic, and Metabolomic Data Integration Strategies. *Biomark Insights*. 2015;10(Suppl 4):1-6. doi:10.4137/BMIS.29511
125. Ussher JR, Elmariam S, Gerszten RE, Dyck JRB. The Emerging Role of Metabolomics in the Diagnosis and Prognosis of Cardiovascular Disease. *J Am Coll Cardiol*. 2016;68(25):2850-2870. doi:10.1016/j.jacc.2016.09.972
126. Leopold JA, Loscalzo J. Emerging Role of Precision Medicine in Cardiovascular Disease. *Circ Res*. 2018;122(9):1302-1315. doi:10.1161/CIRCRESAHA.117.310782
127. Wishart DS, Tzur D, Knox C, et al. HMDB: The human metabolome database. *Nucleic Acids Res*. 2007;35(SUPPL. 1). doi:10.1093/nar/gkl923
128. Deidda M, Piras C, Bassareo PP, Cadeddu Dessalvi C, Mercurio G. Metabolomics, a promising approach to translational research in cardiology. *IJC Metab Endocr*. 2015;9:31-38. doi:10.1016/j.ijcme.2015.10.001
129. Taegtmeyer H. Cardiac metabolism as a target for the treatment of heart failure. *Circulation*. 2004;110(8):894-896. doi:10.1161/01.CIR.0000139340.88769.D5
130. Petersen SE, Matthews PM, Bamberg F, et al. Imaging in population science: cardiovascular magnetic resonance in 100,000 participants of UK Biobank - rationale, challenges and approaches. *J Cardiovasc Magn Reson*. 2013;15(1):46. doi:10.1186/1532-429X-15-46
131. Peng P, Lekadir K, Gooya A, Shao L, Petersen SE, Frangi AF. A review of heart chamber segmentation for structural and functional analysis using cardiac magnetic resonance imaging. *MAGMA*. 2016;29(2):155-195. doi:10.1007/s10334-015-0521-4
132. Nosrati M. Image Segmentation Bibliographic Database.

- <http://www.mnosrati.com/FDBCV/samples/New.html>. Accessed August 1, 2019.
133. Kass M, Witkin A, Terzopoulos D. Snakes: Active Contour Models. *Int J Comput Vision*. 1988;1(4):321-331. doi:10.1007/BF00133570
 134. Jolly MP. Automatic segmentation of the left ventricle in cardiac MR and CT images. *Int J Comput Vis*. 2006;70(2):151-163. doi:10.1007/s11263-006-7936-3
 135. Shi W, Zhuang X, Wang H, et al. Automatic segmentation of different pathologies from cardiac cine MRI using registration and multiple component estimation. In: *Lecture Notes in Computer Science (Including Subseries Lecture Notes in Artificial Intelligence and Lecture Notes in Bioinformatics)*. ; 2011. doi:10.1007/978-3-642-21028-0_21
 136. Bramer M. Avoiding Overfitting of Decision Trees BT - *Principles of Data Mining*. In: Bramer M, ed. London: Springer London; 2013:121-136. doi:10.1007/978-1-4471-4884-5_9
 137. Fukushima K. Neocognitron: A Self-organising Neural Network Model for a Mechanism of Pattern Recognition Unaffected by Shift in Position. *Biol Cybern*. 1980;202:193-202. doi:10.1007/BF00344251
 138. Farley B, Clark W. Stimulation of self-organizing systems by digital computer. *Trans IRE Prof Gr Inf Theory*. 1954;4(4):76-84. doi:10.1109/TIT.1954.1057468
 139. Lecun Y, Bengio Y, Hinton G. Deep learning. *Nature*. 2015;521(7553):436-444. doi:10.1038/nature14539
 140. Litjens G, Kooi T, Bejnordi BE, et al. A survey on deep learning in medical image analysis. *Med Image Anal*. 2017;42(December 2012):60-88. doi:10.1016/j.media.2017.07.005
 141. Krizhevsky A, Sutskever I, Ginton G, E. Hinton G. ImageNet Classification with Deep Convolutional Neural Networks. *Neural Inf Process Syst*. 2012;25:1097–10. doi:10.1145/3065386
 142. Lundervold AS, Lundervold A. An overview of deep learning in medical imaging focusing on MRI. *Z Med Phys*. 2019;29(2):102-127. doi:10.1016/j.zemedi.2018.11.002
 143. Rumelhart DE, Hinton G, Williams R. Learning representation by back-propagating errors. *Nature*. 1986;323(9):533-536.
 144. Lo S-CB, Lou S-LA, Jyh-Shyan Lin, Freedman MT, Chien MV, Mun SK. Artificial convolution neural network techniques and applications for lung nodule detection. *IEEE Trans Med Imaging*. 1995;14(4):711-718. doi:10.1109/42.476112
 145. Greenspan H, Van Ginneken B, Summers RM. Guest Editorial Deep Learning in Medical Imaging: Overview and Future Promise of an Exciting New Technique. *IEEE Trans Med Imaging*. 2016;35(5):1153-1159. doi:10.1109/TMI.2016.2553401
 146. Tao Q, Yan W, Wang Y, et al. Deep Learning – based Method for Fully Automatic Quantification of Left Ventricle Function from Cine MR Images : A Multivendor , Multicenter Study. *Radiology*. 2018;00:1-7. doi:<https://doi.org/10.1148/radiol.2018180513>
 147. Bai W, Sinclair M, Tarroni G, et al. Automated cardiovascular magnetic resonance image analysis with fully convolutional networks. *J Cardiovasc Magn Reson*. 2017;20(65):1-12. doi:arXiv:1710.09289
 148. Saito T, Rehmsmeier M. The Precision-Recall Plot Is More Informative than the ROC Plot When Evaluating Binary Classifiers on Imbalanced Datasets. Brock G, ed. *PLoS One*. 2015;10(3):e0118432. doi:10.1371/journal.pone.0118432
 149. Dahabreh IJ. Index Event Bias as an Explanation for the Paradoxes of Recurrence Risk

References

- Research. JAMA. 2011;305(8):822. doi:10.1001/jama.2011.163
150. Flanders WD, Eldridge RC, McClellan W. A Nearly Unavoidable Mechanism for Collider Bias with Index-Event Studies. *Epidemiology*. 2014;25(5):762-764. doi:10.1097/EDE.0000000000000131
151. Chan H-P, Doi K, Vybrony CJ, et al. Improvement in Radiologists Detection of Clustered Microcalcifications on Mammograms. *Invest Radiol*. 1990;25(10):1102-1110. doi:10.1097/00004424-199010000-00006
152. Fenton JJ, Taplin SH, Carney PA, et al. Influence of Computer-Aided Detection on Performance of Screening Mammography. *N Engl J Med*. 2007;356(14):1399-1409. doi:10.1056/NEJMoa066099
153. Wang P, Berzin TM, Glissen Brown JR, et al. Real-time automatic detection system increases colonoscopic polyp and adenoma detection rates: a prospective randomised controlled study. *Gut*. February 2019:gutjnl-2018-317500. doi:10.1136/gutjnl-2018-317500
154. Artificial Intelligence in Healthcare. Vol January.; 2019. doi:10.1038/s41551-018-0305-z
155. Luo W, Phung D, Tran T, et al. Guidelines for developing and reporting machine learning predictive models in biomedical research: A multidisciplinary view. *J Med Internet Res*. 2016;18(12). doi:10.2196/jmir.5870
156. Oktay O, Ferrante E, Kamnitsas K, et al. Anatomically Constrained Neural Networks (ACNNs): Application to Cardiac Image Enhancement and Segmentation. *IEEE Trans Med Imaging*. 2018;37(2):384-395. doi:10.1109/TMI.2017.2743464
157. Mei W, Deng W. Deep Visual Domain Adaptation: A Survey. *Neurocomputing*. February 2018. doi:10.1016/j.neucom.2018.05.083
158. Toga AW, Thompson PM, Mori S, Amunts K, Zilles K. Towards multimodal atlases of the human brain. *Nat Rev Neurosci*. 2006;7(12):952-966. doi:10.1038/nrn2012
159. Medrano-Gracia P, Cowan BR, Bluemke DA, et al. Atlas-based analysis of cardiac shape and function: correction of regional shape bias due to imaging protocol for population studies. *J Cardiovasc Magn Reson Off J Soc Cardiovasc Magn Reson*. 2013;15:80. doi:10.1186/1532-429X-15-80
160. Bai W, Shi W, Marvao A De, et al. A bi-ventricular cardiac atlas built from 1000+ high resolution MR images of healthy subjects and an analysis of shape and motion. *Med Image Anal*. 2014;26(1):133-145. doi:10.1016/j.media.2015.08.009
161. Gilbert K, Forsch N, Hegde S, et al. Atlas-Based Computational Analysis of Heart Shape and Function in Congenital Heart Disease. *J Cardiovasc Transl Res*. 2018;11(2):123-132. doi:10.1007/s12265-017-9778-5
162. Bruse JL, Zuluaga MA, Khushnood A, et al. Detecting Clinically Meaningful Shape Clusters in Medical Image Data: Metrics Analysis for Hierarchical Clustering Applied to Healthy and Pathological Aortic Arches. *IEEE Trans Biomed Eng*. 2017;64(10):2373-2383. doi:10.1109/TBME.2017.2655364
163. Puyol-Antón E, Sinclair M, Gerber B, et al. A multimodal spatiotemporal cardiac motion atlas from MR and ultrasound data. *Med Image Anal*. 2017;40:96-110. doi:10.1016/J.MEDIA.2017.06.002
164. Trayanova N. Defibrillation of the heart: insights into mechanisms from modelling studies. *Exp Physiol*. 2006;91(2):323-337. doi:10.1113/expphysiol.2005.030973
165. Young AA, Frangi AF. Computational cardiac atlases: from patient to population and

- back. *Exp Physiol.* 2009;94(5):578-596. doi:10.1113/expphysiol.2008.044081
166. Finnegan R, Dowling J, Koh E-S, et al. Feasibility of multi-atlas cardiac segmentation from thoracic planning CT in a probabilistic framework. *Phys Med Biol.* 2019;64(8):085006. doi:10.1088/1361-6560/ab0ea6
167. Zhou R, Liao Z, Pan T, et al. Cardiac atlas development and validation for automatic segmentation of cardiac substructures. *Radiother Oncol.* 2017;122(1):66-71. doi:10.1016/j.radonc.2016.11.016
168. Oktay O, Gomez A, Keraudren K, et al. Probabilistic edge map (PEM) for 3D ultrasound image registration and multi-atlas left ventricle segmentation. *Lect Notes Comput Sci (including Subser Lect Notes Artif Intell Lect Notes Bioinformatics).* 2015;9126(Lv):223-230. doi:10.1007/978-3-319-20309-6_26
169. Mori S, Oishi K, Faria A V, Miller MI. Atlas-based neuroinformatics via MRI: harnessing information from past clinical cases and quantitative image analysis for patient care. *Annu Rev Biomed Eng.* 2013;15:71-92. doi:10.1146/annurev-bioeng-071812-152335
170. Fonseca CG, Backhaus M, Bluemke DA, et al. The Cardiac Atlas Project--an imaging database for computational modeling and statistical atlases of the heart. *Bioinformatics.* 2011;27(16):2288-2295. doi:10.1093/bioinformatics/btr360
171. Oktay O, Bai W, Guerrero R, et al. Stratified Decision Forests for Accurate Anatomical Landmark Localization in Cardiac Images. *IEEE Trans Med Imaging.* 2017. doi:10.1109/TMI.2016.2597270
172. Medrano-Gracia P, Cowan BR, Ambale-Venkatesh B, et al. Left ventricular shape variation in asymptomatic populations: the Multi-Ethnic Study of Atherosclerosis. *J Cardiovasc Magn Reson.* 2014;16:56. doi:10.1186/s12968-014-0056-2
173. Rueckert D, Aljabar P. Nonrigid Registration of Medical Images: Theory, Methods, and Applications [Applications Corner. *IEEE Signal Process Mag.* 2010;27(4):113-119. doi:10.1109/MSP.2010.936850
174. Young AA, Crossman DJ, Ruygrok PN, Cannell MB. Mapping system for coregistration of cardiac mri and ex vivo tissue sampling. *J Magn Reson Imaging.* 2011;34(5):1065-1071. doi:10.1002/jmri.22714
175. Rohlfing T, Brandt R, Maurer CR, Menzel R. Bee brains, B-splines and computational democracy: generating an average shape atlas. In: ; 2002. doi:10.1109/mmbia.2001.991733
176. Rohlfing T, Brandt R, Menzel R, Maurer CR. Evaluation of atlas selection strategies for atlas-based image segmentation with application to confocal microscopy images of bee brains. *Neuroimage.* 2004;21(4):1428-1442. doi:10.1016/J.NEUROIMAGE.2003.11.010
177. Bai W, Shi W, Ledig C, Rueckert D. Multi-atlas segmentation with augmented features for cardiac MR images. *Med Image Anal.* 2014;19(1):98-109. doi:10.1016/j.media.2014.09.005
178. Bai W, Shi W, O'Regan DP, et al. A probabilistic patch-based label fusion model for multi-atlas segmentation with registration refinement: Application to cardiac MR images. *IEEE Trans Med Imaging.* 2013;32(7):1302-1315. doi:10.1109/TMI.2013.2256922
179. Aljabar P, Heckemann RA, Hammers A, Hajnal JV, Rueckert D. Multi-atlas based segmentation of brain images: Atlas selection and its effect on accuracy. *Neuroimage.* 2009;46(3):726-738. doi:10.1016/j.neuroimage.2009.02.018
180. Shi W, Lombaert H, Bai W, et al. Multi-atlas spectral PatchMatch: Application to

- cardiac image segmentation. *Lect Notes Comput Sci (including Subser Lect Notes Artif Intell Lect Notes Bioinformatics)*. 2014;8673 LNCS(PART 1):348-355. doi:10.1007/978-3-319-10404-1_44
181. Barnes C, Shechtman E, Goldman DB, Finkelstein A. The generalized PatchMatch correspondence algorithm. *Lect Notes Comput Sci (including Subser Lect Notes Artif Intell Lect Notes Bioinformatics)*. 2010;6313 LNCS(PART 3):29-43. doi:10.1007/978-3-642-15558-1_3
182. Heckemann RA, Hajnal J V., Aljabar P, Rueckert D, Hammers A. Automatic anatomical brain MRI segmentation combining label propagation and decision fusion. *Neuroimage*. 2006. doi:10.1016/j.neuroimage.2006.05.061
183. Duan J, Bello G, Schlemper J, et al. Automatic 3D bi-ventricular segmentation of cardiac images by a shape-refined multi-task deep learning approach. *IEEE Trans Med Imaging*. 2019;PP(c):1-1. doi:10.1109/tmi.2019.2894322
184. Yu Y, Zhang S, Li K, Metaxas D, Axel L. Deformable models with sparsity constraints for cardiac motion analysis. *Med Image Anal*. 2014. doi:10.1016/j.media.2014.03.002
185. Abdallah A Ben, Ghorbel F, Chatti K, Essabbah H, Bedoui MH. A new uniform parameterization and invariant 3D spherical harmonic shape descriptors for shape analysis of the heart's left ventricle - A pilot study. *Pattern Recognit Lett*. 2010. doi:10.1016/j.patrec.2010.06.009
186. Gilbert K, Bai W, Mauger C, et al. Independent Left Ventricular Morphometric Atlases Show Consistent Relationships with Cardiovascular Risk Factors: A UK Biobank Study. *Sci Rep*. 2019;9(1):1130. doi:10.1038/s41598-018-37916-6
187. Biffi B, Bruse JL, Zuluaga MA, Ntsinjana HN, Taylor AM, Schievano S. Investigating Cardiac Motion Patterns Using Synthetic High-Resolution 3D Cardiovascular Magnetic Resonance Images and Statistical Shape Analysis. *Front Pediatr*. 2017;5:34. doi:10.3389/fped.2017.00034
188. Suinesiaputra A, Frangi AF, Kaandorp TAM, et al. Automated detection of regional wall motion abnormalities based on a statistical model applied to multislice short-axis cardiac MR images. *IEEE Trans Med Imaging*. 2009. doi:10.1109/TMI.2008.2008966
189. Rougon NF, Petitjean C, Preteux FJ. Building and using a statistical 3D motion atlas for analyzing myocardial contraction in MRI. In: *Medical Imaging 2004: Image Processing*. ; 2004. doi:10.1117/12.535609
190. Bai W, Peressutti D, Parisot S, et al. Beyond the AHA 17-segment model: Motion-driven parcellation of the left ventricle. In: *Lecture Notes in Computer Science (Including Subseries Lecture Notes in Artificial Intelligence and Lecture Notes in Bioinformatics)*. ; 2016. doi:10.1007/978-3-319-28712-6_2
191. Suinesiaputra A, Ablin P, Alba X, et al. Statistical shape modeling of the left ventricle: myocardial infarct classification challenge. *IEEE J Biomed Heal informatics*. 2018;22(2):503-515. doi:10.1109/JBHI.2017.2652449
192. Kozerke S, Plein S. Accelerated CMR using zonal, parallel and prior knowledge driven imaging methods. *J Cardiovasc Magn Reson*. 2008;10(1):29. doi:10.1186/1532-429X-10-29
193. de Marvao A, Dawes TJ, Shi W, et al. Adverse changes in left ventricular structure begin at normotensive systolic blood pressures: a high resolution MRI study. *J Cardiovasc Magn Reson*. 2015;17(Suppl 1):M11. doi:10.1186/1532-429X-17-S1-M11
194. de Marvao A, Dawes TJW, Shi W, et al. Precursors of Hypertensive Heart Phenotype Develop in Healthy Adults: A High-Resolution 3D MRI Study. *JACC Cardiovasc*

- Imaging. 2015;8(11):1260-1269. doi:10.1016/j.jcmg.2015.08.007
195. B. Corden, A.S.M. De Marvao, T.J.W. Dawes, W. Shi, D. Rueckert, S.A. Cook DO. Left ventricular remodelling with increasing body fat: a 3D cardiac phenotyping study. *Eur Hear J (Abstract Suppl.* 2015;36(118).
196. Dawes TJW, de Marvao A, Shi W, et al. Machine Learning of Three-dimensional Right Ventricular Motion Enables Outcome Prediction in Pulmonary Hypertension: A Cardiac MR Imaging Study. *Radiology.* 2017;283(2):381-390. doi:10.1148/radiol.2016161315
197. Bruse JL, Khushnood A, McLeod K, et al. How successful is successful? Aortic arch shape after successful aortic coarctation repair correlates with left ventricular function. *J Thorac Cardiovasc Surg.* 2017;153(2):418-427. doi:10.1016/j.jtcvs.2016.09.018
198. Radau P., Lu Y., Connelly K., Paul G., Dick A.J. WGA. Evaluation Framework for Algorithms Segmenting Short Axis Cardiac MRI. The MIDAS Journal- Cardiac MR Left Ventricle Segmentation Challenge. doi:http://hdl.handle.net/10380/3070
199. Bernard O, Bosch JGJG, Heyde B, et al. Standardized Evaluation System for Left Ventricular Segmentation Algorithms in 3D Echocardiography. *IEEE Trans Med Imaging.* 2016;35(4):967-977. doi:10.1109/TMI.2015.2503890
200. De Wit J. <http://juliandewit.github.io/kaggle-ndsb/>. <http://juliandewit.github.io/kaggle-ndsb/>. Accessed May 12, 2017.
201. Erbel R, Aboyans V, Boileau C, et al. 2014 ESC guidelines on the diagnosis and treatment of aortic diseases. *Eur Heart J.* 2014;35(41):2873-2926. doi:10.1093/eurheartj/ehu281
202. Majesky MW. Adventitia and Perivascular Cells. *Arterioscler Thromb Vasc Biol.* 2015;35(8). doi:10.1161/ATVBAHA.115.306088
203. Narayan O, Parker KH, Davies JE, Hughes AD, Meredith IT, Cameron JD. Reservoir pressure analysis of aortic blood pressure: An in-vivo study at five locations in humans. *J Hypertens.* 2017;35(10):2025-2033. doi:10.1097/HJH.0000000000001424
204. Westerhof N, Stergiopoulos N, Noble M. Snapshots in Haemodynamics. 2nd ed. Springer
205. Westerhof N, Lankhaar JW, Westerhof BE. The arterial windkessel. *Med Biol Eng Comput.* 2009;47(2):131-141. doi:10.1007/s11517-008-0359-2
206. London GM, Pannier B. Arterial functions: How to interpret the complex physiology. *Nephrol Dial Transplant.* 2010;25(12):3815-3823. doi:10.1093/ndt/gfq614
207. Westerhof N, Elzinga G, Sipkema P. An artificial arterial system for pumping hearts. *J Appl Physiol.* 1971;31(5):776-781. doi:10.1161/01.RES.56.4.586
208. Wilson PW, D'Agostino RB, Levy D, Belanger AM, Silbershatz H, Kannel WB. Prediction of coronary heart disease using risk factor categories. *Circulation.* 1998;97(18):1837-1847.
209. Benetos A, Safar M, Rudnicki A, et al. Pulse pressure: a predictor of long-term cardiovascular mortality in a French male population. *Hypertension.* 1997;30(6):1410-1415. doi:10.1161/01.HYP.30.6.1410
210. Safar ME, Levy BI, Struijker-Boudier H. Current perspectives on arterial stiffness and pulse pressure in hypertension and cardiovascular diseases. *Circulation.* 2003;107(22):2864-2869. doi:10.1161/01.CIR.0000069826.36125.B4
211. Mancia G, Fagard R, Narkiewicz K, et al. 2013 ESH/ESC guidelines for the management of arterial hypertension: the Task Force for the Management of Arterial Hypertension of the European Society of Hypertension (ESH) and of the European Society of Cardiology (ESC). *Eur Heart J.* 2013;34(28):2159-2219.

References

- doi:10.1093/eurheartj/eh151
212. Segers P, Kips J, Trachet B, et al. Limitations and pitfalls of non-invasive measurement of arterial pressure wave reflections and pulse wave velocity. *Artery Res.* 2009;3(2):79-88. doi:10.1016/j.artres.2009.02.006
213. Hughes AD, Park C, Davies J, et al. Limitations of augmentation index in the assessment of wave reflection in normotensive healthy individuals. *PLoS One.* 2013;8(3):e59371. doi:10.1371/journal.pone.0059371
214. Guerin AP, Blacher J, Pannier B, Marchais SJ, Safar ME, London GM. Impact of Aortic Stiffness Attenuation on Survival of Patients in End-Stage Renal Failure. *Circulation.* 2001;103(7):987-992. doi:10.1161/01.CIR.103.7.987
215. London GM, Blacher J, Pannier B, Guérin AP, Marchais SJ, Safar ME. Arterial Wave Reflections and Survival in End-Stage Renal Failure. *Hypertension.* 2001;38(3):434-438. doi:10.1161/01.HYP.38.3.434
216. Laurent S, Boutouyrie P, Asmar R, et al. Aortic Stiffness Is an Independent Predictor of All-Cause and Cardiovascular Mortality in Hypertensive Patients. *Hypertension.* 2001;37(5):1236-1241. doi:10.1161/01.HYP.37.5.1236
217. Vlachopoulos C, Aznaouridis K, O'Rourke MF, Safar ME, Baou K, Stefanadis C. Prediction of cardiovascular events and all-cause mortality with central haemodynamics: a systematic review and meta-analysis. *Eur Heart J.* 2010;31(15):1865-1871. doi:10.1093/eurheartj/ehq024
218. Mitchell GF, Moyé LA, Braunwald E, et al. Sphygmomanometrically determined pulse pressure is a powerful independent predictor of recurrent events after myocardial infarction in patients with impaired left ventricular function. SAVE investigators. Survival and Ventricular Enlargement. *Circulation.* 1997;96(12):4254-4260. doi:10.1161/01.cir.96.12.4254
219. Chae CU, Pfeffer M a, Glynn RJ, Mitchell GF, Taylor JO, Hennekens CH. Increased pulse pressure and risk of heart failure in the elderly. *JAMA.* 1999;281(7):634-639.
220. Black HR. The paradigm has shifted to systolic blood pressure. *J Hum Hypertens.* 2004;18:S3-S7. doi:10.1038/sj.jhh.1001795
221. John Baksi A, Davies JE, Hadjiloizou N, et al. Attenuation of reflected waves in man during retrograde propagation from femoral artery to proximal aorta. *Int J Cardiol.* 2016;202:441-445. doi:10.1016/j.ijcard.2015.09.064
222. Sipkema P, Westerhof N. Effective length of the arterial system. *Ann Biomed Eng.* 1975;3(3):296-307. doi:10.1007/BF02390974
223. Westerhof BE, Van Den Wijngaard JP, Murgo JP, Westerhof N. Location of a reflection site is elusive: Consequences for the calculation of aortic pulse wave velocity. *Hypertension.* 2008;52(3):478-483. doi:10.1161/HYPERTENSIONAHA.108.116525
224. Davies JE, Alastruey J, Francis DP, et al. Attenuation of Wave Reflection by Wave Entrapment Creates a "Horizon Effect" in the Human Aorta. *Hypertension.* 2012;60(3):778-785. doi:10.1161/HYPERTENSIONAHA.111.180604
225. Mitchell GF, Parise H, Benjamin EJ, et al. Changes in arterial stiffness and wave reflection with advancing age in healthy men and women: The Framingham Heart Study. *Hypertension.* 2004;43(6):1239-1245. doi:10.1161/01.HYP.0000128420.01881.aa
226. Baksi AJ, Treibel TA, Davies JE, et al. A Meta-Analysis of the Mechanism of Blood Pressure Change With Aging. *J Am Coll Cardiol.* 2009;54(22):2087-2092. doi:10.1016/j.jacc.2009.06.049

References

227. Laurent S, Cockcroft J, Van Bortel L, et al. Expert consensus document on arterial stiffness: Methodological issues and clinical applications. *Eur Heart J*. 2006;27(21):2588-2605. doi:10.1093/eurheartj/ehl254
228. Westerhof BE, Guelen I, Westerhof N, Karmaker JM, Avolio A. Quantification of Wave Reflection in the Human Aorta From Pressure Alone. *Hypertension*. 2006;48(4):595-601. doi:10.1161/01.HYP.0000238330.08894.17
229. Kelly R, Hayward C, Avolio A, O'Rourke M. Noninvasive determination of age-related changes in the human arterial pulse. *Circulation*. 1989;80(6):1652-1659. doi:10.1161/01.CIR.80.6.1652
230. Murgo JP, Westerhof N, Giolma JP, Altobelli SA. Aortic input impedance in normal man: relationship to pressure wave forms. *Circulation*. 1980;62(1):105-116. doi:10.1161/01.CIR.62.1.105
231. London GM, Guerin AP, Pannier BM, Marchais SJ, Metivier F. Body height as a determinant of carotid pulse contour in humans. *J Hypertens Suppl*. 1992;10(6):S93--5.
232. Wilkinson IB, MacCallum H, Flint L, Cockcroft JR, Newby DE, Webb DJ. The influence of heart rate on augmentation index and central arterial pressure in humans. *J Physiol*. 2000;525(1):263-270. doi:10.1111/j.1469-7793.2000.t01-1-00263.x
233. Shimizu M, Kario K. Role of the augmentation index in hypertension. *Ther Adv Cardiovasc Dis*. 2008;2(1):25-35. doi:10.1177/1753944707086935
234. Gatzka CD, Kingwell BA, Cameron JD, et al. Gender differences in the timing of arterial wave reflection beyond differences in body height. *J Hypertens*. 2001;19(12):2197-2203. doi:10.1097/00004872-200112000-00013
235. Chirinos JA, Zambrano JP, Chakko S, et al. Aortic pressure augmentation predicts adverse cardiovascular events in patients with established coronary artery disease. *Hypertension*. 2005;45(5):980-985. doi:10.1161/01.HYP.0000165025.16381.44
236. Dart AM, Gatzka CD, Kingwell BA, et al. Brachial blood pressure but not carotid arterial waveforms predict cardiovascular events in elderly female hypertensives. *Hypertension*. 2006;47(4):785-790. doi:10.1161/01.HYP.0000209340.33592.50
237. Sabbah HN, Stein PD. Valve origin of the aortic incisura. *Am J Cardiol*. 1978;41(1):32-38. doi:10.1016/0002-9149(78)90128-5
238. Tyberg J V., Davies JE, Wang Z, et al. Wave intensity analysis and the development of the reservoir-wave approach. *Med Biol Eng Comput*. 2009;47(2):221-232. doi:10.1007/s11517-008-0430-z
239. Wang J-J, O'Brien AB, Shrive NG, Parker KH, Tyberg J V. Time-domain representation of ventricular-arterial coupling as a windkessel and wave system. *Am J Physiol Circ Physiol*. 2003. doi:10.1152/ajpheart.00175.2002
240. Parker K, Jones C, Dawson J, Gibson D. What stops the flow of blood from the heart? *Hear Vessel*. 1988;(4):241-245. doi:10.1161/CIRCULATIONAHA.105.603050
241. Hughes AD, Davies JE, Parker KH. The importance of wave reflection: A comparison of wave intensity analysis and separation of pressure into forward and backward components. *Conf Proc . Annu Int Conf IEEE Eng Med Biol Soc IEEE Eng Med Biol Soc Annu Conf*. 2013;2013:229-232. doi:10.1109/EMBC.2013.6609479
242. Chen C-H, Nevo E, Fetis B, et al. Estimation of Central Aortic Pressure Waveform by Mathematical Transformation of Radial Tonometry Pressure. *Circulation*. 1997;95(7):1827-1836. doi:10.1161/01.CIR.95.7.1827
243. Davies JJ, Struthers AD. Pulse wave analysis and pulse wave velocity. *J Hypertens*.

- 2003;21(3):463-472. doi:10.1097/00004872-200303000-00004
244. Karamanogul M, O'Rourke MF, Avolio AP, Kelly RP. An analysis of the relationship between central aortic and peripheral upper limb pressure waves in man. *Eur Heart J*. 1993;14(2):160-167. doi:10.1093/eurheartj/14.2.160
245. Fetters B, Nevo E, Chen-Huan Chen, Kass DA. Parametric model derivation of transfer function for noninvasive estimation of aortic pressure by radial tonometry. *IEEE Trans Biomed Eng*. 1999;46(6):698-706. doi:10.1109/10.764946
246. Sharman JE, Lim R, Qasem AM, et al. Validation of a generalized transfer function to noninvasively derive central blood pressure during exercise. *Hypertension*. 2006. doi:10.1161/01.HYP.0000223013.60612.72
247. Pauca AL, O'Rourke MF, Kon ND. Prospective evaluation of a method for estimating ascending aortic pressure from the radial artery pressure waveform. In: *Hypertension*. ; 2001. doi:10.1161/hy1001.096106
248. Hope SA, Tay DB, Meredith IT, Cameron JD. Use of Arterial Transfer Functions for the Derivation of Central Aortic Waveform Characteristics in Subjects With Type 2 Diabetes and Cardiovascular Disease: Response to Wilkinson and McEniery and Avolio, Cockcroft, and O'Rourke. *Diabetes Care*. 2004;27(10):2565-2567. doi:10.2337/diacare.27.10.2565
249. Stergiopoulos N, Westerhof BE, Westerhof N. Physical basis of pressure transfer from periphery to aorta: a model-based study. *Am J Physiol Circ Physiol*. 1998;274(4):H1386-H1392. doi:10.1152/ajpheart.1998.274.4.H1386
250. Lowe A, Harrison W, El-Aklouk E, Ruygrok P, Al-Jumaily AM. Non-invasive model-based estimation of aortic pulse pressure using suprasystolic brachial pressure waveforms. *J Biomech*. 2009;42(13):2111-2115. doi:10.1016/j.jbiomech.2009.05.029
251. Lin ACW, Lowe A, Sidhu K, Harrison W, Ruygrok P, Stewart R. Evaluation of a novel sphygmomanometer, which estimates central aortic blood pressure from analysis of brachial artery suprasystolic pressure waves. *J Hypertens*. 2012;30(9):1743-1750. doi:10.1097/HJH.0b013e3283567b94
252. Climie RED, Schultz MG, Nikolic SB, Ahuja KDK, Fell JW, Sharman JE. Validity and reliability of central blood pressure estimated by upper arm oscillometric cuff pressure. *Am J Hypertens*. 2012;25(4):414-420. doi:10.1038/ajh.2011.238
253. Park CM, Korolkova O, Davies JE, et al. Arterial pressure: agreement between a brachial cuff-based device and radial tonometry. *J Hypertens*. 2014;32(4):865-872. doi:10.1097/HJH.0000000000000082
254. Fischer GM, Llaurodo JG. Collagen and elastin content in canine arteries selected from functionally different vascular beds. *Circ Res*. 1966;19(2):394-399. doi:10.1161/01.RES.19.2.394
255. Feng J, Khir AW. Determination of wave speed and wave separation in the arteries using diameter and velocity. *J Biomech*. 2010;43(3):455-462. doi:10.1016/j.jbiomech.2009.09.046
256. Zambanini A. Wave-energy patterns in carotid, brachial, and radial arteries: a noninvasive approach using wave-intensity analysis. *AJP Hear Circ Physiol*. 2005;289(1):H270-H276. doi:10.1152/ajpheart.00636.2003
257. Alastruey J. Numerical assessment of time-domain methods for the estimation of local arterial pulse wave speed. *J Biomech*. 2011;44(5):885-891. doi:10.1016/j.jbiomech.2010.12.002

References

258. Latham RD, Westerhof N, Sipkema P, Rubal BJ, Reuderink P, Murgo JP. Regional wave travel and reflections along the human aorta: a study with six simultaneous micromanometric pressures. *Circulation*. 1985;72(6):1257-1269. doi:10.1161/01.CIR.72.6.1257
259. Blacher J, Guerin AP, Pannier B, Marchais SJ, Safar ME, London GM. Impact of aortic stiffness on survival in end-stage renal disease. *Circulation*. 1999;99(18):2434-2439. doi:10.1161/01.CIR.99.18.2434
260. Cruickshank K, Riste L, Anderson SG, Wright JS, Dunn G, Gosling RG. Aortic pulse-wave velocity and its relationship to mortality in diabetes and glucose intolerance: An integrated index of vascular function? *Circulation*. 2002;106(16):2085-2090. doi:10.1161/01.CIR.0000033824.02722.F7
261. Laurent S, Katsahian S, Fassot C, et al. Aortic stiffness is an independent predictor of fatal stroke in essential hypertension. *Stroke*. 2003;34(5):1203-1206. doi:10.1161/01.STR.0000065428.03209.64
262. Meaume S, Benetos A, Henry OF, Rudnichi A, Safar ME. Aortic Pulse Wave Velocity Predicts Cardiovascular Mortality in Subjects >70 Years of Age. *Arterioscler Thromb Vasc Biol*. 2001;21(12):2046-2050. doi:10.1161/hq1201.100226
263. Ben-Shlomo Y, Spears M, Boustred C, et al. Aortic Pulse Wave Velocity Improves Cardiovascular Event Prediction. *J Am Coll Cardiol*. 2014;63(7):636-646. doi:10.1016/j.jacc.2013.09.063
264. Dogui A, Redheuil A, Lefort M, et al. Measurement of aortic arch pulse wave velocity in cardiovascular MR: Comparison of transit time estimators and description of a new approach. *J Magn Reson Imaging*. 2011;33(6):1321-1329. doi:10.1002/jmri.22570
265. Dogui A, Kachenoura N, Frouin F, et al. Consistency of aortic distensibility and pulse wave velocity estimates with respect to the Bramwell-Hill theoretical model: a cardiovascular magnetic resonance study. *J Cardiovasc Magn Reson*. 2011;13(1):11. doi:10.1186/1532-429X-13-11
266. Noda C, Ambale Venkatesh B, Ohyama Y, et al. Reproducibility of functional aortic analysis using magnetic resonance imaging: the MESA. *Eur Heart J Cardiovasc Imaging*. 2016;17(8):909-917. doi:10.1093/ehjci/jev215
267. Boutouyrie P, Laurent S, Girerd X, et al. Common carotid artery stiffness and patterns of left ventricular hypertrophy in hypertensive patients. *Hypertension*. 1995;25(4 Pt 1):651-659. doi:10.1161/01.HYP.25.4.651
268. Parker KH. An introduction to wave intensity analysis. *Med Biol Eng Comput*. 2009;47(2):175-188. doi:10.1007/s11517-009-0439-y
269. Khir AW, O'Brien A, Gibbs JS, Parker KH. Determination of wave speed and wave separation in the arteries. *J Biomech*. 2001;34(9):1145-1155. doi:doi.org/10.1016/S0021-9290(01)00076-8
270. Davies JE. Use of simultaneous pressure and velocity measurements to estimate arterial wave speed at a single site in humans. *AJP Hear Circ Physiol*. 2005;290(2):H878-H885. doi:10.1152/ajpheart.00751.2005
271. Segers P, Swillens A, Taelman L, Vierendeels J. Wave reflection leads to over- and underestimation of local wave speed by the PU- and QA-loop methods: Theoretical basis and solution to the problem. *Physiol Meas*. 2014;35(5):847-861. doi:10.1088/0967-3334/35/5/847
272. Ohte N, Narita H, Sugawara M, et al. Clinical usefulness of carotid arterial wave intensity in assessing left ventricular systolic and early diastolic performance. *Heart*

References

- Vessels. 2003;18(3):107-111. doi:10.1007/s00380-003-0700-5
273. Hughes AD, Parker KH, Davies JE. Waves in arteries: A review of wave intensity analysis in the systemic and coronary circulations. *Artery Res.* 2008;2(2):51-59. doi:10.1016/J.ARTRES.2008.02.002
274. Li Y, Borlotti A, Hickson SS, McEniery CM, Wilkinson IB, Khir AW. Using magnetic resonance imaging measurements for the determination of local wave speed and arrival time of reflected waves in human ascending aorta. 2010 Annu Int Conf IEEE Eng Med Biol Soc EMBC'10. 2010:5153-5156. doi:10.1109/IEMBS.2010.5626183
275. Li Y, Hickson SS, McEniery CM, Wilkinson IB, Khir AW. Stiffening and ventricular–arterial interaction in the ascending aorta using MRI. *J Hypertens.* 2019;37(2):347-355. doi:10.1097/HJH.0000000000001886
276. Curtis SL, Zambanini A, Mayet J, et al. Reduced systolic wave generation and increased peripheral wave reflection in chronic heart failure. *AJP Hear Circ Physiol.* 2007;293(1):H557-H562. doi:10.1152/ajpheart.01095.2006
277. Ntsinjana HN, Chung R, Ciliberti P, et al. Utility of Cardiovascular Magnetic Resonance-Derived Wave Intensity Analysis As a Marker of Ventricular Function in Children with Heart Failure and Normal Ejection Fraction. *Front Pediatr.* 2017;5:65. doi:10.3389/fped.2017.00065
278. Niki K, Sugawara M, Kayanuma H, et al. Associations of increased arterial stiffness with left ventricular ejection performance and right ventricular systolic pressure in mitral regurgitation before and after surgery: Wave intensity analysis. *Int J Cardiol Hear Vasc.* 2017;16:7-13. doi:10.1016/j.ijcha.2017.06.002
279. Chirinos JA, Akers SR, Schelbert E, et al. Arterial Properties as Determinants of Left Ventricular Mass and Fibrosis in Severe Aortic Stenosis: Findings From ACRIN PA 4008. *J Am Heart Assoc.* 2019;8(1):e03742. doi:10.1161/JAHA.118.010271
280. Manisty C, Mayet J, Tapp RJ, et al. Wave Reflection Predicts Cardiovascular Events in Hypertensive Individuals Independent of Blood Pressure and Other Cardiovascular Risk Factors: An ASCOT (Anglo-Scandinavian Cardiac Outcome Trial) Substudy. *J Am Coll Cardiol.* 2010;56(1):24-30. doi:10.1016/J.JACC.2010.03.030
281. Quail MA, Knight DS, Steeden JA, et al. Noninvasive pulmonary artery wave intensity analysis in pulmonary hypertension. *Am J Physiol Circ Physiol.* 2015;308(12):H1603-H1611. doi:10.1152/ajpheart.00480.2014
282. Su J, Manisty C, Parker KH, et al. Wave Intensity Analysis Provides Novel Insights Into Pulmonary Arterial Hypertension and Chronic Thromboembolic Pulmonary Hypertension. *J Am Heart Assoc.* 2017;6(11). doi:10.1161/JAHA.117.006679
283. Borlotti A, Khir AW, Rietzschel ER, De Buyzere ML, Vermeersch S, Segers P. Noninvasive determination of local pulse wave velocity and wave intensity: changes with age and gender in the carotid and femoral arteries of healthy human. *J Appl Physiol.* 2012;113(5):727-735. doi:10.1152/japplphysiol.00164.2012
284. Quail MA, Steeden JA, Knight D, Segers P, Taylor AM, Muthurangu V. Development and validation of a novel method to derive central aortic systolic pressure from the MR aortic distension curve. *J Magn Reson Imaging.* 2014;40(5):1064-1070. doi:10.1002/jmri.24471
285. Niki K, Sugawara M, Uchida K, et al. A noninvasive method of measuring wave intensity, a new hemodynamic index: application to the carotid artery in patients with mitral regurgitation before and after surgery. *Heart Vessels.* 1999;14(6):263-271. doi:10.1007/BF03257237

References

286. Minners J, Allgeier M, Gohlke-Baerwolf C, Kienzle R-P, Neumann F-J, Jander N. Inconsistencies of echocardiographic criteria for the grading of aortic valve stenosis. *Eur Heart J*. 2008;29(8):1043-1048. doi:10.1093/eurheartj/ehm543
287. Orsinelli DA, Aurigemma GP, Battista S, Krendel S, Gaasch WH. Left ventricular hypertrophy and mortality after aortic valve replacement for aortic stenosis. A high risk subgroup identified by preoperative relative wall thickness. *J Am Coll Cardiol*. 1993;22(0735-1097 (Print)):1679-1683. doi:10.1016/0735-1097(93)90595-R
288. Mehta RH, Bruckman D, Das S, et al. Implications of increased left ventricular mass index on in-hospital outcomes in patients undergoing aortic valve surgery. *J Thorac Cardiovasc Surg*. 2001;122(5):919-928. doi:10.1067/mtc.2001.116558
289. Kupari M, Turto H, Lommi J. Left ventricular hypertrophy in aortic valve stenosis: preventive or promotive of systolic dysfunction and heart failure? *Eur Heart J*. 2005;26(17):1790-1796. doi:10.1093/eurheartj/ehi290
290. Lee JM, Park S-J, Lee S-P, et al. Gender Difference in Ventricular Response to Aortic Stenosis: Insight from Cardiovascular Magnetic Resonance. Cavarretta E, ed. *PLoS One*. 2015;10(3):e0121684. doi:10.1371/journal.pone.0121684
291. Cioffi G, Faggiano P, Vizzardi E, et al. Prognostic effect of inappropriately high left ventricular mass in asymptomatic severe aortic stenosis. *Heart*. 2011;97(4):301-307. doi:10.1136/hrt.2010.192997
292. Carabello BA. Should severe aortic stenosis be operated on before symptom onset? Aortic valve replacement should be operated on before symptom onset. *Circulation*. 2012;126(1):112-117. doi:10.1161/CIRCULATIONAHA.111.079350
293. Shah PK. Severe aortic stenosis should not be operated on before symptom onset. *Circulation*. 2012;126(1):118-125. doi:10.1161/CIRCULATIONAHA.111.079368
294. Tuseth N, Cramariuc D, Rieck ÅE, et al. Asymmetric septal hypertrophy – a marker of hypertension in aortic stenosis (a SEAS substudy). *Blood Press*. 2010;19(3):140-144. doi:10.3109/08037051.2010.481816
295. Dellgren G, Eriksson MJ, Blange I, Brodin LA, Radegran K, Sylven C. Angiotensin-converting enzyme gene polymorphism influences degree of left ventricular hypertrophy and its regression in patients undergoing operation for aortic stenosis. *Am J Cardiol*. 1999;84(8):909-913. doi:10.1016/S0002-9149(99)00464-6
296. YOKOTA Y, TENG S-S, EMOTO R, et al. Mechanism of development of asymmetric septal hypertrophy in patients with essential systemic hypertension. *Jpn Circ J*. 2011. doi:10.1253/jcj.53.1173
297. Treibel TA, Kozor R, Fontana M, et al. Sex Dimorphism in the Myocardial Response to Aortic Stenosis. *JACC Cardiovasc Imaging*. 2017;11:962-973. doi:10.1016/j.jcmg.2017.08.025
298. Orłowska-Baranowska E, Placha G, Gaciong Z, et al. Influence of ACE I/D genotypes on left ventricular hypertrophy in aortic stenosis: gender-related differences. *J Heart Valve Dis*. 2004;13(4):574-581.
299. Salcedo EE, Korzick DH, Currie PJ, Stewart WJ, Lever HM, Goormastic M. Determinants of left ventricular hypertrophy in patients with aortic stenosis. *Cleve Clin J Med*. 1989;56(6):590-596.
300. Lavie CJ, Milani R V, Patel D, Artham SM, Ventura HO. Disparate effects of obesity and left ventricular geometry on mortality in 8088 elderly patients with preserved systolic function. *Postgrad Med*. 2009;121(3):119-125. doi:10.3810/pgm.2009.05.2011
301. Douglas PS, Katz SE, Weinberg EO, Chen MH, Bishop SP, Lorell BH. Hypertrophic

References

- remodeling: gender differences in the early response to left ventricular pressure overload. *J Am Coll Cardiol.* 1998;32(4):1118-1125. doi:10.1016/S0735-1097(98)00347-7
302. Humphries KH, Toggweiler S, Rodés-Cabau J, et al. Sex differences in mortality after transcatheter aortic valve replacement for severe aortic stenosis. *J Am Coll Cardiol.* 2012;60(10):882-886. doi:10.1016/j.jacc.2012.05.009
303. Lindman BR, Arnold S V, Madrazo JA, et al. The adverse impact of diabetes mellitus on left ventricular remodeling and function in patients with severe aortic stenosis. *Circ Heart Fail.* 2011;4(3):286-292. doi:10.1161/CIRCHEARTFAILURE.110.960039
304. Gavina C, Falcão-Pires I, Rodrigues J, et al. Load independent impairment of reverse remodeling after valve replacement in hypertensive aortic stenosis patients. *Int J Cardiol.* 2014;170(3):324-330. doi:10.1016/j.ijcard.2013.11.006
305. Rieck ÅE, Cramariuc D, Staal EM, Rossebø AB, Wachtell K, Gerds E. Impact of hypertension on left ventricular structure in patients with asymptomatic aortic valve stenosis (a SEAS substudy). *J Hypertens.* 2010;28(2):377-383. doi:10.1097/HJH.0b013e328332fa44
306. Briand M, Dumesnil JG, Kadem L, et al. Reduced Systemic Arterial Compliance Impacts Significantly on Left Ventricular Afterload and Function in Aortic Stenosis. *J Am Coll Cardiol.* 2005;46(2):291-298. doi:10.1016/j.jacc.2004.10.081
307. Gavina C, Falcão-Pires I, Pinho P, et al. Relevance of residual left ventricular hypertrophy after surgery for isolated aortic stenosis. *Eur J Cardio-thoracic Surg.* 2016;49(3):952-959. doi:10.1093/ejcts/ezv240
308. Monrad ES, Hess OM, Murakami T, Nonogi H, Corin WJ, Kräyenbuehl HP. Time course of regression of left ventricular hypertrophy after aortic valve replacement. *Circulation.* 1988;77(6):1345-1355.
309. Lund O, Emmertsen K, Dørup I, Jensen FT, Flø C. Regression of left ventricular hypertrophy during 10 years after valve replacement for aortic stenosis is related to the preoperative risk profile. *Eur Heart J.* 2003;24(15):1437-1446.
310. Del Rizzo DF, Abdoh A, Cartier P, Doty D, Westaby S. Factors affecting left ventricular mass regression after aortic valve replacement with stentless valves. *Semin Thorac Cardiovasc Surg.* 1999;11(4 Suppl 1):114-120.
311. Gelsomino S, Frassani R, Morocutti G, et al. Time course of left ventricular remodeling after stentless aortic valve replacement. *Am Heart J.* 2001;142(3):556-562. doi:10.1067/MHJ.2001.117777
312. Petrov G, Regitz-Zagrosek V, Lehmkuhl E, et al. Regression of myocardial hypertrophy after aortic valve replacement: Faster in women? *Circulation.* 2010;122(11 SUPPL. 1). doi:10.1161/CIRCULATIONAHA.109.927764
313. Köhl HP, Franke A, Puschmann D, Schöndube FA, Hoffmann R, Hanrath P. Regression of left ventricular mass one year after aortic valve replacement for pure severe aortic stenosis. *Am J Cardiol.* 2002;89(4):408-413.
314. Dobson LE, Fairbairn TA, Musa TA, et al. Sex-related differences in left ventricular remodeling in severe aortic stenosis and reverse remodeling after aortic valve replacement: A cardiovascular magnetic resonance study. *Am Heart J.* 2016;175:101-111. doi:10.1016/j.ahj.2016.02.010
315. Treibel TA, Kozor R, Schofield R, et al. Reverse Myocardial Remodeling Following Valve Replacement in Patients With Aortic Stenosis. *J Am Coll Cardiol.* 2018;71(8):860-871. doi:10.1016/j.jacc.2017.12.035

References

316. Camm CW, Möllmann H, Bassand JP, Van de Werf F. The ESC Textbook of Cardiovascular Medicine: Second edition. Oxford Univ Press. 2009. doi:10.1093/med/9780199566990.001.0001
317. La Gerche A, Burns AT, Mooney DJ, et al. Exercise-induced right ventricular dysfunction and structural remodelling in endurance athletes. *Eur Heart J*. 2012;33(8):998-1006. doi:10.1093/eurheartj/ehr397
318. Mediaromid AK, Swoboda PP, Erhayiem B, et al. Ventricular Structure and Function Athletic Cardiac Adaptation in Males Is a Consequence of Elevated Myocyte Mass. *Circ Cardiovasc Imaging*. 2016;9:1-9. doi:10.1161/CIRCIMAGING.115.003579
319. Piercy KL, Troiano RP, Ballard RM, et al. The Physical Activity Guidelines for Americans. *JAMA*. 2018;320(19):2020. doi:10.1001/jama.2018.14854
320. Shephard RJ, Balady GJ. Exercise as Cardiovascular Therapy. *Circulation*. 1999;99:963-972. doi:10.1161/01.CIR.0000069330.41022.90
321. Batacan RB, Duncan MJ, Dalbo VJ, Tucker PS, Fenning AS. Effects of high-intensity interval training on cardiometabolic health: A systematic review and meta-analysis of intervention studies. *Br J Sports Med*. 2017. doi:10.1136/bjsports-2015-095841
322. Thompson PD. Exercise and Physical Activity in the Prevention and Treatment of Atherosclerotic Cardiovascular Disease. *Prevention*. 2003;23:1319-1321. doi:10.1161/01.ATV.0000087143.33998.F2
323. THUNE I, FURBERG A-S. Physical activity and cancer risk: dose-response and cancer, all sites and site-specific. *Med Sci Sports Exerc*. 2001;33(Supplement):S530-S550. doi:10.1097/00005768-200106001-00025
324. Wen CP, Wai JPM, Tsai MK, et al. Minimum amount of physical activity for reduced mortality and extended life expectancy: a prospective cohort study. *Lancet*. 2011;378(9798):1244-1253. doi:10.1016/S0140-6736(11)60749-6
325. Physical Activity Guidelines Advisory Committee Report and 2008 Physical Activity Guidelines for Americans.; 2008.
326. Start Active, Stay Active: Report on Physical Activity in the UK.; 2011.
327. Saint-Maurice PF, Coughlan D, Kelly SP, et al. Association of Leisure-Time Physical Activity Across the Adult Life Course With All-Cause and Cause-Specific Mortality. *JAMA Netw Open*. 2019;2(3):e190355. doi:10.1001/jamanetworkopen.2019.0355
328. Lee IM, Shiroma EJ, Kamada M, Bassett DR, Matthews CE, Buring JE. Association of Step Volume and Intensity with All-Cause Mortality in Older Women. *JAMA Intern Med*. 2019. doi:10.1001/jamainternmed.2019.0899
329. Morris J, Heady M, Raffle P, Roberts C, Parks J. CORONARY HEART-DISEASE AND PHYSICAL ACTIVITY OF WORK. *Lancet*. 1953;262(6796):1111-1120. doi:https://doi.org/10.1016/S0140-6736(53)91495-0
330. Marijon E, Tafflet M, Antero-Jacquemin J, et al. Mortality of French participants in the Tour de France (1947-2012). *Eur Heart J*. 2013. doi:10.1093/eurheartj/eh347
331. Mohlenkamp S, Lehmann N, Breuckmann F, et al. Running: the risk of coronary events : Prevalence and prognostic relevance of coronary atherosclerosis in marathon runners. *Eur Heart J*. 2008;29(15):1903-1910. doi:10.1093/eurheartj/ehn163
332. Sattelmair J, Pertman J, Ding EL, Kohl HW, Haskell W, Lee IM. Dose response between physical activity and risk of coronary heart disease: A meta-analysis. *Circulation*. 2011. doi:10.1161/CIRCULATIONAHA.110.010710
333. Möhlenkamp S, Halle M. Myocardial Adaptation in Response to Marathon Training.

- Circ Cardiovasc Imaging. 2015;8(2):1-3. doi:10.1161/circimaging.115.003030
334. Schnohr P, Marott JL, Lange P, Jensen GB. Longevity in Male and Female Joggers: The Copenhagen City Heart Study. *Am J Epidemiol*. 2013;177(7):683-689. doi:10.1093/aje/kws301
335. Baggish AL, Wang F, Weiner RB, et al. Training-specific changes in cardiac structure and function: a prospective and longitudinal assessment of competitive athletes. *J Appl Physiol*. 2008. doi:10.1152/japplphysiol.01170.2007
336. Baggish AL, Yared K, Wang F, et al. The impact of endurance exercise training on left ventricular systolic mechanics. *Am J Physiol Circ Physiol*. 2008. doi:10.1152/ajpheart.00395.2008
337. Lepers R, Cattagni T. Do older athletes reach limits in their performance during marathon running? *Age (Dordr)*. 2012;34(3):773-781. doi:10.1007/s11357-011-9271-z
338. Neilan TG, Januzzi JL, Lee-Lewandrowski E, et al. Myocardial Injury and Ventricular Dysfunction Related to Training Levels Among Nonelite Participants in the Boston Marathon. *Circulation*. 2006;114(22):2325-2333. doi:10.1161/CIRCULATIONAHA.106.647461
339. Gaudreault V, Tizon-Marcos H, Poirier P, et al. Transient Myocardial Tissue and Function Changes During a Marathon in Less Fit Marathon Runners. *Can J Cardiol*. 2013;29(10):1269-1276. doi:10.1016/j.cjca.2013.04.022
340. Vlachopoulos C, Kardara D, Anastasakis A, et al. Arterial Stiffness and Wave Reflections in Marathon Runners. *Am J Hypertens*. 2010;23(9):974-979. doi:10.1038/ajh.2010.99
341. Predel H-GHG. Marathon run: Cardiovascular adaptation and cardiovascular risk. *Eur Heart J*. 2014;35(44):3091-3096. doi:10.1093/eurheartj/ehz502
342. L. AV, T.E. HM, D. TP, et al. Exercise-Induced Cardiac Troponin I Increase and Incident Mortality and Cardiovascular Events. *Circulation*. 2019;0(0). doi:10.1161/CIRCULATIONAHA.119.041627
343. Shephard RJ, Balady GJ. Clinical Cardiology : New Frontiers Exercise as Cardiovascular Therapy. *Circulation*. 1999;0(99):963-972. doi:10.1161/01.CIR.99.7.963
344. Roberts WO, Maron BJ. Evidence for Decreasing Occurrence of Sudden Cardiac Death Associated With the Marathon. *J Am Coll Cardiol*. 2005;46(7):1373-1374. doi:10.1016/j.jacc.2005.07.008
345. Van Sloten TT, Sedaghat S, Laurent S, et al. Carotid Stiffness Is Associated with Incident Stroke A Systematic Review and Individual Participant Data Meta-Analysis. *J Am Coll Cardiol*. 2015;9(1):1130. doi:10.1016/j.jacc.2015.08.888
346. Chiesa ST, Masi S, Shipley MJ, et al. Carotid artery wave intensity in mid- to late-life predicts cognitive decline: the Whitehall II study. *Eur Heart J*. 2019;40(28):2300-2309. doi:10.1093/eurheartj/ehz189
347. Cornelissen VA, Fagard RH. Effects of Endurance Training on Blood Pressure, Blood Pressure-Regulating Mechanisms, and Cardiovascular Risk Factors. *Hypertension*. 2005;46:667-678. doi:10.1161/01.HYP.0000184225.05629.51
348. Cornelissen VA, Goetschalckx K, Verheyden B, et al. Effect of endurance training on blood pressure regulation, biomarkers and the heart in subjects at a higher age. *Scand J Med Sci Sport*. 2011;21(4):526-534. doi:10.1111/j.1600-0838.2010.01094.x
349. Naci H, Salcher-Konrad M, Dias S, et al. How does exercise treatment compare with antihypertensive medications? A network meta-analysis of 391 randomised controlled

- trials assessing exercise and medication effects on systolic blood pressure. *Br J Sport Med.* 2018;0:1-12. doi:10.1136/bjsports-2018-099921
350. Seals DR, Tanaka H, Clevenger CM, et al. Blood pressure reductions with exercise and sodium restriction in postmenopausal women with elevated systolic pressure: role of arterial stiffness. *J Am Coll Cardiol.* 2001;38(2):506-513.
351. Tanaka H, Dinunno FA, Monahan KD, Clevenger CM, Desouza CA, Seals DR. Aging, Habitual Exercise, and Dynamic Arterial Compliance. *Circulation.* 2000;102:1270-1275.
352. Ashor AW, Lara J, Siervo M, Celis-Morales C, Mathers JC. Effects of exercise modalities on arterial stiffness and wave reflection: a systematic review and meta-analysis of randomized controlled trials. *PLoS One.* 2014;9(10):e110034. doi:10.1371/journal.pone.0110034
353. Martin JS, Casey DP, Gurovich AN, Beck DT, Braith RW. Association of Age With Timing and Amplitude of Reflected Pressure Waves During Exercise in Men. *Am J Hypertens.* 2009;24(4):415-420. doi:10.1038/ajh.2010.261
354. Townsend RR, Wilkinson IB, Schiffrin EL, et al. Recommendations for Improving and Standardizing Vascular Research on Arterial Stiffness: A Scientific Statement from the American Heart Association. Vol 66.; 2015. doi:10.1161/HYP.0000000000000033
355. Hafner NM, Womack CJ, Luden ND, Todd MK. Arterial adaptations to training among first time marathoners. *Cardiovasc Ultrasound.* 2016;14(1):19. doi:10.1186/s12947-016-0063-6
356. Pierce GL. Initiating life-long aerobic exercise 4-5 days/week before or near age 50 years: is this the “holy-grail” of preventing age-related central artery stiffness? *J Physiol.* 2018;0:1-2. doi:10.1113/JP276253
357. Kramer CM, Barkhausen J, Flamm SD, Kim RJ, Nagel E. Standardized cardiovascular magnetic resonance (CMR) protocols 2013 update. *J Cardiovasc Magn Reson.* 2013;15(1):91. doi:10.1186/1532-429X-15-91
358. Treibel TA, López B, González A, et al. Reappraising myocardial fibrosis in severe aortic stenosis: an invasive and non-invasive study in 133 patients. *Eur Heart J.* 2018;39(8):699-709. doi:10.1093/eurheartj/ehx353
359. Crapo RO, Casaburi R, Coates AL, et al. ATS statement: Guidelines for the six-minute walk test. *Am J Respir Crit Care Med.* 2002. doi:10.1164/ajrcm.166.1.at1102
360. Jones S, D'Silva A, Bhuva A, et al. Improved exercise-related skeletal muscle oxygen consumption following uptake of endurance training measured using near-infrared spectroscopy. *Front Physiol.* 2017;8(DEC):1-8. doi:10.3389/fphys.2017.01018
361. Virgin Money London Marathon Beginner 17 week training plan. <https://www.virginmoneylondonmarathon.com/en-gb/trainingplans/beginner-17-week-training-plan/>. Accessed January 28, 2018.
362. Williams B, N.R. P, M.J. B, et al. Guidelines for management of hypertension: Report of the fourth working party of the British Hypertension Society, 2004 - BHS IV. *J Hum Hypertens.* 2004;18(3):139-185. doi:http://dx.doi.org/10.1038/sj.jhh.1001683
363. St. Pierre TG, House MJ, Bangma SJ, et al. Stereological analysis of liver biopsy histology sections as a reference standard for validating non-invasive liver fat fraction measurements by MRI. *PLoS One.* 2016;11(8):1-18. doi:10.1371/journal.pone.0160789
364. Yushkevich PA, Piven J, Hazlett HC, et al. User-guided 3D active contour segmentation of anatomical structures: Significantly improved efficiency and reliability. *Neuroimage.* 2006;31(3):1116-1128. doi:10.1016/j.neuroimage.2006.01.015

References

365. Shi W, Caballero J, Ledig C, et al. Cardiac Image Super-Resolution with Global Correspondence Using Multi-Atlas PatchMatch. In: *Lecture Notes in Computer Science (Including Subseries Lecture Notes in Artificial Intelligence and Lecture Notes in Bioinformatics)*. Vol 8151 LNCS. ; 2013:9-16. doi:10.1007/978-3-642-40760-4_2
366. Smith SM, Nichols TE. Threshold-free cluster enhancement: Addressing problems of smoothing, threshold dependence and localisation in cluster inference. *Neuroimage*. 2009;44(1):83-98. doi:10.1016/j.neuroimage.2008.03.061
367. Benjamini Y, Hochberg Y. Controlling the false discovery rate: a practical and powerful approach to multiple testing. *J R Stat Soc B*. 1995;57(1):289-300. doi:10.2307/2346101
368. Biffi C, de Marvao A, Attard MI, et al. Three-dimensional cardiovascular imaging-genetics: a mass univariate framework. *Bioinformatics*. 2017;34(September 2017):97-103. doi:10.1093/bioinformatics/btx552
369. Freedman D, Lane D. A nonstochastic interpretation of reported significance levels. *J Bus Econ Stat*. 1983;1(4):292-298. doi:10.1080/07350015.1983.10509354
370. Ahrens J, Geveci B, Law C. ParaView: An End-User Tool for Large Data Visualization. *Vis Handb*. January 2005.
371. Zhong L, Su Y, Yeo S-Y, Tan R-S, Ghista DN, Kassab G. Left ventricular regional wall curvedness and wall stress in patients with ischemic dilated cardiomyopathy. *AJP Hear Circ Physiol*. 2009;296(3):H573-H584. doi:10.1152/ajpheart.00525.2008
372. Arts T, Bovendeerd PHM, Renemant RS. Relation between left ventricular cavity pressure and volume and systolic fibre stress and strain in the wall. *Biophys J*. 1991;59(January):93-102.
373. Grossman W, Braunwald E, Mann T, McLaurin LP, Green LH. Contractile state of the left ventricle in man as evaluated from end-systolic pressure-volume relations. *Circulation*. 1977;56(5):845-852. doi:10.1161/01.CIR.56.5.845
374. Savitzky A, Golay MJE. Smoothing and Differentiation of Data by Simplified Least Squares Procedures. *Anal Chem*. 1964;36(8):1627-1639. doi:10.1021/ac60214a047
375. De Cesare A, Redheuil A, Dogui A, et al. ART-FUN: an integrated software for functional analysis of the aorta. *J Cardiovasc Magn Reson*. 2009;11(Suppl 1):P182. doi:10.1186/1532-429X-11-S1-P182
376. Herment A, Kachenoura N, Lefort M, et al. Automated segmentation of the aorta from phase contrast MR images: Validation against expert tracing in healthy volunteers and in patients with a dilated aorta. *J Magn Reson Imaging*. 2010;31(4):881-888. doi:10.1002/jmri.22124
377. Herment A, Lefort M, Kachenoura N, et al. Automated estimation of aortic strain from steady-state free-precession and phase contrast MR images. *Magn Reson Med*. 2011;65(4):986-993. doi:10.1002/mrm.22678
378. Redheuil A, Yu W-C, Wu CO, et al. Reduced ascending aortic strain and distensibility: earliest manifestations of vascular aging in humans. *Hypertens (Dallas, Tex 1979)*. 2010;55(2):319-326. doi:10.1161/HYPERTENSIONAHA.109.141275
379. Multicenter Postinfarction Research Group. Risk Stratification and Survival after Myocardial Infarction. *N Engl J Med*. 1983;309(6):331-336. doi:10.1056/NEJM198308113090602
380. Grothues F, Smith GC, Moon JCC, et al. Comparison of interstudy reproducibility of cardiovascular magnetic resonance with two-dimensional echocardiography in normal subjects and in patients with heart failure or left ventricular hypertrophy. *Am J Cardiol*. 2002;90(1):29-34.

References

381. Captur G, Radenkovic D, Li C, et al. Community delivery of semiautomated fractal analysis tool in cardiac mr for trabecular phenotyping. *J Magn Reson Imaging*. 2017;46(4):1082-1088. doi:10.1002/jmri.25644
382. Musa TA, Treibel TA, Vassiliou VS, et al. Myocardial Scar and Mortality in Severe Aortic Stenosis. *Circulation*. 2018;138(18):1935-1947. doi:10.1161/CIRCULATIONAHA.117.032839
383. Najjar SS, Scuteri A, Shetty V, et al. Pulse Wave Velocity Is an Independent Predictor of the Longitudinal Increase in Systolic Blood Pressure and of Incident Hypertension in the Baltimore Longitudinal Study of Aging. *J Am Coll Cardiol*. 2008;51(14):1377-1383. doi:10.1016/j.jacc.2007.10.065
384. NHS England. NHS Standard contract for CMR. <https://www.england.nhs.uk/wp-content/uploads/2013/06/a09-cari-cardiac-mag-reson-imaging.pdf>. Published 2013.
385. Henglin M, Stein G, Hushcha P V., Snoek J, Wiltschko AB, Cheng S. Machine Learning Approaches in Cardiovascular Imaging. *Circ Cardiovasc Imaging*. 2017;10(10):1-10. doi:10.1161/CIRCIMAGING.117.005614
386. Avendi MR, Kheradvar A, Jafarkhani H. A combined deep-learning and deformable-model approach to fully automatic segmentation of the left ventricle in cardiac MRI. *Med Image Anal*. 2016;30:108-119. doi:10.1016/j.media.2016.01.005
387. Bellenger NG, Marcus NJ, Rajappan K, Yacoub M, Banner NR, Pennell DJ. Comparison of techniques for the measurement of left ventricular function following cardiac transplantation. *J Cardiovasc Magn Reson*. 2002;4(2):255-263.
388. Semelka RC, Tomei E, Wagner S, et al. Interstudy reproducibility of dimensional and functional measurements between cine magnetic resonance studies in the morphologically abnormal left ventricle. *Am Heart J*. 1990;119(6):1367-1373. doi:10.1016/S0002-8703(05)80187-5
389. Farrance I, Frenkel R. Uncertainty of measurement: A review of the rules for calculating Uncertainty components through functional relationships. *Clin Biochem Rev*. 2012;33(2):49-75.
390. Nkomo VT, Gardin JM, Skelton TN, Gottdiener JS, Scott CG, Enriquez-Sarano M. Burden of valvular heart diseases: a population-based study. *Lancet*. 2006;368(9540):1005-1011. doi:10.1016/S0140-6736(06)69208-8
391. Minamino-Muta E, Kato T, Morimoto T, et al. Impact of the left ventricular mass index on the outcomes of severe aortic stenosis. *Heart*. 2017;103(24):1992-1999. doi:10.1136/heartjnl-2016-311022
392. McCann GP, Singh A. Revisiting Reverse Remodeling After Aortic Valve Replacement for Aortic Stenosis. *J Am Coll Cardiol*. 2018;71(8):872-874. doi:10.1016/j.jacc.2017.12.036
393. Lindman BR, Stewart WJ, Pibarot P, et al. Early regression of severe left ventricular hypertrophy after transcatheter aortic valve replacement is associated with decreased hospitalizations. *JACC Cardiovasc Interv*. 2014;7(6):662-673. doi:10.1016/j.jcin.2014.02.011
394. Porras AM, McCoy CM, Masters KS. Calcific Aortic Valve Disease: A Battle of the Sexes. *Circ Res*. 2017;120(4):604-606. doi:10.1161/CIRCRESAHA.117.310440
395. Simard L, Côté N, Dagenais F, et al. Sex-Related Discordance Between Aortic Valve Calcification and Hemodynamic Severity of Aortic Stenosis: Is Valvular Fibrosis the Explanation? *Circ Res*. 2017;120(4):681-691. doi:10.1161/CIRCRESAHA.116.309306
396. Singh A, Chan DCS, Greenwood JP, et al. Symptom Onset in Aortic Stenosis. Relation

References

- to Sex Differences in Left Ventricular Remodeling. *JACC Cardiovasc Imaging*. 2019;12(1):96-105. doi:10.1016/j.jcmg.2017.09.019
397. Kwiecinski J, Chin CWL, Everett RJ, et al. Adverse prognosis associated with asymmetric myocardial thickening in aortic stenosis. *Eur Heart J Cardiovasc Imaging*. 2018;19(3):347-356. doi:10.1093/ehjci/jex052
398. Bello GA, Dawes TJW, Duan J, et al. Deep-learning cardiac motion analysis for human survival prediction. *Nat Mach Intell*. 2019;1(2):95-104. doi:10.1038/s42256-019-0019-2
399. Maceira AM, Cosín-Sales J, Roughton M, Prasad SK, Pennell DJ. Reference left atrial dimensions and volumes by steady state free precession cardiovascular magnetic resonance. *J Cardiovasc Magn Reson*. 2010;12(1):65. doi:10.1186/1532-429X-12-65
400. Petrov G, Dworatzek E, Schulze TM, et al. Maladaptive Remodeling Is Associated With Impaired Survival in Women But Not in Men After Aortic Valve Replacement. *JACC Cardiovasc Imaging*. 2014;7(11):1073-1080. doi:10.1016/j.jcmg.2014.06.017
401. Fliegner D, Schubert C, Penkalla A, et al. Female sex and estrogen receptor- attenuate cardiac remodeling and apoptosis in pressure overload. *AJP Regul Integr Comp Physiol*. 2010;298(6):R1597-R1606. doi:10.1152/ajpregu.00825.2009
402. Haddad GE, Saunders LJ, Crosby SD, et al. Human cardiac-specific cDNA array for idiopathic dilated cardiomyopathy: sex-related differences. *Physiol Genomics*. 2008;33(2):267-277. doi:10.1152/physiolgenomics.00265.2007
403. Bueno OF. The MEK1-ERK1/2 signaling pathway promotes compensated cardiac hypertrophy in transgenic mice. *EMBO J*. 2000;19(23):6341-6350. doi:10.1093/emboj/19.23.6341
404. Zwadlo C, Schmidtman E, Szaroszyk M, et al. Antiandrogenic Therapy With Finasteride Attenuates Cardiac Hypertrophy and Left Ventricular Dysfunction. *Circulation*. 2015;131(12):1071-1081. doi:10.1161/CIRCULATIONAHA.114.012066
405. Yang J, Wang F, Sun W, Dong Y, Li M, Fu L. Testosterone Replacement Modulates Cardiac Metabolic Remodeling after Myocardial Infarction by Upregulating PPAR α . *PPAR Res*. 2016;2016:4518754. doi:10.1155/2016/4518754
406. Dweck MR, Kwiecinski J. Emerging Sex Differences in Aortic Stenosis. *JACC Cardiovasc Imaging*. 2017;12(1):14-16. doi:10.1016/j.jcmg.2017.09.018
407. Corden B, de Marvao A, Dawes TJ, et al. Relationship between body composition and left ventricular geometry using three dimensional cardiovascular magnetic resonance. *J Cardiovasc Magn Reson*. 2016;18(1):32. doi:10.1186/s12968-016-0251-4
408. Gotzmann M, Grabbe S, Schöne D, et al. Alterations in Titin Properties and Myocardial Fibrosis Correlate With Clinical Phenotypes in Hemodynamic Subgroups of Severe Aortic Stenosis. *JACC Basic to Transl Sci*. 2018;3(3):335-346. doi:10.1016/j.jacbts.2018.02.002
409. Wicker P, Tarazi RC, Kobayashi K. Coronary blood flow during the development and regression of left ventricular hypertrophy in renovascular hypertensive rats. *Am J Cardiol*. 1983;51(10):1744-1749. doi:10.1016/0002-9149(83)90222-9
410. Villari B, Vassalli G, Betocchi S, Briguori C, Chiariello M, Hess OM. Normalization of left ventricular nonuniformity late after valve replacement for aortic stenosis. *Am J Cardiol*. 1996;78(1):66-71. doi:10.1016/S0002-9149(96)00229-9
411. Mitchell GF, Tardif J-C, Arnold JMO, et al. Pulsatile Hemodynamics in Congestive Heart Failure. *Hypertension*. 2001;38(6):1433-1439. doi:10.1161/hy1201.098298
412. Parker KH, Jones C. Forward and Backward Running Waves in the Arteries: Analysis

References

- Using the Method of Characteristics. *J Biomech Eng.* 1990;112:322-326.
413. Laurent S, Boutouyrie P, Asmar R, et al. Aortic stiffness is an independent predictor of all-cause and cardiovascular mortality in hypertensive patients. *Hypertension.* 2001;37(5):1236-1241. doi:10.1161/01.HYP.37.5.1236
414. Sen S, Escaned J, Malik IS, et al. Development and Validation of a New Adenosine-Independent Index of Stenosis Severity From Coronary Wave-Intensity Analysis. *J Am Coll Cardiol.* 2012;59(15):1392-1402. doi:10.1016/j.jacc.2011.11.003
415. Weber T, Chirinos JA. Pulsatile arterial haemodynamics in heart failure. *Eur Heart J.* 2018;39(43):3847-3854. doi:10.1093/eurheartj/ehy346
416. Koh TW, Pepper JR, Desouza AC, Parker KH. Analysis of wave reflections in the arterial system using wave intensity: A novel method for predicting the timing and amplitude of reflected waves. *Heart Vessels.* 1998;13(3):103-113. doi:10.1007/BF01747827
417. A. Felinger. Chapter 9 Quantitative analysis. In: *Data Analysis and Signal Processing in Chromatography.* Vol 21. ; 1998:191-209. doi:10.1016/S0922-3487(98)80028-2
418. Aguado-Sierra J, Parker KH, Davies JE, Francis D, Hughes AD, Mayet J. Arterial pulse wave velocity in coronary arteries. In: *2006 International Conference of the IEEE Engineering in Medicine and Biology Society.* Vol 1. IEEE; 2006:867-870. doi:10.1109/IEMBS.2006.259375
419. Phan TS, Li JK-J, Segers P, et al. Aging is Associated With an Earlier Arrival of Reflected Waves Without a Distal Shift in Reflection Sites. *J Am Heart Assoc.* 2016;5(9). doi:10.1161/JAHA.116.003733
420. Biglino G, Steeden JA, Baker C, et al. A non-invasive clinical application of wave intensity analysis based on ultrahigh temporal resolution phase-contrast cardiovascular magnetic resonance. *J Cardiovasc Magn Reson.* 2012;14(1):57. doi:10.1186/1532-429X-14-57
421. Mitchell GF, van Buchem MA, Sigurdsson S, et al. Arterial stiffness, pressure and flow pulsatility and brain structure and function: the Age, Gene/Environment Susceptibility – Reykjavik Study. *Brain.* 2011;134(11):3398-3407. doi:10.1093/brain/awr253
422. Mitchell GF, Hwang S-J, Vasan RS, et al. Arterial Stiffness and Cardiovascular Events. *Circulation.* 2010;121(4):505-511. doi:10.1016/S0167-8493(85)90305-5
423. Townsend RR, Wimmer NJ, Chirinos JA, et al. Aortic PWV in Chronic Kidney Disease: A CRIC Ancillary Study. *Am J Hypertens.* 2010;23(3):282-289. doi:10.1038/ajh.2009.240
424. Hoeks APG, Breteler MMB, Witteman Popele JCM, et al. Arterial Stiffness and Risk of Coronary Heart Disease and Stroke: The Rotterdam Study Arterial Stiffness and Risk of Coronary Heart Disease and Stroke The Rotterdam Study. *Circulation.* 2006;113:657-663. doi:10.1161/CIRCULATIONAHA.105.555235
425. Feigin VL, Norrving B, Mensah GA. Primary prevention of cardiovascular disease through population-wide motivational strategies: insights from using smartphones in stroke prevention. *BMJ Glob Heal.* 2016;2(2):e000306. doi:10.1136/bmjgh-2017-000306
426. Runningusa.org. Running USA Releases 2019 U.S. Running Trends Report - 2019 Running USA U.S. Running Trends Report. https://runningusa.org/RUSA/News/2019/Running_USA_Releases_2019_U.S._Running_Trends_Report.aspx. Accessed March 29, 2019.
427. Vaitkevicius P V, Fleg JL, Engel JH, et al. Effects of Age and Aerobic Capacity on

References

- Arterial Stiffness in Healthy-Adults. *Circulation*. 1993;88(4):1456-1462. doi:10.1161/01.cir.88.4.1456
428. Fujimoto N, Prasad A, Hastings J, et al. Cardiovascular Effects of 1 Year of Progressive and Vigorous Exercise Training in Previously Sedentary Individuals Older Than 65 Years of Age. *Circulation*. 2010;122(18):1797-1805. doi:10.1038/mp.2011.182.doi
429. Hickson SS, Butlin M, Graves M, et al. The Relationship of Age With Regional Aortic Stiffness and Diameter. *JACC Cardiovasc Imaging*. 2010;3(12):1247-1255. doi:10.1016/J.JCMG.2010.09.016
430. Schlatmann TJM, Becker AE. Histologic changes in the normal aging aorta: Implications for dissecting aortic aneurysm. *Am J Cardiol*. 1977;39(1):13-20. doi:10.1016/S0002-9149(77)80004-0
431. Reese RJ, Fuehrer D, Fennessy C. Runners With More Training Miles Finish Marathons Faster. [Web Page] Runners World. <https://www.runnersworld.com/run-the-numbers/runners-with-more-training-miles-finish-marathons-faster>. Published 2014.
432. Thomopoulos C, Parati G, Zanchetti A. Effects of blood-pressure-lowering treatment on outcome incidence. *J Hypertens*. 2017;35(11):2150-2160. doi:10.1097/HJH.0000000000001547
433. Hughson RL, Robertson AD, Arbeille P, et al. Increased postflight carotid artery stiffness and inflight insulin resistance resulting from 6-mo spaceflight in male and female astronauts. *Am J Physiol - Hear Circ Physiol*. 2016;310(5):H628-H638. doi:10.1152/ajpheart.00802.2015
434. Shibata S, Fujimoto N, Hastings JL, et al. The effect of lifelong exercise frequency on arterial stiffness. *J Physiol*. 2018;0:1-13. doi:10.1113/JP275301
435. Howden EJ, Sarma S, Lawley JS, et al. Reversing the Cardiac Effects of Sedentary Aging in Middle Age-A Randomized Controlled Trial: Implications for Heart Failure Prevention. *Circulation*. 2018;137(15):1549-1560. doi:10.1161/CIRCULATIONAHA.117.030617
436. Lewington S, Clarke R, Qizilbash N, Peto R, Collins R, Prospective Studies Collaboration. Age-specific relevance of usual blood pressure to vascular mortality: a meta-analysis of individual data for one million adults in 61 prospective studies. *Lancet* (London, England). 2002;360(9349):1903-1913. doi:10.1016/s0140-6736(02)11911-8
437. Cameron JD, Dart AM. Exercise training increases total systemic arterial compliance in humans. *Am J Physiol Circ Physiol*. 1994. doi:10.1152/ajpheart.1994.266.2.H693
438. Vogel T, Lepretre PM, Brechat PH, Lonsdorfer-Wolf E, Kaltenbach G, Lonsdorfer J, Benetos A. Effect of a short-term intermittent exercise-training programme on the pulse wave velocity and arterial pressure: a prospective study among 71 healthy older subjects. *Int J Clin Pract*. 2013. doi:10.1111/ijcp.12021
439. Hayashi K, Sugawara J, Komine H, Maeda S, Yokoi T. Effects of Aerobic Exercise Training on the Stiffness of Central and Peripheral Arteries in Middle-Aged Sedentary Men. *Jpn J Physiol*. 2005;55(4):235-239. doi:10.2170/jjphysiol.S2116
440. McEniery CM, Yasmin, Hall IR, et al. Normal Vascular Aging : Differential Effects on Wave Reflection and Aortic Pulse Wave Velocity. *J Am Coll Cardiol*. 2005;46(9):1753-1760. doi:10.1016/j.jacc.2005.07.037
441. Topouchian J, Asmar R, Sayegh F, et al. Changes in arterial structure and function under trandolapril-verapamil combination in hypertension. *Stroke*. 1999;30(5):1056-1064.
442. Pierce GL. Aortic Stiffness in Aging and Hypertension : Prevention and Treatment with Habitual Aerobic Exercise. *Curr Hypertens Rep*. 2017;19(90). doi:10.1007/s11906-017-

References

0788-0

443. Voges I, Jerosch-Herold M, Hedderich J, et al. Normal values of aortic dimensions, distensibility, and pulse wave velocity in children and young adults: a cross-sectional study. *J Cardiovasc Magn Reson*. 2012;14:77. doi:10.1186/1532-429X-14-77
444. Sado DM, Flett AS, Moon JC. Novel imaging techniques for diffuse myocardial fibrosis. *Rev Futur Cardiol*. 2011:16-18.
445. Mahmood SS, Levy D, Vasan RS, Wang TJ. The Framingham Heart Study and the epidemiology of cardiovascular disease: A historical perspective. *Lancet*. 2014;383(9921):999-1008. doi:10.1016/S0140-6736(13)61752-3
446. Thavendiranathan P, Grant AD, Negishi T, Plana JC, Popović ZB, Marwick TH. Reproducibility of echocardiographic techniques for sequential assessment of left ventricular ejection fraction and volumes: Application to patients undergoing cancer chemotherapy. *J Am Coll Cardiol*. 2013;61(1):77-84. doi:10.1016/j.jacc.2012.09.035
447. Bardy GH, Lee KL, Mark DB, et al. Amiodarone or an Implantable Cardioverter–Defibrillator for Congestive Heart Failure. *N Engl J Med*. 2005. doi:10.1056/nejmoa043399
448. Kadish A. Prophylactic Defibrillator Implantation — Toward an Evidence-Based Approach. *N Engl J Med*. 2005. doi:10.1056/nejme048351
449. Burki TK. Defining precision medicine. *Lancet Oncol*. 2017;18(12):e719. doi:10.1016/S1470-2045(17)30865-3
450. Bhuva A, Treibel T, Doumou G, et al. In severe aortic stenosis, decreased systemic vascular resistance is associated with a larger, thicker walled ventricle except for the septum. *Artery Res*. 2017;20:107. doi:https://doi.org/10.1016/j.artres.2017.10.188
451. Broyd CJ, Rigo F, Nijjer S, et al. Regression of left ventricular hypertrophy provides an additive physiological benefit following treatment of aortic stenosis: Insights from serial coronary wave intensity analysis. *Acta Physiol*. 2018;224(4). doi:10.1111/apha.13109
452. Hametner B, Parragh S, Weber T, Wassertheurer S. Wave intensity of aortic root pressure as diagnostic marker of left ventricular systolic dysfunction. *PLoS One*. 2017;12(6):1-14. doi:10.1371/journal.pone.0179938